Dissertation
submitted to the
Combined Faculties for the Natural Sciences and for Mathematics
of the Ruperto-Carola University of Heidelberg, Germany
for the degree of
Doctor of Natural Sciences

Put forward by
Diplom-Physikerin Korinna Christine Zapp
born in Eckernförde
Oral examination: 18 December 2008

A Monte Carlo Model for Jet Evolution With Energy Loss

Referees: Prof. Dr. Johanna Stachel
Prof. Dr. Carlo Ewerz

Ein Monte Carlo Modell für Jet Entwicklung mit Energieverlust

In dieser Arbeit wird das Monte Carlo Modell JEWEL (Jet Evolution With Energy Loss) vorgestellt. Es verbindet die störungstheoretische Entwicklung einer Partonkaskade im Endzustand einer harten Reaktion mit Wechselwirkungen in einem Medium, wie sie in ultrarelativistischen Kollisionen von Atomkernen auftreten. Es enthält ein mikroskopisches Modell für elastische Streuung, so dass in jedem Schritt während der Entwicklung die Wahrscheinlichkeit für eine Verzweigung (splitting) mit der für Streuung verglichen werden kann. Radiative Prozesse werden schematisch durch eine Erhöhung der Verzweigungswahrscheinlichkeit behandelt. Die störungstheoretische Partonkaskade ist mit einem Hadronisierungsmodell verbunden, das auch für Jets in nuklearen Umgebungen geeignet ist. In der Abwesenheit von Mediumeffekten wird gezeigt, dass JEWEL wichtige Messungen von Jeteigenschaften in e^{+}+e^{-} Kollisionen reproduziert. Im Medium werden Modifikationen von Jetcharakteristika durch elastischen und radiativen Energieverlust sowie jetinduzierte Veränderungen des Mediums charakterisiert. Einige Jetobservablen, die eine Unterscheidung zwischen elastischem und radiativem Energieverlust ermöglichen sollten, können gefunden werden. Die Verbreiterung von Jets durch Energieverlust ist auf die Hadronisierung sensitiv, aber allgemein ist in JEWEL nur eine geringe Verbreiterung zu beobachten. Schließlich werden Weiterentwicklungen des Modells skizziert. Dazu zählen die Geometrie und Expansion des Mediums und eine mikroskopische Beschreibung von inelastischer Streuung. Außerdem wird ein Verfahren vorgestellt, wie die Unterdrückung von induzierter Gluonabstrahlung aufgrund eines Interferenzphänomens (LPM-Effekt) in Monte Carlo-Modelle implementiert werden kann.

A Monte Carlo Model for Jet Evolution With Energy Loss

In this thesis the Monte Carlo generator JEWEL (Jet Evolution With Energy Loss) is presented. It interleaves the perturbative final state parton shower evolution with medium interactions occurring in ultra-relativistic nuclear collisions. It contains a microscopic model of elastic scattering so that the probability for scattering can be compared to the splitting probability in each step during the evolution. Radiative processes are included in a schematic way by increasing the splitting probability. The perturbative parton shower is interfaced with a string hadronisation model that is suited also for jets in a nuclear environment. In the absence of medium effects JEWEL reproduces important benchmark measurements in e^{+}+e^{-} collisions. In the medium the modifications of jet characteristics due to collisional and radiative energy loss as well as the jet-induced modifications of the medium are characterised. A set of jet observables that should allow to discriminate between elastic and radiative energy loss is identified. Broadening of jets due to energy loss is sensitive to hadronisation, but generally very little broadening is observed in JEWEL. Finally, further developments of the model are outlined. This includes the geometry and expansion of the medium and a microscopic model of inelastic scattering. Furthermore, a prescription how to include the suppression of induced gluon radiation due to an interference phenomenon (LPM effect) in a Monte Carlo model is presented.

Contents

CHAPTER 1

Introduction

In collisions of ultra-relativistic heavy nuclei the produced matter is hot and dense enough to form a state of deconfined quarks and gluons with restored chiral symmetry, the quark-gluon plasma (QGP). Due to the rapid expansion of the system the QGP can only exist for a few fm/c before it undergoes a phase transition to normal hadronic matter, which means that it cannot be observed directly. Thus information about the properties of the QGP can only be inferred from indirect measurements. Among other observables the energy loss of energetic partons due to interactions with the medium, which leads to a suppression of high transverse momentum hadrons known as 'jet quenching', is used to probe the medium.

The interactions of a hard parton with the medium can be either elastic [1–9] or inelastic [10–15]. In both cases energy is transferred to the scattering centre, but in inelastic collisions the main source of energy loss is the radiation of additional gluons. The projectile parton hadronises with reduced energy, which leads – in combination with the steeply falling partonic spectrum – to a suppression of energetic hadrons relative to the expectations from proton-proton collisions. Experiments at the Relativistic Heavy Ion Collider (RHIC) at the Brookhaven National Laboratory support this picture [16–19]. It is commonly believed that gluon bremsstrahlung is responsible for the dominant part of the energy loss, but the microscopic mechanisms are not entirely understood.

Due to the limited reach in transverse momentum the observation of jets at RHIC is largely limited to leading hadrons. The suppression of single-inclusive hadron spectra is rather well described by different models of radiative energy loss. There are, however, good reasons to go beyond leading hadrons and study the distributions of sub-leading fragments. Firstly, at the Large Hadron Collider (LHC) at CERN a large fraction of the jet fragmentation pattern will become accessible above the soft background from the medium [20–22]. Secondly, distributions of sub-leading fragments are likely to be sensitive to the nature of the microscopic mechanism underlying partonic energy loss and can thus help to discriminate between different models. This will then also lead to a better characterisation of medium properties. And last but not least the energy lost by the leading parton must be carried by associated particles so that a model for the modification of the entire jet fragmentation pattern is necessary in order to disentangle jets from background and understand the jet-induced modifications of the medium.

Monte Carlo generators are widely used for the simulation of final state parton showers in vacuum [23–25] where one has theoretical control over the dynamics. An extended version of such a parton shower including medium effects can help to understand jet quenching. In particular, it has the following advantages:

1. Parton showers correctly describe jet evolution and – provided they are supplemented with a suitable hadronisation model – hadronisation in vacuum thus providing a sound baseline on top of which medium effects can be added. Furhermore, conclusions from heavy ion data are usually drawn by comparing them to a proton-proton baseline with jet evolution in vacuum and models should be able to do the same.

2. Monte Carlo generators produce complete final states with exact energy and momentum conservation. This is particularly important since sub-leading particles are sensitive to energy-momentum conservation and affected by trigger conditions. Apart from that most of the analytical calculations of radiative energy loss are based on an interference phenomenon but do not conserve energy and momentum exactly at each vertex. It is therefore interesting to investigate the role of exact energy-momentum conservation.

3. In a Monte Carlo model it is relatively easy to implement different microscopic descriptions of the interaction of a hard parton with the medium in the same framework. One can thus directly compare and hopefully constrain different mechanisms conjectured to underly jet quenching. Ideally, this would in the end lead to a better understanding also of the medium and its properties.

4. Experimental cuts, trigger conditions and other constraints can easily be implemented in Monte Carlo models thus facilitating the comparison between data and theory. Furthermore, the final states produced by the parton shower can be used in detector simulations and help to develop analysis strategies.

The most severe disadvantage of Monte Carlo implementations of parton showers is that, since they are based on probabilistic iterations, they have no natural way of including interference phenomena. There are, however, cases in which an effective description suitable for Monte Carlo implementations can be found. Another problem is that interlinking the parton shower evolution in vacuum with medium effects will involve model dependent assumptions. Thanks to the flexibility of Monte Carlo models one can, however, try to quantify the uncertainties related to details of the modelling.

In this work the first version of a Monte Carlo model for parton shower evolution in a medium called JEWEL (which stands for Jet Evolution With Energy Loss) is presented. It is based on a parton shower ordered in virtuality where the shower evolution is interleaved with scatterings in the medium. The relative probabilities for splitting and scattering are given by the lifetime of virtual states compared to the mean free path in the medium.

It is related to the so-called 'quenching weights' [26, 27], which are energy loss probabilities obtained by probabilistic iteration of gluon radiation or elastic scattering which has also lead to modified DGLAP evolution equations [9, 28]. These approaches have partly been extended beyond leading hadron spectra to include jet broadening [29, 30], two particle correlations [31], the effect of collective flow on jets [32,33], modifications of jet multiplicity distributions [29,34] and jet hadrochemistry [35]. A Monte Carlo model has the potential to advance this field due to its flexibility and the advantages listed above.

CHAPTER 2

Basics of Quantum Chromodynamics

This chapter briefly introduces basic concepts of Quantum Chromodynamics, which is the theory of the strong interaction, with emphasis on jet physics, i.e. how jets arise, how they can be characterised and how they can be described theoretically. It follows to a large extent [36] and, to a somewhat lesser extent, [37]. Other standard textbooks, that focus more on the theoretical framework, are [38–41].

2.1. Fundamentals of Quantum Chromodynamics

2.1.1. Symmetries

In the early days of investigations of the strong interaction it was noticed that the hadrons form multiplets, which can be identified as irreducible representations of $SU(3)$. As an example, the light pseudoscalar mesons, which are the lightest hadrons, are shown in figure 2.1. This class contains nine particles, that form a singlet (the η') and an octet. The η and the π^0 occupy the same place in the $S - I_3$ (strangeness-isospin) diagram, but the η is an isospin singlet while the π^0 is part of the isospin triplet. The pseudoscalar particles have vanishing total angular momentum and odd parity.

There are more multiplets, a baryon octet and decuplet, for instance. This observation suggests that there are also particles that transform under the fundamental respresentation of $SU(3)$. These are the light quarks up (u), down (d) and strange (s), which are also called the light quark *flavours*. The hadrons are combinations of quarks and antiquarks. However, $SU(3)_{\text{flavour}}$ was found to be only an approximate symmetry of the strong interaction. Later three more flavours were discovered, namely charm (c), beauty (also called bottom, b) and top (t), which are much heavier and are therefore called the heavy flavours. The top is in fact so heavy that it doesn't bind into hadrons because its lifetime is very short.

So far the observation that not all representations of $SU(3)_{\text{flavour}}$ are realised can-

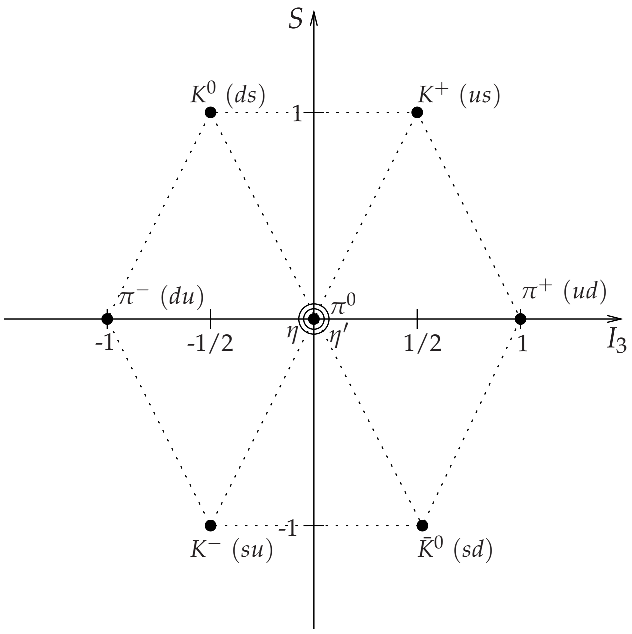

Figure 2.1.: $S - I_3$ diagram of the light pseudoscalar mesons, S is the strangeness and I_3 the third isospin component.

not be explained. In particular, the fundamental representation is not observed. All observed particles are either a combination of a quark and an antiquark or of three quarks. This lead to the postulation of *colour*. The colour is the 'charge' of the strong interaction, the corresponding symmetry group is $SU(3)_{\text{colour}}$. The quarks transform under the fundamental representation of $SU(3)_{\text{colour}}$, the adjoint respresentation is realised by the gluons. The colour charge can take the values red, green and blue. The quarks carry one of the colours, the antiquarks carry the anticolour and the gluons can be thought of as having a colour and an anticolour. There are nine colour-anticolour combinations, but one of them is a singlet and would correspond to a non-interacting gluon. Only colour neutral combinations of quarks and antiquarks, which are invariant under $SU(3)_{\text{colour}}$ transformations, correspond to observable particles. This means that two types of hadrons are allowed: the mesons, which consist of a quark and an antiquark, and the baryons, which are a combination of three quarks. This also means that the quarks and gluons themselves are not observable.

2.1.2. The QCD Lagrangian

The theory of the strong interaction, which describes the behaviour and interactions of quarks and gluons, is called Quantum Chromodynamics (QCD). Its core is the Langrangian density, which is given by

$$\mathcal{L}_{\text{QCD}} = \mathcal{L}_{\text{classical}} + \mathcal{L}_{\text{gauge-fixing}} + \mathcal{L}_{\text{ghost}}\,, \tag{2.1}$$

with the classical Langrangian density

$$\mathcal{L}_{\text{classical}} = -\frac{1}{4}F^{A}_{\alpha\beta}F^{\alpha\beta}_{A} + \sum_{\text{flavours}} \bar{q}_a(i\not{D} - m)_{ab}q_b\,. \tag{2.2}$$

Indices $a, b, \ldots$ run over the three colour triplet charges of the quarks and antiquarks, $A, B, \ldots$ denote the colour octet charges carried by gluons. D is the covariant derivative, q_a are the quark fields with masses m and $F^{A}_{\alpha\beta}$ is the field strength tensor, which is related to the gluon field $\mathcal{A}^{A}_{\alpha}$ via

$$F^{A}_{\alpha\beta} = \partial_\alpha \mathcal{A}^{A}_{\beta} - \partial_\beta \mathcal{A}^{A}_{\alpha} - g f^{ABC}\mathcal{A}^{B}_{\alpha}\mathcal{A}^{C}_{\beta}\,. \tag{2.3}$$

f^{ABC} are the structure constants of $SU(3)$ and g is the coupling constant. The classical Lagrangian density describes the propagation and interaction of quarks and gluons. The gluons are the so-called gauge bosons, which mediate the strong force. Unlike in QED, where the photon carries no electric charge, the gluons carry themselves colour charge. This leads to the gluon self-interaction and gives rise to the last term of equation (2.3) making QCD a non-abelian theory.

The Langrangian has a very important symmetry: It is invariant under local gauge transformations, i.e. a local redefinition of the quark and gluon fields. However, in order for quantisation to work out the gauge has to be fixed by adding the gauge-fixing term $\mathcal{L}_{\text{gauge-fixing}}$ to the Lagrangian. This creates unphysical degrees of freedom, which have to be cancelled by the ghost term. The ghost fields do not correspond to physical particles. The result of a calculation will not depend on the gauge chosen, but there are usually clever choices which simplify the computations. Gauge invariance requires the gluons to be massless, while the quarks can be massive. QCD makes no prediction about the quark masses, they enter the theory as parameters.

The full theory is not exactly solvable, but in regimes with sufficiently weak interactions perturbation theory is applicable. The interaction is then regarded as a small perturbation of the free theory and useful results can be obtained from an expansion around the free theory with the coupling constant as expansion parameter. The contributions to the series can be constructed systematically order by order using Feynman diagrams (figure 2.2). The lines represent freely propagating particles, the interaction takes place at the vertices. In addition to the quark-gluon vertex, which is analogous to QED, there is also the three-gluon and the four-gluon vertex, which express the gluon self-interaction. Each vertex comes with a factor g (except the four-gluon vertex, which is proportional to g^2). For a given process, i.e. given initial and final particles, all diagrams with the same number of vertices contribute to the same order in perturbation theory. Figure 2.2 shows examples for diagrams of different orders for elastic quark-quark scattering.

Higher order calculations contain diagrams with loops. The loop momentum is unconstrained and has to be integrated giving rise to divergent integrals. In *renormalisable* field theories such as QCD [42, 43] the divergent parts can be absorbed in a redefinition of the parameters of the theory (masses and coupling constants) to all orders in perturbation theory. The observable quantities are the renormalised ones, which are finite (implying that the unphysical 'bare' quantities are infinite).

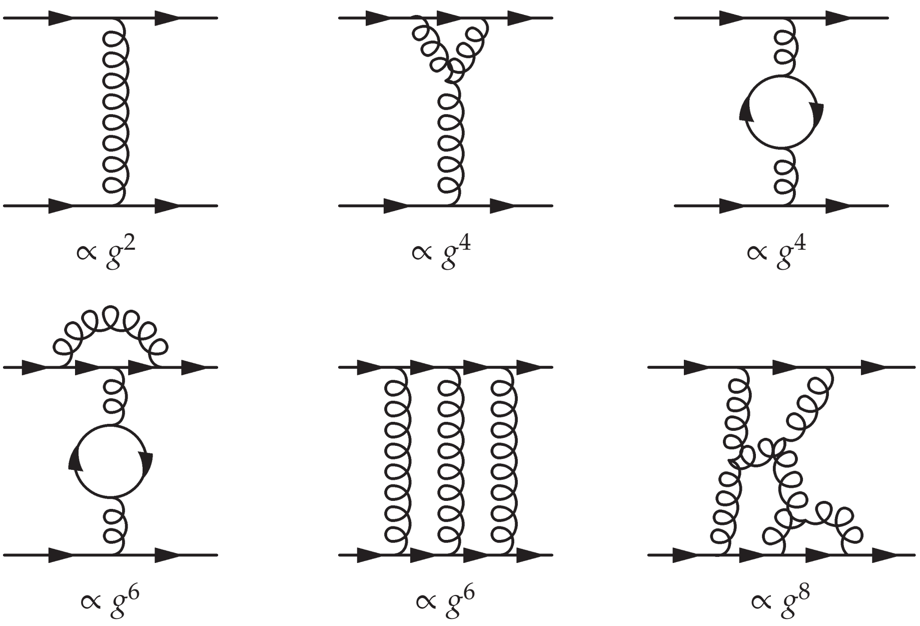

Figure 2.2.: Examples of Feynman diagrams contributing to quark-quark scattering; straight lines stand for quarks, curly lines represent gluons.

The renormalisation procedure is not unique, but in any case it introduces a dimensionful parameter, the renormalisation scale μ. One widely used renormalisation scheme is the *dimensional regularisation* [44, 45], where the number d of space-time dimensions is reduced such that the loop integrals become finite. In the limit $d \to 4$ the singular part of the integral can be isolated and absorbed in the renormalised parameters. The renormalisation scale μ is in this case needed to keep the coupling dimensionless when d is changed. Different renormalisation schemes lead to different renormalisation scales, the transformations of renormalised quantities when μ is changed are generated by the *renormalisation group* [46]. Observable quantities must be independent of the choice of renormalisation scheme, which is ensured by the *renormalisation group equations*.

2.1.3. The Running Coupling

It is common practice to characterise the (strong) coupling strength in terms of

$$\alpha_s \equiv \frac{g^2}{4\pi}, \tag{2.4}$$

which is analogous to the fine structure constant in QED.

A dimensionless observable O with a large scale Q^2 can in fact only depend on the ratio Q^2/μ^2 and the coupling, which also depends on μ. The renormalisation group equation stating the invariance of the observable with respect to μ reads in this case

$$\mu^2 \frac{\mathrm{d}}{\mathrm{d}\mu^2} O\left(\frac{Q^2}{\mu^2}, \alpha_s(\mu^2)\right) = \left[\mu^2 \frac{\partial}{\partial \mu^2} + \mu^2 \frac{\partial \alpha_s(\mu^2)}{\partial \mu^2} \frac{\partial}{\partial \alpha_s}\right] O\left(\frac{Q^2}{\mu^2}, \alpha_s(\mu^2)\right) = 0\,. \tag{2.5}$$

Figure 2.3.: Leading order contributions to the β-function.

It is convenient to define

$$t = \ln\left(\frac{Q^2}{\mu^2}\right) \quad \text{and} \quad \beta(\alpha_\mathrm{s}) = \mu^2 \frac{\partial \alpha_\mathrm{s}(\mu^2)}{\partial \mu^2} \tag{2.6}$$

and to rewrite equation (2.5) as

$$\left[-\frac{\partial}{\partial t} + \beta(\alpha_\mathrm{s}) \frac{\partial}{\partial \alpha_\mathrm{s}}\right] O(e^t, \alpha_\mathrm{s}) = 0\,. \tag{2.7}$$

This equation can be solved by introducing a running coupling $\alpha_\mathrm{s}(Q^2)$ via

$$t = \int\limits_{\alpha_\mathrm{s}(\mu^2)}^{\alpha_\mathrm{s}(Q^2)} \frac{\mathrm{d}\alpha'}{\beta(\alpha')}\,. \tag{2.8}$$

The scale dependence is then completely in the running coupling and $O(1, \alpha_\mathrm{s}(Q^2))$ is a solution of equation (2.7).

The β-function defined in equation (2.6) can be calculated in perturbation theory [47,48] and is of the form

$$\beta(\alpha_\mathrm{s}) = -b\alpha_\mathrm{s}^2(1 + b'\alpha_\mathrm{s} + b''\alpha_\mathrm{s}^2 + \mathcal{O}(\alpha_\mathrm{s}^3))\,. \tag{2.9}$$

The diagrams contributing to leading order (one loop approximation) are shown in figure 2.3. The result for b is

$$b = \frac{33 - 2n_\mathrm{f}}{12\pi}\,, \tag{2.10}$$

where n_f is the number of quark flavours that can be excited in the quark loop (figure 2.3).

In leading order equation (2.8) can be integrated directly. The integration constant Λ^2_QCD is chosen such that it represents the scale at which the coupling diverges [49].

$$\ln\left(\frac{Q^2}{\Lambda^2_\mathrm{QCD}}\right) = -\int\limits_{\alpha_\mathrm{s}(Q^2)}^{\infty} \frac{\mathrm{d}\alpha'}{\beta(\alpha')} = \int\limits_{\alpha_\mathrm{s}(Q^2)}^{\infty} \frac{\mathrm{d}\alpha'}{b\alpha'^2} = \frac{1}{b\alpha_\mathrm{s}(Q^2)} \tag{2.11}$$

$$\Rightarrow \quad \alpha_\mathrm{s}(Q^2) = \frac{12\pi}{(33 - 2n_\mathrm{f}) \ln\left(\frac{Q^2}{\Lambda^2_\mathrm{QCD}}\right)} \tag{2.12}$$

The parameter Λ_{QCD} cannot be calculated in QCD, but α_s can be measured. The experimentally found value is

$$\Lambda_{\mathrm{QCD}} \simeq 200\,\mathrm{MeV}\,. \tag{2.13}$$

The running of the coupling has important consequences for the phenomenology of QCD, as will be discussed briefly in the next section.

2.1.4. Asymptotic Freedom and Confinement

The scale Q^2 depends on the process under consideration. Elastic scattering, for instance, is characterised by the momentum transfer while in the case of heavy quark production one would rather chose the heavy quark mass. The coupling constant α_s decreases with increasing Q^2 (equation (2.12)), i.e. the interaction gets weaker for higher momentum transfers, which correspond to small distances. This behaviour is called *asymptotic freedom* and is a consequence of the non-abelian nature of QCD. Diagrams like the right hand side of figure 2.3 with gluon loops lead to the negative sign of the β-function, which is responsible for asymptotic freedom. In QED these kinds of diagrams are absent and the coupling increases with the scale. This can be interpreted as screening of the electric charge due to polarisation of the vacuum fluctuations. In QCD, however, there is no simple intuitive picture to explain the anti-screening of the colour charge.

As a consequence of asymptotic freedom, perturbation theory is a meaningful concept for processes with large scales ('hard' processes), where one can think of quarks and gluons as individual objects. In regimes of small ('soft') scales perturbation theory breaks down and the intuitive way of thinking in terms of Feynman diagrams is not appropriate any more. Calculations become more difficult and less reliable. Perturbation theory is expected to be applicable for scales larger than a few GeV.

In contrast to the weak coupling regime, where quarks and gluons are the relevant degrees of freedom, they bind to form hadrons when the coupling becomes large. As discussed already in section 2.1.1 hadrons are colour neutral combinations of quarks, which carry the quantum numbers, and gluons, which are responsible for the quark binding. The formation of colour neutral states as only observable objects is known as *confinement*. Confinement – contrary to asymptotic freedom – is not a prediction of perturbative QCD. It is currently not well understood due to the problems with calculations in the strong coupling regime, but numerical solutions of QCD (lattice QCD) suggest that confinement is in fact a property of the QCD Langrangian.

2.2. Jets and Jet Evolution

Confinement dictates that when quarks or gluons are produced or kicked out of a hadron in an experiment they have to transform into hadrons. The process of hadronisation must conserve energy and momentum. The hadrons stemming from an energetic parton form a collimated spray, which is called *jet*. The production of hard partons involves a large scale and is thus calculable in perturbation theory. This fact together with the experimental signature makes jets an interesting tool for testing and understanding QCD.

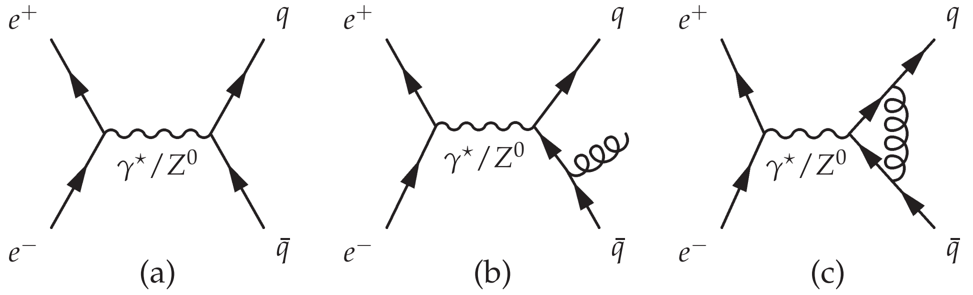

Figure 2.4.: Leading order diagram for $e^+ + e^- \rightarrow q + \bar{q}$ and examples for $\mathcal{O}(\alpha_\mathrm{s})$ QCD corrections (real and virtual gluon emission).

2.2.1. Electron-Positron Annihilation into Hadrons

The production of hadrons in e^++e^- collisions is a process, that is well suited for a variety of QCD studies, because it has a well defined initial state and strong interactions are only present in the final state. The electron-positron pair annihilates into a virtual photon or a Z^0 boson, which decays in leading order into a quark-antiquark pair (figure 2.4 (a)). The relevant scale for this process is the centre-of-momentum energy $\sqrt{s}$ of the electron-positron pair (assuming for the moment that the quarks are massless). Confinement dictates that the quark and antiquark have to be converted into hadrons. However, this happens at a lower scale Λ_QCD. For sufficiently high energies $\sqrt{s}$ the timescale $1/\sqrt{s}$ for the hard process is much smaller than the timescale $1/\Lambda_\mathrm{QCD}$ for the hadronisation so that the latter cannot influence the physics at the hard vertex. Therefore, the cross section for $\mathrm{e}^+\mathrm{e}^-$ annihilation into any hadronic final state is given by the cross section for annihilation into a quark-antiquark pair plus any number of gluons.

For values of $\sqrt{s}$ that are much smaller than the Z^0 mass (91.2 GeV) the contribution from the Z^0 can be neglected and life becomes much easier because there are no complications due to weak interaction effects. The leading order (figure 2.4 (a)) cross section for the production of any quark-antiquark pair is then given by

$$\sigma_\mathrm{LO}(e^+e^- \rightarrow q\bar{q}) = N_\mathrm{c} \sum_q \frac{4\pi\alpha^2}{3s} e_q^2 = \sigma_0 N_\mathrm{c} \sum_q e_q^2 , \tag{2.14}$$

where e_q is the quark charge, N_c is the number of colours and α is the fine structure constant. The only difference between the cross section for the production of hadrons and the one for production of a muon pair is the charge. The ratio of the two is therefore simply

$$R = \frac{\sigma_\mathrm{LO}(e^+e^- \rightarrow q\bar{q})}{\sigma_\mathrm{LO}(e^+e^- \rightarrow \mu^+\mu^-)} = N_\mathrm{c} \sum_q e_q^2 . \tag{2.15}$$

The experimental results are consistent with $N_\mathrm{c} = 3$ and 5 flavours with different masses, that start to contribute at different beam energies (the top quark is too heavy to be seen).

The quark or the antiquark can radiate a real gluon as shown in figure 2.4 (b) giving rise to a next-to-leading order correction to the total cross section. Written in terms of the variables $x_1 = 2E_\mathrm{q}/\sqrt{s}$ and $x_2 = 2E_{\bar{\mathrm{q}}}/\sqrt{s}$, i.e. the energy fractions of the quark and the antiquark respectively, the cross section reads

$$\sigma_{\mathrm{q}\bar{\mathrm{q}}\mathrm{g}} = \sigma_0\, 3 \sum_q e_q^2 \int \mathrm{d}x_1 \mathrm{d}x_2\, \frac{4}{3}\,\frac{\alpha_\mathrm{s}}{2\pi}\,\frac{x_1^2 + x_2^2}{(1-x_1)(1-x_2)}\,. \tag{2.16}$$

The integrand has two kinds of singularities: When the gluon is soft (i.e. $E_\mathrm{g} \to 0$) and when it is collinear with either the quark or the antiquark. These kinds of singularities are called infra-red singularities (in contrast to the ultra-violet divergences that were taken care of by renormalisation) and are often encountered in perturbative calculations. They are connected to the break-down of perturbation theory and have to be removed in a physically meaningful way.

There is another kind of higher-order corrections called vertex corrections (figure 2.4 (c)). This diagram is also divergent but has the opposite sign. There are two additional diagrams where the virtual gluon is emitted and absorbed by the same (anti)quark line. When the real and virtual gluon corrections are added the divergences cancel and the result for the total cross section is finite [1].

$$\sigma_\mathrm{NLO} = \sigma_0\, 3 \sum_q e_q^2 \left(1 + \frac{\alpha_\mathrm{s}}{\pi}\right) \tag{2.17}$$

This is so because the total cross section is an infra-red safe quantity, which means that splitting a particle in two with one of them soft or collinear does not change the outcome. In this case it is only required that at least one hadron is produced and this result is not affected by additional gluons in the final state. There is a theorem stating that perturbative results for suitably defined infra-red save and inclusive quantities are always finite when the complete order in perturbation theory is calculated [50–52].

2.2.2. Fragmentation Functions, Scaling Violations and the DGLAP Equations

The cross section for $\mathrm{e}^+\mathrm{e}^-$ annihilation into hadrons is an inclusive quantity in the sense that it does not require a particular hadronic final state. In this case it was not necessary to have any knowledge about the hadronisation. As soon as one is interested in a particular hadronic final state one has to deal with the hadronisation process, which is not calculable in perturbation theory. This section is devoted to single-inclusive cross sections, where a certain hadron h is produced and the rest of the final state is irrelevant. Generally, the calculations become more and more complicated as the quantity gets more exclusive, i.e. a more detailed knowledge about the hadronic final state is required.

The fragmentation function $D_i^h(x, Q^2)$ is defined as the differential probability for a parton i (quark or gluon) to fragment into a hadron h taking a fraction x of the

---

[1] The virtual gluon corrections have infra-red and ultra-violet divergences, but the latter cancel and so the $\mathcal{O}(\alpha_\mathrm{s})$ result is independent of μ.

parton's energy. The cross section for the production of h with energy E_h in a process $a + b \rightarrow h + X$ can be written as

$$\frac{\mathrm{d}\sigma}{\mathrm{d}E_h}(ab \rightarrow hX) = \sum_i \int \mathrm{d}E_i \frac{\mathrm{d}\sigma}{\mathrm{d}E_i}(ab \rightarrow iX) D_i^h \left(\frac{E_h}{E_i}, Q^2_{\text{hard}} \right) , \tag{2.18}$$

where $\mathrm{d}\sigma/\mathrm{d}E_\mathrm{i}$ is the differential cross section for the production of a parton i with energy E_i and Q^2_{hard} is the characteristic scale of the hard process (e.g. s in the case of $\mathrm{e}^+\mathrm{e}^-$ annihilation). It is also useful to define a fragmentation function D_i^j for the fragmentation of a parton i into another parton j.

The fragmentation functions are scale dependent, this effect is called *scaling violation*. An intuitive explanation can be given in terms of virtuality of the partons. The partons, that are produced in the hard interactions, are virtual, i.e. $E^2 \neq p^2$ (assuming massless partons). Such states are allowed by the uncertainty principle, but can exist only for a short time. The virtuality quantifies the deviation from the mass-shell and is usually chosen as the virtual mass squared $E^2 - p^2$. The initial virtuality directly after production in the hard process is of order Q^2_{hard}. The partons reduce their virtuality through radiation of gluons (gluons can also split into a quark-antiquark pair) thus giving rise to the scaling violations. But the probability for radiation of a soft or collinear gluon was already found to be divergent, so that a perturbative calculation of the scaling violation seems at first sight to be impossible. This divergence is of course not real but arises from an attempt to use perturbation theory in a regime where it is not applicable. The *factorisation theorem* states that the soft non-perturbative part can be separated from the perturbative one leaving two finite pieces. The non-perturbative function is universal, i.e. it does not depend on the hard process. It has to be measured, but once it is measured in one process it can be used in any other to make predictions. It can also be measured for different processes and compared, since QCD predicts the two to be equal this measurement can be used as a test of QCD. Factorisation means for the fragmentation functions, that they can be written in the form

$$D_i^{j/h}(x, Q^2) = \sum_k \int \mathrm{d}z\, K_i^k(z, Q^2, Q_0^2) D_k^{j/h} \left(\frac{x}{z}, Q_0^2 \right) . \tag{2.19}$$

The kernel K_i^k can be calculated, provided Q^2 and Q_0^2 are in the perturbative regime, and $D_k^{j/h}(x, Q_0^2)$ is the non-perturbative piece that has to be measured.

There are three possible splitting processes: $q \rightarrow q + g$, $g \rightarrow g + g$ and $g \rightarrow q + \bar{q}$. The differential splitting probability for a parton of type a with virtuality Q^2 is given by

$$\mathrm{d}\mathcal{P}^{(a)}_{\text{split}}(z, Q^2) = \sum_b \frac{\alpha_\mathrm{s}}{2\pi} \hat{P}_{ba}(z)\, \mathrm{d}z\, \frac{\mathrm{d}Q^2}{Q^2} , \tag{2.20}$$

where $\hat{P}_{ba}(z)$ is the unregularised splitting function for the process $a \rightarrow b + c$ with the energy fraction z taken by b. The splitting functions have a perturbative expansion,

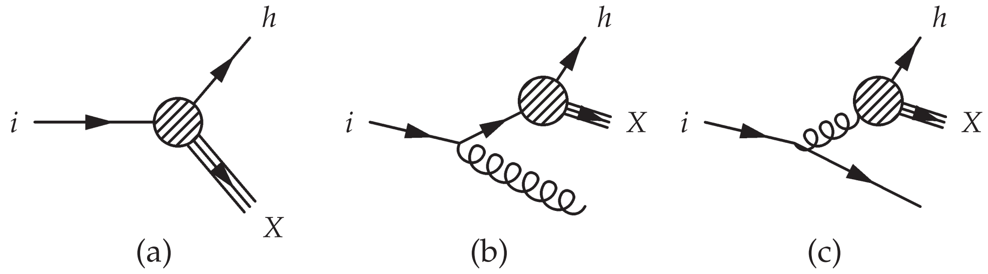

Figure 2.5.: Diagrams for the fragmentation of i to h, (b) and (c) lead to scaling violations.

the leading order terms are

$$\hat{P}_{qq}(z) = \frac{4}{3}\frac{1+z^2}{1-z} \tag{2.21}$$

$$\hat{P}_{gg}(z) = 3\left[\frac{z}{1-z}+\frac{1-z}{z}+z(1-z)\right] \tag{2.22}$$

$$\hat{P}_{qg}(z) = \frac{1}{2}\left[z^2+(1-z)^2\right] \tag{2.23}$$

The change of the quark into h (or j) fragmentation function in a small virtuality interval is given by

$$\begin{aligned} Q^2\frac{\partial D_{\mathrm{q}}^{h/j}(x,Q^2)}{\partial Q^2} &= \int_0^1 \mathrm{d}z\,\frac{\alpha_{\mathrm{s}}}{2\pi}\hat{P}_{\mathrm{qq}}(z)\int_0^1 \mathrm{d}y\,D_{\mathrm{q}}^{h/j}(y,Q^2)\delta(yz-x) \\ &+ \int_0^1 \mathrm{d}z\,\frac{\alpha_{\mathrm{s}}}{2\pi}\hat{P}_{\mathrm{gq}}(z)\int_0^1 \mathrm{d}y\,D_{\mathrm{g}}^{h/j}(y,Q^2)\delta(yz-x) \\ &- \int_0^1 \mathrm{d}z\,\frac{\alpha_{\mathrm{s}}}{2\pi}\hat{P}_{\mathrm{qq}}(z)D_{\mathrm{q}}^{h/j}(x,Q^2) \qquad (2.24) \\ &= \int_x^1 \frac{\mathrm{d}z}{z}\,\frac{\alpha_{\mathrm{s}}}{2\pi}\left\{\hat{P}_{\mathrm{qq}}(z)D_{\mathrm{q}}^{h/j}\left(\frac{x}{z},Q^2\right)+\hat{P}_{\mathrm{gq}}(z)D_{\mathrm{g}}^{h/j}\left(\frac{x}{z},Q^2\right)\right\} \\ &- \int_0^1 \mathrm{d}z\,\frac{\alpha_{\mathrm{s}}}{2\pi}\hat{P}_{\mathrm{qq}}(z)D_{\mathrm{q}}^{h/j}(x,Q^2)\,. \qquad (2.25) \end{aligned}$$

The first term corresponds to figure 2.5 (b) and represents the probability for radiating a gluon with subsequent fragmentation of the quark into h (or j). The second contribution comes from a splitting process where the radiated gluon fragments into h/j (figure 2.5 (c)). The last term is needed to conserve probability and comes from the fact that a quark that has split in a quark and a gluon cannot itself produce the hadron (figure 2.5 (a)). This expression is finite, since the singularity of $\hat{P}_{\mathrm{gq}}(z)$ at $x \rightarrow 0$ lies outside the integration region and the singularity of $\hat{P}_{\mathrm{qq}}(z)$ at $x \rightarrow 1$ is the same in both integrals. It is often convenient to make this explicit by defining the regularised splitting functions as

$$P_{ba}(z) = \hat{P}_{ba}(z)_+ \,, \tag{2.26}$$

where the 'plus prescription' is defined by

$$\int_0^1 \mathrm{d}x \, \frac{f(x)}{(1-x)_+} = \int_0^1 \mathrm{d}x \, \frac{f(x)-f(1)}{(1-x)} \quad \text{and} \quad \frac{1}{(1-x)_+} = \frac{1}{1-x} \text{ for } 0 \leq x < 1 \,. \tag{2.27}$$

Written in terms of the regularised splitting functions

$$\begin{aligned}
P_{\mathrm{qq}}(z) &= \frac{4}{3}\left[\frac{1+z^2}{(1-z)_+} + \frac{3}{2}\delta(1-z)\right] && (2.28)\\
P_{\mathrm{gg}}(z) &= 6\left[\frac{z}{(1-z)_+} + \frac{1-z}{z} + z(1-z)\right] + \frac{1}{6}(33-2n_{\mathrm{f}})\delta(1-z) && (2.29)\\
P_{\mathrm{qg}}(z) &= \frac{1}{2}\left[z^2 + (1-z)^2\right] && (2.30)
\end{aligned}$$

equation (2.25) reads

$$\frac{\partial D_{\mathrm{q}}^{h/j}(x,Q^2)}{\partial(\ln Q^2)} = \int_0^1 \frac{\mathrm{d}z}{z}\,\frac{\alpha_{\mathrm{s}}}{2\pi}\left\{P_{\mathrm{qq}}(z) D_{\mathrm{q}}^{h/j}\left(\frac{x}{z},Q^2\right) + P_{\mathrm{gq}}(z) D_{\mathrm{g}}^{h/j}\left(\frac{x}{z},Q^2\right)\right\} . \tag{2.31}$$

For the gluon to h/j fragmentation function one finds

$$\begin{aligned}
\frac{\partial D_{\mathrm{g}}^{h/j}(x,Q^2)}{\partial(\ln Q^2)} &= \int_0^1 \frac{\mathrm{d}z}{z}\,\frac{\alpha_{\mathrm{s}}}{2\pi}\left\{P_{\mathrm{qg}}(z)\sum_q \left(D_{\mathrm{q}}^{h/j}\left(\frac{x}{z},Q^2\right) + D_{\bar{\mathrm{q}}}^{h/j}\left(\frac{x}{z},Q^2\right)\right)\right.\\
&\qquad \left. + P_{\mathrm{gg}}(z) D_{\mathrm{g}}^{h/j}\left(\frac{x}{z},Q^2\right)\right\} . && (2.32)
\end{aligned}$$

These are the DGLAP (Dokshitzer-Gribov-Lipatov-Altarelli-Parisi) equations [53–56] for the Q^2 evolution of the fragmentation functions. These equations resum leading logarithms of the form $\alpha_{\mathrm{s}}^n \ln^n(Q^2/\mu^2)$ to all orders, which can become large even for small α_{s} when the logarithm is large. Next-lo-leading logs of the form $\alpha_{\mathrm{s}}^n \ln^{n-1}(Q^2/\mu^2)$ can be included by using next-to-leading order splitting functions. The evolution equations contain only planar diagrams, where at each splitting the scale is much smaller than in the previous one so that there is no interference between subsequent emissions. The DGLAP equations can be solved either by Mellin transformation (which converts the convolution to a product) or by direct numerical integration. The starting distribution at Q_0^2 is usually parametrised and fitted to data.

The evolution equations can be formulated in a slightly different way with the help of the *Sudakov form factor* [57], which is defined as

$$\begin{aligned}
\mathcal{S}_{\mathrm{q}}(Q_i^2, Q_f^2) &= \exp\left(-\int\limits_{Q_f^2}^{Q_i^2} \frac{\mathrm{d}Q'^2}{Q'^2} \int \mathrm{d}z \, \frac{\alpha_{\mathrm{s}}}{2\pi} \hat{P}_{\mathrm{qq}}(z) \right) \\
\mathcal{S}_{\mathrm{g}}(Q_i^2, Q_f^2) &= \exp\left(-\int\limits_{Q_f^2}^{Q_i^2} \frac{\mathrm{d}Q'^2}{Q'^2} \int \mathrm{d}z \, \frac{\alpha_{\mathrm{s}}}{2\pi} \left[\hat{P}_{\mathrm{gg}}(z) + \hat{P}_{\mathrm{qg}}(z)\right] \right) . \qquad (2.33)
\end{aligned}$$

Then the DGLAP equation for the quark (equation (2.25)) can be rewritten as

$$\begin{aligned}
\frac{\partial D_{\mathrm{q}}^{h/j}(x, Q^2)}{\partial(\ln Q^2)} &= \int\limits_x^1 \frac{\mathrm{d}z}{z} \frac{\alpha_{\mathrm{s}}}{2\pi} \left\{ \hat{P}_{\mathrm{qq}}(z) D_{\mathrm{q}}^{h/j}\left(\frac{x}{z}, Q^2\right) + \hat{P}_{\mathrm{gq}}(z) D_{\mathrm{g}}^{h/j}\left(\frac{x}{z}, Q^2\right) \right\} \\
&\quad + \frac{D_{\mathrm{g}}^{h/j}(x, Q^2)}{\mathcal{S}_{\mathrm{q}}(Q^2, Q_0^2)} Q^2 \frac{\partial \mathcal{S}_{\mathrm{q}}(Q^2, Q_0^2)}{\partial Q^2} , \qquad (2.34)
\end{aligned}$$

from which follows

$$\begin{aligned}
&\frac{\partial}{\partial(\ln Q^2)} \left(\frac{D_{\mathrm{q}}^{h/j}(x, Q^2)}{\mathcal{S}_{\mathrm{q}}(Q^2, Q_0^2)} \right) = \\
&\qquad \frac{1}{\mathcal{S}_{\mathrm{q}}(Q^2, Q_0^2)} \int\limits_x^1 \frac{\mathrm{d}z}{z} \frac{\alpha_{\mathrm{s}}}{2\pi} \left\{ \hat{P}_{\mathrm{qq}}(z) D_{\mathrm{q}}^{h/j}\left(\frac{x}{z}, Q^2\right) + \hat{P}_{\mathrm{gq}}(z) D_{\mathrm{g}}^{h/j}\left(\frac{x}{z}, Q^2\right) \right\} . \qquad (2.35)
\end{aligned}$$

Finally, this equation can be integrated yielding

$$\begin{aligned}
&D_{\mathrm{q}}^{h/j}(x, Q^2) = \mathcal{S}_{\mathrm{q}}(Q^2, Q_0^2) D_{\mathrm{q}}^{h/j}(x, Q_0^2) + \\
&\quad \int\limits_{Q_0^2}^{Q^2} \frac{\mathrm{d}Q'^2}{Q'^2} \mathcal{S}_{\mathrm{q}}(Q^2, Q'^2) \int\limits_x^1 \frac{\mathrm{d}z}{z} \frac{\alpha_{\mathrm{s}}}{2\pi} \left\{ \hat{P}_{\mathrm{qq}}(z) D_{\mathrm{q}}^{h/j}\left(\frac{x}{z}, Q^2\right) + \hat{P}_{\mathrm{gq}}(z) D_{\mathrm{g}}^{h/j}\left(\frac{x}{z}, Q^2\right) \right\} \quad (2.36)
\end{aligned}$$

The Sudakov form factor can thus be interpreted as the probability that no splitting occurs between Q_i^2 and Q_f^2. The first term in the above equation describes the possibility that nothing happens between Q^2 and Q_0^2 and the integral contains all contributions from splittings at an intermediate scale. This formulation of the evolution equations is suited for implementation in Monte Carlo event generators, where configurations of subsequent splittings for the evolution from the initial hard scale to the factorisation scale Q_0^2 are generated according to their probability. Some of the radiated partons will in turn split into new pairs so that a whole parton cascade or parton shower evolves.

The DGLAP equations resum collinear enhanced splittings to all orders, but there is also the divergence due to radiation of soft gluons, which have large emission angles. A coherence effect, which is the QCD analogue of the Chudakov effect [58] (a suppression of soft photon radiation from an electron-positron pair) in QED, leads to the phenomenon of *angular ordering* [59,60]. This means that the emission angles are strictly ordered and decreasing during the evolution leading to a suppression of soft gluon emission. A qualitative explanation of the Chudakov effect is that photons with emission angles larger than the opening angle of the pair cannot resolve the charge and are thus suppressed.

This soft gluon suppression is not respected by the DGLAP equations, where the z integration diverges for $x \to 0$ meaning that they do not correctly describe the low x region. But it can be shown that the suppression due to angular ordering can be incorporated by making the replacement $D_i^{h/j}(x/z, Q^2) \to D_i^{h/j}(x/z, z^2Q^2)$ in the evolution equations. The modified DGLAP equations predict, for instance, the right dependence of the total multiplicity on $\sqrt{s}$.

2.2.3. Event Shape Variables and Jet Rates

The event shape variables are a set of observables that characterise the shape, i.e. the energy flow of an event. One group of them is derived from the momentum tensor

$$\mathcal{M}_{\alpha\beta} = \frac{\sum_i p_{i\alpha} p_{i\beta}}{\sum_i |\vec{p}_i|^2}\,, \tag{2.37}$$

where α and β run over the three spatial components and $\vec{p}_i$ is the momentum of hadron i. It has three ordered eigenvalues $\lambda_1 \geq \lambda_2 \geq \lambda_3$ satisfying $\lambda_1 + \lambda_2 + \lambda_3 = 1$. The combination

$$S = \frac{3}{2}(\lambda_2 + \lambda_3) = \frac{3}{2} \min_{\vec{n}_\mathrm{S}} \frac{\sum_i p_{i\perp}^2}{\sum_i |\vec{p}_i|^2}\,, \tag{2.38}$$

where $p_{i\perp}$ denotes the transverse momentum of hadron i with respect to $\vec{n}_\mathrm{S}$, is called *sphericity*. The unit vector $\vec{n}_\mathrm{S}$ minimising the numerator defines the sphericity axis. S lies between 0 and 1, an event with $S = 1$ is perfectly spherical while $S \ll 1$ corresponds to a two-jet-like configuration. The *aplanarity*, defined as

$$A = \frac{3}{2}\lambda_3\,, \tag{2.39}$$

quantifies the energy flow out of the event plane. It is 0 for coplanar (and collinear) and 1/2 for spherical events. The combination

$$P = \lambda_2 - \lambda_3 = \frac{2}{3}(S - 2A) \tag{2.40}$$

is the *planarity*. These observables have a serious disadvantage: They are quadratic in the momenta and therefore infra-red sensitive and cannot be calculated in perturbation theory. Infra-red sensitive quantities can be very sensitive to hadronisation, where the partons are replaced typically by several softer but essentially collinear hadrons, and require careful modelling of the hadronisation in Monte Carlo models.

Variables, that are composed from linear sums of the momenta, have the benefit of being infra-red safe. The most commonly used such quantity is *thrust* [61,62]

$$T = \max_{\vec{n}_\mathrm{T}} \frac{\sum_i |\vec{p}_i \cdot \vec{n}_\mathrm{T}|}{\sum_i |\vec{p}_i|}\,. \tag{2.41}$$

The thrust axis $\vec{n}_{\mathrm{T}}$, which is the direction with the maximal longitudinal momentum, can be used to define the jet axis. For a perfect pencil-like two-jet event $T = 1$ and a spherical distribution has $T = 1/2$. Once the thrust axis is found the procedure of finding the direction of maximal momentum flow can be repeated in the plane orthogonal to $\vec{n}_{\mathrm{T}}$. This quantity is called *thrust major*

$$T_{\mathrm{maj}} = \max_{\vec{n}_{\mathrm{maj}}, \vec{n}_{\mathrm{T}} \cdot n_{\mathrm{maj}}=0} \frac{\sum_i |\vec{p}_i \cdot \vec{n}_{\mathrm{maj}}|}{\sum_i |\vec{p}_i|} . \tag{2.42}$$

The fractional momentum along the axis orthogonal to $\vec{n}_{\mathrm{T}}$ and $\vec{n}_{\mathrm{maj}}$ is *thrust minor*

$$T_{\mathrm{min}} = \frac{\sum_i |\vec{p}_i \cdot \vec{n}_{\mathrm{min}}|}{\sum_i |\vec{p}_i|} \quad , \quad \vec{n}_{\mathrm{min}} = \vec{n}_{\mathrm{T}} \times \vec{n}_{\mathrm{maj}} . \tag{2.43}$$

Other examples for infra-red safe event shape variables are *spherocity* [63]

$$S' = \left(\frac{4}{\pi}\right)^2 \min_{\vec{n}_{S'}} \left(\frac{\sum_i |\vec{p}_i \times \vec{n}_{S'}|}{\sum_i |\vec{p}_i|}\right)^2 , \tag{2.44}$$

which is a measure for the flatness of an event, and the *C-parameter* [64]

$$C = \frac{3}{2} \frac{\sum_{i,j} \left\{|\vec{p}_i||\vec{p}_j| - (\vec{p}_i \cdot \vec{p}_j)^2/|\vec{p}_i||\vec{p}_j|\right\}}{\left(\sum_i |\vec{p}_i|\right)^2} . \tag{2.45}$$

Spherocity and the C-parameter are both 0 for a pencil-like and 1 for a spherical event.

These variables are calculable in perturbation theory; thrust, for instance, can to leading order be obtained from the $e^+ + e^- \rightarrow q + \bar{q} + g$ cross section (equation (2.16))

$$\frac{1}{\sigma} \frac{\mathrm{d}^2 \sigma_{\mathrm{q\bar{q}\,g}}}{\mathrm{d}x_1 \mathrm{d}x_2} = \frac{4}{3} \frac{\alpha_{\mathrm{s}}}{2\pi} \frac{x_1^2 + x_2^2}{(1-x_1)(1-x_2)} . \tag{2.46}$$

by integration with the constraint $\delta(T - \max(x_1, x_2, x_3 = 2 - x_1 - x_2))$ over the (x_1, x_2) plane. The resulting T distribution is

$$\frac{1}{\sigma} \frac{\mathrm{d}\sigma}{\mathrm{d}T} = \frac{4}{3} \frac{\alpha_{\mathrm{s}}}{2\pi} \left[\frac{2(3T^2 - 3T + 2)}{T(1-T)} \ln\left(\frac{2T-1}{1-T}\right) - \frac{3(3T-2)(2-T)}{1-T}\right] . \tag{2.47}$$

The divergence at $T \rightarrow 1$ reflects the soft and collinear singularities in the matrix element. In the large T region the perturbative expansion has the form

$$\frac{1}{\sigma} \frac{\mathrm{d}\sigma}{\mathrm{d}T} \sim \sum_n \alpha_{\mathrm{s}}^n \frac{\ln^{2n-1}(1-T)}{1-T} \tag{2.48}$$

and has to be resumed to all orders.

Events can also be characterised by the number of jets they contain. This requires an unambiguous and infra-red safe definition of a jet. There is no unique choice, a suitable and widely used definition is the Durham algorithm [65], which belongs to the class of $k_\perp$ clustering algorithms. It defines a distance measure for any pair of particles or clusters as

$$y_{ij} = \frac{\min(E_i^2, E_j^2)(1-\cos\vartheta_{ij})}{s} \tag{2.49}$$

and a resolution y_{cut}. The pair with the smallest distance is combined into a pseudo-particle or cluster, provided that $y_{ij} < y_{\mathrm{cut}}$. This procedure is repeated until all particles or clusters in the event have separations larger than the resolution. The number of remaining objects is then the number of jets, which obviously depends on y_{cut}.

At large y_{cut} the dominant contributions are from 2- and 3-jet events, higher jet multiplicities are negligible. The jets are well separated and the 3-jet contribution can be calculated by integrating the $e^+ + e^- \to q + \bar{q} + g$ cross section (equation (2.46)) over the corresponding (x_1, x_2) region. The soft and collinear singularities lie outside this region, since they would not give rise to a well separated jet. The 2-jet fraction is given by the constraint that the two have to add up to unity.

At finer resolutions, however, higher jet multiplicities start to contribute, which are related to large logarithms and the perturbative result has to be resumed. Physically, these are the collinear enhanced emissions that give rise to the scaling violations in the fragmentation functions and lead to the formation of the parton shower and the resumed jet rates can be expressed in terms of the Sudakov form factor. But there are also contributions from fixed order calculations of n-jet matrix elements. The two have to be matched in order to avoid double counting.

2.2.4. Jets in Hadronic Collisions

Jets can also be produced in hadronic collisions. At large scales, in this case momentum transfers, the partonic structure of the hadrons is resolved and the relevant processes are scatterings of the partons. The density of partons of type i in the hadron with a fraction x of the hadron's momentum is described by the *parton distribution function* (pdf) f_i^h and is dominated by non-perturbative physics. They have in some respects the same properties as the fragmentation functions. Not only the outgoing partons after the hard process are virtual, also the incoming partons have a virtuality of the order of the hard scale. The partons acquire this virtuality by splitting processes, which have the known collinear and soft divergences. Consequently, the Q^2 dependence of the pdf's is described by the same evolution equations as that of the fragmentation functions. As in the case of the fragmentation functions the factorisation theorem allows to separate the soft from the hard part and write the cross section a factorised form. The total cross section for hard scattering of two hadrons with momenta P_1 and P_2 is given by

$$\sigma(P_1, P_2) = \sum_{ij} \int \mathrm{d}x_1\, \mathrm{d}x_2\, f_i(x_1, Q^2) f_j(x_2, Q^2) \hat{\sigma}_{ij}(x_1, x_2, \alpha_\mathrm{s}(Q^2))\,. \tag{2.50}$$

The factorisation scale is as usual chosen to be equal to the renormalisation scale and the hard scale Q^2. Quantities with hats generally refer to the parton level; the partonic cross section, for instance, is denoted by $\hat{\sigma}$. Figure 2.6 shows a few examples

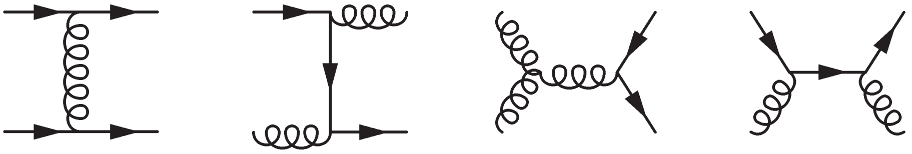

Figure 2.6.: Examples for 2 → 2 scattering processes at $\mathcal{O}(\alpha_s)$.

	$\lvert\mathcal{M}\rvert^2/\alpha_s^2$
$qq' \rightarrow qq'$	$\frac{4}{9}\frac{\hat{s}^2+\hat{u}^2}{\hat{t}^2}$
$q\bar{q}' \rightarrow q\bar{q}'$	$\frac{4}{9}\frac{\hat{s}^2+\hat{u}^2}{\hat{t}^2}$
$qq \rightarrow qq$	$\frac{4}{9}\left(\frac{\hat{s}^2+\hat{u}^2}{\hat{t}^2}+\frac{\hat{s}^2+\hat{t}^2}{\hat{u}^2}\right)-\frac{8}{27}\frac{\hat{s}^2}{\hat{u}\hat{t}}$
$q\bar{q} \rightarrow q'\bar{q}'$	$\frac{4}{9}\frac{\hat{t}^2+\hat{u}^2}{\hat{s}^2}$
$q\bar{q} \rightarrow q\bar{q}$	$\frac{4}{9}\left(\frac{\hat{s}^2+\hat{u}^2}{\hat{t}^2}+\frac{\hat{t}^2+\hat{u}^2}{\hat{s}^2}\right)-\frac{8}{27}\frac{\hat{u}^2}{\hat{s}\hat{t}}$
$q\bar{q} \rightarrow gg$	$\frac{32}{27}\frac{\hat{t}^2+\hat{u}^2}{\hat{t}\hat{u}}-\frac{8}{3}\frac{\hat{t}^2+\hat{u}^2}{\hat{s}^2}$
$gg \rightarrow q\bar{q}$	$\frac{1}{6}\frac{\hat{t}^2+\hat{u}^2}{\hat{t}\hat{u}}-\frac{3}{8}\frac{\hat{t}^2+\hat{u}^2}{\hat{s}^2}$
$gq \rightarrow gq$	$-\frac{4}{9}\frac{\hat{s}^2+\hat{u}^2}{\hat{s}\hat{u}}-\frac{\hat{u}^2+\hat{s}^2}{\hat{t}^2}$
$gg \rightarrow gg$	$\frac{9}{3}\left(3-\frac{\hat{t}\hat{u}}{\hat{s}^2}-\frac{\hat{s}\hat{u}}{\hat{t}^2}-\frac{\hat{s}\hat{t}}{\hat{u}^2}\right)$

Table 2.1.: Invariant leading order matrix elements squared for the partonic 2 → 2 scattering processes [66]. Colour and spins are averaged (summed) over the initial (final) states.

for possible partonic scattering processes. The kinematics of 2 → 2 processes $a+b \rightarrow c+d$ is best described in terms of the Mandelstam variables, which are Lorentz invariant combinations of the four-momenta.

$$s = (p_a + p_b)^2 \tag{2.51}$$
$$t = (p_a - p_c)^2 \tag{2.52}$$
$$u = (p_a - p_d)^2 \tag{2.53}$$

$\sqrt{s}$ is the centre-of-momentum energy and $\sqrt{t}$ the four-momentum transfer. The partonic cross section for a specific process can be written as

$$\frac{\mathrm{d}\hat{\sigma}}{\mathrm{d}\hat{t}}(ab \rightarrow cd) = \frac{\pi}{\hat{s}^2}\left|\mathcal{M}_{ab\rightarrow cb}\right|^2 . \tag{2.54}$$

The leading order matrix elements for the 2 → 2 processes are listed in table 2.1.

A large momentum transfer implies that the partons have large scattering angles, which usually means that the hadron breaks up. The coloured remnants (the scattered partons and the hadron remnants) hadronise giving rise to jets.

The single-inclusive cross sections at high transverse momenta exhibit an approximate scaling in the dimensionless variable $x_\perp$ [67–69]

$$E\frac{\mathrm{d}^3\sigma}{\mathrm{d}^3p} \simeq \frac{1}{p_\perp^n} f(x_\perp) \quad \text{with} \quad x_\perp = \frac{2p_\perp}{\sqrt{s}} . \tag{2.55}$$

In leading order one finds $n = 4$, but higher order effects like running of the coupling and evolution of the parton densities and fragmentation function lead to a larger exponent $n \simeq 8$ that becomes slightly $p_\perp$ and $\sqrt{s}$ dependent. Measured values are between 5 and 8 for different beam energies, at RHIC n is found to be between 6 and 7.

2.2.5. Hadronisation Models

Instead of using single-inclusive fragmentation functions, one can also construct explicit hadronisation models. These are particularly useful in Monte Carlo generators, because they can be turned in a prescription that generates the complete hadronic state. Often, event generators simulate the perturbative evolution described in section 2.2.2 and interface the result with a hadronisation model at the scale Q_0. In this section the most important hadronisation models will be introduced.

Lund String Fragmentation

A quark-antiquark pair produced in e^++e^- collisions is in a colour-singlet state. The colour charges give rise to a (colour) field connecting the colour and the anticolour. Due to the gluon self-interaction it does not fill the whole space as the electric field, but formes a 'colour flux tube' with a transverse size of roughly 1 fm. The quark-antiquark potential is of the form $V(r) \sim \kappa r$ at large distances r, with $\kappa \sim 1\,\mathrm{GeV/fm}$. As the separation of the quark-antiquark pair increases there will a point, when a new quark-antiquark pair can be formed from the field energy and the pair breaks up in two colour neutral systems. They can form mesons if their invariant mass is small, otherwise more additional pairs will be produced.

In the Lund string fragmentation model [70–74] the field is described as a massless relativistic string with energy density κ. A newly produced pair can classically not be produced at the same point, because the energy needed for the mass and/or transverse momentum relative to the string has to come from the string piece between the quark and the antiquark. The quantum-mechanical picture is that the pair is produced at the same point thus conserving flavour locally and tunnels out of the classically allowed region. This leads to an exponential suppression of the tunnelling probability with transverse mass

$$\mathcal{P} = \exp\left(-\frac{\pi m_\perp^2}{\kappa}\right) = \exp\left(-\frac{\pi m^2}{\kappa}\right)\exp\left(-\frac{\pi p_\perp^2}{\kappa}\right), \tag{2.56}$$

which leads to a Gaussian distribution in both components of the transverse momentum. The total $p_\perp$ of the pair has to vanish due to momentum conservation.

Subsequent break-ups of the string are assumed to be independent. The Lund model is covariant and symmetric with respect to the string ends. Thus, it can be formulated as an iteration of the same process in the following way: Starting from the quark a break-up is generated leading to a meson, which consists of the quark from the end and the antiquark from the produced pair, and a remainder string. This is repeated until there is no more energy available. The termination procedure requires extra care in order to preserve the symmetry between the two ends.

The flavour composition and the transverse momentum of the produced meson are given by the flavour and $p_\perp$ carried by the quark and the antiquark. The creation of heavy quark pairs is suppressed by equation (2.56). Only u, d and s pairs are produced with a ratio of strange to light quarks $\gamma_\mathrm{s} = s\bar{s}/u\bar{u} \simeq 0.3$. The spin and orbital angular momentum have to be assigned according to suitable probabilities including, for instance, the degeneracy. The mixing of flavour-diagonal states also has to be taken into account. When the meson species is chosen also the mass is fixed. What remains to be determined is the longitudinal momentum or the energy. In fact, it is convenient to let the meson take a fraction z of the $E + p_\parallel$ of the string. This leaves

$$\begin{aligned} (E + p_\parallel)_\mathrm{new} &= (1-z)(E + p_\parallel)_\mathrm{old} && (2.57) \\ (E - p_\parallel)_\mathrm{new} &= (E - p_\parallel)_\mathrm{old} - \frac{m_\perp^2}{z(E + p_\parallel)_\mathrm{old}} && (2.58) \end{aligned}$$

for the rest of the string. The z-distribution is described by a function $f(z)$ which is also called fragmentation function but should not be confused with the fragmentation function $D_i^h(x, Q^2)$ discussed in the section 2.2.2. The constraint that the result should be independent of the choice from which end to start leads to the 'Lund symmetric fragmentation function'

$$f(z) \propto z^{-1}(1-z)^a \exp\left(-\frac{bm_\perp^2}{z}\right) . \tag{2.59}$$

So far only the production of mesons, which is more natural in the string fragmentation, was discussed. There are two scenarios for baryon production, the diquark and the popcorn picture. The former assumes that in a break-up not only quark-antiquark but also diquark-antidiquark pairs can be formed. The diquark, which is a state of two quarks carrying anticolour, combines with the neighboring quark to form a baryon. Baryon production is suppressed due to the larger mass of the diquark. The distribution of three-quark states on the baryons is analogous to the meson case. In the popcorn model a quark-antiquark pair that does not match the string colour can be created. The string does not break in this case, but a pair carrying the third colour can be created inbetween. Then the three (anti)quarks are a colour-neutral combination. In contrast to the diquark picture, where the baryon and the antibaryon are always neighbours, the popcorn model allows mesons to be formed between the baryon and the antibaryon. The suppression of baryons arises in this scenario from the fact that a pair with the 'wrong' colour can only exist as a quantum fluctuation.

When a gluon is radiated off one of the initial (anti)quark lines it lines up in the string as a 'kink' carrying momentum, since colour has to be conserved at the vertex. In the planar diagrams of the leading logarithmic evolution the colour structure is such that neighboring partons have matching colour and the whole cascade can be organised in one or several colour neutral systems (figure 2.7 (a)). The fragmentation of such a system works in principle in the same way as described for the $q\bar{q}$ string,

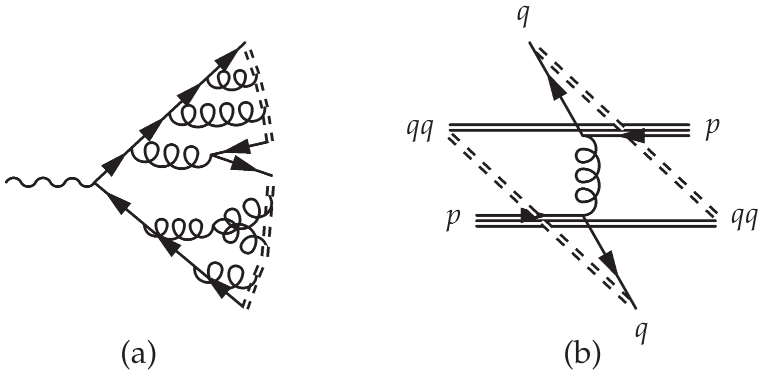

Figure 2.7.: (a) String configuration in an $e^{+}+e^{-}$ event with final state parton shower. (b) Example for a string configuration in proton-proton scattering without parton shower.

but the details are complicated when many different string pieces or regions have to be considered.

The Lund model is also applicable to jet production in hadronic collisions. In proton-proton collisions only a part of the proton participates in the hard interaction. The string configuration without the parton shower is slightly more complicated than in $e^{+}+e^{-}$ collisions because there are now two colour neutral systems. Figure 2.7 (b) shows an example where the hard subprocess is quark-quark scattering. When the scattered constituent of the proton is a gluon, the proton remnant has to be split into a quark and a diquark. The scattered quarks (or gluons) develop a final state parton shower in exactly the same way as in $e^{+}e^{-}$ annihilation. Furthermore, as explained in section 2.2.4, the quarks also radiate gluons before the hard process forming an initial state parton shower. Again, the showers can be incorporated in the string system.

The strengths of the Lund model are that it is Lorentz-invariant, infra-red safe, conserves by construction energy, momentum and additive quantum numbers and provides a fairly good description of data. A qualitative explanation for the infra-red safety can be given in terms of the string motion. It turns out that the string of a $q\bar{q}g$ system, for instance, looks 'two-jet-like' when the gluon is soft or collinear with one of the quark lines, because it effectively gets 'absorbed'. Because of these properties the Lund string fragmentation depends only weakly on the factorisation scale Q_0^2.

Independent Fragmentation

The independent fragmentation model [75–81] assumes that each parton hadronises on its own, so that the hadronisation of a multi-parton event is the incoherent sum of the fragmentations of the partons. The colour structure is thus ignored. The hadronisation mechanism is essentially the fragmentation of a string that has only one well-defined end. The $q\bar{q}$ pair creation works as in the Lund model with local conservation of flavour and transverse momentum. For the energy sharing the same fragmentation function can be used. There is, however, a problem with small z values: They correspond to backward moving hadrons (i.e. $p_{\|} < 0$) that are regarded as unphysical and have to be rejected.

Gluons are split into a quark-antiquark pair where the energy sharing can either be described by the perturbative splitting function or one of the partners gets all the energy.

While momentum and flavour are conserved in each break-up this is not the case in the global balance. The hadronisation of each string is stopped when the parton energy is used up leaving an unpaired (anti)quark behind. This means that in general flavour, charge, energy, momentum etc. are globally not conserved. The independent fragmentation model suffers from more conceptual weaknesses: It is infra-red sensitive and not Lorentz invariant. The problem of frame dependence is circumvented by the requirement that the hadronisation has to be carried out in the global centre-of-momentum frame. But two collinear partons and a single one with the same energy always behave differently. Because of this problem with the infra-red instability the independent fragmentation is quite sensitive to the choice of Q_0.

Cluster Hadronisation

The cluster hadronisation [82–84] is related to the concept of *preconfinement* [85, 86], which implies that neighboring partners in the parton cascade, that in planar configurations are colour connected, have an universal and steeply falling mass distribution. In a simple version of the cluster model a parton shower is generated down to Q_0. At this scale all gluons are split in quark-antiquark pairs resulting in a configuration where each quark has an antiquark as neighbour with which it forms a colour singlet. These clusters decay in two hadrons, the decay is isotropic in the cluster rest frame.

Local Parton Hadron Duality

The concept of local parton hadron duality (LPHD) [87, 88] emerged from the observation that perturbation theory seems to work relatively well also at low scales where one would not expect it, and that hadronisation does then not lead to major redistributions. One thus basically runs a perturbative evolution down to a hadronic scale and assumes that colour is neutralised locally so that the hadronic distributions resemble the partonic results.

CHAPTER 3

Jet Quenching in Heavy Ion Collisions

Jets that are produced in nucleus-nucleus collisions are altered as compared to jets in elementary reactions due to interactions with the produced medium. These modifications of jet characteristics may reveal important information about the properties of the medium; the microscopic mechanisms are, however, not yet sufficiently well understood. One of the most striking phenomena is a strong suppression of leading hadrons, which is attributed to energy loss of fast partons in the produced medium and is known as 'jet quenching'. In the first section of this chapter a few aspects of heavy-ion collisions that are important for jet propagation (mainly geometry and space-time evolution) are introduced. In the next section an overview over important experimental results concerning the phenomenology of jet quenching is given. The last section is a summary of different attempts to theoretically describe partonic energy loss.

3.1. Selected Aspects of Nuclear Collisions

Ultra-relativistic collisions of heavy nuclei have a very rich and divers phenomenology. Here, only a brief introduction into those aspects that are important for this study can be given, but this does clearly not do justice to the topic.

3.1.1. Collision Geometry: A Glauber Model

In Glauber calculations (or simulations) a collision of two nuclei is assumed to be an incoherent sum of nucleon-nucleon interactions. They can be used to calculate cross sections and to characterise the centrality of nucleus-nucleus collisions. In analytic models like [89] the matter distribution inside a nucleus is assumed to be continuous. It is described by the density distribution $n_A(r)$ satisfying

$$\int \mathrm{d}^3 r \, n_A(r) = A \,. \tag{3.1}$$

Nuclei are rather well described by the Woods-Saxon distribution

$$n_A^{\mathrm{WS}}(r) = \frac{n_0}{e^{(r-R_A)/d}+1} \quad \text{with} \quad n_0 = \frac{3A}{4\pi R_A^3(1+\pi^2 d^2/R_A^2)} \,. \tag{3.2}$$

The z-direction is chosen to be the beam axis, the *impact parameter* $\vec{b}$ lies in the plane perpendicular to the beam and points from the centre of the beam nucleus to the centre of the target nucleus. The magnitude of the impact parameter is a measure for the centrality, $0 \leq b < \min(R_A, R_B)$ where $b = 0$ corresponds to a head-on collision. Beam axis and impact parameter define the *reaction plane*.

A single nucleon passing through a nucleus at a distance b from the centre sees a part

$$T_A(b) = \int\limits_{-\infty}^{\infty} \mathrm{d}z\, n_A(\sqrt{b^2+z^2}) \tag{3.3}$$

of the target. T_A is called the *nuclear thickness function*. When the projectile is a nucleus the overlap is characterised by

$$T_{AB}(b) = \int \mathrm{d}^2 b_1\, \mathrm{d}^2 b_2\, \delta^2(\vec{b}-\vec{b}_1-\vec{b}_2) T_A(|\vec{b}_1|) T_B(|\vec{b}_2|) \,. \tag{3.4}$$

The product $\sigma_{\mathrm{inel}}^{\mathrm{NN}} T_{AB}(b)$, where $\sigma_{\mathrm{inel}}^{\mathrm{NN}}$ is the total inelastic nucleon-nucleon cross section at the respective collision energy, can be interpreted as the *mean number of binary nucleon-nucleon collisions* $\langle N_{\mathrm{bin}} \rangle$ at impact parameter b. The total nucleus-nucleus cross section is obtained by integrating $\sigma_{\mathrm{inel}}^{\mathrm{NN}} T_{AB}(b)$ over b:

$$\sigma_{\mathrm{inel}}^{AB} = \int \mathrm{d}^2 b\, \sigma_{\mathrm{inel}}^{\mathrm{NN}} T_{AB}(b) = AB\sigma_{\mathrm{inel}}^{\mathrm{NN}} \tag{3.5}$$

Similarly, $T_{AB}(b)$ can be multiplied with any cross section to get the mean number of events of a particular kind per $A + B$ collision at impact parameter b.

Another interesting quantity is the *mean number of nucleons participating in the collision*. It is given by

$$\langle N_{\mathrm{part}}(b) \rangle = \int \mathrm{d}^2 b_1\, \mathrm{d}^2 b_2\, \delta(\vec{b}-\vec{b}_1-\vec{b}_2) \left\{ T_A(|\vec{b}_1|) p_{\geq 1}^{(B)}(|\vec{b}_2|) + T_B(|\vec{b}_2|) p_{\geq 1}^{(A)}(|\vec{b}_1|) \right\} , \tag{3.6}$$

where $p_{\geq 1}^{(A)}(b_1)$ is the probability that a nucleon passing through the nucleus A with impact parameter b_1 takes part in at least one interaction. It can be obtained from the Binomial distribution:

$$\begin{aligned} p_{\geq 1}^{(A)}(b_1) =& 1 - \binom{A}{0} \left(\frac{\sigma_{\mathrm{inel}}^{\mathrm{NN}} T_A(b_1)}{A} \right)^0 \left(1 - \frac{\sigma_{\mathrm{inel}}^{\mathrm{NN}} T_A(b_1)}{A} \right)^{A-0} \\ =& 1 - \left(1 - \frac{\sigma_{\mathrm{inel}}^{\mathrm{NN}} T_A(b_1)}{A} \right)^A \\ \approx& 1 - e^{-\sigma_{\mathrm{inel}}^{\mathrm{NN}} T_A(b_1)} \qquad \text{for large } A \,. \end{aligned} \tag{3.7}$$

Soft processes are expected to scale with the number of participants while hard processes should scale with the number of binary collisions.

3.1.2. The Ideal Quark-Gluon Gas

A non-interacting (ideal) gas of quarks, antiquarks and gluons is described by the grand-canonical partition sum, since the particle numbers are not fixed[1]. One-particle states are characterised by a set $\vec{v}$ of quantum numbers, the occupation number $n(\vec{v})$ and the one-particle energy $E(\vec{v})$. In the case of bosons the occupation number can take any value while in the case of fermions a state can be occupied by at most one particle. A complete set of occupation numbers for all the states is denoted by $\{n(\vec{v})\}$. The grand-canonical partition sum is given by

$$\begin{aligned}
\Xi(T,V,\mu) &= \sum_{\text{all states}} \exp(-\beta(E_{\text{tot}} - \mu N)) \\
&= \sum_{\{n(\vec{v})\}} \exp\left(-\beta \sum_{\vec{v}} n(\vec{v})(E(\vec{v}) - \mu)\right) \\
&= \sum_{\{n(\vec{v})\}} \prod_{\vec{v}} \{\exp(-\beta(E(\vec{v}) - \mu))\}^{n(\vec{v})} \\
&= \prod_{\vec{v}} \sum_{n(\vec{v})=0}^{\infty/1} \{\exp(-\beta(E(\vec{v}) - \mu))\}^{n(\vec{v})} \\
&= \prod_{\vec{v}} \frac{1}{1 \pm \exp(-\beta(E(\vec{v}) - \mu))}
\end{aligned} \tag{3.8}$$

$$\Rightarrow \ln \Xi(T,V,\mu) = \pm \sum_{\vec{v}} \ln\left(1 \pm e^{-\beta(E(\vec{v})-\mu)}\right), \tag{3.9}$$

where $\beta = 1/T$, μ is the chemical potential and E_{tot} and N denote the total energy and number of particles in the ensemble. The plus sign applies to fermions and the minus sign to bosons. When the energy levels are not discrete but continuous the sum can be transformed into an integral yielding

$$\ln \Xi(T,V,\mu) = \pm \int \frac{\mathrm{d}^3 q\, \mathrm{d}^3 p}{(2\pi)^3} \ln\left(1 \pm e^{-\beta(E(\vec{v})-\mu)}\right), \tag{3.10}$$

where p and q are the momentum and spatial coordinates.

The mean occupation number of a state is given by

$$\bar{n}(\vec{v}) = -\frac{\partial \ln \Xi}{\partial(\beta E(\vec{v}))} = \frac{1}{e^{\beta(E(\vec{v})-\mu)} \pm 1} \tag{3.11}$$

The central rapidity region in relativistic nuclear collisions is nearly baryon-free, so that the chemical potential can be neglected. It is convenient to characterise the one-particle states by their momentum, but then the degeneracy has to be taken into account. The number of one-particle states with a given momentum is for a (anti)quarks and gluons given by

$$\begin{aligned}
g_{\text{g}} &= 2(\text{polarisation}) \cdot 8(\text{colour}) = 16 \\
g_{\text{q}} &= g_{\bar{\text{q}}} = n_{\text{f}}(\text{flavour}) \cdot 2(\text{spin}) \cdot 3(\text{colour}) = 6n_{\text{f}}
\end{aligned} \tag{3.12}$$

---

[1] A detailed discussion of the thermodynamics of quantum gases can, for instance, be found in [90].

The mean occupation number of the state with momentum p is given by

$$\bar{n}_p = \frac{g_{\mathrm{g/q}}}{e^{E/T} \pm 1} \quad \text{with} \quad E = \sqrt{\vec{p}^{\,2} + m^2} \tag{3.13}$$

The particle and energy density can only be calculated analytically for massless particles and in the case of massive particles for temperatures that are large compared to the masses. Neglecting the masses one gets

$$\begin{aligned}
n_{\mathrm{g}} =& \frac{1}{V}\frac{1}{(2\pi)^3}\int \mathrm{d}^3q\,\mathrm{d}^3p\,\bar{n}_p = \frac{g_{\mathrm{g}}}{2\pi^2}T^3 2\,\zeta(3) \simeq 1.2\,\frac{g_{\mathrm{g}}}{\pi^2}T^3 \\
n_{\mathrm{q}} =& n_{\bar{\mathrm{q}}} = \frac{1}{V}\frac{1}{(2\pi)^3}\int \mathrm{d}^3q\,\mathrm{d}^3p\,\bar{n}_p = \frac{g_{\mathrm{q}}}{\pi^2}\,T^3 d(3) \simeq 0.9\,\frac{g_{\mathrm{q}}}{\pi^2}T^3 \\
\epsilon_{\mathrm{g}} =& \frac{1}{V}\frac{1}{(2\pi)^3}\int \mathrm{d}^3q\,\mathrm{d}^3p\,p\,\bar{n}_p \ = \frac{3g_{\mathrm{g}}}{\pi^2}\,T^4\,\zeta(4) = \frac{\pi^2 g_{\mathrm{g}}}{30}\,T^4 \\
\epsilon_{\mathrm{q}} =& \epsilon_{\bar{\mathrm{q}}} = \frac{3g_{\mathrm{q}}}{\pi^2}\,T^4\,d(4) = \frac{7\pi^2 g_{\mathrm{q}}}{240}\,T^4
\end{aligned} \tag{3.14}$$

with

$$\zeta(\xi) = \frac{1}{\Gamma(\xi)}\int_0^\infty \mathrm{d}\alpha\,\frac{\alpha^{\xi-1}}{e^{\alpha}-1} \qquad \text{and} \qquad d(\xi) = \frac{1}{\Gamma(\xi)}\int_0^\infty \mathrm{d}\alpha\,\frac{\alpha^{\xi-1}}{e^{\alpha}+1}\,. \tag{3.15}$$

Thus, the mean energy per particle is given by

$$\begin{aligned}
\langle E_{\mathrm{g}}\rangle =& \frac{\epsilon_{\mathrm{g}}}{n_{\mathrm{g}}} = 3T\,\frac{\zeta(4)}{\zeta(3)} \simeq 2.7\,T \\
\langle E_{\mathrm{q}}\rangle =& \frac{\epsilon_{\mathrm{q}}}{n_{\mathrm{q}}} = 3T\,\frac{d(4)}{d(3)} \simeq 3.2\,T\,.
\end{aligned} \tag{3.16}$$

3.1.3. Space-Time Evolution: The Bjorken Model

The Bjorken model for the space-time evolution of the matter created in collisions of relativistic nuclei in the central rapidity region [91] is based on the observation that the rapidity density of produced hadrons (which can be related to the initial energy density of the produced matter) is large and shows a plateau around midrapidity and that the central rapidity region has a small net baryon number. The inferred picture of the collision is that the nuclei are essentially transparent to each other. This means that the baryon number is carried by the Lorentz contracted remnants of the nuclei receding from the interaction point with nearly speed of light. They leave the produced matter behind, which (for small times and distances from the interaction point) expands longitudinally with velocity $v = z/t$ (the collision takes place at $t = 0$ and $z = 0$, where z is the longitudinal coordinate). The energy density is high enough that fast thermalisation occurs and the system enters a phase of hydrodynamic evolution shortly after the collision. The existence of the central plateau implies that the collision looks the same in all centre-of-momentum-like

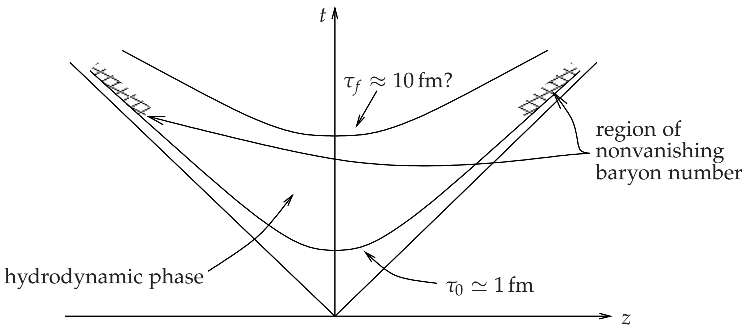

Figure 3.1.: Space-time evolution of the matter undergoing boost-invariant longitudinal expansion, figure from [91].

frames, which translates into a symmetry under boosts of the initial conditions for the hydrodynamic evolution.

A system in local thermal equilibrium is described by a local energy density $\epsilon(x)$, pressure $p(x)$, temperature $T(x)$ and four velocity $u_\mu(x)$. In this case they do not depend on the transverse coordinates and the dependence on time and longitudinal distance is best described in terms of the proper time τ and space-time rapidity y_s.

$$\begin{aligned} \tau &= \sqrt{t^2 - z^2} & \qquad t &= \tau \cosh y_\mathrm{s} \\ y_\mathrm{s} &= \frac{1}{2} \ln\left(\frac{t+z}{t-z}\right) & \qquad z &= \tau \sinh y_\mathrm{s} \end{aligned} \tag{3.17}$$

The boost invariance implies that the initial conditions are independent of y_s,

$$\begin{aligned} \epsilon(\tau_0, y_\mathrm{s}) &= \epsilon_0 \quad \text{etc.} \\ u_\mu(\tau_0, y_\mathrm{s}) &= \frac{1}{\tau_0}(t, 0, 0, z)\,. \end{aligned} \tag{3.18}$$

This property is preserved during the hydrodynamic evolution. The space-time evolution is shown in figure 3.1. The energy density, pressure and temperature are constant on hyperbolas of constant proper time.

When viscosity and heat conductivity are neglected the energy-momentum tensor

$$T_{\mu\nu} = (\epsilon + p) u_\mu u_\nu - g_{\mu\nu} p \tag{3.19}$$

is conserved:

$$\frac{\partial T_{\mu\nu}}{\partial x_\mu} = 0\,. \tag{3.20}$$

Using the boost invariance this equation simplifies to

$$\frac{\mathrm{d}\epsilon}{\mathrm{d}\tau} = -\frac{\epsilon + p}{\tau}\,. \tag{3.21}$$

The conservation law

$$\frac{\partial s_\mu}{\partial x_\mu} = 0 \tag{3.22}$$

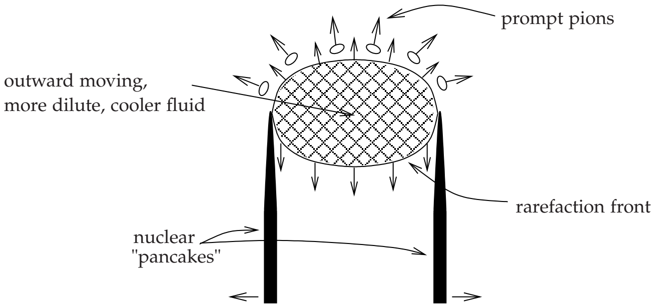

Figure 3.2.: Rarefaction front travelling inwards from the surface of the matter, figure from [91].

for the entropy density current

$$s_\mu = \frac{S}{V} u_\mu = \frac{\epsilon + p}{T} u_\mu \tag{3.23}$$

can also be derived from equation (3.20). With equation (3.18) this leads to

$$\frac{\mathrm{d}s}{\mathrm{d}\tau} = -\frac{s}{\tau} \quad \Rightarrow \quad s(\tau) = s(\tau_0)\frac{\tau_0}{\tau}\,, \tag{3.24}$$

which implies that the entropy per unit rapidity is conserved.

The time dependence of the temperature can be derived from equation (3.21):

$$\frac{\mathrm{d}\epsilon}{\mathrm{d}\tau} = \frac{\mathrm{d}\epsilon}{\mathrm{d}p}\frac{\mathrm{d}p}{\mathrm{d}T}\frac{\mathrm{d}T}{\mathrm{d}\tau} = -\frac{\epsilon + p}{\tau} = -\frac{Ts}{\tau}\,. \tag{3.25}$$

With

$$\frac{\mathrm{d}p}{\mathrm{d}T} = s \qquad \text{and} \qquad \frac{\mathrm{d}\epsilon}{\mathrm{d}p} = \frac{1}{v_\mathrm{s}} \tag{3.26}$$

one arrives at

$$\frac{1}{T}\frac{\mathrm{d}T}{\mathrm{d}\tau} = -\frac{v_\mathrm{s}^2}{\tau}\,. \tag{3.27}$$

In an ideal relativistic fluid the equation of state is $\epsilon = 3p$ and the sound velocity is $v_\mathrm{s}^2 = 1/3$. Inserting this into equation (3.21) and equation (3.27) one finds for the time dependence of the energy density and temperature

$$\epsilon(\tau) = \epsilon(\tau_0)\left(\frac{\tau_0}{\tau}\right)^{\frac{4}{3}} \quad \text{and} \quad T(\tau) = T(\tau_0)\left(\frac{\tau_0}{\tau}\right)^{\frac{1}{3}}\,. \tag{3.28}$$

The picture of pure longitudinal expansion is strictly speaking only valid near the centre of the medium. A rarefaction front is expected to propagate inwards from the edges at the velocity of sound (figure 3.2). When the sound velocity is independent of time the rarefaction front is described by

$$\rho(t) = R - \int\limits_0^{\sqrt{t^2-z^2}} \mathrm{d}t' v_\mathrm{s}(t') = R - v_\mathrm{s}\sqrt{t^2 - z^2} \tag{3.29}$$

At transverse distances not yet reached by the front the matter expands only longitudinally because the information about the finite size of the matter has not yet reached this region. Beyond the front, on the other hand, a more complex three dimensional expansion leading to a faster cooling is expected.

3.2. Jet Quenching at RHIC

In terms of data the jet physics field is currently dominated by the four experiments Brahms, Phenix, Phobos and Star at the Relativistic Heavy Ion Collider Rhic in Brookhaven, which has a beam energy of up to 200 GeV per nucleon. Due to the enormous background and the steeply falling partonic spectrum these experiments are largely limited to leading hadrons, although first results on reconstructed jets have recently been presented [92–94]. This will be different at Cern's Large Hadron Collider Lhc, which also has a heavy ion program with lead ions at 5.5 TeV per nucleon starting in 2009. Due to the higher beam energy and the larger kinematical range reconstruction of jets with 100 GeV energy and more using classical cone or even $k_\perp$-algorithms [95, 96] will be possible [20–22]. The Alice experiment is dedicated to heavy ion physics, but Cms will also contribute to this field.

3.2.1. Single-Inclusive Spectra

High transverse momentum hadrons are believed to be produced solely from the fragmentation of hard partons, which stem from a hard partonic scattering event that falls in the perturbative regime. Hard processes are short-distance phenomena with a resolution of the order $1/Q \simeq 1/p_\perp$, which is much smaller than the size of a nucleon. The hard process itself happens on a very short timescale ($\mathcal{O}(1/Q)$), i.e. before the formation of a thermalised medium. Due to the factorisation of the cross section the hard matrix element remains unaffected and only the parton densities and the fragmentation functions can be modified in nuclear collisions. In the absence of nuclear effects in the initial state a nucleus is the incoherent sum of its nucleons and the production of high $p_\perp$ partons scales with the number of binary nucleon-nucleon collisions. The quantity used to characterise single-inclusive high-$p_\perp$ hadron production in nuclear collisions is the *nuclear modification factor*

$$R_{AB} = \left(\frac{1}{N_{\text{evt}}} \frac{\mathrm{d}^2 N^{AB}}{\mathrm{d}p_\perp \mathrm{d}\eta} \right) \cdot \left(T_{AB} \frac{\mathrm{d}^2 \sigma^{\text{pp}}}{\mathrm{d}p_\perp \mathrm{d}\eta} \right)^{-1} , \tag{3.30}$$

which is unity in the absence of nuclear effects. It contains modifications of the initial and the final state. Soft particle production ($p_\perp \lesssim 1\,\text{GeV}$) is naively expected to scale with the number of participating nucleons, which is larger than the number of binary collisions. This leads to a decrease of R_{AB} below unity for small $p_\perp$ even without nuclear modifications.

Charged particle spectra measured by the Phenix experiment in p+p collisions exhibit $x_\perp$ scaling (equation (2.55)) with a power $n = 6.3$ [16]. The π^0 $p_\perp$-spectrum is found to be in good agreement with pQCD predictions. The π^0 spectrum in Au+Au collisions also scales with $x_\perp$ and the same power 6.3 is found indicating that hard

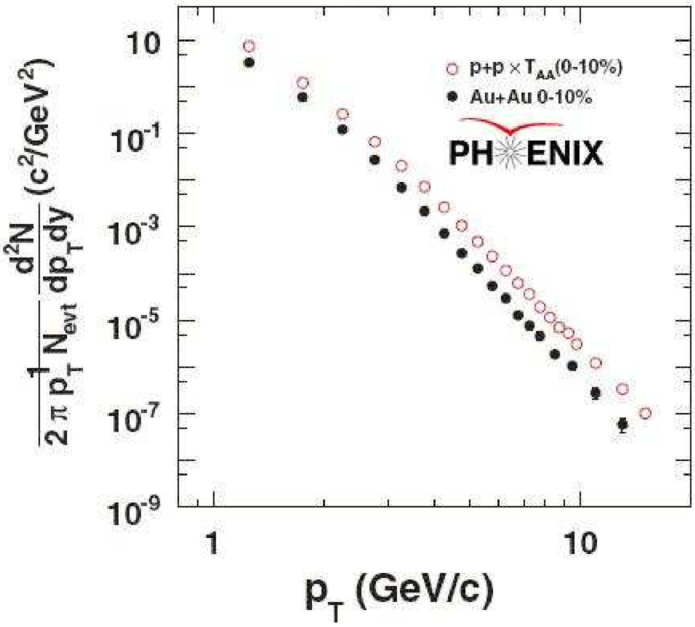

Figure 3.3.: Transverse momentum spectrum of neutral pions in central Au+Au collisions compared to the p+p reference measurement scaled with the number of binary collisions in the $0 - 10\,\%$ centrality class [97].

processes as described by pQCD are the dominant source of high $p_\perp$ neutral pions in nucleus-nucleus collisions [16].

The π^0 spectrum in central Au+Au collisions is shown in figure 3.3 together with the p+p result scaled with the number of binary collisions. The shape is similar, but the yield is significantly lower in Au+Au. This is better seen in figure 3.4, which shows the nuclear modification factor in different centrality bins. There is a reduction of the π^0 yield at intermediate and high $p_\perp$ by roughly a factor 5 in central gold-gold collisions as compared to the naive expectation from p+p collisions. The suppression increases smoothly with centrality, there is no sign for a threshold behaviour. The high-$p_\perp$ spectra scale neither with the number of binary collisions nor with the number of participants. The centrality classes are characterised in table 3.1.

In order to disentangle initial and final state effects the nuclear modification factor has also been measured in deuteron-gold collisions at the same energy (figure 3.5). In this reaction nuclear modifications of the initial state are expected to be present while there should be no effects on the final state. The absence of high-$p_\perp$ hadron suppression in d+Au collisions indicates that the strong modification in Au+Au can be attributed to final state effects. It also implies that the initial state can (for high-$p_\perp$ particle production at mid-rapidity) be viewed as the incoherent sum of the individual nucleons. This is further supported by direct photon and charm production in nucleus-nucleus collisions, which scales approximately with the number of binary collisions (figure 3.6). These observables are insensitive to final state effects since

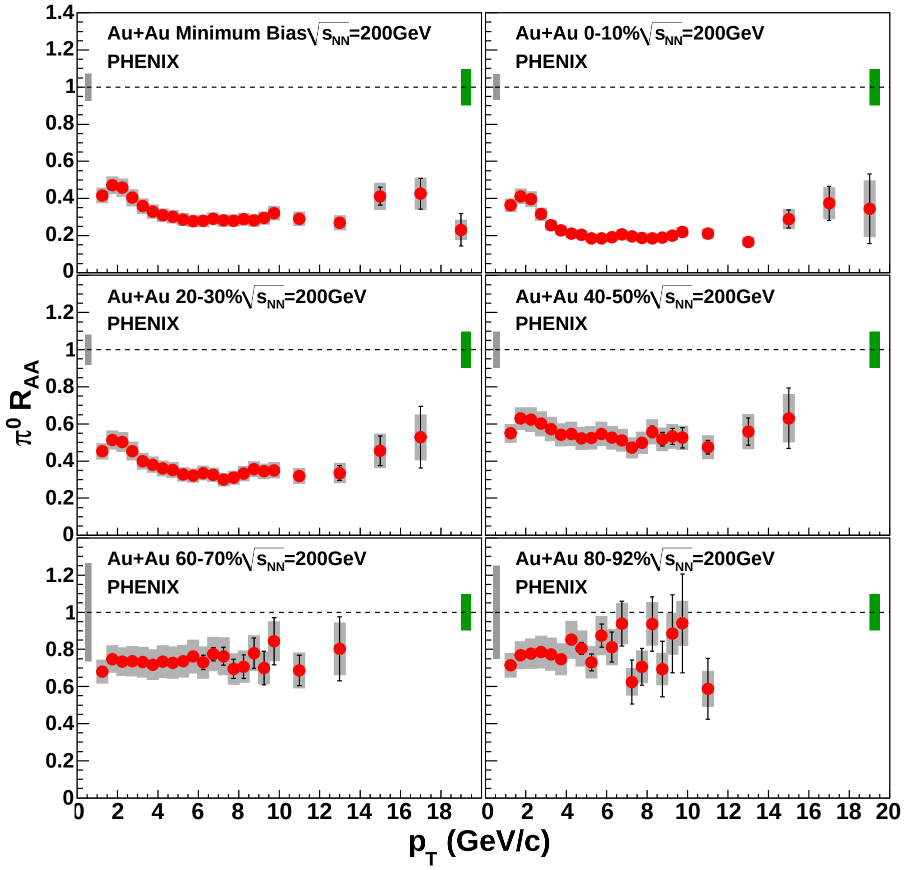

Figure 3.4.: Nuclear modification factor of neutral pions in Au+Au collisions for different centralities [98].

centrality	$\langle N_{\mathrm{bin}} \rangle$	$\langle N_{\mathrm{part}} \rangle$
$0-10\%$	955.4 ± 93.6	325.2 ± 3.3
$10-20\%$	602.6 ± 59.3	234.6 ± 4.7
$20-30\%$	373.8 ± 39.6	166.6 ± 5.4
$30-40\%$	219.8 ± 22.6	114.2 ± 4.4
$40-50\%$	120.3 ± 13.7	74.4 ± 3.8
$50-60\%$	61.0 ± 9.9	45.5 ± 3.3
$60-70\%$	28.5 ± 7.6	25.7 ± 3.8
$70-80\%$	12.4 ± 4.2	13.4 ± 3.0
$80-92\%$	4.9 ± 1.2	6.3 ± 1.2
min. bias	257.8 ± 25.4	109.1 ± 4.1

Table 3.1.: Centrality classes with the number of participants and binary collisions as used by PHENIX [99], the percent values characterising the centrality classes give the fraction of the total cross section $\sigma^{\mathrm{AuAu}} = 6.9\,\mathrm{b}$.

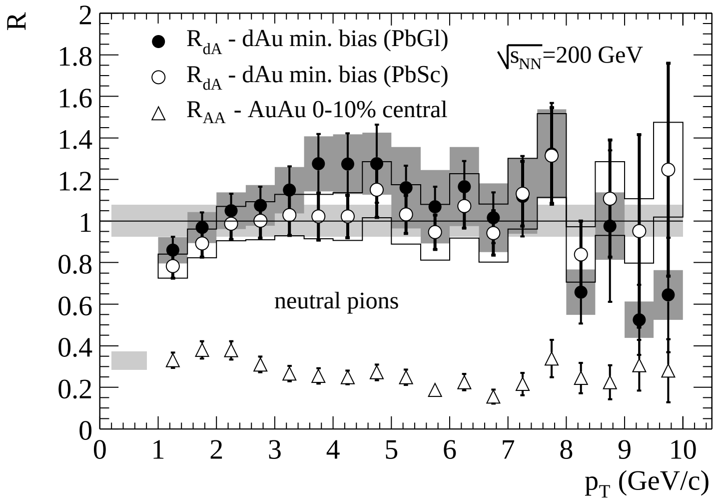

Figure 3.5.: Nuclear modification factor of neutral pions in d+Au collisions measured by two different calorimeters compared to the central Au+Au result (PHENIX data [100]).

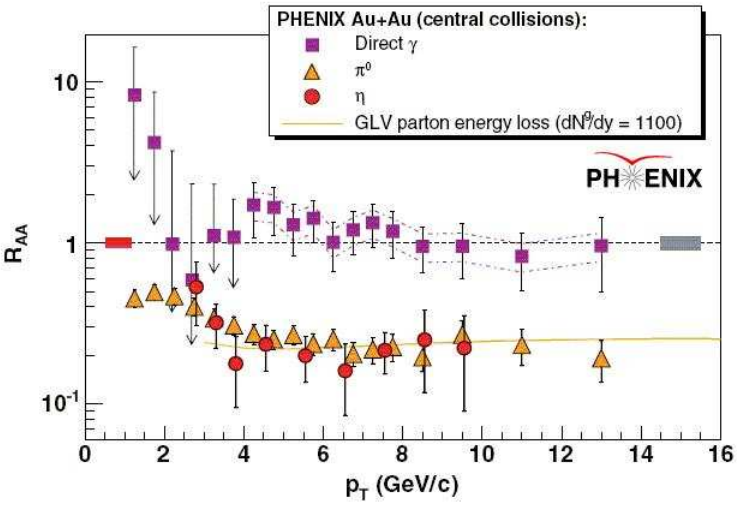

Figure 3.6.: Nuclear modification factor of direct photons, π^0 and η in central Au+Au collisions [101].

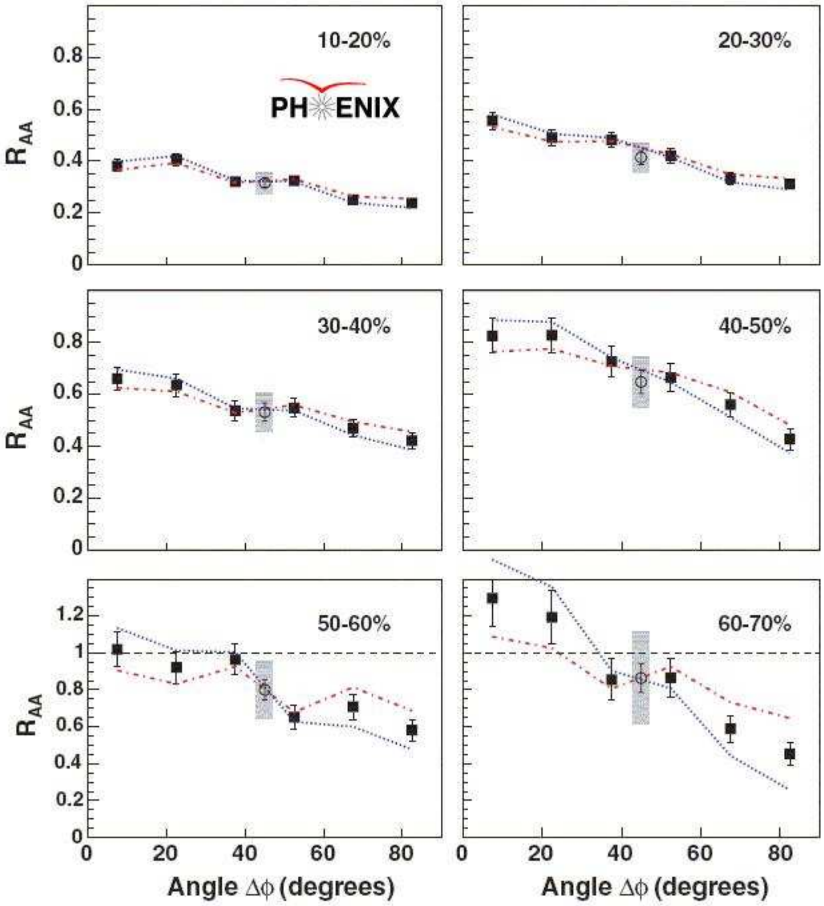

Figure 3.7.: Nuclear modification factor of neutral pions in Au+Au collisions at $\sqrt{s_{\mathrm{NN}}} = 200\,\mathrm{GeV}$ as a function of the angle relative to the reaction plane [97]. The π^0 yields are integrated in the region $5 < p_\perp < 8\,\mathrm{GeV}$.

photons do not interact strongly and final state modifications of charm affect only the shape of the spectrum, not the yield. There is, however, room for a slight increase of R_{dAu} above unity. This has been interpreted as Cronin effect, which is known from proton-nucleus and nucleus-nucleus collisions at lower energies and denotes an increase of high-$p_\perp$ particle production relative to binary scaling. This effect is commonly attributed to multiple soft scattering of the incoming nucleon or its partons prior to the hard interaction.

The strong suppression of high-$p_\perp$ hadrons in nucleus-nucleus collisions is believed to arise mainly from induced gluon radiation off hard partons in the quark-gluon plasma. The parton loses a significant fraction of its energy and fragments into softer hadrons. There are several energy loss models which describe the measured R_{AA} quite well (section 3.3.2). The role of energy loss due to elastic scattering (section 3.3.1) in the QGP is currently under debate. In both scenarios, however, the energy loss depends on the path length inside the medium. Different centrality

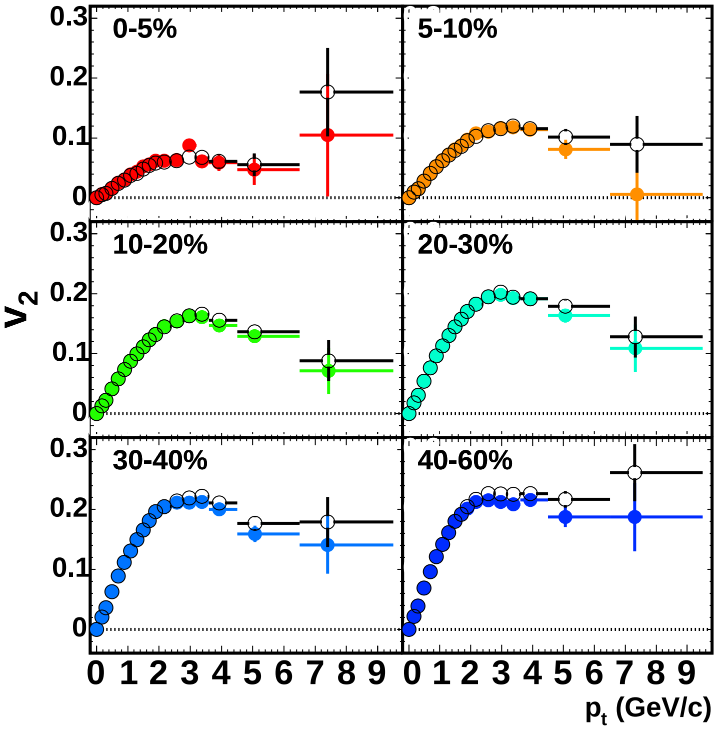

Figure 3.8.: Elliptic flow coefficient v_2 for charged particles measured by STAR [102] in Au+Au collisions at $\sqrt{s_{\mathrm{NN}}} = 200\,\mathrm{GeV}$ as a function of $p_\perp$. Open and closed symbols correspond to different reaction plane determination methods.

classes have different mean path lengths, but possibly also different energy densities. A cleaner way to study the path length dependence is thus to measure the nuclear modification factor in a given centrality class as a function of the angle relative to the reaction plane. The reaction plane is defined by the beam direction and the impact parameter. The diameter of the overlap region in the transverse plane is smallest in the reaction plane and largest perpendicular to it. The data show in fact a variation of the nuclear modification factor with the angle of the hadron relative to the reaction plane (figure 3.7). This asymmetry also manifests itself in the azimuthal distribution of particles. It is quantified by the second coefficient v_2 in the Fourier expansion of the particle spectrum

$$E\frac{\mathrm{d}^3N}{\mathrm{d}^3p} = \frac{1}{2\pi}\frac{\mathrm{d}^2N}{p_\perp \mathrm{d}p_\perp \mathrm{d}y}\left[1 + \sum_{n=1}^{\infty} 2v_n \cos(n\varphi)\right], \tag{3.31}$$

which is called elliptic flow coefficient. It can be written as

$$v_2 = \langle\cos(2\varphi)\rangle\,, \tag{3.32}$$

where φ is the angle relative to the reaction plane. The azimuthal anisotropy observed at low transverse momenta is caused by the collective flow of the expanding

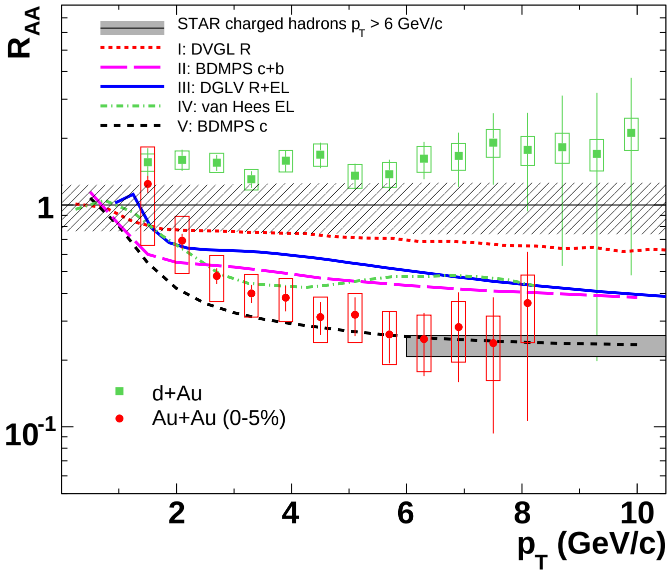

Figure 3.9.: Nuclear modification factors of non-photonic electrons in d+Au and central Au+Au collisions measured by STAR [103]. The lines give the results of different energy loss models, the charged hadron R_{AA} is also indicated.

medium. It is not expected to influence hadron spectra at high transverse momenta and can therefore not explain the large values of v_2 found at high $p_\perp$ (figure 3.8). This observation is qualitatively in agreement with the energy loss scenario, but the energy loss models cannot explain the large asymmetry in peripheral collisions.

Heavy flavours are at high $p_\perp$ measured via the electrons from their semi-leptonic decays. It has so far not been possible to discriminate between charm and beauty decays due to missing vertex tracking capabilities. The inclusive electron spectrum is at low $p_\perp$ dominated by charm and at high $p_\perp$ by beauty. The crossing point is at $p_\perp \approx 4\,\text{GeV}$ with a large (theoretical) uncertainty. First attempts to experimentally determine the beauty contribution on a statistical basis in p+p collisions are consistent with theoretical expectations [104, 105]. The nuclear modification factor of non-photonic electrons is shown in figure 3.9 to be the same as for light hadrons at high $p_\perp$. At face value this contradicts expectations from radiative energy loss models, which predict a clear mass hierarchy of the energy loss. It has been argued that collisional energy loss could explain the apparent equal suppression of light and heavy flavours, but the kinematics of elastic scattering favours a smaller energy loss of heavy projectiles [106]. Another explanation is that experimental and theoretical uncertainties may be largely underestimated [107].

Another surprise is the finding that the suppression of neutral pions is stronger than that of unidentified charged particles in the intermediate $p_\perp$ region. This is connected to an anomalously large proton to pion ratio, which increases with centrality (figure 3.10). The picture that the fragmentation of a hard parton is described by

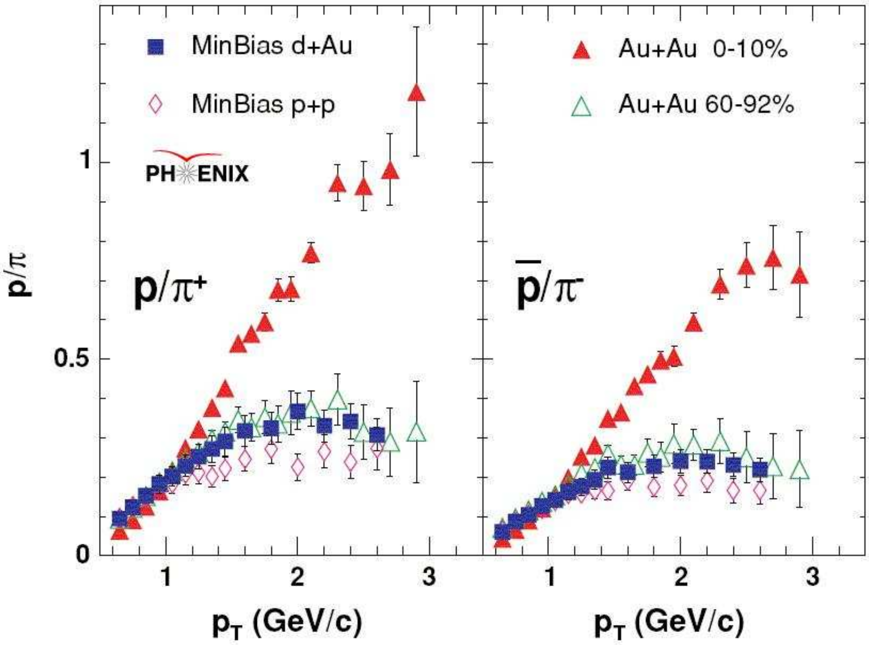

Figure 3.10.: Proton to pion ratio as a function of $p_\perp$ for p+p, d+Au, central and peripheral Au+Au collisions [108].

a vacuum fragmentation function shifted by the energy loss is obviously too naive, although the argument that energetic partons hadronise outside the medium due to time dilatation effects is probably correct. The enhanced p/π ratio has been counted as sign for recombination. This is an alternative hadronisation model that allows jet fragments to pick up (anti)quarks from the medium to form hadrons [109–113]. On the other hand, changes in the hadrochemical composition of jets may well be a natural consequence of radiative energy loss even if the hadronisation happens outside the medium [35].

3.2.2. Dihadron Azimuthal Correlations

An alternative way of accessing energetic hadrons from jet fragmentation are dihadron correlations. In the original form used by the Star experiment an energetic trigger particle is required. The azimuthal distribution $D(\Delta\phi)$ is defined as the distribution of azimuthal angles relative to the trigger of associated hadrons in a certain $p_\perp$ window

$$D(\Delta\phi) = \frac{1}{N_{\text{trig}}} \frac{\mathrm{d}N}{\mathrm{d}(\Delta\phi)} \,. \tag{3.33}$$

In proton-proton collisions $D(\Delta\phi)$ reflects the geometry of two-jet events. It contains a relatively narrow peak at $\Delta\phi \sim 0$, which is the near-side jet to which the trigger particle belongs, and a broader peak at $\Delta\phi \sim \pi$, which is the away-side jet

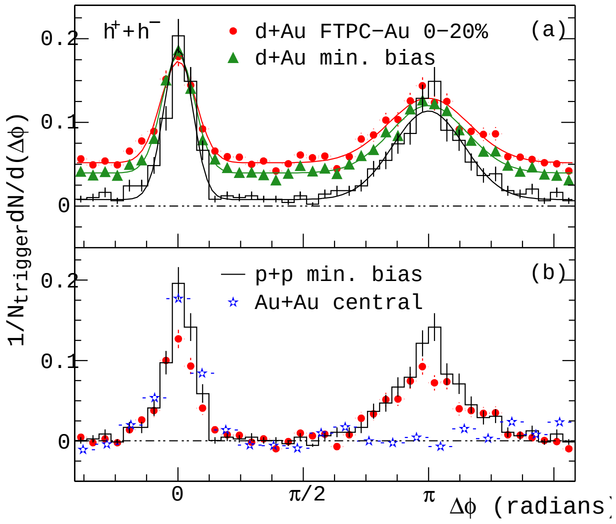

Figure 3.11.: Azimuthal distribution $D(\Delta\phi)$ measured by Star [114] for p+p, d+Au and central Au+Au collisions (elliptic flow and pedestal distributions have been subtracted in (b)), solid lines in (a) are Gaussian fits. Trigger particles have $4 < p_\perp^{\text{trig}} < 6\,\text{GeV}$, associated particles have transverse momenta in the range $2\,\text{GeV} < p_\perp^{\text{ass}} < p_\perp^{\text{trig}}$.

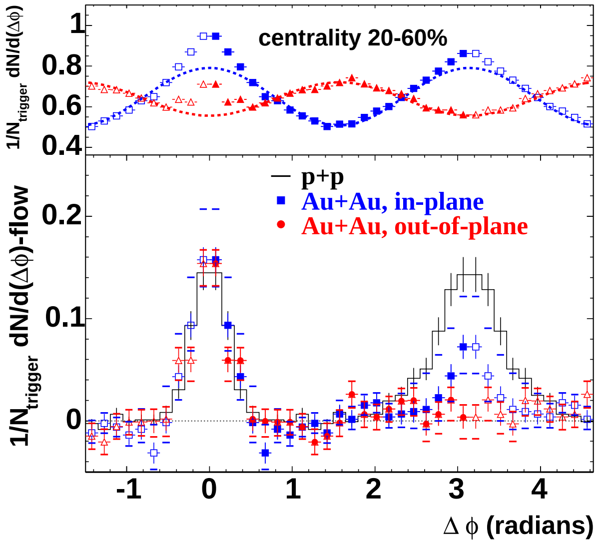

Figure 3.12.: Upper panel: Two-particle correlations from Star [115] for trigger particles in-plane (squares) and out-of-plane (triangles) in mid-central Au+Au collisions. The contribution from elliptic flow is shown by dashed lines. Lower panel: Azimuthal distributions after subtracting the elliptic flow and p+p data.

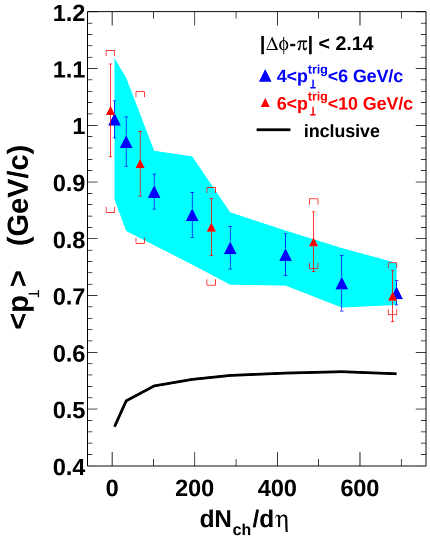

Figure 3.13.: Mean transverse momentum of associated particles ($0.15 < p_\perp^{\mathrm{ass}} < 4\,\mathrm{GeV}$) on the away-side of an energetic trigger as a function of collision centrality (Star data [116]).

(figure 3.11). Because of the steeply falling $p_\perp$-spectrum the requirement of an energetic trigger hadron strongly biases the trigger jets. It is much more likely to pick up a lower energy jet with a leading parton carrying an anomalously large fraction of the energy than a more energetic jet with a normal fragmentation pattern. The away-side jet, on the other hand, is unbiased. Therefore, the width of the trigger jet is significantly smaller than that of the away-side jet and nearly independent of the trigger $p_\perp$, while the away-side width decreases with $p_\perp^{\mathrm{trig}}$.

The azimuthal correlation measured in d+Au collisions resembles the p+p result (figure 3.11), apart from a constant off-set. In non-central nucleus-nucleus collisions there is an additional contribution from the elliptic flow

$$\frac{\mathrm{d}N_{\mathrm{ef}}}{\mathrm{d}(\Delta\phi)} \propto 1 + 2v_2^{\mathrm{trig}} v_2^{\mathrm{ass}} \cos(2\Delta\phi)\,, \tag{3.34}$$

where v_2^{trig} and v_2^{ass} are the coefficients for triggers and associated particles, respectively. The elliptic flow contribution has to be subtracted in order to obtain the jet-like correlation. Figure 3.11 shows that in central Au+Au collisions the away-side jet disappears while the trigger jet remains essentially unchanged. In nuclear collisions there is an additional trigger bias which favours trigger jets that experienced an unusually small energy loss and look like jets in p+p collisions. The disappearance of the away-side jet is again attributed to energy loss of fast partons in the QGP. As in the case of single-inclusive hadron suppression this interpretation gets support from a measurement of the dependence of the suppression on the angle relative to the reaction plane. Here, a pair is defined to be in-plane if the azimuthal angle of the trigger particles satisfies $|\phi^{\mathrm{trig}} - \Psi_2| < \pi/4$ or $|\phi^{\mathrm{trig}} - \Psi_2| > 3\pi/4$ where Ψ_2 is the reaction plane angle of the event. A trigger is out-of-plane if $\pi/4 < |\phi^{\mathrm{trig}} - \Psi_2| < 3\pi/4$. The elliptic flow contribution is different for the two components:

$$\frac{\mathrm{d}N^{\mathrm{in}}_{\mathrm{out}}}{\mathrm{d}\Delta\phi} = B\left[1 + 2v_2^{\mathrm{ass}}\left(\frac{\pi v_2^{\mathrm{trig}} \pm 2\langle\cos(2\Delta\Psi)\rangle}{\pi \pm 4v_2^{\mathrm{trig}}\langle\cos(2\Delta\Psi)\rangle}\right)\cos(2\Delta\phi)\right], \tag{3.35}$$

where $\langle\cos(2\Delta\Psi)\rangle$ is the reaction plane resolution. The resulting in-plane and out-of-plane contributions are shown in figure 3.12 for mid-central collisions. The suppression of the away-side jet is clearly stronger out-of-plane (where the mean path length in the medium is longer) than in-plane.

The energy of the away-side jet cannot disappear but has to show up at lower transverse momenta. The associated yields can be reconstructed on a statistical basis with low associated particle momenta ($0.15 < p_\perp^{\mathrm{ass}} < 4\,\mathrm{GeV}$). The associated hadron multiplicity and the transverse momentum distribution are similar to p+p data on the near-side indicating that the near-side correlation is jet-like and not much affected by the medium. This is further supported by the observation that the near-side correlation is stronger for particles with opposite charge, which is a characteristic of jet fragmentation. On the away-side, on the other hand, the associated multiplicity increases with centrality and the $p_\perp$ spectrum becomes softer. Figure 3.13 shows that the mean transverse momentum of associated particles on the away-side decreases with centrality and approaches the value of the bulk matter. This is counted as a sign for strong medium modifications and progressing thermalisation of the away-side jet.

At high momenta of trigger and associated particles a jet-like structure emerges on the away-side (figure 3.14). The yield is suppressed in agreement with expectations from energy loss models, but the distribution is narrow in angle and the shape of the transverse momentum distribution is similar to d+Au results and the near-side yield. This reappearance of the away-side jet is interpreted as 'punch-through', i.e. di-jets where either both have a short path length inside the medium and/or the energy is high enough to survive a moderate energy loss.

The angular shape of the away-side yield changes dramatically at lower momenta (figure 3.15). It develops a double-hump structure with maxima, that are shifted by $D \simeq 1\,\mathrm{rad}$ away from $\Delta\phi = \pi$. D is independent of the system size (i.e. the species of the colliding nuclei) and the beam energy and nearly independent of centrality. The most popular explanations are a Mach cone produced by a supersonic jet travelling through the medium [118–123], Čerenkov gluons [124–127] and deflected jets [30,32, 128,129]. Recent measurements of three-particle correlations seem to favour a conical emission pattern [130].

The near-side part of the azimuthal correlation also has a surprise in store that becomes apparent if one looks at the correlation in pseudo-rapidity[2]. In central Au+Au collisions the $\Delta\eta$ distribution of pairs with low momenta becomes very wide, but at higher momenta it looks like the p+p result (figure 3.16). This phenomenon,

---

[2] The pseudo-rapidity is defined as $\eta \equiv -\ln\tan(\theta/2)$.

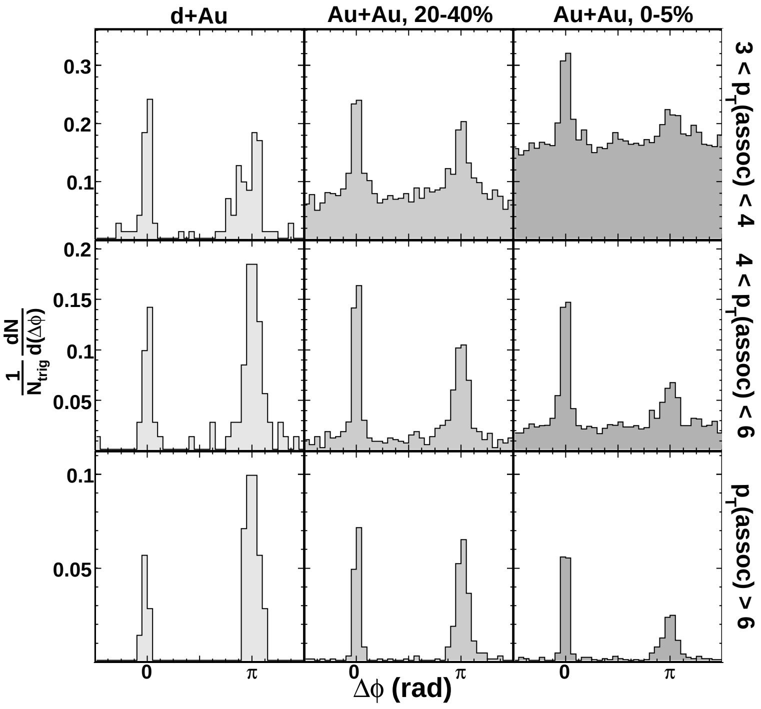

Figure 3.14.: Azimuthal correlation for high-$p_\perp$ triggers ($8 < p_\perp^{\mathrm{trig}} < 15\,\mathrm{GeV}$) in d+Au and mid-central and central Au+Au collisions (STAR data [117]).

which is called the ‘ridge’, is commonly ascribed to a medium modification of the jet fragmentation that imprints the strong longitudinal flow of the medium on the jet fragments leading to the $\Delta\eta$ broadening [32, 133–136].

The picture emerging from the study of dihadron correlations is that both the near- and the away-side have a high-$p_\perp$ component, which is essentially unaffected by the medium, and a strongly modified low-$p_\perp$ contribution, which shows characteristics of the medium. The medium modifications are stronger for the away-side jet while the near-side is more jet-like and closer to jets in p+p collisions due to the trigger bias.

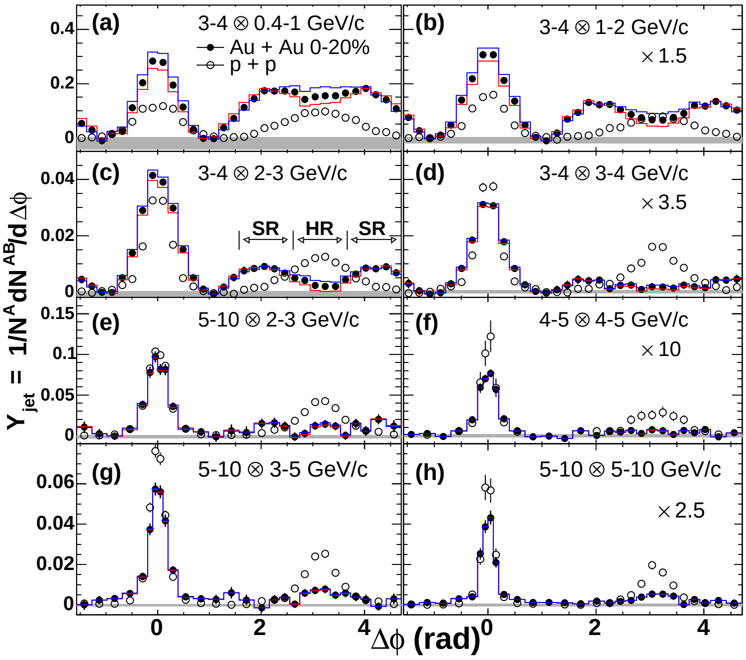

Figure 3.15.: Azimuthal correlation in p+p and central Au+Au collisions measured by Phenix [131] for different trigger and associated $p_\perp$ bins.

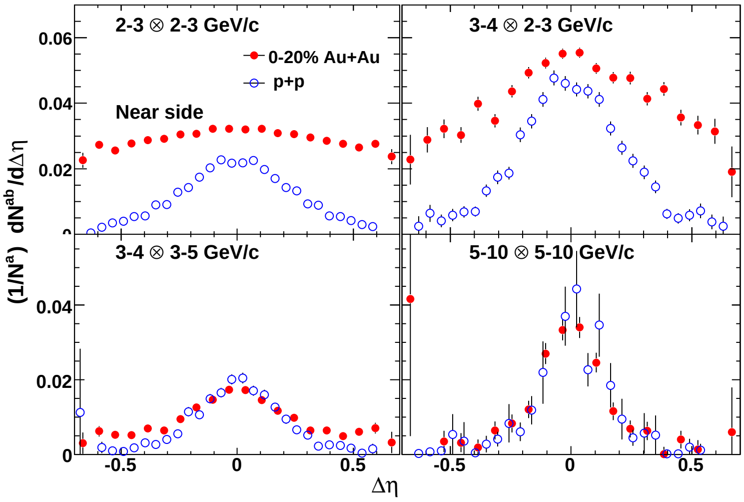

Figure 3.16.: Pseudo-rapidity correlation of near-side (in $\Delta\phi$) hadron pairs with different trigger and associated $p_\perp$ in p+p and central Au+Au collisions (Phenix data [132]).

3.3. Energy Loss Models

Partonic energy loss is attributed to elastic and inelastic scattering of the fast projectile in the medium, where the inelastic processes are commonly believed to be the dominant source of energy loss. This section briefly summarises the most prevalent ideas and models how energy loss can be treated theoretically.

3.3.1. Collisional Energy Loss

The first estimate of collisional energy loss of a fast parton in a QGP was presented by Bjorken [1]. He calculated the energy loss in perturbation theory from

$$-\frac{\mathrm{d}E}{\mathrm{d}x} = \int \mathrm{d}^3k\, \rho_{\mathrm{eff}}(k)\phi \int \mathrm{d}t\, \nu \frac{\mathrm{d}\sigma}{\mathrm{d}t} \tag{3.36}$$

with the effective plasma density

$$\rho_{\mathrm{eff}}(k) = \frac{2}{3}\rho_{\mathrm{q}}(k) + \frac{3}{2}\rho_{\mathrm{g}}(k)\,, \tag{3.37}$$

where the colour factors in the cross section have partly been absorbed in the density. Here, ϕ is the flux factor and $\nu = E' - E$ the energy loss in a single scattering. Keeping only the logarithmically enhanced part the scattering cross section is approximated as

$$\frac{\mathrm{d}\sigma}{\mathrm{d}t} = \left(\frac{2}{3}\right)^{\pm 1} \frac{2\pi\alpha_{\mathrm{s}}^2}{t^2}\,, \tag{3.38}$$

where the plus sign applies to projectile quarks and the minus sign to gluons, the rest of the colour factor resides in the effective density. In the case of massless partons and projectile energies that are large compared to the temperature the kinematics simplifies to

$$s = 2kE(1 - \cos\theta) \tag{3.39}$$

$$\nu = \frac{E|t|}{s} = \frac{|t|}{2k(1 - \cos\theta)} \tag{3.40}$$

$$\phi = (1 - \cos\theta)\,, \tag{3.41}$$

where θ is the angle between the incoming partons in the laboratory frame. Then the t integration in equation (3.36) can be carried out leading to

$$-\frac{\mathrm{d}E}{\mathrm{d}x} = \left(\frac{2}{3}\right)^{\pm 1} \pi\alpha_{\mathrm{s}}^2 \ln\left(\frac{|t_{\mathrm{max}}|}{|t_{\mathrm{min}}|}\right) \int \frac{\mathrm{d}^3k}{k}\, \rho_{\mathrm{eff}}(k)\,, \tag{3.42}$$

which is logarithmically infra-red divergent. The lower cut-off is related to colour screening in the medium and has later been argued to be given by the Debye screening mass. Bjorken also realised that screening affects the scattering in the regime of small momentum transfers, but chose $\sqrt{|t_{\mathrm{min}}|} = M \simeq 0.5 - 1\,\mathrm{GeV}$. The upper integration limit is given by kinematic constraints, Bjorken chose $\nu_{\mathrm{max}} = E/2$ because transferring essentially all the projectile energy to the target only exchanges the roles of the two. This leads to

$$\frac{|t_{\max}|}{|t_{\min}|} = \frac{s}{2M^2} = \frac{kE(1-\cos\theta)}{M^2} \simeq \frac{kE}{M^2} \,. \tag{3.43}$$

Finally, the integration over k can be carried out for an ideal gas of massless (anti)quarks and gluons if a minimum momentum $k_{\min} \simeq M \ll T$ is assumed and the variation of k in the logarithm is neglected

$$\begin{aligned} -\frac{\mathrm{d}E}{\mathrm{d}x} &= \left(\frac{2}{3}\right)^{\pm 1} 4\pi^2\alpha_\mathrm{s}^2 \ln\left(\frac{\langle k\rangle E}{M^2}\right) \int k \frac{\mathrm{d}k}{(2\pi)^3} \left(\frac{2}{3}\frac{12n_\mathrm{f}}{e^{k/T}+1} + \frac{3}{2}\frac{16}{e^{k/T}-1}\right) \\ &= \left(\frac{2}{3}\right)^{\pm 1} 2\pi\alpha_\mathrm{s}^2 T^2 \left(1+\frac{n_\mathrm{f}}{6}\right) \ln\left(\frac{\langle k\rangle E}{M^2}\right) . \end{aligned} \tag{3.44}$$

This type of calculation has been repeated with different improvements [3,6,7,137, 138] like more accurate matrix elements, running of the coupling or more sophisticed kinematic considerations. However, they all suffer from the infra-red divergence and the heuristic arguments that have to be invoked to regularise the integral. Screening can only be treated correctly in thermal field theory, which has its own problems and complications (cf. [139]).

In the following the most important ingredients to the energy loss computations in the framework of thermal field theory will be introduced[3]. Strictly speaking, they are limited to a regime of weak coupling $g \ll 1$ and high temperature, so that the masses of thermal particles can be neglected. This allows for a separation of hard ($\mathcal{O}(T)$) and soft ($\mathcal{O}(gT)$) scales.

In the imaginary time formalism of QCD at finite temperature the bare propagator, which is the vacuum expectation value of the time ordered product of two fields at different space-time points x and y in the zero-temperature theory, becomes a thermal expectation value. For a scalar field theory, for instance, one gets

$$\langle 0|\mathcal{T}\{\phi(x)\phi(y)\}|0\rangle \longrightarrow \frac{1}{Z}\sum_n \langle n|\mathcal{T}\{\phi(x)\phi(y)\}|n\rangle e^{-E_n/T} \,, \tag{3.45}$$

where E_n and $|n\rangle$ are the eigenvalues and eigenstates of the free Hamiltonian and Z is the partition function, for instance the grand-canonical partition function at vanishing chemical potential

$$Z = \operatorname{tr} e^{-\hat{H}/T} = \int [\mathrm{d}\phi] \exp\left(-\int_0^{1/T} \mathrm{d}\tau \int \mathrm{d}^3x \mathcal{L}_\mathrm{E}(\phi,\partial\phi)\right) \,, \tag{3.46}$$

with the Lagrangian density in Euclidean space-time. The initial and final state must be the same, which implies the boundary condition $\phi(0,\vec{x}) = \phi(1/T,\vec{x})$. Analogously, the partition function in QCD is

$$Z = \int [\mathrm{d}A\, \mathrm{d}q\, \mathrm{d}\bar{q}\, \mathrm{d}c\, \mathrm{d}\bar{c}] \exp\left(-\int_0^{1/T} \mathrm{d}\tau \int \mathrm{d}^3x \mathcal{L}_{\mathrm{QCD,E}}\right) \,, \tag{3.47}$$

---

[3] The following discussion is based on [139].

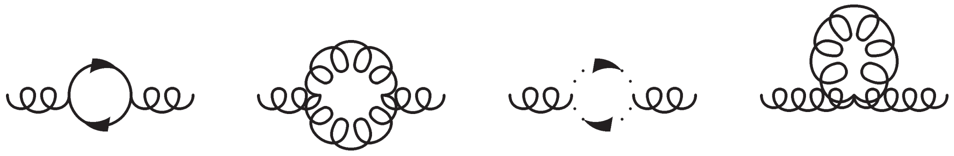

Figure 3.17.: Lowest order gluon self energy diagrams, dotted lines represent ghost fields.

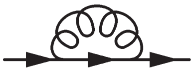

Figure 3.18.: Lowest order quark self energy.

where c is the ghost field. Due to the finite extension in temporal direction the energies of the particles can only take discrete values, the Matsubara frequencies, which are $\omega_n = 2n\pi T$ for gluons and $\nu_n = (2n+1)\pi T$ for quarks. The measure of loop integrals becomes

$$T\sum_n \int \frac{\mathrm{d}^3k}{(2\pi)^3}\,. \tag{3.48}$$

The free thermal gluon and quark propagators in momentum space are

$$\begin{aligned} D_{\mu\nu}(K) &= \frac{1}{K^2}\left(\delta_{\mu\nu} - (1-\xi)\frac{K_\mu K_\nu}{K^2}\right) \\ S(P) &= \frac{1}{-\gamma_4\nu_n + \vec{\gamma}\cdot\vec{p} + m}\,, \end{aligned} \tag{3.49}$$

where ξ is the gauge fixing parameter. Capital letters denote four-momenta, small letters stand for three-momenta, greek indices run over the four space-time components and latin indices over the three space-components.

Among the most important quantities in thermal field theory are the self energies. The diagrams contributing to lowest order to the gluon self energy $\Pi_{\mu\nu}$ are given in figure 3.17. From the transversality of the polarisation tensor it follows that $\Pi_{\mu\nu}$ has only two independent components, which can be chosen as the longitudinal and transverse component

$$\begin{aligned} \Pi_{\mathrm{L}}(K) &= \Pi_{00}(K) \\ \Pi_{\mathrm{T}}(K) &= \frac{1}{2}\left(\delta_{ij} - \frac{k_i k_j}{k^2}\right)\Pi_{ij}(K)\,. \end{aligned} \tag{3.50}$$

In the limit where the momenta in the loops are hard ($\gtrsim T$) and large compared to the gluon momentum analytic expressions for the gluon self energy can be derived.

This hard thermal loop (HTL) limit is equivalent to the high temperature limit. The leading term in the expansion is given by

$$
\begin{aligned}
\Pi_{\mathrm{L}}(K) &= -3m_{\mathrm{g}}^2\left[1-\frac{\omega}{2k}\ln\left(\frac{\omega+k}{\omega-k}\right)\right] \\
\Pi_{\mathrm{T}}(K) &= \frac{3}{2}m_{\mathrm{g}}^2\frac{\omega^2}{k^2}\left[1-\left(1-\frac{k^2}{\omega^2}\right)\frac{\omega}{2k}\ln\left(\frac{\omega+k}{\omega-k}\right)\right]
\end{aligned}
\tag{3.51}
$$

with the thermal gluon mass

$$
m_{\mathrm{g}}^2 = \frac{g^2T^2}{3}\left(1+\frac{n_{\mathrm{f}}}{6}\right). \tag{3.52}
$$

The gluon self energy is related to the dielectric constants of the medium

$$
\begin{aligned}
\epsilon_{\mathrm{L}}(K) &= 1-\frac{\Pi_{\mathrm{L}}(K)}{k^2} \\
\epsilon_{\mathrm{T}}(K) &= 1-\frac{\Pi_{\mathrm{T}}(K)}{\omega^2}
\end{aligned}
\tag{3.53}
$$

and can also be calculated in classical transport theory. The quark self energy can be derived from the diagram in figure 3.18 and reads in the HTL limit

$$
\begin{aligned}
\Sigma(P) = -\frac{1}{4p^2}&\left[4m_{\mathrm{q}}^2 - p_0\frac{2m_{\mathrm{q}}^2}{p}\ln\left(\frac{p_0+p}{p_0-p}\right)\right]P^{\mu}\gamma_{\mu} \\
&-\frac{1}{4p^2}\left[P^2\frac{2m_{\mathrm{q}}^2}{p}\ln\left(\frac{p_0+p}{p_0-p}\right)-p_0 4m_{\mathrm{q}}^2\right]\gamma_0\,,
\end{aligned}
\tag{3.54}
$$

where the bare quark mass is neglected and the thermal quark mass is

$$
m_{\mathrm{q}}^2 = \frac{g^2T^2}{6}\,. \tag{3.55}
$$

Naive perturbation theory, which is formulated in terms of the bare Green's functions, fails because for some quantities it does not reproduce all contributions to a certain order in the coupling. Braaten and Pisarski realised this incompleteness of the naive perturbative expansion and developed a method to systematically generate all diagrams contributing to a certain order [140]. When the external momenta are hard ($\mathcal{O}(T)$) only the bare Green's functions contribute, but when the external momenta are soft ($\mathcal{O}(gT)$) HTL diagrams contribute to the same order. The strategy is thus to first identify the diagrams that are proportional to g^2T^2. In the next step these have to be resummed into effective Green's functions. Finally, the desired quantities can be calculated using either the bare or the effective Green's functions in ordinary perturbation theory, depending on the momentum scales.

The effective propagators are defined by Dyson-Schwinger equations, the equation for the gluon propagator is given diagrammatically in figure 3.19. The resulting

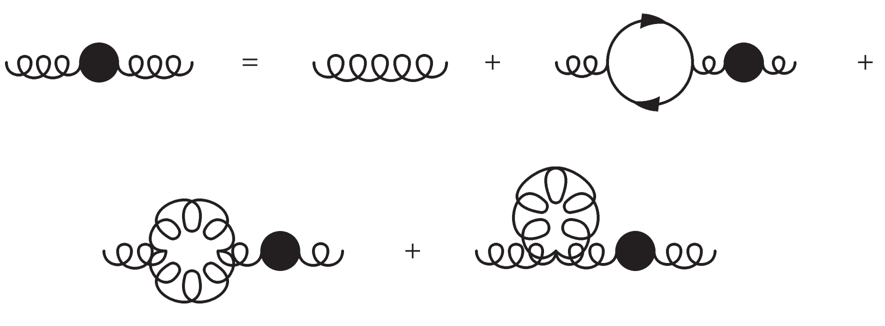

Figure 3.19.: Dyson-Schwinger equation defining the effective gluon propagator (denoted by a curly line with a blob).

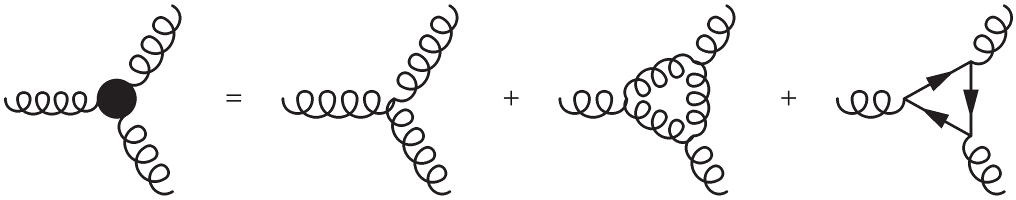

Figure 3.20.: Effective three-gluon vertex.

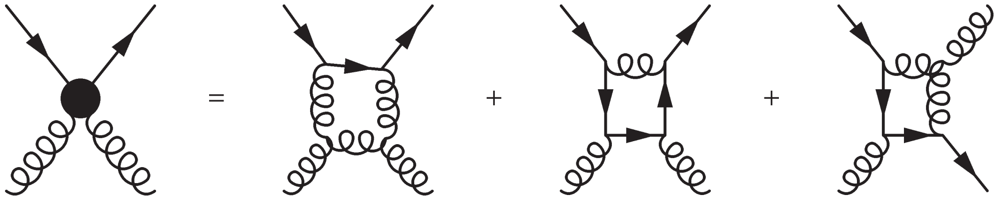

Figure 3.21.: Effective two-quark-two-gluon vertex.

effective gluon propagator is

$$\begin{aligned}
D_{\mathrm{L}}^{*-1}(K) &= k^2 - \Pi_{\mathrm{L}}(K) = k^2 + 3m_{\mathrm{g}}^2 \left[1 - \frac{\omega}{2k}\ln\left(\frac{\omega+k}{\omega-k}\right)\right] \\
D_{\mathrm{T}}^{*-1}(K) &= K^2 - \Pi_{\mathrm{T}}(K) = \omega^2 - k^2 - \frac{3}{2}m_{\mathrm{g}}^2\frac{\omega^2}{k^2}\left[1 - \left(1 - \frac{k^2}{\omega^2}\right)\frac{\omega}{2k}\ln\left(\frac{\omega+k}{\omega-k}\right)\right] .
\end{aligned} \tag{3.56}$$

The effective quark propagator can be derived in an analogous way. In gauge theories also the vertices receive HTL corrections, the effective vertices are found by adding the HTL correction to the bare vertex (e.g. figure 3.20). In QCD all n-gluon and n-gluon-plus-one-quark-pair amplitudes have to be corrected. This also gives rise to an effective two-quark-two-gluon vertex which has no bare contribution (figure 3.21). Then the calculation of the desired quantities can be performed using the effective Green's functions whenever all attached momenta are soft. The result is a complete order in the perturbative expansion in the coupling and it is gauge independent (for amplitudes on the mass-shell).

The energy loss of energetic projectiles in a plasma is one of the important applications of the Braaten-Pisarski method. It should be noted that except for the energy loss of heavy quarks there is always some ambiguity in the definition of the energy loss, because the scattering can produce energetic recoils that can contribute to the jet or take over the role of the projectile.

There are several ways to access the problem of collisional energy loss. In classical field theory the energy loss of a colour charge in a medium due to small momentum transfer scattering can be understood in the following way: The current induces a chromoelectric field in the medium which reacts back on the charge via the Lorentz force and causes its energy loss. The energy loss is then determined by the dielectric functions of the medium. For a quark one gets [2]

$$\frac{\mathrm{d}E}{\mathrm{d}x} = -\frac{C_\mathrm{F} g^2}{v} \int \frac{\mathrm{d}^3k}{(2\pi)^3} \left\{ \frac{\omega}{k^2} \left[\mathrm{Im}\, \epsilon_\mathrm{L}^{-1}(K) + (v^2k^2 - \omega^2) \mathrm{Im}\, (\omega^2 \epsilon_\mathrm{T}(K) - k^2)^{-1} \right] \right\} \tag{3.57}$$

With the help of equation (3.53) and inserting the HTL expression for the gluon self energy (equation (3.51)) one arrives at a lengthy but infra-red finite expression for the energy loss.

$$\mathrm{Im}\, \epsilon_\mathrm{L}^{-1}(K) = -\frac{3\pi m_\mathrm{g}^2}{2} \omega k \left\{ \left[k^2 + 3m_\mathrm{g}^2 - \frac{3m_\mathrm{g}^2}{2} \frac{\omega}{k} \ln \left(\frac{k+\omega}{k-\omega} \right) \right]^2 + \left[\frac{3\pi m_\mathrm{g}^2}{2} \frac{\omega}{k} \right]^2 \right\}^{-1} \tag{3.58}$$

$$\begin{aligned} \mathrm{Im}\, (\omega^2 \epsilon_\mathrm{T}(K) - k^2)^{-1} = {} & -\frac{3\pi m_\mathrm{g}^2}{4} \frac{\omega(k^2-\omega^2)}{k^3} \\ & \left\{ \left[k^2 - \omega^2 + \frac{3m_\mathrm{g}^2}{2} \frac{\omega^2}{k^2} \left(1 + \frac{k^2-\omega^2}{2\omega k} \ln \left(\frac{k+\omega}{k-\omega} \right) \right) \right]^2 \right. \\ & \left. \qquad + \left[\frac{3\pi m_\mathrm{g}^2}{4} \frac{\omega(k^2-\omega^2)}{k^3} \right]^2 \right\}^{-1} , \end{aligned} \tag{3.59}$$

where v is the quark velocity. The integral in equation (3.57) can only be evaluated analytically in the leading logarithm approximation, which means that on the right hand side of the Dyson-Schwinger equation for the effective propagator only free propagators are entered and which amounts to setting $m_\mathrm{g} = 0$ in the denominator of equation (3.58). Then the integral has to be cut off at an infra-red scale, for which the Debye momentum $k_\mathrm{D} = \sqrt{3} m_\mathrm{g}$ is chosen in [2]. The energy loss is then given by

$$\frac{\mathrm{d}E}{\mathrm{d}x} = \frac{4\pi}{3} C_\mathrm{F} \alpha_\mathrm{s}^2 T^2 \ln \left(\frac{k_\mathrm{max}}{k_\mathrm{D}} \right) \frac{1}{v^2} \left[v + \frac{v^2-1}{2} \ln \left(\frac{1+v}{1-v} \right) \right] \tag{3.60}$$

The deviation from the full expression is roughly 10 %.

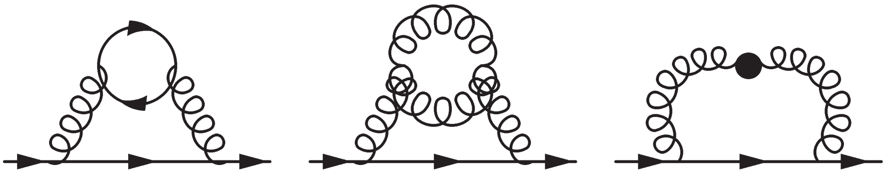

Figure 3.22.: Lowest order contributions to the imaginary part of the self energy of a heavy and/or energetic quark in naive (left and middle) and effective (right) perturbation theory.

This calculation only takes soft momentum transfers into account. The contribution from hard momentum transfers can be calculated using bare Green's functions and added to the soft part using the Braaten-Yuan prescription [141] . In this approach the soft and hard regime are separated by an arbitrary scale q^* satisfying $gT \ll q^* \ll T$. The contribution from soft momentum transfers $q < q^*$ can be calculated using the Braaten-Pisarski method and the hard part for $q > q^*$ can be obtained from ordinary perturbation theory with bare Green's functions. Both contribution depend logarithmically on q^* such that the sum is independent of q^*.

The energy loss computation in this framework has been extended in [5, 7] to include finite size effects.

The quantum field theoretical definition of the energy loss is in terms of the interaction rate Γ

$$-\frac{\mathrm{d}E}{\mathrm{d}x} = \frac{1}{v}\int \mathrm{d}E'\,(E-E')\frac{\mathrm{d}\Gamma(E,E')}{\mathrm{d}E'}\,, \tag{3.61}$$

where E and E' are the energies of the incoming and outgoing projectile in the medium rest frame, respectively. The interaction rate can be written analogously to the zero-temperature case as

$$\Gamma(E) = \sum_i \frac{1}{2E}\int\frac{\mathrm{d}^3p'}{(2\pi)^3 2E'}\int\frac{\mathrm{d}^3k}{(2\pi)^3 2\omega}n_i(k)\int\frac{\mathrm{d}^3k'}{(2\pi)^3 2\omega'}\left[1\pm n_i(k')\right] \\ \times (2\pi)^4\delta(P+K-P'-K')d\langle|\mathcal{M}_i|^2\rangle\,. \tag{3.62}$$

$P = (E, \vec{p})$ (P') is the incoming (outgoing) projectile momentum and K and K' belong to the scattering centre from the medium. $n_i(k)$ is the Bose-Einstein or Fermi-Dirac distribution of scattering centres and $[1 \pm n_i(k')]$ accounts for corresponding Bose enhancement or Pauli blocking of the scattered particle. $\mathcal{M}_i$ are the matrix elements, i runs over all possible scattering processes and d is a degeneracy factor. The computation of the hard momentum transfer contribution by Bjorken presented at the beginning of this section is also of this type. If one wants to include also the soft contribution it is advantageous to relate the interaction rate via cutting rules [142, 143] to the self energy. In the case of quarks this leads to

$$\Gamma(E) = -\frac{1}{2E}(1-n_\mathrm{F}(E))\mathrm{tr}\left[(P^\mu\gamma_\mu + M)\mathrm{Im}\,\Sigma(E+i\epsilon,\vec{p})\right] \tag{3.63}$$

with the quark mass M. The self energy takes a simple form when the quark is either heavy ($m \gg T$) or has a high energy. The leading order contributions for this case are given in figure 3.22. Again, for the hard momentum transfer it is sufficient to perform the calculations in naive perturbation theory. Cutting the internal quark lines in left diagram in figure 3.22 shows the equivalence to t-channel scattering of the fast quark from a quark in the plasma. For the soft momentum transfer contribution the effective quark self energy has to be computed. For the fast and/or heavy quark the leading order contribution is given by the right digram in figure 3.22 which contains the effective gluon propagator $D^*_{\mu\nu}$ but bare vertices and quark propagator. The effective self energy is then given by [144]

$$\Sigma^*(P) = iC_\mathrm{F}g^2 \int \frac{\mathrm{d}^4Q}{(2\pi)^4}\, D^*_{\mu\nu}(Q)\gamma^\mu S(P')\gamma^\nu\,, \tag{3.64}$$

where Q is the gluon momentum and P' the internal quark momentum. In the general case one would have to include the effective vertices and quark propagator as well. Inserting equation (3.56) finally leads to

$$\begin{aligned} -\frac{\mathrm{d}E}{\mathrm{d}x}\bigg|_\mathrm{soft} &= \frac{g^4T^2}{6\pi}\left(1+\frac{n_\mathrm{f}}{6}\right)\left\{\left[\frac{1}{v}-\frac{1-v^2}{2v^2}\ln\left(\frac{1+v}{1-v}\right)\right]\ln\left(\frac{q^*}{m_\mathrm{g}}\right)\right.\\ &\quad -\frac{1}{v^2}\int\limits_0^v \mathrm{d}x\, x^2\left[\ln\left(\frac{3\pi x}{4}\right)+\frac{1}{2}\ln\left(1+Q_\mathrm{l}^2(x)\right)+Q_\mathrm{l}(x)\left(\frac{\pi}{2}-\arctan\left(Q_\mathrm{l}(x)\right)\right)\right]\\ &\quad -\frac{1}{2v^2}\int\limits_0^v \mathrm{d}x\, x^2\frac{v^2-x^2}{1-x^2}\left[\ln\left(\frac{3\pi x}{4}\right)+\frac{1}{2}\ln\left(1+Q_\mathrm{t}^2(x)\right)\right.\\ &\quad \left.\left. +Q_\mathrm{t}(x)\left(\frac{\pi}{2}-\arctan\left(Q_\mathrm{t}(x)\right)\right)\right]\right\} \end{aligned} \tag{3.65}$$

with

$$Q_\mathrm{l}(x) = \frac{1}{\pi}\left[-\ln\left(\frac{1+x}{1-x}\right)+\frac{2}{x}\right] \quad \text{and} \quad Q_\mathrm{t}(x) = \frac{1}{\pi}\left[\ln\left(\frac{1+x}{1-x}\right)+\frac{2x}{1-x^2}\right] \tag{3.66}$$

The integration over x can only be done numerically.

For the computation of the hard contribution from scattering matrix elements approximations have to be made. In [144] the cases $E \ll M^2/T$ and $E \gg M^2/T$ for a heavy quark are treated. In the former case the total energy loss (soft and hard) is of the form

$$-\frac{\mathrm{d}E}{\mathrm{d}x} = \frac{8\pi\alpha_\mathrm{s}^2T^2}{3}\left(1+\frac{n_\mathrm{f}}{6}\right)\left[\frac{1}{v}-\frac{1-v^2}{2v^2}\ln\left(\frac{1+v}{1-v}\right)\right]\ln\left(2^{n_\mathrm{f}/(6+n_\mathrm{f})}B(v)\frac{ET}{m_\mathrm{g}M}\right), \tag{3.67}$$

where B is a smooth function of the heavy quark's velocity. In the high energy limit the energy loss becomes

$$-\frac{\mathrm{d}E}{\mathrm{d}x} = \frac{8\pi\alpha_\mathrm{s}^2T^2}{3}\left(1+\frac{n_\mathrm{f}}{6}\right)\ln\left(2^{n_\mathrm{f}/2(6+n_\mathrm{f})}0.920\frac{\sqrt{ET}}{m_\mathrm{g}}\right). \tag{3.68}$$

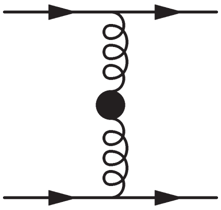

Figure 3.23.: Quark-quark scattering with effective gluon propagator in the t-channel.

Then both expressions are extrapolated into the intermediate energy region and at the point where both become equal one has to switch from one to the other.

For a fast light quark the soft contribution is again given by equation (3.65) with $v = 1$. For the hard contribution a second separation scale $\tilde{q}$ is introduced in [137] to separate the hard form the ultra-hard collisions. In the latter u- and s-channel exchanges become singular, which corresponds to a transfer of essentially all the projectile energy to the scattering centre. This regime is therefore excluded from the energy loss calculations, but then the energy loss depends logarithmically on $\tilde{q}$. The medium hard regime for light quarks corresponds to the high energy limit for heavy quarks.

$$-\frac{\mathrm{d}E}{\mathrm{d}x} = \frac{8\pi\alpha_{\mathrm{s}}^2 T^2}{3}\left(1+\frac{n_{\mathrm{f}}}{6}\right)\ln\left(2^{n_{\mathrm{f}}/2(6+n_{\mathrm{f}})}0.920\frac{\sqrt{\tilde{q}T}}{m_{\mathrm{g}}}\right) \tag{3.69}$$

The calculation of the hard momentum transfer part has been improved in [7, 138] beyond logarithmic accuracy.

An alternative approach is the computation of the energy loss from equation (3.62) using effective propagators for the exchanged particles in the matrix elements as shown in figure 3.23 for quark-quark scattering in the t-channel. This prescription was shown to yield the same result as the ansatz using the self energy for the energy loss of a muon in a QED plasma [144] and in [4] a complete calculation of the soft and hard contribution to the energy loss of an energetic quark in a finite size QGP was given. In this case the result was obtained numerically.

Most of the calculations of collisional energy loss lead to a mean energy loss of the order $-\mathrm{d}E/\mathrm{d}x \simeq 0.2\,\mathrm{GeV/fm}$ for a 10 GeV quark at temperatures in the range $T = 200 - 250\,\mathrm{MeV}$ [2–6, 137]. In [7] the authors report a somewhat higher value ($-\mathrm{d}E/\mathrm{d}x \simeq 0.6\,\mathrm{GeV/fm}$) and an even larger energy loss is found in [138], but in this calculation also energy transfers of the order of the projectile energy are counted as energy loss.

3.3.2. Radiative Energy Loss

The scattering of a projectile parton in a medium induces gluon radiation[4]. For the phenomenology of bremsstrahlung induced by multiple scattering in QCD the analogue of the Landau-Pomeranchuk-Migdal (LPM) effect in QED [147, 148] was found

---

[4] For a review see [145, 146].

to be of great importance. The decoherence due to rescattering of the projectile-gluon state on the scale of the gluon formation time suppresses gluon radiation and leads to an effective $1/\sqrt{\omega}$ gluon spectrum instead of the $1/\omega$ bremsstrahlung spectrum induced by a single scattering (ω is the gluon energy). This can be illustrated by a heuristic discussion of the propagation of an energetic projectile through a medium of length L in the multiple soft scattering limit [146]. It is assumed that the mean free path is much larger than the range of the static screened scattering potentials. The radiated gluon decoheres from the projectile when it has accumulated a relative phase larger than unity. The phase difference built up by multiple scattering is given by

$$\varphi = \left\langle \frac{k_\perp^2}{2\omega} \Delta z \right\rangle \simeq \frac{\hat{q} L^2}{2\omega} = \frac{\omega_\mathrm{c}}{\omega}\,, \tag{3.70}$$

where the transport coefficient $\hat{q}$ is the average transverse momentum squared that the medium transfers to the gluon per mean free path

$$\hat{q} \simeq \rho \int \mathrm{d}^2 q_\perp\, q_\perp^2 \frac{\mathrm{d}\sigma}{\mathrm{d}^2 q_\perp} \tag{3.71}$$

and ω_c is the characteristic gluon energy

$$\omega_\mathrm{c} = \frac{1}{2} \hat{q} L^2\,. \tag{3.72}$$

The requirement $\varphi > 1$ implies that only gluons with energies below the characteristic energy can be radiated. The coherence time of the gluon is given by

$$t_\mathrm{coh} \simeq \frac{2\omega}{k_\perp^2} \simeq \frac{2\omega}{\hat{q} t_\mathrm{coh}} \quad \Rightarrow \quad t_\mathrm{coh} \simeq \sqrt{\frac{2\omega}{\hat{q}}} \tag{3.73}$$

and determines the number $N_\mathrm{coh} = t_\mathrm{coh}/\lambda$ of scattering centres acting coherently to build up the gluon phase. The gluon energy spectrum per unit path length can be estimated as

$$\omega \frac{\mathrm{d}^2 I}{\mathrm{d}\omega \mathrm{d}z} \simeq \frac{1}{N_\mathrm{coh}} \omega \frac{\mathrm{d}^2 I^{(1)}}{\mathrm{d}\omega \mathrm{d}z} \propto \alpha_\mathrm{s} \sqrt{\frac{\hat{q}}{\omega}}\,, \tag{3.74}$$

which has the $1/\sqrt{\omega}$ dependence characteristic for LPM suppression. The gluon spectrum induced by a single scattering is $\mathrm{d}^2 I^{(1)}/\mathrm{d}\omega \mathrm{d}z \propto \alpha_\mathrm{s}/\omega$. The radiative energy loss is obtained by integrating the gluon spectrum

$$\Delta E = \int_0^L \mathrm{d}z \int_0^{\omega_\mathrm{c}} \mathrm{d}\omega\, \omega \frac{\mathrm{d}^2 I}{\mathrm{d}\omega \mathrm{d}z} \propto \alpha_\mathrm{s} \hat{q} L^2 \tag{3.75}$$

and has the characteristic quadratic dependence on the path length inside the medium.

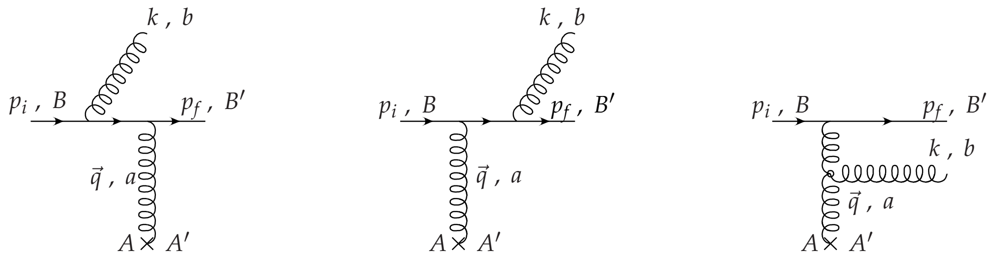

Figure 3.24.: Radiation amplitude induced by a single scattering; A, A', B, B', a and b denote the colour indices, figure from [149].

BDMPS model

The BDMPS model [11,149] for radiative energy loss also works in the multiple soft scattering limit. It uses the Gyulassy-Wang (GW) model [10] for the medium, which regards the medium as a collection of static scattering centres at locations $\vec{x}_i$ with a screened Coulomb potential

$$V_i(\vec{x}) = \frac{g}{4\pi}\frac{e^{-\mu_\mathrm{D}|\vec{x}-\vec{x}_i|}}{|\vec{x}-\vec{x}_i|} \qquad \tilde{V}_i(\vec{q}) = \frac{g}{q^2+\mu_\mathrm{D}^2}e^{-i\vec{q}\cdot\vec{x}}\,, \tag{3.76}$$

where μ_D is the Debye screening mass, $\vec{q}$ is the momentum transfer and $\tilde{V}(\vec{q})$ is the Fourier transform of the scattering potential. It is assumed that the range μ_D^{-1} of the potential is much smaller than the distance λ between the scattering centres, so that successive scatterings are independent and radiation associated with scattering off two or more scattering centres can be neglected. In this scenario the collisional energy loss vanishes, because a static scattering centre does not recoil against the projectile.

The BDMPS model works in the high energy limit, in which the projectile (in this case a quark) energy E is much larger than the energy ω of the radiated gluons. In this limit the longitudinal momentum transfer in the scattering vanishes. The gluon spectrum induced by a single scattering (figure 3.24) is given by

$$\omega\frac{\mathrm{d}^3I^{(1)}}{\mathrm{d}\omega\mathrm{d}^2\vec{k}_\perp} = \frac{\alpha_\mathrm{s}}{\pi^2}\frac{\langle|\vec{J}_\mathrm{eff}(\vec{k}_\perp,\vec{q}_\perp)|^2\rangle}{C_\mathrm{F}N_\mathrm{c}} \tag{3.77}$$

with the emission current

$$\vec{J}(\vec{k}_\perp,\vec{q}_\perp) = \frac{\vec{k}_\perp}{k_\perp^2} - \frac{\vec{k}_\perp-\vec{q}_\perp}{(\vec{k}_\perp-\vec{q}_\perp)^2} \quad \text{and} \quad \vec{J}_\mathrm{eff}(\vec{k}_\perp,\vec{q}_\perp) = \vec{J}(\vec{k}_\perp,\vec{q}_\perp)[T^a,T^b]_{BB'}\,. \tag{3.78}$$

The T^a are the generators of the fundamental representation of $SU(N_\mathrm{c})$, the colour labels are indicated in figure 3.24. The emission current has to be averaged over momentum transfers

$$\langle|\vec{J}_\mathrm{eff}(\vec{k}_\perp,\vec{q}_\perp)|^2\rangle \equiv \int \mathrm{d}^2\vec{q}_\perp\,\frac{\mu_\mathrm{D}^2}{\pi(q_\perp^2+\mu_\mathrm{D}^2)^2}|\vec{J}_\mathrm{eff}(\vec{k}_\perp,\vec{q}_\perp)|^2\,. \tag{3.79}$$

The radiation amplitude for multiple scattering can be calculated in time-ordered perturbation theory and reads

$$\mathcal{M}_{\mathrm{rad}} \propto \sum_{i=1}^{N} \sum_{r=1}^{2^{N-i}} \vec{J}_{\mathrm{eff}}(\vec{k}_{i_r}, \vec{q}_i) e^{i\varphi_{i_r}} . \tag{3.80}$$

The first sum runs over the scattering centres and the second over the 2^{N-i} possibilities (labelled by i_r) for the quark-gluon system, where the gluon radiation was induced by scattering centre i, to rescatter. Finally, the radiation spectrum induced by N scatterings can be written as

$$\omega \frac{\mathrm{d}I^{(N)}}{\mathrm{d}\omega} = \frac{\alpha_{\mathrm{s}}}{2\pi} \int \mathrm{d}^2\vec{k}_{\perp} \left\langle \sum_{i=1}^{N} \sum_{j=1}^{N} \frac{\vec{J}^{i}_{\mathrm{eff}} \cdot J^{j\dagger}_{\mathrm{eff}}}{N_{\mathrm{c}} C_{\mathrm{F}}^{N}} e^{i(\varphi_i - \varphi_j)} \right\rangle . \tag{3.81}$$

For a qualitative understanding of the induced radiation spectrum it is instructive to approximate the spectrum ignoring logarithmic factors and numerical factors of order unity, which leads to

$$\omega \frac{\mathrm{d}^2 I}{\mathrm{d}\omega \mathrm{d}z} \simeq \begin{cases} \frac{\alpha_{\mathrm{s}}}{\lambda} & \omega < \omega_{\mathrm{BH}} \\ \frac{\alpha_{\mathrm{s}}}{\lambda} \sqrt{\frac{\lambda \mu_{\mathrm{D}}^2}{\omega}} & \omega_{\mathrm{BH}} < \omega < \omega_{\mathrm{fact}} \\ \frac{\alpha_{\mathrm{s}}}{L} & \omega_{\mathrm{fact}} < \omega \end{cases} . \tag{3.82}$$

In the soft regime $\omega < \omega_{\mathrm{BH}} \simeq \lambda \mu_{\mathrm{D}}^2$ the radiation is due to incoherent scattering from the individual scattering centres (Bethe-Heitler regime). In the intermediate regime the scattering becomes coherent and the LPM effect becomes important. Finally, at the highest gluon energies, the whole medium acts coherently as one effective scattering centre giving rise to the so-called factorisation contribution, which is medium-independent. To logarithmic accuracy the total energy loss becomes

$$-\Delta E = \frac{\alpha_{\mathrm{s}} C_{\mathrm{R}}}{8} \frac{\mu_{\mathrm{D}}^2}{\lambda_{\mathrm{g}}^2} L^2 \ln\left(\frac{L}{\lambda_{\mathrm{g}}}\right) , \tag{3.83}$$

where C_{R} is the squared (projectile) colour charge and λ_{g} is the gluon mean free path.

GLV model

In the GLV approach [14, 150, 151] the gluon spectrum is constructed by recursive summation of the radiative gluon distribution. Diagrams are classified according to their order in opacity $\chi = \langle n \rangle = L/\lambda$, which gives the number of interactions in the medium. The zeroth order in opacity is the vacuum contribution, the first corresponds to one interaction with the medium and so on. The GLV model is also built on the GW model for the medium. The inclusive gluon distribution P_n in the case of n interactions is written is terms of the amplitude $\mathcal{A}_{i_1 \ldots i_n}$ describing the propagation of the projectile-gluon system that experienced n scatterings

$$P_n(x, \vec{k}) = \bar{\mathcal{A}}^{i_1 \ldots i_n}(x, \vec{k}, c) \mathcal{A}_{i_1 \ldots i_n}(x, \vec{k}, c) , \tag{3.84}$$

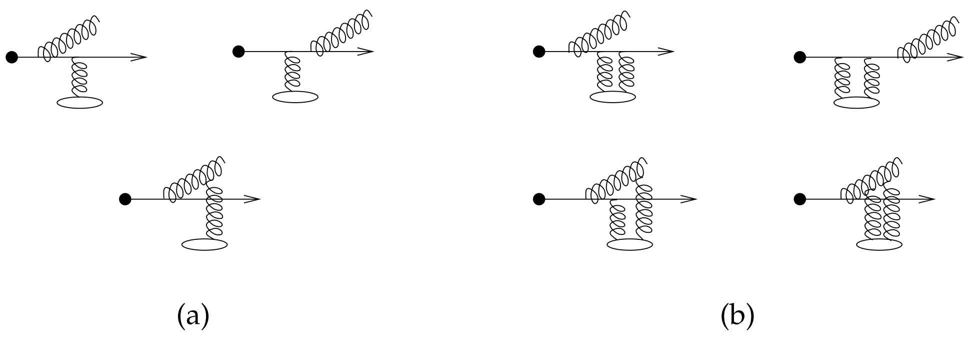
(a) (b)

Figure 3.25.: Amplitudes defining the direct (a) and virtual (b) part of the reaction operator.

where x is the energy fraction carried by the gluon, $\vec{k}$ its transverse momentum and c is the colour matrix. The gluon distribution P_n can be constructed recursively from lower opacity classes

$$P_n = \bar{\mathcal{A}}^{i_1 \dots i_{n-1}} \hat{R}_n \mathcal{A}_{i_1 \dots i_{n-1}} \quad \text{with} \quad \hat{R}_n = \hat{D}_n^\dagger \hat{D}_n + \hat{V}_n + \hat{V}_n^\dagger \,, \tag{3.85}$$

where $\hat{R}_n$ is the GLV reaction operator generating a scattering from scattering centre n. The 'direct' and 'virtual' amplitudes defining $\hat{D}_n$ and $\hat{V}_n$, respectively, are given in figure 3.25. The recursion relation can be solved leading to

$$\begin{aligned} P_n(\vec{k}) = -2C_\mathrm{R}C_\mathrm{A}^n \mathrm{Re} \sum_{i=1}^{n} & \left\{ \prod_{j=i+1}^{n} \left(e^{i(\vec{q}_j \cdot \hat{\vec{b}})} - 1 \right) \right\} \otimes \vec{B}_i e^{i\vec{q}_i \cdot \hat{\vec{b}}} e^{-i\omega_0 z_i} \\ & \times \left\{ \prod_{m=1}^{i-1} \left(e^{i(\omega_0 - \omega_m) z_m} e^{i(\vec{q}_m \cdot \hat{\vec{b}})} - 1 \right) \right\} \otimes \vec{H} \left(e^{i\omega_0 z_1} - e^{i\omega_0 z_0} \right) \,, \end{aligned} \tag{3.86}$$

where $\hat{\vec{b}} = i\nabla_{\vec{k}}$ is the transverse momentum shift operator, z_i are the positions of the scattering centres, ω_i the gluon energy after the scattering i, $\vec{H} = \vec{k}/k^2$ and $\vec{B}_i$ is the Gunion-Bertsch amplitude for the radiation of a gluon in scattering i

$$\vec{B}_i = \frac{\vec{k}}{k^2} - \frac{\vec{k} - \vec{q}_i}{(\vec{k} - \vec{q}_i)^2} \,. \tag{3.87}$$

Finally, the induced gluon number distribution valid to all orders in opacity can be constructed, which is a very general but complicated expression. It turns out that the first order in opacity gives the dominant contribution. The first order radiation intensity is given by

$$\frac{\mathrm{d}I^{(1)}}{\mathrm{d}x} = \frac{C_\mathrm{R}\alpha_\mathrm{s}}{\pi} \left(1 - x + \frac{x^2}{2} \right) E \frac{L}{\lambda_\mathrm{g}} \frac{\gamma(\pi + 2\gamma \ln \gamma)}{1 + \gamma^2} \qquad \gamma = \frac{L\mu_\mathrm{D}^2}{4xE} \,, \tag{3.88}$$

which in the limit $\gamma \ll 1$ becomes

$$\frac{\mathrm{d}I^{(1)}}{\mathrm{d}x} \approx \frac{C_\mathrm{R}\alpha_\mathrm{s}}{4x} \left(1 - x + \frac{x^2}{2} \right) \frac{L^2 \mu_\mathrm{D}^2}{\lambda_\mathrm{g}} \,. \tag{3.89}$$

The resulting average energy loss is

$$-\Delta E^{(1)} = \frac{C_{\mathrm{R}}\alpha_{\mathrm{s}}}{4}\frac{L^2\mu_{\mathrm{D}}^2}{\lambda_{\mathrm{g}}}\ln\left(\frac{E}{\mu_{\mathrm{D}}}\right). \tag{3.90}$$

ASW model

An alternative approach is the path integral formulation [13, 152–155], which contains the multiple soft and single hard scattering picture (or first order in opacity) as limiting cases. The projectile can be viewed as a superposition of Fock states. The quark wave function, for instance, is the bare quark state accompanied by a Weizsäcker-Williams field $f(\vec{x})$ of coherent gluons

$$\psi_{\mathrm{in}}^{\alpha} = |\alpha\rangle + \int \mathrm{d}\vec{x}\, f(\vec{x}) T^b_{\alpha\beta}|\beta; b(\vec{x})\rangle \qquad f(\vec{x}) \propto g\frac{\vec{x}}{x^2}\,. \tag{3.91}$$

In the eikonal approximation the transverse positions $\vec{x}$ of the projectile components do not change during the propagation through the medium. The interactions with the medium only lead to an eikonal phase acquired by the projectile, which is different for the quark and gluon component and thus decoheres the incoming state. The outgoing wave function becomes

$$\psi_{\mathrm{out}}^{\alpha} = W^{\mathrm{F}}_{\alpha\gamma}(\vec{0})|\gamma\rangle + \int \mathrm{d}\vec{x}\, f(\vec{x}) T^b_{\alpha\beta} W^{\mathrm{F}}_{\beta\gamma}(\vec{0}) W^{\mathrm{A}}_{b\gamma}(\vec{x})|\gamma; c(\vec{x})\rangle\,, \tag{3.92}$$

where W^{F} and W^{A} are the Wilson lines along the projectile trajectories in the fundamental and adjoint representation, respectively,

$$W(\vec{x}) = \mathcal{P}\exp\left(i\int \mathrm{d}z^-\, T^a A^+_a(\vec{x}, z^-)\right) \tag{3.93}$$

with the generator T^a in the corresponding representation. The projectile is chosen to propagate in negative z direction and A^+ is the target gauge field. As a consequence of the decoherence of the projectile wave function the outgoing wave function contains real radiated gluons. This component can be isolated by projecting out the component of the outgoing wave function that is orthogonal to the incoming one

$$|\delta\psi^{\alpha}\rangle = |\psi^{\alpha}_{\mathrm{out}}\rangle - \sum_{\gamma}|\psi_{\mathrm{in}}(\gamma)\rangle\langle\psi_{\mathrm{in}}(\gamma)|\psi_{\mathrm{out}}\rangle\,, \tag{3.94}$$

where γ runs over the quark colour index. The number spectrum of radiated gluons is given by the expectation value of the number operator in the state $|\delta\psi^{\alpha}\rangle$

$$N_{\mathrm{g}}(\vec{k}) = \frac{1}{N}\sum_{\alpha}\langle\delta\psi^{\alpha}|a^{\dagger}(\vec{k})a(\vec{k})|\delta\psi^{\alpha}\rangle\,. \tag{3.95}$$

This expression contains averages of products of Wilson lines over the target gluon fields which require a specific model of the medium. A collection of static scattering centres with scattering potentials $a^+(\vec{q})$, for instance, is characterised by the dipole cross section

$$\sigma(\vec{x}-\vec{y}) = 2\int \frac{\mathrm{d}^2\vec{q}}{(2\pi)^2} |a^+(\vec{q})|^2 \left(1 - e^{i\vec{q}\cdot(\vec{x}-\vec{y})}\right) . \tag{3.96}$$

The gluon number spectrum can be investigated in the two limiting cases (multiple soft and single hard scattering), in which it takes a simple form. In both cases it is proportional to the integral over the Gunion-Bertsch cross section for gluon radiation in quark scattering. But while in the single hard scattering scenario the momentum transfer comes from a single scattering potential it is in the multiple soft scattering limit the entire medium that acts coherently as one effective scattering potential with Gaussian momentum transfer. This is so because in the eikonal approximation the momentum transfer from the medium to the projectile is small.

For the more general case where only parts of the medium act coherently and also incoherent scatterings occur one has to go beyond the eikonal approximation and allow for a transverse motion of the projectile. The Wilson line is then not along a straight path any more and the motion of the projectile is described by a Green's function taking the scattering into account. Finally, the induced gluon radiation spectrum is found to be

$$\begin{aligned}\omega\frac{\mathrm{d}I}{\mathrm{d}\omega} = \frac{\alpha_\mathrm{s} C_\mathrm{R}}{(2\pi)^2\omega^2} 2\mathrm{Re} \int_{\xi_0}^{\infty} \mathrm{d}y_1 \int_{y_1}^{\infty} \mathrm{d}\bar{y}_1 \int \mathrm{d}\vec{u} \int_0^{\chi\omega} \mathrm{d}\vec{k}_\perp e^{-i\vec{k}_\perp\cdot\vec{u}}\, e^{-\frac{1}{2}\int_{\bar{y}_1}^{\infty} \mathrm{d}\xi\, n(\xi)\sigma(\vec{u})} \\ \frac{\partial}{\partial\vec{y}}\frac{\partial}{\partial\vec{u}} \int_{\vec{y}=0}^{\vec{u}=\vec{r}(\bar{y}_1)} \mathcal{D}\vec{r}\, \exp\left(i\int_{y_1}^{\bar{y}_1} \mathrm{d}\xi\, \frac{\omega}{2}\left[\dot{\vec{r}}^2 - \frac{n(\xi)\sigma(\vec{r})}{i\omega}\right]\right) .\end{aligned} \tag{3.97}$$

Here, $\vec{k}_\perp$ is the transverse momentum of the radiated gluon, which can be restricted by the integration limit $\chi\omega$ so that the transverse momentum cannot be larger than the energy and finite cone sizes can be implemented. The transverse coordinates are $\vec{u}$, $\vec{y}$ and $\vec{r}$ and y_1 and $\bar{y}_1$ are the longitudinal gluon emission points. The medium properties enter through the longitudinal density n and the dipole cross section.

In the multiple soft scattering limit the dipole cross section can be approximated by the first term in the Taylor expansion leading to

$$n(\xi)\sigma(\vec{r}) \simeq \frac{1}{2}\hat{q}(\xi)r^2 , \tag{3.98}$$

where the medium is characterised by the transport coefficient. In the limit of a large medium in the sense that $L \gg \lambda$ the BDMPS result is recovered

$$\omega\frac{\mathrm{d}I}{\mathrm{d}\omega} = \frac{2\alpha_\mathrm{s} C_\mathrm{R}}{\pi} \ln\left(\cosh^2\sqrt{\frac{\omega_\mathrm{c}}{2\omega}} - \sin^2\sqrt{\frac{\omega_\mathrm{c}}{2\omega}}\right) \simeq \frac{2\alpha_\mathrm{s} C_\mathrm{R}}{\pi} \begin{cases} \sqrt{\frac{\omega_\mathrm{c}}{2\omega}} & \omega < \omega_\mathrm{c} \\ \frac{1}{12}\left(\frac{\omega_\mathrm{c}}{\omega}\right)^2 & \omega > \omega_\mathrm{c} \end{cases} . \tag{3.99}$$

It shows the characteristic $1/\sqrt{\omega}$ dependence and the suppression of radiation with energies larger than the characteristic energy.

The opacity expansion is obtained by expanding the path integral in equation (3.97) in powers of the dipole cross section. In the limit of large L the gluon spectrum in first order in opacity

$$\omega\frac{\mathrm{d}I^{(1)}}{\mathrm{d}\omega} = \frac{2\alpha_{\mathrm{s}}C_{\mathrm{R}}}{\pi}\frac{L}{\lambda}\gamma\int\limits_0^\infty \mathrm{d}r\,\frac{1}{r+\gamma}\,\frac{r-\sin r}{r^2} \simeq \frac{2\alpha_{\mathrm{s}}C_{\mathrm{R}}}{\pi}\frac{L}{\lambda}\left\{\begin{array}{ll}\ln\left(\frac{\bar{\omega}_{\mathrm{c}}}{\omega}\right) & \omega<\bar{\omega}_{\mathrm{c}}\\ \frac{\pi}{4}\frac{\bar{\omega}_{\mathrm{c}}}{\omega} & \omega>\bar{\omega}_{\mathrm{c}}\end{array}\right. \tag{3.100}$$

with

$$\bar{\omega}_{\mathrm{c}} = \frac{1}{2}\mu_{\mathrm{D}}^2 L \quad \text{and} \quad \gamma = \frac{\bar{\omega}_{\mathrm{c}}}{\omega} \tag{3.101}$$

coincides with the findings in the GLV model. For large gluon energies the $1/\omega$ dependence is recovered, while there is a suppression of small energies. The gluon spectrum is qualitatively similar in both limiting cases.

From Induced Radiation to Hadron Suppression

The relevant quantity for the energy loss is the quenching weight [27], which is the probability $P(\Delta E)$ that a certain amount of energy ΔE is carried by radiated gluons. Assuming subsequent emissions to be independent of each other the quenching weight is the normalised sum of the probabilities for radiating an arbitrary number n of gluons with total energy ΔE

$$P(\Delta E) = \sum_{n=0}^{\infty}\frac{1}{n!}\left[\prod_{i=1}^{n}\int \mathrm{d}\omega_i\,\frac{\mathrm{d}I(\omega_i)}{\mathrm{d}\omega}\right]\delta\left(\Delta E - \sum_{i=1}^{n}\omega_i\right)\exp\left(-\int \mathrm{d}\omega\,\frac{\mathrm{d}I}{\mathrm{d}\omega}\right)\,. \tag{3.102}$$

It has a discrete part, which arises from the fact that for finite path lengths there is a finite probability for no medium induced radiation, and a continuous part, which contains the extra radiation.

In order to make contact with experimental data one has to calculate the effect of energy loss on hadronic $p_\perp$ spectra. This can, for instance, be done by calculating the effect of energy loss on the fragmentation functions. This leads to medium modified fragmentation functions of the form [156, 157]

$$D_k^{h\,(\mathrm{med})}(x,Q^2) = \int\limits_0^1 \mathrm{d}\epsilon\,P(\epsilon)\frac{1}{1-\epsilon}D_k^h\left(\frac{x}{1-\epsilon},Q^2\right)\,, \tag{3.103}$$

where $P(\epsilon)$ is the probability for losing a fraction $\epsilon = \Delta E/E_k$ of the incoming energy. In this ansatz the contribution from the fragmentation of radiated gluons is neglected because it is assumed to be soft.

Higher twist model

Additional gluon radiation can also arise from higher twist matrix elements. They are suppressed by powers of the hard scale but there is a class of diagrams that are enhanced in an extended medium. For jet production the leading twist (in this case twist-two) process is the well-known tree level process, the next terms in the twist

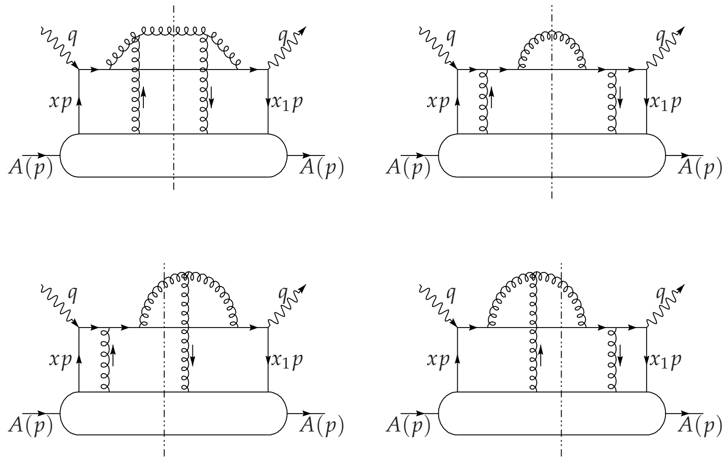

Figure 3.26.: Double scattering diagrams contributing to the final result. Figure from [151].

expansion are twist-four processes. In the case of pure final state interactions there are two important contributions: The fast parton is on-shell after the hard interaction and exchanges a soft gluon with the target or it exchanges a hard gluon and radiates a gluon to get back on the mass-shell. These processes are obviously enhanced by the path length in the target [145].

The higher twist approach [15, 151, 158, 159] can be applied to energy loss in cold nuclei as well as in a QGP. The former is best studied in the semi-inclusive hadron production process $e(L_1) + A(p) \rightarrow e(L_2) + h(l_h) + X$ in deeply inelastic scattering of electrons off nuclei. The factorisation theorem allows one to write the cross section for this process in the form

$$E_{L_2} E_{l_h} \frac{\mathrm{d}^6\sigma^h}{\mathrm{d}^3 L_2\,\mathrm{d}^3 l_h} = \frac{\alpha^2}{2\pi s}\frac{1}{Q^4} L_{\mu\nu} E_{l_h} \frac{\mathrm{d}W^{\mu\nu}}{\mathrm{d}^2 l_h}\,, \tag{3.104}$$

where $L_{\mu\nu} = 1/2\mathrm{tr}(\gamma \cdot L_1 \gamma_\mu \gamma \cdot L_2 \gamma_\nu)$ is the leptonic tensor and the semi-inclusive hadronic tensor can to lowest order for a single $\gamma^* + q$ scattering be written as

$$\frac{\mathrm{d}W^{\mathrm{S}}_{\mu\nu}}{\mathrm{d}z_h} = \sum_q e_q^2 \int \mathrm{d}x\, f_{\mathrm{q}}^A(x, Q^2) H^{(0)}_{\mu\nu}(x, p, q) D_{\mathrm{q}}^h(z_h, Q^2)\,. \tag{3.105}$$

Here, $H^{(0)}_{\mu\nu}(x, p, q)$ is the leading order matrix element, p is the nucleon momentum, $q = L_2 - L_1$ is the momentum transfer. and f_{q}^A the quark distribution in the nucleus.

The twist-four contribution accounting for double scattering including the four surviving diagrams shown in figure 3.26 is given by

$$\frac{\mathrm{d}W^{\mathrm{D,q}}_{\mu\nu}}{\mathrm{d}z_h} = \sum_q \int \mathrm{d}x\, H^{(0)}_{\mu\nu}(x, p, q) \int_{z_h}^{1} \frac{\mathrm{d}z}{z} D_{\mathrm{q}}^h\left(\frac{z_h}{z}\right) \frac{\alpha_{\mathrm{s}}}{2\pi} \frac{1+z^2}{1-z} \int \frac{\mathrm{d}l_\perp^2}{l_\perp^4} \frac{2\pi\alpha_{\mathrm{s}}}{N_{\mathrm{c}}} T^A_{\mathrm{qg}}(x, x_{\mathrm{L}}) \tag{3.106}$$

It contains hard-soft and hard-hard processes and the interference between both, which gives rise to the LPM suppression. The twist-four matrix element can be approximated by

$$T^A_{\mathrm{qg}}(x,x_\mathrm{L}) = \frac{C}{x_A}\left(1-\exp\left(-\frac{x_\mathrm{L}^2}{x_\mathrm{A}^2}\right)\right)\times \\ \times\left[f^A_\mathrm{q}(x+x_\mathrm{L})x_\mathrm{T}f^\mathrm{N}_\mathrm{g}(x_\mathrm{T})+f^A_\mathrm{q}(x)(x_\mathrm{L}+x_\mathrm{T})f^\mathrm{N}_\mathrm{g}(x_\mathrm{L}+x_\mathrm{T})\right] \quad (3.107)$$

with

$$x_\mathrm{L} = \frac{l_\perp^2}{2p^+q^-z(1-z)} \quad \text{and} \quad x_\mathrm{A} = \frac{1}{M_\mathrm{N}R_A}\,, \quad (3.108)$$

where M_N is the nucleon mass and R_A the nuclear radius. Equation (3.106) can also be written in terms of modified fragmentation functions

$$\frac{\mathrm{d}W^{\mathrm{D,q}}_{\mu\nu}}{\mathrm{d}z_h} = \sum_q\int \mathrm{d}x\, f^A_\mathrm{q}(x,Q^2)H^{(0)}_{\mu\nu}(x,p,q)D^{h(\mathrm{med})}_\mathrm{q}(z_h,Q^2)\,. \quad (3.109)$$

In principle, also the parton density should be replaced by a twist-four parton density including the effect of double scattering in the initial state. The modified fragmentation function satisfies a DGLAP-like evolution equation with modified splitting functions.

$$P^{(\mathrm{med})}_{\mathrm{qq}}(z,x,x_\mathrm{L},l_\perp^2) = P_{\mathrm{qq}}(z)+\Delta P_{\mathrm{qq}}(z,x,x_\mathrm{L},l_\perp^2) \\ \Delta P_{\mathrm{qq}}(z,x,x_\mathrm{L},l_\perp^2) = \frac{2\pi\alpha_\mathrm{s}C_\mathrm{A}}{l_\perp^2N_\mathrm{c}f^A_\mathrm{q}(x,Q^2)}\left(\frac{1+z^2}{(1-z)_+}T^A_{\mathrm{qg}}(x,x_\mathrm{L})+\delta(1-z)\Delta T^A_{\mathrm{qg}}(x,Q^2)\right) \quad (3.110)$$

The solution can be written as

$$D^{h\,(\mathrm{med})}_\mathrm{q}(z_h,Q^2) = D^h_\mathrm{q}(z_h,Q^2)+\int_0^{Q^2}\frac{\mathrm{d}l_\perp^2}{l_\perp^2}\frac{\alpha_\mathrm{s}}{2\pi}\int_{z_h}^1\frac{\mathrm{d}z}{z}\left[\Delta P_{\mathrm{qq}}D^h_\mathrm{q}(z_h/z,Q^2) \right. \\ \left. +\,\Delta P_{\mathrm{gq}}D^h_\mathrm{g}(z_h/z,Q^2)\right] \quad (3.111)$$

The gluon fragmentation function can be derived analogously.

In a QGP undergoing longitudinal Bjorken expansion the twist-four matrix element is estimated as

$$\frac{\alpha_\mathrm{s}T^A_{\mathrm{qg}}(x,x_\mathrm{T})}{f^A_\mathrm{q}(x)} \sim \mu_\mathrm{D}^2\int \mathrm{d}y\,\sigma_\mathrm{g}\rho(y)\left[1-\cos\left(\frac{y}{\tau_\mathrm{f}}\right)\right] \quad \text{with} \quad \frac{\rho(y)}{\rho_0} = \frac{\tau_0}{\tau}\theta(R_A-y)\,, \quad (3.112)$$

where $\tau_\mathrm{f} = 2Ez(1-z)/l_\perp^2$ is the gluon formation time. The energy loss is given by the energy carried by the radiated gluon and coincides with the result obtained in the opacity expansion.

$$
\begin{aligned}
\langle \Delta z_{\mathrm{g}} \rangle (x, Q^2) =& \frac{C_{\mathrm{A}} \alpha_{\mathrm{s}}^2}{N_{\mathrm{c}}} \int_0^{Q^2} \frac{\mathrm{d}l_\perp^2}{l_\perp^4} \int_0^1 \mathrm{d}z \, \left[1 + (1-z)^2\right] \frac{T^A_{\mathrm{qg}}(x, x_{\mathrm{L}})}{f^A_{\mathrm{q}}(x, Q^2)} \\
=& \frac{C_{\mathrm{A}} \alpha_{\mathrm{s}}}{\pi} \int_0^1 \mathrm{d}z \int_0^{Q^2/\mu_{\mathrm{D}}^2} \mathrm{d}u \, \frac{1 + (1-z)^2}{u(1-u)} \\
& \times \int_{\tau_0}^{R_A} \mathrm{d}\tau \, \sigma_{\mathrm{g}} \rho(\tau) \left[1 - \cos\left(\frac{(\tau - \tau_0) u \mu_{\mathrm{D}}^2}{2Ez(1-z)}\right)\right]
\end{aligned}
\tag{3.113}
$$

Assuming $\sigma_{\mathrm{g}} = C_{\mathrm{R}} 2\pi \alpha_{\mathrm{s}}^2 / \mu_{\mathrm{D}}^2$ and keeping only the dominant contribution one obtains for the mean energy loss

$$
-\frac{\mathrm{d}E}{\mathrm{d}x} \approx \frac{\pi C_{\mathrm{R}} C_{\mathrm{A}} \alpha_{\mathrm{s}}^3}{R_A} \int_{\tau_0}^{R_A} \mathrm{d}\tau \, \rho(\tau)(\tau - \tau_0) \ln\left(\frac{2E}{\tau \mu_{\mathrm{D}}^2}\right) \tag{3.114}
$$

Due to the expansion, which suppresses the energy loss, the energy loss does in this case not depend quadratically on the path length. In cold nuclear matter, which is static, the energy loss in found to depend quadratically on the size of the nucleus.

AMY model

In the AMY formalism [160–163], which is a thermal field theory approach to radiative energy loss, the transition rates for the 1 → 2 processes are obtained from the imaginary part of the HTL-resummed self energy.

$$
\frac{\mathrm{d}^2\Gamma}{\mathrm{d}k \, \mathrm{d}t} = \frac{g^2}{16\pi p^7} \frac{1}{e^{-k/T} \pm 1} \frac{1}{e^{-(p-k)/T} \pm 1} g(x) \int \frac{\mathrm{d}^2 \vec{h}}{(2\pi)^2} 2\vec{h} \cdot \mathrm{Re} \, \vec{F}(\vec{h}, p, k) \tag{3.115}
$$

with

$$
g(x) = \begin{cases} \frac{4}{3} \frac{1+(1-x)^2}{x^3(1-x)^2} & q \to qg \\ n_{\mathrm{f}} \frac{4}{3} \frac{x^2+(1-x)^2}{x^2(1-x)^2} & g \to q\bar{q} \\ 3 \frac{1+x^4+(1-x)^4}{x^3(1-x)^3} & g \to gg \end{cases} \tag{3.116}
$$

and where p and k are the incoming projectile's and the radiated parton's momentum, respectively, and $x = k/p$. The transverse momentum of the radiated parton $\vec{h} \equiv \vec{p} \times \vec{k}$ is assumed to be small. $(e^{-k/T} \pm 1)^{-1}$ are the appropriate Bose enhancement or Pauli blocking factors for the final state particles. $\vec{F}(\vec{h}, p, k)$ is the solution of

$$
\begin{aligned}
2\vec{h} = i\delta E(\vec{h}, p, k) \vec{F}(\vec{h}) + g^2 \int \frac{\mathrm{d}^2 \vec{q}_\perp}{(2\pi)^2} C(\vec{q}_\perp) \Bigg\{ & \left(C_{\mathrm{s}} - \frac{C_{\mathrm{A}}}{2}\right) \left[\vec{F}(\vec{h}) - \vec{F}(\vec{h} - k\vec{q}_\perp)\right] \\
& + \frac{C_{\mathrm{A}}}{2} \left[\vec{F}(\vec{h}) - \vec{F}(\vec{h} + p\vec{q}_\perp)\right] + \frac{C_{\mathrm{A}}}{2} \left[\vec{F}(\vec{h}) - \vec{F}(\vec{h} - (p-k)\vec{q}_\perp)\right] \Bigg\} ,
\end{aligned}
\tag{3.117}
$$

which describes the evolution of the states $|p\rangle$ and $|p-k,k\rangle$ due to elastic scattering and their energy difference δE

$$\delta E = \frac{h^2}{2pk(p-k)} + \frac{m_k^2}{2k} + \frac{m_{p-k}^2}{2(p-k)} - \frac{m_p^2}{2p} \quad \text{and} \quad C(\vec{q}_\perp) = \frac{\mu_\mathrm{D}^2}{q_\perp^2(q_\perp^2+\mu_\mathrm{D}^2)} . \tag{3.118}$$

The transition rates enter the Fokker-Planck equation describing the evolution of the gluon and quark plus antiquark distributions as they propagate through the medium

$$\begin{aligned} \frac{\mathrm{d}P_{\mathrm{q\bar{q}}}(p)}{\mathrm{d}t} &= \int_{-\infty}^{\infty} \mathrm{d}k\, P_{\mathrm{q\bar{q}}}(p+k)\frac{\mathrm{d}^2\Gamma^{\mathrm{q}}_{\mathrm{qg}}(p+k,k)}{\mathrm{d}k\,\mathrm{d}t} - P_{\mathrm{q\bar{q}}}(p)\frac{\mathrm{d}^2\Gamma^{\mathrm{q}}_{\mathrm{qg}}(p,k)}{\mathrm{d}k\,\mathrm{d}t} \\ &\quad + 2P_\mathrm{g}(p+k)\frac{\mathrm{d}^2\Gamma^{\mathrm{g}}_{\mathrm{q\bar{q}}}(p+k,k)}{\mathrm{d}k\,\mathrm{d}t} \\ \frac{\mathrm{d}P_\mathrm{g}(p)}{\mathrm{d}t} &= \int_{-\infty}^{\infty} \mathrm{d}k\, P_{\mathrm{q\bar{q}}}(p+k)\frac{\mathrm{d}^2\Gamma^{\mathrm{q}}_{\mathrm{qg}}(p+k,k)}{\mathrm{d}k\,\mathrm{d}t} + P_\mathrm{g}(p+k)\frac{\mathrm{d}^2\Gamma^{\mathrm{g}}_{\mathrm{gg}}(p+k,k)}{\mathrm{d}k\,\mathrm{d}t} \\ &\quad - P_\mathrm{g}(p+k)\left(\frac{\mathrm{d}^2\Gamma^{\mathrm{g}}_{\mathrm{q\bar{q}}}(p,k)}{\mathrm{d}k\,\mathrm{d}t} + \frac{\mathrm{d}^2\Gamma^{\mathrm{g}}_{\mathrm{gg}}(p,k)}{\mathrm{d}k\,\mathrm{d}t}\Theta(2k-p)\right) . \end{aligned} \tag{3.119}$$

The initial condition at $t=0$ can be a single quark or gluon or a distribution obtained from a hard matrix element.

From the parton distributions modified fragmentation functions can be constructed

$$D_\mathrm{k}^{h\,(\mathrm{med})}(z_h, Q^2; \vec{r}, \vec{n}) = \int \mathrm{d}p_\mathrm{f}\, \frac{z'}{z_h}\left\{P_{\mathrm{q\bar{q}}/k}(p_\mathrm{f}; p_\mathrm{i})D^h_\mathrm{q}(z', Q^2) + P_{\mathrm{g}/k}(p_\mathrm{f}; p_\mathrm{i})D^h_\mathrm{g}(z', Q^2)\right\} , \tag{3.120}$$

where $z = p_h/p_\mathrm{i}$ and $z' = p_h/p_\mathrm{f}$. $P_{a/k}(p_\mathrm{f}; p_\mathrm{i})$ are solutions of equation (3.119), i.e. they are the probability that a parton k with momentum p_i evolves into a parton a with momentum p_f. They depend on the production point $\vec{r}$ and the direction $\vec{n}$ of motion of the initial parton. The fragmentation function thus has to be convolved with the distribution of production points and directions.

All the different approaches to radiative energy loss describe the nuclear modification factor measured at RHIC equally well. However, the transport coefficients needed are different reaching from $2\,\mathrm{GeV}^2/\mathrm{fm}$ to $10\,\mathrm{GeV}^2/\mathrm{fm}$ [164,165]. These values are larger than what can be expected from perturbative QCD indicating that the coupling may be large in the RHIC regime. In order to discriminate between the different models one has to go beyond leading particle distributions to more differential observables.

3.3.3. Monte Carlo Models

HIJING

The HIJING Monte Carlo generator [166] simulates multiple jet and minijet production in p+p, p+A and A+A collisions. For nuclear collisions modifications of the parton densities and initial and final state interactions are included. A string fragmentation model is used for hadronisation. The hard jets lose energy in the produced medium via induced radiation of gluons. The mean energy loss is estimated as

$$-\frac{\mathrm{d}E}{\mathrm{d}x} \approx \frac{3\alpha_\mathrm{s}}{\pi}\mu_\mathrm{D}^2 \mathcal{L}\left(\frac{E}{\lambda\mu_\mathrm{D}^2}, \frac{s}{4\mu_\mathrm{D}^2}\right) \tag{3.121}$$

with

$$\mathcal{L}(x,y) = \ln x \left(\ln x - 1 + \frac{1}{x}\right) + \ln y \left(1 - \frac{x}{y}\right) \quad \text{and} \quad s \approx 6ET\,. \tag{3.122}$$

The gluon emission points are chosen according to

$$\frac{\mathrm{d}P}{\mathrm{d}l} = \frac{1}{\lambda} e^{-\frac{l}{\lambda}} \tag{3.123}$$

and a collinear splitting is performed with

$$\Delta E(l) = l\frac{\mathrm{d}E}{\mathrm{d}x}\,. \tag{3.124}$$

This changes the colour topology and leads to a different string configuration resulting in jet quenching in the hadronic stage.

PYQUEN

In Pyquen [167] the jets including the hard matrix elements and the perturbative parton shower evolution are produced by Pythia. The jet production points are distributed according to the distribution of binary collisions in a nucleus-nucleus collision. The longitudinal and transverse expansion of the medium is taken into account. The scattering cross section defining the collisional energy loss is taken as

$$\frac{\mathrm{d}\sigma}{\mathrm{d}t} = C_\mathrm{R}\frac{2\pi\alpha_\mathrm{s}^2(|t|)}{t^2}\frac{E^2}{E^2 - m^2} \tag{3.125}$$

with one-loop running coupling. This cross section also determines the mean free path, which enters in the transport coefficient.

$$\hat{q} = \frac{\mu_\mathrm{D}^2}{\lambda} \quad \text{with} \quad \mu_\mathrm{D}^2 = 4\pi\alpha_\mathrm{s} T^2 \left(1 + \frac{n_\mathrm{f}}{6}\right) \tag{3.126}$$

The energy of radiated gluons is determined by the BDMPS gluon spectrum

$$\frac{\mathrm{d}I}{\mathrm{d}\omega} = \frac{2\alpha_\mathrm{s}(\mu_\mathrm{D}^2)\lambda C_\mathrm{R}}{\pi L \omega}\left(1 - x + \frac{x^2}{2}\right)\ln|\cos(\omega_1\tau_1)| \tag{3.127}$$

$$\omega_1 = \sqrt{i\left(1 - x + \frac{C_\mathrm{R}}{3}x^2\right)\bar{\kappa}\ln\frac{16}{\bar{\kappa}}} \quad \text{with} \quad \bar{\kappa} = \frac{\mu_\mathrm{D}^2\lambda}{\omega(1-x)}\,. \tag{3.128}$$

τ is the proper time.

The simulation procedure is to first determine the position of the next scattering i according to

$$\frac{\mathrm{d}P}{\mathrm{d}l_i} = \frac{1}{\lambda(\tau_{i+1})} \exp\left(- \int_0^{l_i} \mathrm{d}s \, \frac{1}{\lambda(\tau_i + s)} \right) . \tag{3.129}$$

Then the collisional and radiative energy loss is determined

$$\Delta E_i = \Delta E_i^{\mathrm{coll}} + \Delta E_i^{\mathrm{rad}} = \frac{t_i}{2m_0} + \omega_i \tag{3.130}$$

with $m_0 = 3T$, t_i and ω_i are determined by equation (3.125) and equation (3.127), respectively. The transverse momentum kick received by the projectile is calculated and the radiated gluon is added to the event. The procedure is repeated until the projectile leaves the medium, the temperature drops below the critical temperature or the projectile energy is reduced to the thermal energy. Finally, the event is hadronised using the Pythia routine.

PQM

The Parton Quenching Model Pqm [168] is a Monte Carlo implementation of the BDMPS quenching weights [27] (equation (3.102)). It is based on the factorised ansatz

$$\left.\frac{\mathrm{d}^2\sigma}{\mathrm{d}p_\perp \, \mathrm{d}y}\right|_{y=0} = \sum_{a,b,j=\mathrm{q},\bar{\mathrm{q}},\mathrm{g}} \int \mathrm{d}x_a \, \mathrm{d}x_b \, \mathrm{d}\Delta E_j \, \mathrm{d}z_j f_a(x_a) f_b(x_b) \left.\frac{\mathrm{d}^2\hat{\sigma}^{ab\to jX}}{\mathrm{d}p^{\mathrm{in}}_{\perp,j} \, \mathrm{d}y_j}\right|_{y=0}$$
$$\delta(p^{\mathrm{in}}_{\perp,j} - (p_{\perp,j} + \Delta E_j)) P(\Delta E_j; R_j, \omega_{\mathrm{c},j}) \frac{D_j^h(z_j)}{z_j^2} \tag{3.131}$$

The initial parton $p_\perp$-distribution is generated from LO matrix elements using Pythia. Then the energy loss ΔE is determined from the probability distribution $P(\Delta E; R, \omega_{\mathrm{c}})$, the information about the path length and the medium density along the path is encoded in the parameters R and ω_{c}. The geometry is obtained from a Glauber model and expansion of the medium is taken into account. The radiated energy ΔE is subtracted from the initial $p_\perp$ and finally the partons are hadronised independently using KKP fragmentation functions.

Modified parton showers

There are also two attempts to include induced gluon radiation in the parton shower evolution. In [169] it is assumed that the interactions with the medium increase the virtuality of fast partons and thus lead to enhanced splitting. A standard parton shower based on the Sudakov form factor is simulated. The lifetime of a state b produced with virtuality Q_b^2 in the decay of a mother a is estimated as

$$\tau_b = \frac{E_b}{Q_b^2} - \frac{E_b}{Q_a^2} . \tag{3.132}$$

During this time the virtuality change is given by

$$\Delta Q_b^2 = \int\limits_{\tau_b^0}^{\tau_b^0+\tau_b} \mathrm{d}\zeta\, \hat{q}(\zeta)\,, \tag{3.133}$$

where τ_b^0 is the production time of the parton b. The transport coefficient is assumed to be

$$\hat{q}(\zeta) = K2\epsilon^{3/4}(\zeta)(\cosh\rho(\zeta) - \sinh\rho(\zeta)\cos\psi) \tag{3.134}$$

where the energy density ϵ, the local flow rapidity ρ and the angle ψ between the flow and the fast parton's direction of motion are obtained from a hydrodynamic calculation. In the end the cascade is hadronised using the Lund string fragmentation model.

In [28, 170] a medium modified splitting function including induced gluon radiation is constructed

$$P^{\mathrm{med}}(z,Q^2) = P^{\mathrm{vac}}(z) + \Delta P(z,Q^2) \quad \text{with} \quad \Delta P(x,Q^2) = \frac{2\pi Q^2}{\alpha_\mathrm{s}} \frac{\mathrm{d}I^{\mathrm{med}}}{\mathrm{d}z\mathrm{d}Q^2}\,. \tag{3.135}$$

The medium induced gluon spectrum is constructed by dividing the gluon spectrum obtained from equation (3.97) in the multiple soft scattering approximation in a vacuum and a medium induced part. The energy sharing z and Q^2 are related to ω and $k_\perp$ via $\omega = (1-z)E$ and $k_\perp^2 = z(1-z)Q^2$. The modified splitting function has already been used in DGLAP evolution equations and a Monte Carlo implementation of a parton shower based on P^{med} called Q-PYTHIA is available [170].

CHAPTER 4

Medium-Modified Fragmentation Functions

In section 2.2.2 it was outlined how branching processes lead to the Q^2 evolution of the fragmentation functions. In a medium elastic an inelastic scattering will also influence the jet evolution. In this section a way how elastic collisions can be included in the DGLAP evolution equations is presented [9].

The formation of the parton shower does not happen instantaneously, but needs a certain time. As discussed on page 87 (section 5.2) the lifetime of virtual states during the parton shower evolution can be estimated as

$$\tau = E\left(\frac{1}{Q_\mathrm{f}^2} - \frac{1}{Q_\mathrm{i}^2}\right) \quad \Rightarrow \quad \mathrm{d}\tau = \frac{E}{Q^2}\frac{\mathrm{d}Q^2}{Q^2}\,, \tag{4.1}$$

although this choice is not unique. The time the shower needs to develop to a cut-off scale $Q_0 \simeq 1\,\mathrm{GeV}$ can then be estimated by the time a parton needs to reduce its virtuality from the starting scale $Q_\mathrm{i} \simeq E$ to Q_0. For high parton energies $E/Q_\mathrm{i}^2 \simeq 1/E$ is negligible and the lifetime becomes $E/Q_0^2 \simeq E$, which is of the order of a few fm. The QGP formation times are estimated to be of the order 0.2 fm at RHIC and 0.1 fm at LHC and the lifetime of the plasma phase is found to be several fm [16, 171]. Consequently the shower evolution overlaps in time with the plasma phase and one has to consider the effect that a dense and hot medium can have on the parton shower evolution. In this section a study of a parton cascade, that includes scattering from the medium as only modification to the well known QCD evolution in vacuum, is presented.

The scattering of partons in a quark-gluon plasma can be taken into account by modifying the DGLAP evolution equations accordingly. The hadronisation at the infrared cut-off Q_0 is assumed to be unchanged so that the standard fragmentation functions, which describe the hadronisation at Q_0, can be used as input. In this way one can separate the effects coming from the medium-induced modifications of the parton shower from others like energy loss of on-shell partons and modified hadronisation at Q_0.

In analogy to the unregularised splitting function, which is the splitting probability density, a scattering function $\hat{K}$ can be defined such that the differential scattering probability can be written as

$$\mathrm{d}\mathcal{P}_{a,\,\mathrm{scat}}(z, E_\mathrm{p}, Q^2) = \hat{K}_a(z, E_\mathrm{p}, Q^2)\mathrm{d}z\frac{\mathrm{d}Q^2}{Q^2} \tag{4.2}$$

The scattering function depends on the parton energy. In a DGLAP-like equation it is not possible to keep track of the energy of the parton. But the total jet energy can be set and the parton must have at least the hadron energy xE_jet after a scattering and xE_jet/z before. This lower bound is used as estimate of the parton energy.

Written in terms of the unregularised splitting functions $\hat{P}$ the medium modified DGLAP equations for the fragmentation functions take the form

$$\begin{aligned}
&\frac{\partial D(x, E, Q^2)}{\partial(\ln Q^2)} \\
&= \int_x^1 \frac{\mathrm{d}z}{z}\left\{\left[\frac{\alpha_\mathrm{s}}{2\pi}\hat{P}_\mathrm{qq}(z) + \hat{K}_\mathrm{q}\left(z, \frac{x}{z}E_\mathrm{jet}, Q^2\right)\right] D_\mathrm{q}^{h/j}\left(\frac{x}{z}, Q^2\right)\right. \\
&\qquad\qquad \left. + \frac{\alpha_\mathrm{s}}{2\pi}\hat{P}_\mathrm{gq}(z) D_\mathrm{g}^{h/j}\left(\frac{x}{z}, Q^2\right)\right\} \\
&\quad - \int_0^1 \mathrm{d}z\left[\frac{\alpha_\mathrm{s}}{2\pi}\hat{P}_\mathrm{qq}(z) + \hat{K}_\mathrm{q}(z, xE_\mathrm{jet}, Q^2)\right] D_\mathrm{q}^{h/j}(x, Q^2)
\end{aligned} \tag{4.3}$$

$$\begin{aligned}
&\frac{\partial D_\mathrm{g}^{h/j}(x, Q^2)}{\partial(\ln Q^2)} \\
&= \int_x^1 \frac{\mathrm{d}z}{z}\left\{\frac{\alpha_\mathrm{s}}{2\pi}\hat{P}_\mathrm{qg}(z)\sum_q\left(D_\mathrm{q}^{h/j}\left(\frac{x}{z}, Q^2\right) + D_{\bar{\mathrm{q}}}^{h/j}\left(\frac{x}{z}, Q^2\right)\right)\right. \\
&\qquad\qquad \left. + \left[2\frac{\alpha_\mathrm{s}}{2\pi}\hat{P}_\mathrm{gg}(z) + \hat{K}_\mathrm{g}\left(z, \frac{x}{z}E_\mathrm{jet}, Q^2\right)\right] D_\mathrm{g}^{h/j}\left(\frac{x}{z}, Q^2\right)\right\} \\
&\quad - \int_0^1 \mathrm{d}z\left[\frac{\alpha_\mathrm{s}}{2\pi}\hat{P}_\mathrm{gg}(z) + \frac{\alpha_\mathrm{s}}{2\pi}\hat{P}_\mathrm{qg}(z) + \hat{K}_\mathrm{g}(z, xE_\mathrm{jet}, Q^2)\right] D_\mathrm{g}^{h/j}(x, Q^2)\,.
\end{aligned} \tag{4.4}$$

The scattering function depends on the medium properties and the scattering cross section. For the medium a relativistic ideal gas of quarks and gluons is assumed, for the kinematics the scattering centre is taken to be at rest. This is justified for large jet energies at intermediate and large values of x where the gluon energy is large compared to the temperature. For small x this is not necessarily the case, but in this region the DGLAP equations without soft gluon resummation are not an accurate description of the shower evolution anyway. For the scattering cross section a simplified and regularised form of the perturbative scattering cross section is used.

$$\frac{\mathrm{d}\sigma_{ab}}{\mathrm{d}|t|} = C_{ab}\,\frac{2\pi\alpha_\mathrm{s}^2(Q^2)}{(|t| + \mu_\mathrm{D}^2)^2}\,, \tag{4.5}$$

where μ_D is the Debye mass and C_{ab} the colour factor ($C_{qq} = 4/9$, $C_{qg} = C_{gq} = 1$, $C_{gg} = 9/4$). This cross section is well behaved down to $|t| = 0$ although it cannot be expected that perturbation theory makes sense in the this regime. Still, it may be useful to see what effects one gets from this cross section.

For sufficiently small scattering cross sections and densities the mean number of scatterings equals the scattering probability. The probability for scattering per virtuality interval and z interval is then

$$\mathrm{d}\mathcal{P}_{ab,\,\mathrm{scat}}(z, E_\mathrm{p}, Q^2) = n_b(T)\,\frac{\mathrm{d}\sigma_{ab}}{\mathrm{d}z}\,\mathrm{d}z\,\frac{E_\mathrm{p}}{Q^2}\frac{\mathrm{d}Q^2}{Q^2} = \hat{K}_{ab}(z, E_\mathrm{p}, Q^2)\,\frac{\mathrm{d}Q^2}{Q^2}\,\mathrm{d}z\,, \tag{4.6}$$

$$\mathrm{d}\mathcal{P}_{a,\,\mathrm{scat}}(z, E_\mathrm{p}, Q^2) = \sum_b \hat{K}_{ab}(z, E_\mathrm{p}, Q^2)\,\frac{\mathrm{d}Q^2}{Q^2}\,\mathrm{d}z = \hat{K}_{a}(z, E_\mathrm{p}, Q^2)\,\frac{\mathrm{d}Q^2}{Q^2}\,\mathrm{d}z\,, \tag{4.7}$$

where the density of an ideal relativistic gas is given by (section 3.1.2)

$$n_{\mathrm{q}+\bar{\mathrm{q}}}(T) = 12\,n_\mathrm{f}\,d(3)\frac{T^3}{\pi^2} \qquad n_\mathrm{g}(T) = 16\,\zeta(3)\frac{T^3}{\pi^2}\,. \tag{4.8}$$

For a static scattering centre with mass m_s one finds

$$t = 2m_\mathrm{s}E_\mathrm{p}(z-1)\,, \tag{4.9}$$

where E_p is the energy of the incoming fast parton and z is the energy fraction that the scattered parton takes.

Putting everything together one finds

$$\hat{K}_a(z, E_\mathrm{p}, Q^2) = \frac{(16\,\zeta(3)\,C_{a\mathrm{g}} + 12\,n_\mathrm{f}\,d(3)\,C_{a\mathrm{q}})T^3 4m_\mathrm{s}E_\mathrm{p}^2\alpha_\mathrm{s}^2(Q^2)}{Q^2\pi(2m_\mathrm{s}E_\mathrm{p}(1-z) + \mu_\mathrm{D}^2)^2}\,. \tag{4.10}$$

For the scale of α_s several choices are conceivable. Results are shown for a one-loop running coupling $\alpha_\mathrm{s}(Q^2)$, since the parton is virtual, i. e. does not have a full gluon cloud and should therefore interact with a smaller cross section. This scattering function has no singularities, but it is convenient to define a 'regularised' scattering function K_a in analogy to the regularised splitting function and write the modified evolution equations in a more compact form

$$\begin{aligned}\frac{\partial D_\mathrm{q}(x, E, Q^2)}{\partial(\ln Q^2)}\\ = \int_0^1 \frac{\mathrm{d}z}{z}\,\Big\{\Big[\frac{\alpha_\mathrm{s}}{2\pi}P_\mathrm{qq}(z) + K_\mathrm{q}\left(z, \frac{x}{z}E_\mathrm{jet}, Q^2\right)\Big]\,D_\mathrm{q}^{h/j}\left(\frac{x}{z}, Q^2\right)\\ + \frac{\alpha_\mathrm{s}}{2\pi}P_\mathrm{gq}(z)D_\mathrm{g}^{h/j}\left(\frac{x}{z}, Q^2\right)\Big\}\end{aligned} \tag{4.11}$$

$$\begin{aligned}\frac{\partial D_\mathrm{g}^{h/j}(x, Q^2)}{\partial(\ln Q^2)}\\ = \int_0^1 \frac{\mathrm{d}z}{z}\,\left\{\frac{\alpha_\mathrm{s}}{2\pi}P_\mathrm{qg}(z)\sum_q\left(D_\mathrm{q}^{h/j}\left(\frac{x}{z}, Q^2\right) + D_{\bar{\mathrm{q}}}^{h/j}\left(\frac{x}{z}, Q^2\right)\right)\right.\\ \left. + \Big[2\frac{\alpha_\mathrm{s}}{2\pi}P_\mathrm{gg}(z) + K_\mathrm{g}\left(z, \frac{x}{z}E_\mathrm{jet}, Q^2\right)\Big]\,D_\mathrm{g}^{h/j}\left(\frac{x}{z}, Q^2\right)\right\}\,.\end{aligned} \tag{4.12}$$

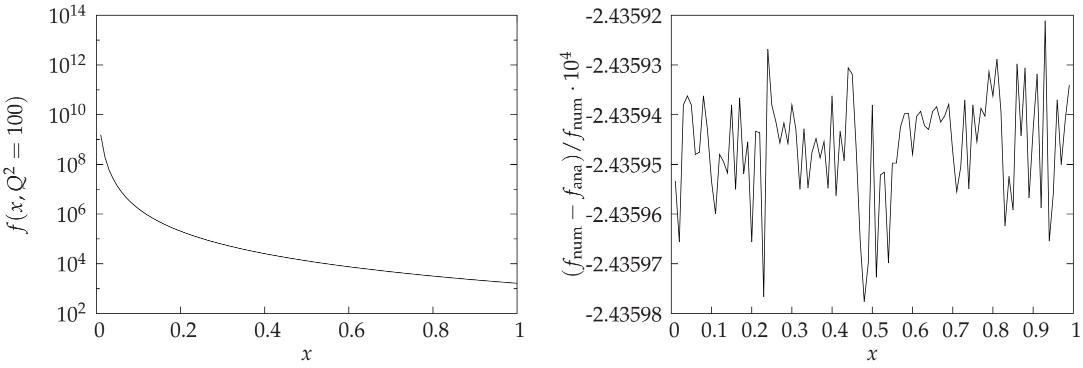

Figure 4.1.: Test function used to check the numerical integration routine and relative deviation of the numerical result from the analytical solution (10^5 steps in t'-integration, 100 x-points, $\epsilon = 10^{-4}$ precision in Runge-Kutta integration).

These equations can only be solved be numerically. For this purpose it is advantageous to further reformulate them

$$\begin{aligned}
&D_{\mathrm{q}}(x,E,Q^2)\\
&= D_{\mathrm{q}}(x,E,Q_0^2) + \int\limits_{Q_0^2}^{Q^2} \frac{\mathrm{d}Q'^2}{Q'^2} \int\limits_0^1 \frac{\mathrm{d}z}{z} \left\{ \left[\frac{\alpha_{\mathrm{s}}}{2\pi} P_{\mathrm{qq}}(z) + K_{\mathrm{q}}\left(z, \frac{x}{z}E_{\mathrm{jet}}, Q'^2\right)\right] D_{\mathrm{q}}^{h/j}\left(\frac{x}{z}, Q'^2\right)\right.\\
&\qquad \left. + \frac{\alpha_{\mathrm{s}}}{2\pi} P_{\mathrm{gq}}(z) D_{\mathrm{g}}^{h/j}\left(\frac{x}{z}, Q'^2\right)\right\} \qquad (4.13)\\
&= D_{\mathrm{q}}(x,E,Q_0^2) + \int\limits_{t_0'}^{t'} \mathrm{d}t'' \int\limits_0^1 \frac{\mathrm{d}z}{z} \left\{ \left[\frac{\alpha_{\mathrm{s}}}{2\pi} P_{\mathrm{qq}}(z) + K_{\mathrm{q}}\left(z, \frac{x}{z}E_{\mathrm{jet}}, \Lambda_{\mathrm{QCD}}^2 e^{t''}\right)\right] D_{\mathrm{q}}^{h/j}\left(\frac{x}{z}, \Lambda_{\mathrm{QCD}}^2 e^{t''}\right)\right.\\
&\qquad \left. + \frac{\alpha_{\mathrm{s}}}{2\pi} P_{\mathrm{gq}}(z) D_{\mathrm{g}}^{h/j}\left(\frac{x}{z}, \Lambda_{\mathrm{QCD}}^2 e^{t''}\right)\right\} \qquad \text{with} \qquad t' = \ln\left(\frac{Q^2}{\Lambda_{\mathrm{QCD}}^2}\right) \qquad (4.14)\\
&= D_{\mathrm{q}}(x,E,Q_0^2) + \lim_{n\to\infty} \sum_{i=1}^{n} \Delta t_i' \int\limits_0^1 \frac{\mathrm{d}z}{z} \left\{ \left[\frac{\alpha_{\mathrm{s}}}{2\pi} P_{\mathrm{qq}}(z) + K_{\mathrm{q}}\left(z, \frac{x}{z}E_{\mathrm{jet}}, \Lambda_{\mathrm{QCD}}^2 e^{t_i'}\right)\right] D_{\mathrm{q}}^{h/j}\left(\frac{x}{z}, \Lambda_{\mathrm{QCD}}^2 e^{t_i'}\right)\right.\\
&\qquad \left. + \frac{\alpha_{\mathrm{s}}}{2\pi} P_{\mathrm{gq}}(z) D_{\mathrm{g}}^{h/j}\left(\frac{x}{z}, \Lambda_{\mathrm{QCD}}^2 e^{t_i'}\right)\right\} . \qquad (4.15)
\end{aligned}$$

The t'-integral is approximated by the left Riemann sum and the z-integration is performed using a quality-controlled fourth order Runge - Kutta integration [172], which is suited for strongly peaked integrants. Because of the appearance of the function D_i^h in the integral this methods cannot be used for the t'-integration.

The routine is tested with a simple test function that can also be integrated ana-

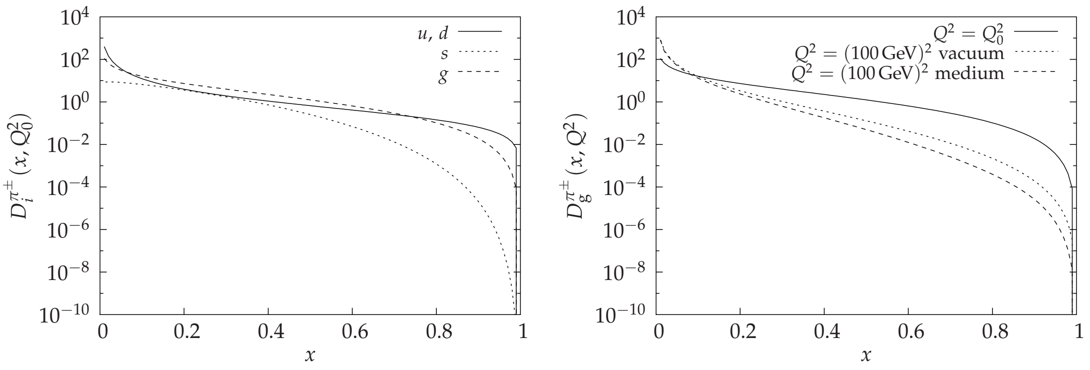

Figure 4.2.: **Left:** Input distributions at $Q_0^2 = 2\,\mathrm{GeV}^2$ for the fragmentation functions of light partons into charged pions. **Right:** Gluon into charged pion fragmentation function at Q_0 and evolved to $Q^2 = (100\,\mathrm{GeV})^2$ in vacuum and in a static medium with temperature $T = 500\,\mathrm{MeV}$ using $E_{\mathrm{jet}} = Q = 100\,\mathrm{GeV}$.

lytically:

$$\begin{aligned} f(x, Q^2) &= \int_{t_0}^{t} \mathrm{d}t' \int_{0}^{1} \frac{\mathrm{d}z}{z} \left(\frac{x}{z}\right)^{-3} \left(\Lambda_{\mathrm{QCD}}^4 e^{2t'} - \Lambda_{\mathrm{QCD}}^2 e^{t'}\right) \\ &= x^{-3} \frac{1}{3} \left(\frac{Q^2}{2} - Q^2 - \frac{Q_0^2}{2} + Q_0^2\right) . \end{aligned} \tag{4.16}$$

In figure 4.1 the numerical result is compared to the analytical solution for $Q_0^2 = 2\,\mathrm{GeV}^2$ and $Q^2 = 100\,\mathrm{GeV}^2$. The agreement is satisfactory, but a large number of steps in the t'-integration is needed. Here one has to make a compromise between precision and run-time. The numerical result is systematically too small, since the t'-integral is approximated by the left Riemann sum and the test function f increases with t'.

In the case of the evolution equations for fragmentation functions into light hadrons a set of seven coupled equations including the three light quark flavours u, d and s, the corresponding antiquarks and the gluon has to be solved. If instead the fragmentation function into a hadron and its antiparticle is studied the number of equations reduces to four because the contribution from an antiquark is the same as that from the corresponding quark. The charged pion fragmentation functions are shown here as an example. This combination is also symmetric under exchange of u and d so that effectively only three equations are left. The input distributions at Q_0 are a KKP

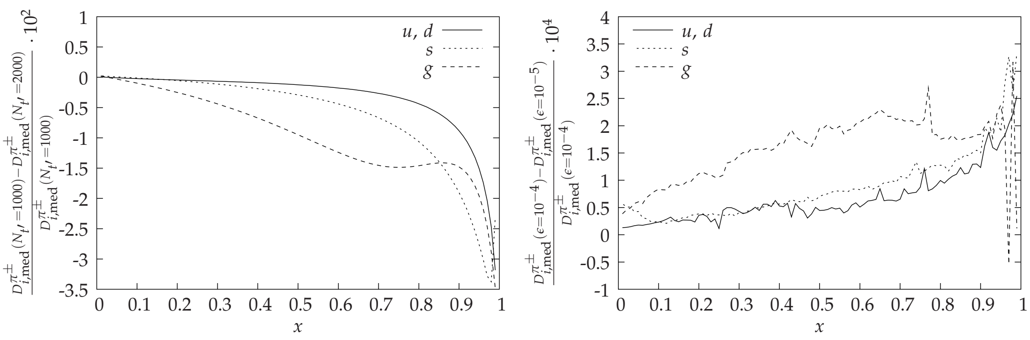

Figure 4.3.: **Left:** Relative change of the medium fragmentation functions at $Q^2 = (100\,\mathrm{GeV})^2$ ($T = 500\,\mathrm{MeV}$ static) after doubling the number of steps in the t'-integration from 1000 to 2000. **Right:** Relative change due to changing the precision in the Runge-Kutta integration from 10^{-4} to 10^{-5}.

parametrisation [173] at $Q_0^2 = 2\,\mathrm{GeV}^2$:

$$D_{\mathrm{u}}^{\pi^\pm}(x, Q_0^2) = 0.448\, x^{-1.48}\, (1-x)^{0.913} \tag{4.17}$$

$$D_{\mathrm{d}}^{\pi^\pm}(x, Q_0^2) = 0.448\, x^{-1.48}\, (1-x)^{0.913} \tag{4.18}$$

$$D_{\mathrm{s}}^{\pi^\pm}(x, Q_0^2) = 16.6\, x^{0.133}\, (1-x)^{5.90} \tag{4.19}$$

$$D_{\mathrm{g}}^{\pi^\pm}(x, Q_0^2) = 3.73\, x^{-0.742}\, (1-x)^{2.33}\,. \tag{4.20}$$

The fragmentation functions at Q_0 are shown in figure 4.2 (left). At large x u and d, which are the valence quarks, and the gluon dominate over the contribution from s quarks. In the right panel of figure 4.2 the gluon part is shown at Q_0 and evolved to $Q^2 = (100\,\mathrm{GeV})^2$. In vacuum, the evolution to higher Q^2 depletes the high x region and enhances the low x part since the energy is shared among more and more partons. For the medium functions a constant temperature of $T = 500\,\mathrm{MeV}$ was used. The Debye mass is $\mu_{\mathrm{D}} = 1.97\,\mathrm{GeV}$ taken from the parametrisation in [174] and the mass of the scattering centre is taken as $m_{\mathrm{s}} = \mu_{\mathrm{D}}/\sqrt{2}$. The scale, up to which the fragmentation function is evolved, is $Q^2 = E_{\mathrm{jet}}^2$, i.e. the maximum possible virtuality of a parton with energy E_{jet}.

The results in figure 4.2 were obtained with 1000 steps in the t'-integration, a precision of 10^{-4} in the Runge-Kutta integration and 100 x-sampling points. The choice of $N_{t'} = 1000$ is essentially dictated by the requirement to have a reasonable run-time. The resulting uncertainty is shown in figure 4.3, doubling the number of steps leads to a relative deviation of up to 3.5 % at large x. Compared to this the uncertainty due to limited precision of the Runge-Kutta integration is negligible (figure 4.3 right). The first and last x points have a large uncertainty due to the strong variation of the fragmentation functions in these regions and termination effects (figure 4.4). In the intermediate x region the accuracy is much better.

The scattering term acts in principle in the same way as the evolution in vacuum shifting activity from large to small x, but since it does not keep track of struck scattering centres it effectively removes energy from the jet. The fragmentation functions

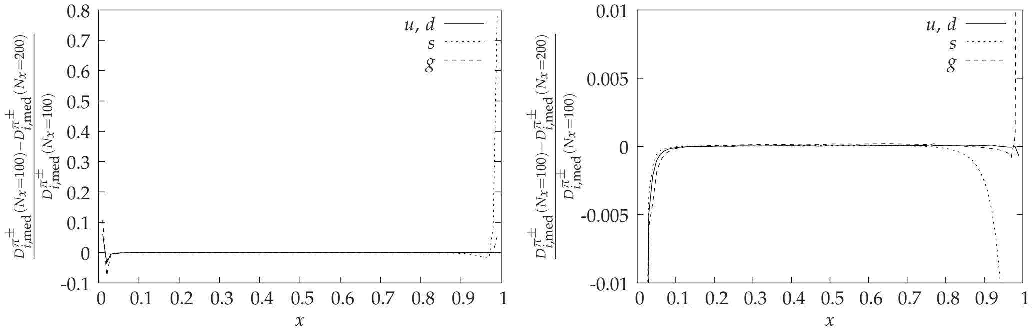

Figure 4.4.: **Left:** Relative change of the medium fragmentation functions at $Q^2 = (100\,\mathrm{GeV})^2$ ($T = 500\,\mathrm{MeV}$ static) due to doubling the number of x-sampling points from 100 to 200. **Right:** Region with relative deviation smaller than 1 %.

in medium are thus always smaller than those in vacuum. This is better seen in the ratios of the fragmentation functions in medium and in vacuum (figure 4.5), which are always smaller than unity. There is a significant reduction of the fragmentation functions due to elastic scattering in the medium.

The evolution equations can be modified such that they take the recoiling scattering centre into account. Since the scattering centres are assumed to be at rest, their momentum comes solely from the scattering event. The fragmentation of a struck scattering centre is described by the same fragmentation function as the jet partons, the thermal mass is here ignored. The version of equations (4.11)–(4.12) that includes the recoil reads

$$\begin{aligned}\frac{\partial D_\mathrm{q}(x,E,Q^2)}{\partial(\ln Q^2)} = \int_0^1 \frac{\mathrm{d}z}{z} \Big\{ &\Big[\frac{\alpha_\mathrm{s}}{2\pi}P_\mathrm{qq}(z) + K_\mathrm{q}\Big(z,\frac{x}{z}E_\mathrm{jet},Q^2\Big)\Big] D_\mathrm{q}^{h/j}\Big(\frac{x}{z},Q^2\Big) \\ &+\frac{\alpha_\mathrm{s}}{2\pi}P_\mathrm{gq}(z)D_\mathrm{g}^{h/j}\Big(\frac{x}{z},Q^2\Big) + \hat{K}_\mathrm{qq}\Big(1-z,\frac{x}{z}E_\mathrm{jet},Q^2\Big) D_\mathrm{q}^{h/j}\Big(\frac{x}{z},Q^2\Big) \\ &+\hat{K}_\mathrm{qg}\Big(1-z,\frac{x}{z}E_\mathrm{jet},Q^2\Big) D_\mathrm{g}^{h/j}\Big(\frac{x}{z},Q^2\Big)\Big\}\end{aligned} \tag{4.21}$$

$$\begin{aligned}\frac{\partial D_\mathrm{g}^{h/j}(x,Q^2)}{\partial(\ln Q^2)} = \int_0^1 \frac{\mathrm{d}z}{z} \Bigg\{ &\frac{\alpha_\mathrm{s}}{2\pi}P_\mathrm{qg}(z)\sum_q \Big(D_\mathrm{q}^{h/j}\Big(\frac{x}{z},Q^2\Big) + D_{\bar{\mathrm{q}}}^{h/j}\Big(\frac{x}{z},Q^2\Big)\Big) \\ &+\Big[2\frac{\alpha_\mathrm{s}}{2\pi}P_\mathrm{gg}(z) + K_\mathrm{g}\Big(z,\frac{x}{z}E_\mathrm{jet},Q^2\Big)\Big] D_\mathrm{g}^{h/j}\Big(\frac{x}{z},Q^2\Big) \\ &+\hat{K}_\mathrm{gq}\Big(1-z,\frac{x}{z}E_\mathrm{jet},Q^2\Big) D_\mathrm{q}^{h/j}\Big(\frac{x}{z},Q^2\Big) \\ &+\hat{K}_\mathrm{gg}\Big(1-z,\frac{x}{z}E_\mathrm{jet},Q^2\Big) D_\mathrm{g}^{h/j}\Big(\frac{x}{z},Q^2\Big)\Bigg\}\,.\end{aligned} \tag{4.22}$$

The scattering cross section prefers small momentum transfers, the contribution from recoiling scattering centres is thus only visible at small x (figure 4.5). In this region

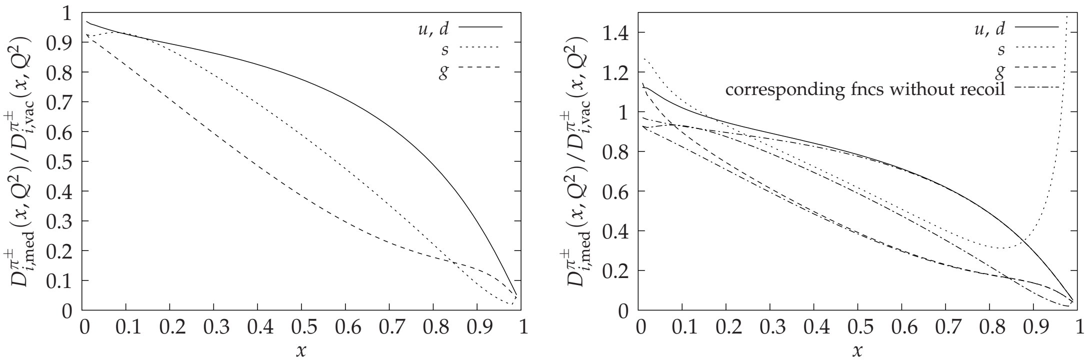

Figure 4.5.: **Left:** Ratios of the fragmentation functions in medium and those in vacuum for a static medium with $T = 500\,\mathrm{MeV}$, the recoiling scattering centre is not included (equations (4.11)–(4.12)). **Right:** The same with the recoiling scattering centre (equations (4.21)–(4.22)).

the ratio of modified and vacuum fragmentation functions is larger than unity. The s quark part shows a somewhat different behaviour: Here the fragmentation function falls extremely steeply at large x so that a scattering with large momentum transfer and subsequent hadronisation of the recoil with a large fraction of the energy taken by the hadron is more likely than the direct hadronisation of the strange quark. This leads to the strong enhancement at large x due to the recoil contribution.

In the framework of the evolution equations the time needed to develop down to the infra-red cut-off scale Q_0 is

$$t_{\mathrm{tot}} = E_{\mathrm{jet}}\left(\frac{1}{Q_0^2} - \frac{1}{Q^2}\right) = \frac{E_{\mathrm{jet}}}{Q_0^2} - \frac{1}{E_{\mathrm{jet}}}\,. \tag{4.23}$$

This leads to a total evolution time of $t_{\mathrm{tot}} = 10\,\mathrm{fm}$ for a $100\,\mathrm{GeV}$ jet. There is no scattering of on-shell partons, i.e. the splittings as well as the scatterings stop at Q_0. One can set a path length L inside the medium, which is related to a virtuality Q_1 via equation (4.23) ,

$$Q_1 = Q_0\sqrt{\frac{E_{\mathrm{jet}}}{E_{\mathrm{jet}} - LQ_0^2}}\,. \tag{4.24}$$

The scattering term can be included in the evolution only for virtualities larger than Q_1 to investigate the path length dependence and the effect of a finite size medium. The result is shown in figure 4.6 for different path lengths. The suppression increases in the intermediate x region linearly with the path length.

One can go one step further and use the information about the time, which corresponds to each step in the evolution, to include a time dependence of the density. In a Bjorken-like longitudinal expansion scenario the (proper) time dependence of the temperature is given by (section 3.1.3)

$$\frac{T(\tau)}{T(\tau_0)} = \left(\frac{\tau_0}{\tau}\right)^{\frac{1}{3}}\,. \tag{4.25}$$

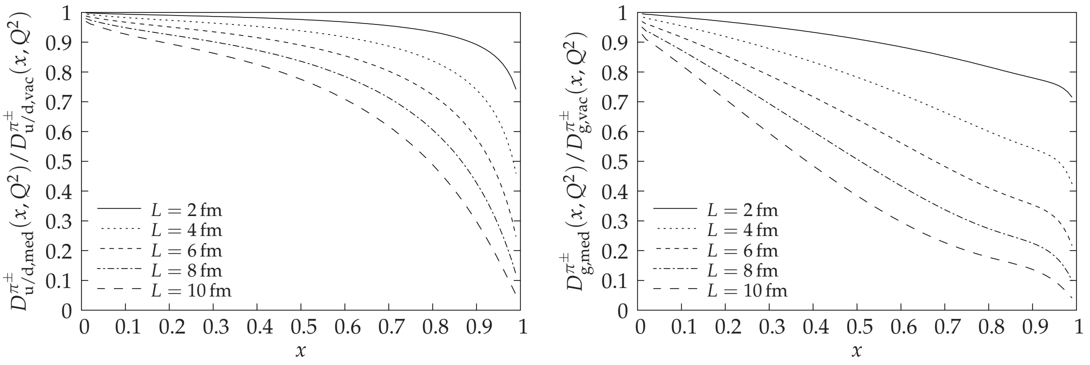

Figure 4.6.: Ratios of fragmentation functions for different path lengths in a static medium with $T = 500\,\mathrm{MeV}$ (left: u and d quarks, right: gluons).

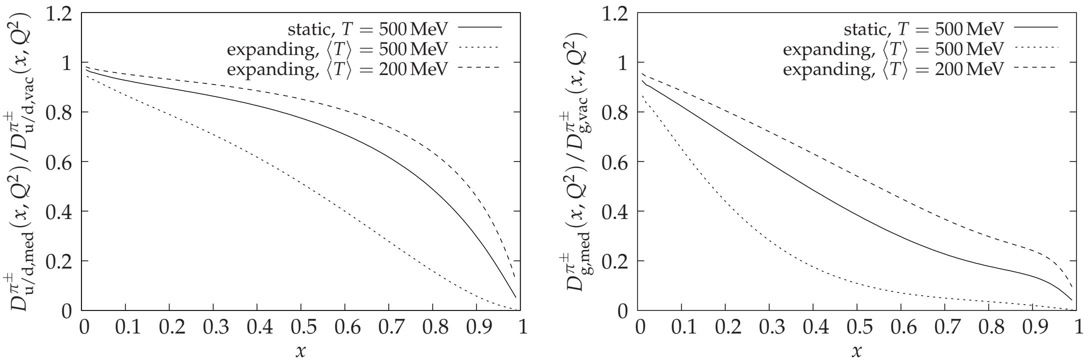

Figure 4.7.: Comparison of medium modified fragmentation functions (left: u and d quarks, right: gluons) in a static ($T = 500\,\mathrm{MeV}$) to an expanding medium ($\langle T\rangle = 200\,\mathrm{MeV}$ and $\langle T\rangle = 500\,\mathrm{MeV}$).

At mid-rapidity $t \approx \tau$ and equation (4.25) can be used to determine the density. At LHC the formation time is estimated as $\tau_0 \simeq 0.1\,\mathrm{fm}$. For times smaller than τ_0 the density is taken as the value at τ_0. An initial temperature of $T(\tau_0) = 3.2\,\mathrm{GeV}$ ($1.3\,\mathrm{GeV}$) then corresponds to an average temperature of $\langle T\rangle = 500\,\mathrm{MeV}$ ($200\,\mathrm{MeV}$), where the average is taken over the first 7 fm. Figure 4.7 shows that the suppression in an expanding medium is stronger than in a static with the same average temperature. The suppression observed in a static medium with 500 MeV temperature is the same as in an expanding medium with an average temperature of 270 MeV. However, these are still unrealistically high temperatures, an initial temperature of 750 MeV leads to an average of only 116 MeV, which translates into a weaker hadron suppression.

The choice of Q^2 as scale for α_s is not unique. In fact, one usually takes the momentum transfer $|t|$ in scattering events. Furthermore, it is not clear how the cross section should be regularised. These are only two examples for the uncertainties in the formulation of the scattering function. The effect that a different choice of the

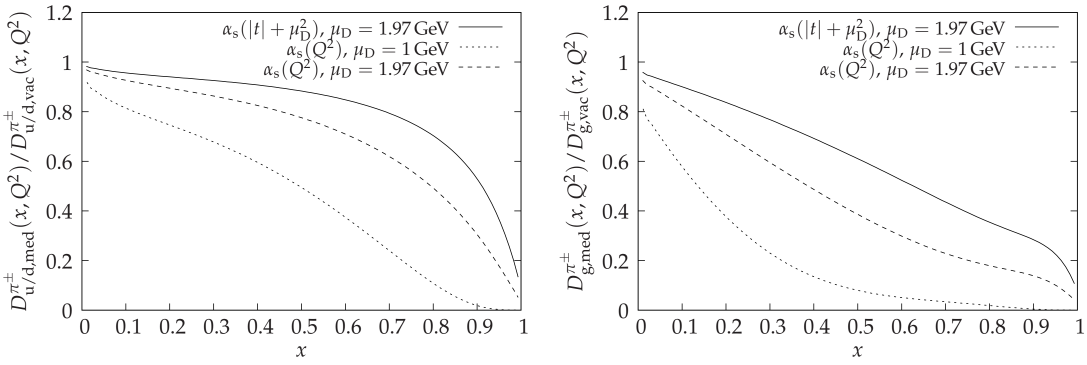

Figure 4.8.: Modified fragmentation functions for different choices of the scale of α_s (the virtuality Q^2 or the momentum transfer $|t|$) and the infra-red regulator μ_D (1 GeV or 1.97 GeV) (left: u and d quarks, right: gluons).

scale of the strong coupling and a different value for the screening mass have on the medium modified fragmentation functions are shown in figure 4.8. Qualitatively, the effect remains the same, but the magnitude depends significantly on the details of the scattering function. Especially the infra-red regulator has a strong influence on the total scattering cross section.

It is not surprising, that the suppression is not as strong as observed in data, since the inelastic processes, which are believed to be the dominant source of energy loss, are not included. However, the modifications of the fragmentation functions due to elastic scattering show a significant suppression of energetic hadrons. The details depend on the exact choice of the scattering function. Although the evolution equations cannot do justice to the stochastic nature of the parton shower formation, the modified evolution equations may serve as a reasonably simple tool to investigate the effect of elastic scattering.

CHAPTER 5

Jet Evolution With Energy Loss

In this chapter the Monte Carlo model Jewel for jet evolution with energy loss is presented [175,176]. It simulates a final state parton shower in a medium. In the current version it has a microscopic model for elastic scattering and a simplified model of radiative energy loss, which will be replaced by a description based on inelastic matrix elements in an upcoming version. The detailed microscopic modelling of medium interactions during the parton shower evolution is a major difference to the existing Monte Carlo models (section 3.3.3).

5.1. Final State Parton Shower in Vacuum

In this section, the baseline on top of which medium-effects are included is introduced and shown to basically reproduce the observed QCD radiation physics of jets in the vacuum. The evolution variable of a parton shower is not unique. The Jewel parton shower is ordered in virtuality Q^2, although modern parton shower implementations usually use the transverse momentum as evolution variable. This has, for instance, the advantage that angular ordering is automatically included. The virtuality, however, is better suited for the description of a shower evolution in a medium, because then the evolution variable traces the lifetime $1/Q$ of the virtual states, which facilitates the embedding of the parton shower in the spatiotemporal geometry of a medium. The parton shower is interfaced with a hadronisation scheme which implements the idea that colour neutralisation occurs locally during hadronisation. However, the scheme invoked here is less sophisticated than the hadronisation prescriptions used in modern event generators, in particular in that it does not require knowledge about the event-specific colour flow in the parton shower. This is a technical simplification, which - in contrast to standard treatments - allows for a straightforward extension of the hadronisation mechanism in the presence of a medium.

5.1.1. A Monte Carlo Implementation of Parton Evolution

A parton of initial energy E produced in a hard scattering process fragments into a multi-parton final state. In the absence of a medium, the JEWEL parton shower is closely related to the mass-ordered shower in the PYTHIA 6.4 event generator [23]. The virtuality, which is the evolution variable, is interpreted as a virtual mass, i.e. $Q^2 = p^2 = E^2 - \vec{p}^2$. The kinematics of each $a \to b + c$ parton branching is given in terms of the virtuality of the parent parton, the momentum fraction z carried by one of its daughters and the daughter virtualities. The four-momenta are chosen as

$$p_{a\mu} = (E_a, \vec{0}, p_a) \quad \text{with} \quad p_a^2 = E_a^2 - Q_a^2 \tag{5.1}$$

$$p_{b\mu} = (zE_a, \vec{k}_\perp, p_b) \tag{5.2}$$

$$p_{c\mu} = ((1-z)E_a, -\vec{k}_\perp, p_a - p_b)\,. \tag{5.3}$$

The conditions

$$p_{b\mu}p_b^\mu = z^2E_a^2 - k_\perp^2 - p_b^2 = Q_b^2 \tag{5.4}$$

$$p_{c\mu}p_c^\mu = (1-z)^2E_a^2 - k_\perp^2 - (p_a - p_b)^2 = Q_c^2 \tag{5.5}$$

lead to

$$p_b = \frac{2zE_a^2 - Q_a^2 - Q_b^2 + Q_c^2}{2p_a} \tag{5.6}$$

$$k_\perp^2 = -z^2\frac{Q_a^2E_a^2}{p_a^2} - z\frac{E_a^2}{p_a^2}\left(Q_c^2 - Q_a^2 - Q_b^2\right) - \frac{\left(Q_c^2 - Q_a^2 - Q_b^2\right)^2}{4p_a^2} - Q_b^2 \tag{5.7}$$

When the energy of the partons is large compared to their virtuality the expression for the transverse momentum simplifies to

$$k_\perp^2 \approx z(1-z)Q_a^2 - (1-z)Q_b^2 - zQ_c^2 \approx z(1-z)Q_a^2\,. \tag{5.8}$$

The last step make use of the strong ordering of the virtualities $Q_a^2 \gg Q_b^2, Q_c^2$ (which is a condition for the parton shower picture to be valid). In this approximation the opening angle θ_a is given by

$$\theta_a \approx \frac{k_\perp}{p_b} + \frac{k_\perp}{p_c} \approx \frac{\sqrt{z(1-z)}Q_a}{zE_a} + \frac{\sqrt{z(1-z)}Q_a}{(1-z)E_a} = \frac{Q_a}{\sqrt{z(1-z)}E_a} \tag{5.9}$$

The Monte Carlo formulation of the parton shower is based on the Sudakov form factor (section 2.2.2), which is the probability that no splitting occurs between an initial and a final virtuality Q_i and Q_f, respectively.

$$S_a(Q_\mathrm{i}^2, Q_\mathrm{f}^2) = \exp\left[-\int\limits_{Q_\mathrm{f}^2}^{Q_\mathrm{i}^2}\frac{\mathrm{d}Q'^2}{Q'^2}\int\limits_{z_-(Q'^2,E_a)}^{z_+(Q'^2,E_a)}\mathrm{d}z\,\frac{\alpha_\mathrm{s}(z(1-z)Q'^2)}{2\pi}\sum_b\hat{P}_{ba}(z)\right]\,. \tag{5.10}$$

Here, $\hat{P}_{ba}(z)$ are the standard LO parton splitting functions for quarks and gluons ($a, b \in \{q, g\}$). The scale of α_s is taken to be the transverse momentum of the splitting (equation (5.8)). This choice effectively includes higher order corrections [177,178]. It also implies that the transverse momentum is larger than Λ_{QCD}, in JEWEL $k_\perp \geq f \cdot \Lambda_{\text{QCD}}$ with $f = 1.1$ is used. The z-integral is divergent due to the singularities in the splitting functions, which arise from the break-down of perturbation theory. One therefore has to define a scale up to which one wants to trust the perturbative description. For the parton shower it is convenient to require a minimal virtuality $Q_0/2$ for the daughters of a branching (this prescription as also used in the mass-ordered PYTHIA cascade). Solving equation (5.7) for z leads to

$$z = \frac{1}{2}\left\{1 + \frac{Q_b^2 - Q_c^2}{Q_a^2} \pm \sqrt{\frac{\left(Q_a^2 + Q_b^2 - Q_c^2\right)^2}{Q_a^2}\left(\frac{1}{Q_a^2} - \frac{1}{E_a^2}\right) - \frac{4p_a^2(Q_b^2 + k_\perp^2)}{E_a^2 Q_a^2}}\right\}. \quad (5.11)$$

With the requirements $k_\perp \geq f \cdot \Lambda_{\text{QCD}}$ and $Q_b, Q_c \geq Q_0/2$ this translates into the allowed z range

$$z_\pm(Q^2, E_a) = \frac{1}{2} \pm \frac{1}{2}\sqrt{\left(1 - \frac{Q_0^2 + 4(f \cdot \Lambda_{\text{QCD}})^2}{Q^2}\right)\left(1 - \frac{Q^2}{E_a^2}\right)}. \quad (5.12)$$

This also implies that only partons with $Q_a > Q_{\text{min}}$ with

$$Q_{\text{min}} = \sqrt{Q_0^2 + 4(f \cdot \Lambda_{\text{QCD}})^2} \quad (5.13)$$

can split, because the virtuality must be large enough to give the daughters the minimal virtuality and transverse momentum.

With the no-splitting probability (equation (5.10)) the probability density $\Sigma_a(Q_\text{i}^2, Q^2)$ for a splitting to happen at virtuality Q^2 is given by

$$\Sigma_a(Q_\text{i}^2, Q^2) = \frac{\mathrm{d}S_a(Q_\text{i}^2, Q^2)}{\mathrm{d}(\ln Q^2)} = S_a(Q_\text{i}^2, Q^2)\sum_b W_{ba}(Q^2), \quad (5.14)$$

where

$$W_{ba}(Q^2) = \int\limits_{z_-(Q^2,E_a)}^{z_+(Q^2,E_a)} \mathrm{d}z\, \frac{\alpha_\text{s}(z(1-z)Q^2)}{2\pi}\hat{P}_{ba}(z) \quad (5.15)$$

is the differential probability for the splitting $a \to b + c$ at Q^2. Figure 5.1 shows examples of the Sudakov form factor and the differential branching probability Σ_a. The larger splitting probability of gluons leads to a smaller no-splitting probability, which in turn means that gluons experience the next branching on average at a higher virtuality than quarks.

JEWEL is a stand-alone parton shower that does not include the hard process. The species and energy of the parent parton of the shower has to be specified externally. Its virtuality Q_a is determined according to the probability density $\Sigma_a(E^2, Q_a^2)$, the maximal possible virtuality is given by the parton energy. This is the natural choice in e^++e^- collisions, whereas in p+p the transverse momentum with respect to the beam axis seems more appropriate. In JEWEL circumvents jets in hadronic (including nuclear) collisions are produced at mid-rapidity so that $p_\perp \approx E$. If the parent

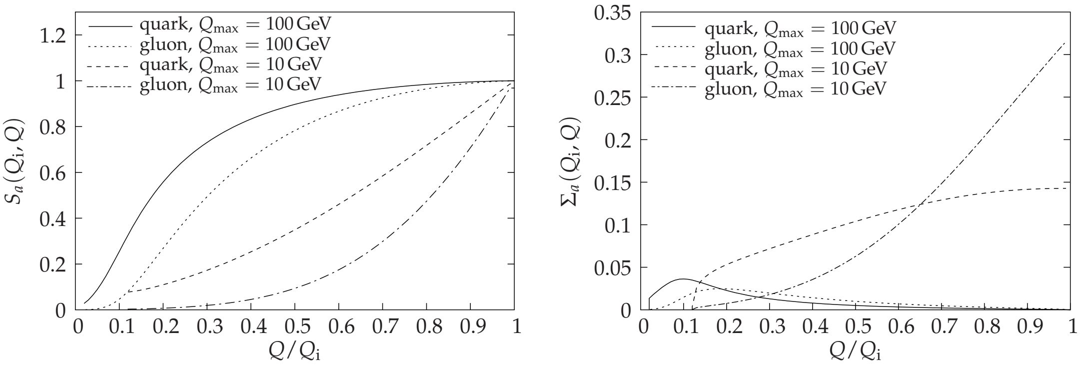

Figure 5.1.: Sudakov form factor and probability density Σ_a for quarks and gluons with different initial virtualities, $E = 100\,\text{GeV}$ and $Q_0 = 1\,\text{GeV}$.

parton is a gluon, the type of branching has to be chosen according to W_{ba}. The energy sharing is then found from the corresponding splitting function. Subsequently, the daughter virtualities are determined with the help of equation (5.14), subject to three constraints: The virtualities Q_b, Q_c of the daughters are required to be smaller than their energy $z\,E$ or $(1-z)E$, respectively, and they must be larger than the cut-off scale $Q_0/2$. In addition, the virtual masses of the daughters satisfy the constraint $Q_b^2 + Q_c^2 < Q_a^2$. If z lies in the kinematically allowed range (equation (5.11) the branching is accepted and the four-momenta are calculated assuming azimuthal symmetry. Otherwise, a new pair of daughter virtualities is generated. It may be very unlikely to find a pair of values that satisfies the kinematical constraints, so that after a certain (large) number of unsuccessful attempts the whole shower is discarded. Partons that do not split above Q_min are declared to be on-shell. The procedure is iterated for the daughters until no virtual partons are left.

Mass-ordered parton showers have to leading order no angular ordering, which has to be built in by hand. With the help of equation (5.9) the condition $\theta_b < \theta_a$ for the opening angles of subsequent branchings translates into

$$\frac{z_b(1-z_b)}{Q_b^2} > \frac{1-z_a}{z_a Q_a^2}\,, \tag{5.16}$$

which can be viewed as an additional constraint on z_b

$$\frac{1}{2}\left(1-\sqrt{1-4Q_b^2\frac{1-z_a}{z_a Q_a^2}}\right) < z_b < \frac{1}{2}\left(1+\sqrt{1-4Q_b^2\frac{1-z_a}{z_a Q_a^2}}\right) \tag{5.17}$$

and Q_b

$$Q_b^2 \le \frac{z_a Q_a^2}{4(1-z_a)}\,. \tag{5.18}$$

The latter can be respected when Q_b is determined and z_b can be chosen such that equation (5.17) is fulfilled. Like this no extra rejection steps are introduced. For the second daughter (particle c) z_a has to be replaced by $1-z_a$ in equations (5.17)–(5.18).

This shower is essentially the 'global' 'constrained' evolution which is one of the alternatives of the Pythia event generator [23].

5.1.2. Hadronisation

If one does not want to rely on Local Parton Hadron Duality to map the partonic distributions onto hadronic ones, the parton shower has to be interfaced with a hadronisation model. The Lund string fragmentation model, although very successful in describing a wealth of data, is not flexible enough to be used for the complex parton states in heavy ion collisions. The reason is that it requires knowledge of the colour flow and is only applicable to parton systems that are globally colour neutral. The colour flow of jets in a nuclear environment is altered due to the interactions with the medium and the question arises how recoiling scattering centres, that are colour connected to the cascade, hadronise. One might also want to apply the hadronisation model only to some energetic part of the shower and assign the soft component to the medium. In any case the cascade is not a well defined colour neutral system. Independent fragmentation would work in this case, but is not used here because of its infra-red sensitivity.

The hadronisation model implemented in Jewel is a variant of the Lund model [70–74] (section 2.2.5) where the information about the colour flow is replaced by the assumption of strong colour correlation of partons close in phase space. It has two variants, one is inspired by jets in e^++e^- collisions and is used for testing the model against e^++e^- data and to check the other version, which is adapted to hadronic collisions.

In the e^++e^- version first the quark (or antiquark) with the highest energy has to be identified. It is the endpoint of the first string, which is then stretched to the parton which is closest in momentum space, subject to the only constraint that quarks cannot be connected to quarks and antiquarks not to antiquarks. If the last connected parton was a gluon the string is continued to the closest neighbour of that gluon until a (anti)quark is connected. If (anti)quarks that are not yet organised in strings are left in the event, the procedure is repeated for the remaining partons. If at the end only gluons are left unconnected, they are built in an existing string, namely next to their nearest neighbour among the already connected gluons. This procedure obviously only works in events that contain an equal number of quarks and antiquarks. Artificial systems of two gluons jets can be hadronised by splitting the most energetic gluon in each jet into a quark-antiquark pair and applying the same procedure. Finally, the strings are hadronised using the Lund string fragmentation routine of Pythia 6.4, which also takes care of the decay of resonances.

The p+p inspired version also starts by finding the most energetic parton, but it accepts also gluons (alternatively, the highest $p_\perp$ may be used in hadron collisions). If this parton is a gluon, it is split into a collinear quark - antiquark pair with the energy sharing given by $\hat{P}_{qg}$. The more energetic of the two is then the endpoint of the first string. In the next step it is connected to the closest parton in momentum space (with the only exception that a quark-antiquark pair from a single gluon splitting is not allowed to recombine into a colour singlet). In contrast to the e^++e^- version only partons in the same hemisphere as the endpoint can be joined in the string, also the termination procedure is slightly different. The string ends when either a matching (anti)quark is connected or there is none left in the same hemisphere. In the latter case an endpoint is generated by adding the required quark or antiquark with momentum in the beam direction to the event. It carries a few GeV momentum in order to avoid strings with low invariant mass which upset the string fragmentation. The whole procedure is repeated until all partons are connected in strings. This approach is inspired by the fragmentation of jets in hadronic collisions where the additional endpoints can be thought of as being part of the proton remnants, to which the jet is connected by colour flow. The hadrons associated with this additional parton endpoint tend to go along the beam direction so that they are well separated from the jet. As long as the jet structure is analysed in a restricted rapidity range of approximately $|\Delta\eta| \leq 1$ around the rapidity of the parent parton, the resulting dependence of the model on this endpoint is negligible. There is the possibility to set a maximum invariant mass of neighboring partons in a string, that could be used to tune the routine to data. However, this possibility is not explored here. This hadronisation mechanism has the advantage of being very flexible, it can be applied also to jets in a nuclear environment since it does not require colour neutral systems.

To account for two-jet events, JEWEL evolves the quark and the antiquark jet separately. The virtuality of the first one is determined according to the probability distribution $\Sigma_a(E^2, Q^2)$ (equation (5.14)). Then, there are different options for the second jets: Its virtuality can be fixed to be the same thus conserving energy and momentum at the hard vertex, or it can be chosen independently according to the same distribution. In this case momentum is not conserved at the hard vertex, since there is no reshuffling of momentum as performed by modern event generators in order to conserve momentum. The differences between the two choices turned out to be negligible for the observables under consideration here, so only results for the second option with two completely independent jets are shown.

Figure 5.2 shows the JEWEL results for e^++e^- - like events with two back-to-back quark jets of the same energy, in this case 100 GeV. The e^++e^- and p+p inspired variants of string fragmentation lead to indistinguishable results for the thrust distributions, jet rates and the intra-jet distribution $dN/d\xi$ ($\xi = \ln(p_{\max}/p)$). The results for independent fragmentation [75–81] (section 2.2.5) were obtained with the PYTHIA 6.4. implementation in the default set-up. They differ clearly from the others in that the jets are significantly softer and the events are less two-jet-like. The latter is seen in the thrust distributions, which favour larger values of $1 - T$, T_{maj} and T_{min} (a perfect pencil-like two-jet event has $1 - T = T_{\mathrm{maj}} = T_{\mathrm{min}} = 0$), and in the jet rates, where all n-jet fractions are shifted to larger values of y_{cut}, i.e. coarser resolutions. While these problems can possibly be cured by a better tuning and matching of the parton shower and the hadronisation, the sensitivity to Q_0 (figure 5.3 right) will always remain. The string fragmentation variants, on the other hand, are practically independent of the exact choice of Q_0 because they preserve the infra-red safety of the Lund string fragmentation model.

Since the results for the e^++e^- and p+p inspired variants are practically identical, the p+p version is the default choice in this study.

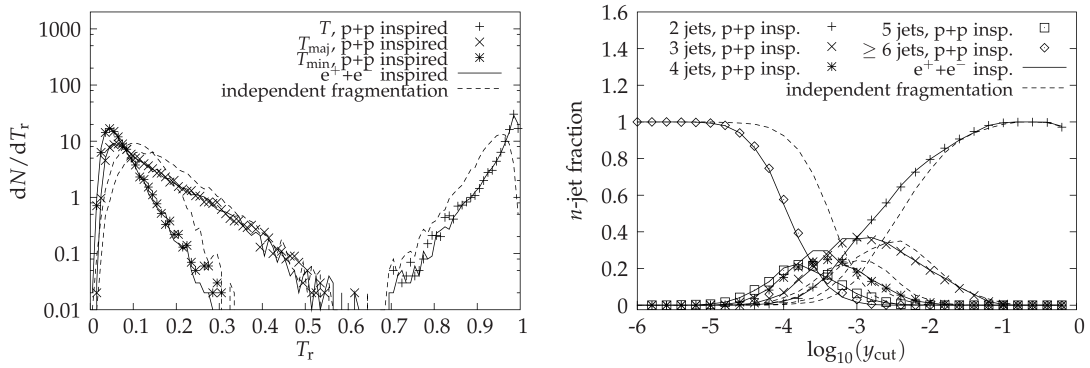

Figure 5.2.: **Left:** Thrust, thrust major and thrust minor distributions ($T_r = (T, T_{\text{maj}}, T_{\text{min}})$) of a system of two back-to-back (anti)quark jets with 100 GeV energy each for three different hadronisation models: the e^++e^- and p+p inspired hadronisation model and independent fragmentation as implemented in Pythia 6.4, all with $Q_0 = 1\,\text{GeV}$. **Right:** Jet rates of the same fragmenting quark-antiquark system for the different hadronisation models ($Q_0 = 1\,\text{GeV}$).

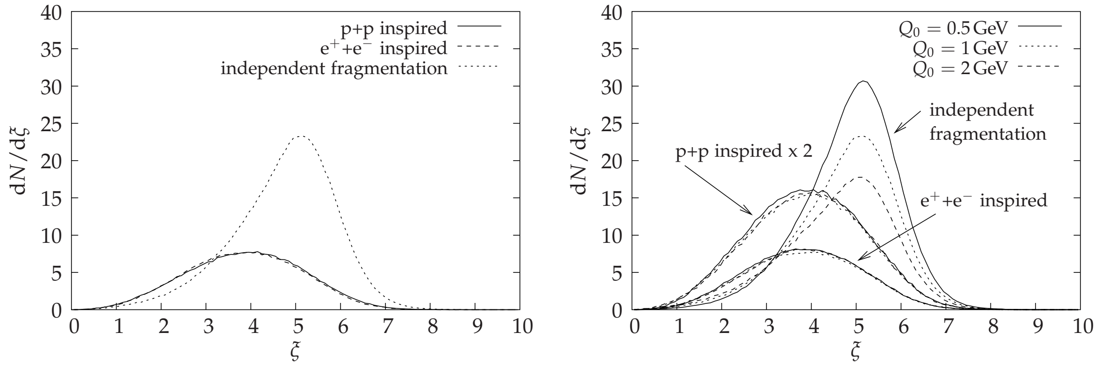

Figure 5.3.: **Left:** The inclusive distribution $\mathrm{d}N/\mathrm{d}\xi$ ($\xi = \ln(p_{\text{max}}/p)$ distribution of a fragmenting back-to-back quark-antiquark system with 100 GeV energy each for the different hadronisation models with $Q_0 = 1\,\text{GeV}$. **Right:** Inclusive distributions $\mathrm{d}N/\mathrm{d}\xi$ for different values of the infra-red cut-off Q_0 on the perturbative evolution.

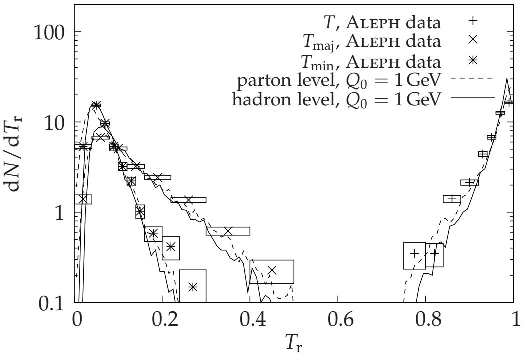

Figure 5.4.: The thrust, thrust major and thrust minor ($T_r = (T, T_{\mathrm{maj}}, T_{\mathrm{min}})$) distributions for $\sqrt{s} = 200\,\mathrm{GeV}$ $e^+ + e^- \rightarrow q + \bar{q} \rightarrow X$ collisions. Data of the ALEPH Collaboration [180] are compared to simulations of JEWEL: i) parton level after parton shower evolved down to $Q_0 = 1\,\mathrm{GeV}$, ii) hadron level after parton shower evolution to $Q_0 = 1\,\mathrm{GeV}$ followed by hadronisation.

However, it should be noted that in the presence of a high-multiplicity environment, novel hadronisation mechanisms may play a role. For instance, hadron formation may occur via recombination of partons [109–113]. Studying the hadrochemistry of jets [35,179] is likely to help characterising such novel hadronisation mechanisms, but an investigation of this is beyond the scope of this study.

5.1.3. Comparison to Data

In this section, the final hadronic states from JEWEL are compared to data on jets measured in $\sqrt{s} = 200\,\mathrm{GeV}$ $\mathrm{e}^+ + \mathrm{e}^-$ collisions at LEP by the ALEPH collaboration [180]. To select the process $e^+ + e^- \rightarrow q + \bar{q} \rightarrow X$ at $\sqrt{s} = 200\,\mathrm{GeV}$, these ALEPH data were taken with a veto on initial state radiation. They have been compared already [180] very favourably to standard event generators such as PYTHIA and HERWIG. The purpose of the present data comparison is to validate the JEWEL parton shower in the absence of medium effects against a set of benchmark data on jets measured at LEP, before studying the extension of the code to medium effects.

In figure 5.4, the thrust distributions, which characterise the overall energy flow (section 2.2.3), from JEWEL are compared to data. Since these are perturbatively calculable, infrared-safe quantities, they are particularly suitable for testing the parton shower implementation. As seen in figure 5.4, the final state parton shower provides a reasonable description of these jet event shapes over most of the measured range.

JEWEL does not contain a matching of the parton cascade to three-jet matrix elements, which could improve the QCD modelling of large angle radiation. This may be the reason why the simulation gives fewer events with large $1 - T$, T_{maj} and T_{min}.

The comparison of other event shape observables like oblateness, sphericity, planarity, aplanarity and total jet broadening to data are of a similar quality as the thrust distributions. Figure 5.5 shows as an example sphericity and aplanarity.

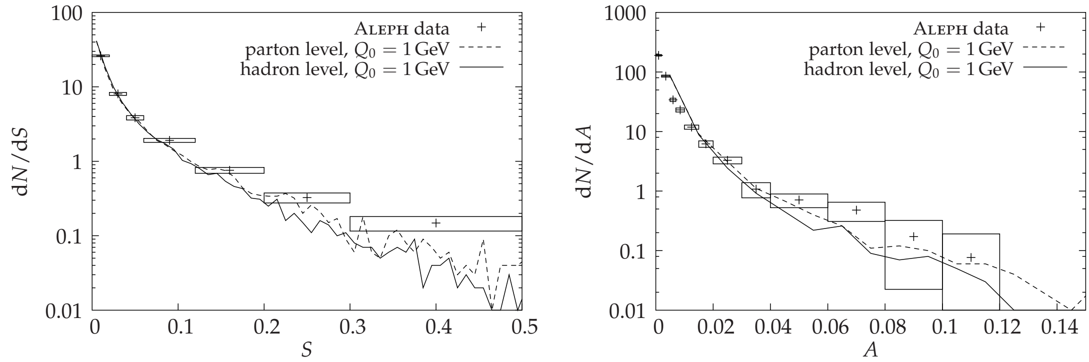

Figure 5.5.: JEWEL results for sphericity and aplanarity for $e^+ + e^- \rightarrow q + \bar{q} \rightarrow X$ at $\sqrt{s} = 200\,\text{GeV}$ on the parton level with perturbative evolution down to $Q_0 = 1\,\text{GeV}$ and on the hadron level compared to ALEPH data [180]

With these studies, it has been shown that JEWEL accounts for global features of jet energy flow with an accuracy which is sufficient to characterise (sufficiently large) medium effects on top of it.

Figure 5.6 shows simulation results for the jet rates (section 2.2.3), which are more sensitive to the discrete and stochastic nature of partonic processes underlying the QCD jet fragmentation. One finds that hadronisation plays a negligible role for the jet rates. They vary mildly with the size of the strong coupling on the partonic as well as on the hadronic level. The choice of $\Lambda_{\text{QCD}} = 300\,\text{MeV}$ in JEWEL leads to a reasonably good description of the data, but the rate of three-jet events is underestimated, possibly also due to the missing matching to three-jet matrix elements.

In contrast to the measurements discussed so far, the modelling of single inclusive

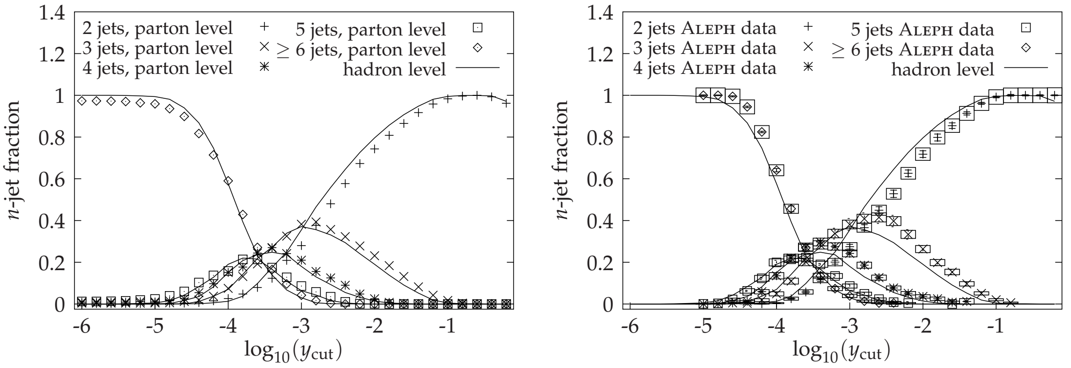

Figure 5.6.: The jet rates as a function of jet resolution scale y_{cut} in $\sqrt{s} = 200\,\text{GeV}$ $e^+ + e^- \rightarrow q + \bar{q} \rightarrow X$ collisions. **Left:** Simulation of JEWEL with and without hadronisation for evolution down to $Q_0 = 1\,\text{GeV}$. **Right:** Data of the ALEPH collaboration [180] compared to simulations of JEWEL with hadronisation.

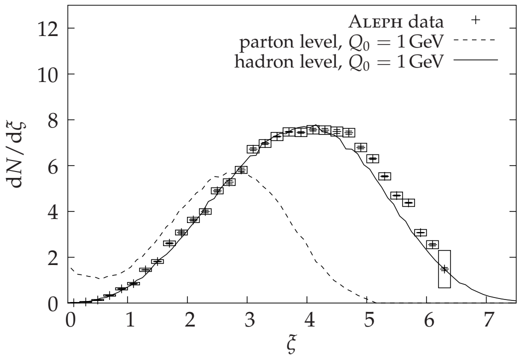

Figure 5.7.: The inclusive distribution $\mathrm{d}N_{\mathrm{ch}}/\mathrm{d}\xi$ ($\xi = \ln(p_{\mathrm{max}}/p_{\mathrm{hadron}})$) of charged hadrons in $e^+ + e^- \to q + \bar{q} \to X$ events at $\sqrt{s} = 200\,\mathrm{GeV}$. Data of the ALEPH Collaboration [180] are compared to simulations of JEWEL: i) parton level after parton shower evolved down to $Q_0 = 1\,\mathrm{GeV}$, ii) hadron level after parton shower evolution to $Q_0 = 1\,\mathrm{GeV}$ followed by hadronisation.

intra-jet hadron distributions and multi-hadron correlations requires detailed knowledge about the hadronisation mechanism. This is seen for instance in figure 5.7, where results of the simulation are compared to data of the inclusive distribution $\mathrm{d}N_{\mathrm{ch}}/\mathrm{d}\xi$ of charged hadrons in $e^+ + e^- \to q + \bar{q} \to X$ events at $\sqrt{s} = 200\,\mathrm{GeV}$. Irrespective of the scale Q_0 down to which the parton cascade is evolved prior to hadronisation, there is a marked difference between the hadronic and the partonic distribution. In particular, the partonic distribution is very 'hard', i.e. the yield of high momentum (small $\xi < 1$) partons exceeds the observed hadronic yield by far. Since high momentum partons are correlated in colour to softer partons, it is likely that any colour neutralisation mechanism, i.e. hadronisation, which takes into account colour flow, will fill the momentum space between these partonic partners. As a consequence, hadronisation is expected to soften the distribution for $\xi < 1$ considerable. This is seen for the string hadronisation mechanism, which accounts for the inclusive hadron distribution $\mathrm{d}N_{\mathrm{ch}}/\mathrm{d}\xi$ to a level better than $\sim 20\%$. An even improved agreement is likely to be achieved by a retuning of the hadronisation parameters in PYTHIA, which can be motivated by the new prescription for stretching the string introduced here.

Within the uncertainties, which are mainly related to the modelling of hadronisation, JEWEL provides a reliable baseline for the characterisation of jet quenching phenomena.

5.2. Medium Modifications of the Parton Shower

So far the parton shower was formulated in momentum space. For the introduction of interactions with a medium the spatiotemporal structure of the cascade has to be specified. Since the four-momenta of all partons in the shower are known, it is sufficient to estimate the lifetimes.

Unfortunately, little is known about the space-time structure of parton shower, which is unobservable in showers that evolve in vacuum. One might therefore even want to turn the usual perspective around and regard the medium as a probe of the spatiotemporal evolution of jets.

In the Jewel parton shower the lifetime of partons in the showers is estimated using a general argument based on the uncertainty principle. A virtual state has a lifetime of order $1/|Q|$ in its own restframe, where Q is the virtuality. In the restframe of the medium this time appears time-dilated and becomes E/Q^2. In the parton shower, however, the virtuality is not reduced in a single process, but via a chain of intermediate states. The lifetime of these states can be expected to be determined by the virtuality change. This means that a parton with virtuality Q_f, that is created from a parton with virtuality Q_i, exists for a time

$$\tau = \frac{E}{Q_\mathrm{f}^2} - \frac{E}{Q_\mathrm{i}^2}\,. \tag{5.19}$$

In the Monte Carlo model this is used as lifetime of virtual states. For the parent parton, which is produced in the hard interaction, the lifetime is $\tau = E/Q_\mathrm{f}^2 - E/Q_\mathrm{hard}^2$. According to equation (5.19) on-shell partons have infinite lifetime, but in practice 'infinity' means in this case 'until hadronisation'.

5.2.1. Interactions With the Medium

The medium is regarded as a collection of scattering centres. The mass and momentum distribution and density have to be specified. In this first study a simple model is used, which treats the medium as an ideal relativistic gas of (anti)quarks and gluons with a thermal mass $m_\mathrm{s} = \mu_\mathrm{D}/\sqrt{2}$, where $\mu_\mathrm{D} \simeq 3T$ is the Debye screening mass. The medium is then characterised by a single parameter, namely the temperature T. The momentum distribution is given by the Fermi-Dirac or Bose-Einstein distribution

$$\frac{\mathrm{d}n}{\mathrm{d}p} \propto \frac{1}{\exp\left(\sqrt{p^2 + m_\mathrm{s}^2}/T\right) \pm 1}\,, \tag{5.20}$$

with the plus for (anti)quarks and the minus for gluons.

In addition, the cross section for the interaction of the jet with the medium has to be given. Here, the leading order t-channel exchange

$$\frac{\mathrm{d}\sigma^\mathrm{elas}}{\mathrm{d}|t|} = \frac{\pi\alpha_\mathrm{s}^2}{s^2} C_\mathrm{R} \frac{s^2 + u^2}{|t|^2} \tag{5.21}$$

is used ($C_\mathrm{R} = 4/9$ for quark-quark, 1 for quark-gluon and $9/4$ for gluon-gluon scattering). Processes with s-channel singularities are neglected because their cross section is small in the relevant kinematic regime and processes singular in u are not considered because they tend to transfer all the energy from the projectile to the target. These processes do not lead to significant energy loss, but simply exchange the role of projectile and scattering centre.

The perturbative scattering cross section diverges for vanishing momentum transfer t and has thus to be regularised. There is no unique recipe how this should be done, the most common choice for scattering from a thermal medium is to use the screening mass as regulator. But even this leaves several possibilities. As in other calculations, this problem cannot be avoided in Jewel, but it offers a possibility to quantify the resulting uncertainties. Therefore, different variants of the regularised cross section can be used, namely case I

$$\sigma_{\mathrm{I}}^{\mathrm{elas}} = \int\limits_{0}^{|t_{\mathrm{max}}|} \mathrm{d}|t| \, \frac{\pi\,\alpha_{\mathrm{s}}^2(|t|+\mu_{\mathrm{D}}^2)}{s^2} C_{\mathrm{R}} \, \frac{s^2+(s-|t|)^2}{\left(|t|+\mu_{\mathrm{D}}^2\right)^2} \,, \tag{5.22}$$

which is the default, case II

$$\sigma_{\mathrm{II}}^{\mathrm{elas}} = \int\limits_{\mu_{\mathrm{D}}^2}^{|t_{\mathrm{max}}|} \mathrm{d}|t| \, \frac{\pi\,\alpha_{\mathrm{s}}^2(|t|)}{s^2} C_{\mathrm{R}} \, \frac{s^2+(s-|t|)^2}{|t|^2} \,, \tag{5.23}$$

and case III, which is a version of case I with fixed coupling $\alpha_{\mathrm{s}} = 0.3$

$$\sigma_{\mathrm{III}}^{\mathrm{elas}} = \int\limits_{0}^{|t_{\mathrm{max}}|} \mathrm{d}|t| \, \frac{\pi\,\alpha_{\mathrm{s}}^2}{s^2} C_{\mathrm{R}} \, \frac{s^2+(s-|t|)^2}{\left(|t|+\mu_{\mathrm{D}}^2\right)^2} \,. \tag{5.24}$$

Cases I and II have a one-loop running α_{s} with a value of Λ_{QCD} (here $\Lambda_{\mathrm{QCD}} = 250\,\mathrm{MeV}$) that can be different from the one used for the splitting processes . For the calculation of the total scattering cross section the scattering centres are assumed to be at rest. Then $s = m_{\mathrm{p}}^2 + m_{\mathrm{s}}^2 + 2m_{\mathrm{s}}E_{\mathrm{p}}$ is a constant and the maximal momentum transfer is given by $|t_{\mathrm{max}}| = 2m_{\mathrm{s}}E_{\mathrm{p}} \simeq 3\sqrt{2}TE_{\mathrm{p}}$, where E_{p} and m_{p} are the incoming projectile's energy and (virtual) mass. The integrated cross sections are

$$\begin{aligned} \sigma_{\mathrm{I}}^{\mathrm{elas}} = {} & \frac{\pi C_{\mathrm{R}}}{s^2}\left(\frac{12\pi}{33-2n_{\mathrm{f}}}\right)^2 \times \\ & \times \left\{ \Lambda_{\mathrm{QCD}}^2 \left[\left(|t|+\mu_{\mathrm{D}}^2\right) \mathrm{Ei}\left[\ln\left(\frac{|t|+\mu_{\mathrm{D}}^2}{\Lambda_{\mathrm{QCD}}^2}\right)\right] \ln\left(\frac{|t|+\mu_{\mathrm{D}}^2}{\Lambda_{\mathrm{QCD}}^2}\right) \Lambda_{\mathrm{QCD}}^2 - 2s^2 - |t|^2 + 2s|t| \right] \right. \\ & \quad \left. - \left(\mu_{\mathrm{D}}^4 + 2s\mu_{\mathrm{D}}^2 + 2s^2\right) \left(|t|+\mu_{\mathrm{D}}^2\right) \mathrm{Ei}\left[-\ln\left(\frac{|t|+\mu_{\mathrm{D}}^2}{\Lambda_{\mathrm{QCD}}^2}\right)\right] \ln\left(\frac{|t|+\mu_{\mathrm{D}}^2}{\Lambda_{\mathrm{QCD}}^2}\right) \right\} \times \\ & \qquad \times \left\{ \Lambda_{\mathrm{QCD}}^2 \left(|t|+\mu_{\mathrm{D}}^2\right) \ln\left(\frac{|t|+\mu_{\mathrm{D}}^2}{\Lambda_{\mathrm{QCD}}^2}\right) \right\}^{-1} \Bigg|_{0}^{|t_{\mathrm{max}}|} \,, \end{aligned} \tag{5.25}$$

$$\sigma_{\mathrm{II}}^{\mathrm{elas}} = \frac{\pi C_{\mathrm{R}}}{s^2}\left(\frac{12\pi}{33-2n_{\mathrm{f}}}\right)^2 \left[-2\mathrm{Ei}\left[-\ln\left(\frac{|t|}{\Lambda_{\mathrm{QCD}}^2}\right)\right]\frac{s^2}{\Lambda_{\mathrm{QCD}}^2} - \frac{2s^2}{|t|\ln\left(\frac{|t|}{\Lambda_{\mathrm{QCD}}^2}\right)}\right.$$
$$\left. + \frac{2s-|t|}{\ln\left(\frac{|t|}{lqcd^2}\right)} + \Lambda_{\mathrm{QCD}}^2\mathrm{Ei}\left[\ln\left(\frac{|t|}{\Lambda_{\mathrm{QCD}}^2}\right)\right]\right]_{\mu_{\mathrm{D}}^2}^{|t_{\max}|} \tag{5.26}$$

and

$$\sigma_{\mathrm{III}}^{\mathrm{elas}} = \frac{\pi C_{\mathrm{R}}\alpha_{\mathrm{s}}^2}{s^2}\left[-\frac{\mu_{\mathrm{D}}^4 + 2s\mu_{\mathrm{D}}^2 + 2s^2}{|t|+\mu_{\mathrm{D}}^2} + |t| - 2(\mu_{\mathrm{D}}^2 + s)\ln(|t|+\mu_{\mathrm{D}}^2)\right]_0^{|t_{\max}|}. \tag{5.27}$$

The exponential integral

$$\mathrm{Ei}(x) = -\int_{-x}^{\infty} \mathrm{d}t\,\frac{e^{-t}}{t} \tag{5.28}$$

has for positive arguments a series expansion

$$\mathrm{Ei}(x) = \gamma + \ln x + \sum_{n=1}^{\infty}\frac{x^n}{n n!} \quad \text{for} \quad x > 0 \tag{5.29}$$

that can be used for numerical evaluation of the function [181].

For the explicit simulation of scattering events the scattering centre is assumed to have an isotropic thermal momentum. The scattering angle is determined by the momentum transfer t, in the centre-of-momentum frame it is given by

$$\cos\theta_{\mathrm{cm}} = \frac{t + 2E_{\mathrm{p}}^2 - 2m_{\mathrm{p}}^2}{2(E_{\mathrm{p}}^2 - m_{\mathrm{p}}^2)}\,. \tag{5.30}$$

The scattering is symmetric in the azimuthal angle.

Medium induced gluon radiation is expected to be the main source of energy loss. In principle, the Monte Carlo formulation allows for the inclusion of the inelastic 2 → 3 scattering process on the same footing as the elastic scattering. While this is desirable because then elastic and inelastic energy loss are treated consistently, the 2 → 3 process introduces additional complications. Therefore, the first version of JEWEL, where manageability is an issue and which is supposed to be as straightforward as possible, does not include an explicit treatment of inelastic collisions. Instead, it has the option to enhance the vacuum splitting function by a factor $(1 + f_{\mathrm{med}})$

$$\hat{P}_{\mathrm{ba}}(z) \to (1 + f_{\mathrm{med}})\hat{P}_{\mathrm{ba}}(z) \tag{5.31}$$

as long as the splitting takes place inside the medium. This prescription has been shown to catch main characteristics of radiative energy loss [34].

Elastic scattering is assumed to leave the projectile virtuality unchanged. The cross section (equation (5.21)) is dominated by small momentum transfers, i.e. small angle scattering, which does not open phase space that could be used to reduce the virtuality. This can be different for the inelastic scattering, where an additional gluon is radiated. In the current framework without explicit $2 \to 3$ scattering the virtuality degradation is governed by parton branching and is affected by a non-zero f_{med}, but not by elastic scattering. The timescales are set by the splitting processes, which produce two partons with known four-momenta and thus lifetime. With the probability

$$P_{\text{no scatt}}(\tau) = \exp\left(- \int\limits_{t_{\mathrm{p}}}^{t_{\mathrm{p}}+\tau} \mathrm{d}t'\, \sigma^{\mathrm{elas}}(\vec{r}(t'),t')n(\vec{r}(t'),t') \right) , \tag{5.32}$$

where τ_{p} is the parton's production time, the parton will not experience elastic scattering during its lifetime and the next process will be the next splitting. In the general case of an evolving medium both the cross section and the density depend on position and time. The information about the parton trajectory is encoded in $\vec{r}(t')$, which is the parton's position at time t'.

$$\vec{r}(t) = t\beta \frac{\vec{p}}{|\vec{p}|} + \vec{r}_{\mathrm{p}} \,, \tag{5.33}$$

where $\vec{r}_{\mathrm{p}}$ is the production point of the parton.

The cross section can depend on the temperature through the infra-red regulator, s and m_{s} (which also determines the integration limit) and/or a temperature dependent coupling. In the simpler case of a static and homogeneous medium equation (5.32) simplifies to

$$P_{\text{no scatt}}(\tau) = e^{-\sigma^{\mathrm{elas}} n \tau \beta} \,. \tag{5.34}$$

With the probability $1 - P_{\text{no scatt}}(\tau)$ the parton undergoes elastic scattering at a time $\tau_{\mathrm{s}} < \tau$. In the Monte Carlo implementation the decision, whether the next process is scattering or splitting, is made after each splitting according to $P_{\text{no scatt}}$. If the parton scatters, the time τ_{s} of the scattering is determined according to

$$p_{\mathrm{s}}(\tau_{\mathrm{s}}) = \sigma^{\mathrm{elas}} n \beta e^{-\sigma^{\mathrm{elas}} n \tau_{\mathrm{s}} \beta} \,. \tag{5.35}$$

Then, a scattering centre is generated with the type (quark or gluon) given by the relative densities and a momentum from the thermal distribution (equation (5.20)) and the scattering is simulated with the momentum transfer given by the differential cross section. The procedure is repeated for the remaining time $\tau - \tau_{\mathrm{s}}$ until the parton lifetime is used up and the next splitting occurs.

Angular ordering is required for subsequent splittings, but is reset when a scattering occurs. Unfortunately, this prescription is not sufficient to specify in detail how angular ordering in a medium is to be treated. The problem is that angular ordering is only an effective way of including an interference phenomenon in a probabilistically iterated parton shower. Another problem is that rejection steps are dangerous because they tend to bias the interactions with the medium. Therefore, the solution chosen in Jewel is to always respect the constraint on the mass (equation (5.18)) but only keep the condition on z (equation (5.17)) when the previous process was a splitting. This procedure generates only splittings that can in principle obey angular ordering when the daughters branch. The decision whether angular ordering has to be fulfilled is made at the time of the daughters' splitting depending on whether the parton has scattered or not. There are thus no rejection steps and full angular ordering in vacuum is naturally restored in the limit of vanishing density.

Of course, scatterings can only take place inside the medium. On-shell partons, that are produced inside the medium, can undergo scattering until they leave the medium. Concerning the fate of the recoiling scattering centres, JEWEL provides two options: The recoiling scattering centres can in turn experience multiple scattering or propagate without interactions. The latter may not be a realistic scenario, but the application of perturbation theory as description of the relatively soft recoils is questionable and this option is very useful for disentangling different effects. For the leading particles of the jet the treatment of the recoil should not be very important.

It is assumed that hadrons cannot form inside the medium so that hadronisation happens after all medium interactions and is not affected by the presence of the medium. The jet is evolved perturbatively down to a scale $Q_0 \simeq 1\,\text{GeV}$ and hadronised using the p+p inspired fragmentation model. After interactions with the medium, however, the parton shower is not a well defined system any more, since partons are colour connected to medium partons, scattering centres can be scattered with considerable energy into the solid angle occupied by the cascade and the shower has a soft component with momenta of the order of the thermal momenta. In the Monte Carlo implementation one can distinguish between partons that were produced in the parton shower and recoiling scattering centres, which is artificial but useful. JEWEL has, in its present form, two options, namely to hadronise only the parton shower or to count the hit scattering centres towards the jet and hadronise them together with the parton shower. It is also conceivable to hadronise the hard component of the parton shower and the recoils using the string fragmentation and invoke some other mechanism for the soft component, but this possibility has not been explored so far.

The way in which medium effects are included in the jet evolution inevitably involves model-dependent assumptions. The major sources of uncertainties will be briefly discussed.

It is difficult to get a handle on the space-time structure of the shower. Even if the lifetime is parametrically of the form of equation (5.19) the details may be designed in a different way. One could, for instance, use an exponential decay law with half life given by equation (5.19) instead of a fixed lifetime. In this case the scattering events may be regarded as measurements that can stabilise the state and delay its decay.

The choice of the scattering cross section also introduces uncertainties. The ambiguity due to different regularisations has already been mentioned. The choice of the regulator poses an additional problem. Using the screening mass is problematic, since the interaction of a hard parton with a thermal parton from the medium is not of thermal nature it is not clear why the propagator should acquire a thermal mass. Furthermore, it is questionable whether the elastic scattering is adequately described

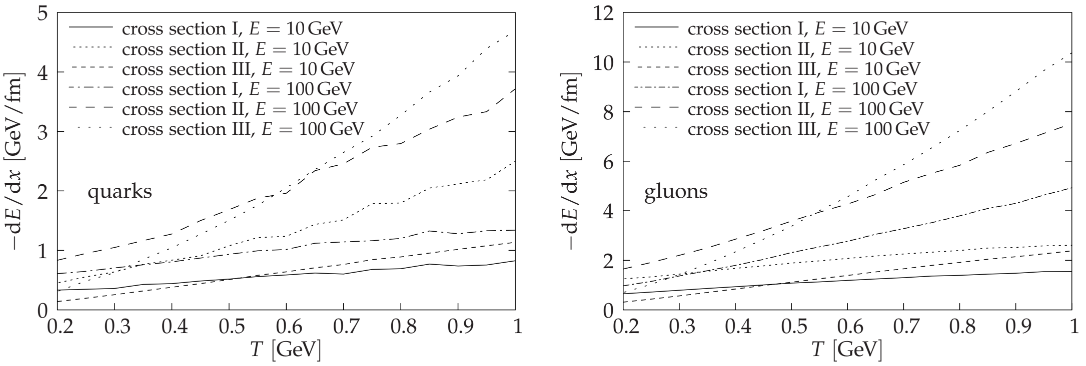

Figure 5.8.: Average energy loss of an on-shell quark (left) or gluon (right) with energy E experiencing multiple elastic scattering in a static medium of temperature T over a pathlength $L = 1\,\text{fm}$ for three different regularisations of the elastic scattering cross section (equations (5.22)–(5.24)).

by leading order perturbation theory. Not all involved momenta are large and there is evidence from Rhic data for strong coupling.

Enhancing the splitting function by a factor $1 + f_{\text{med}}$ does not do justice to medium induced radiation. It may be sufficient to study generic features of radiative energy loss, but it is desirable to include the full inelastic scattering process in a later version.

Little is known about hadronisation mechanisms and possible medium modifications in heavy ion collisions. The assumption of unmodified hadronisation may be not well justified. The observation of changes in the hadrochemistry seems to hint at a modification of the hadronisation. However, hadronisation in a nuclear environment is to a large extent an unsolved problem.

Jewel alone is currently not in the position to resolve any of these issues. It provides, however, a tool for their systematic study. As a first step it may help to quantify uncertainties and identify observables that are insensitive to details of the modelling.

5.2.2. Energy Loss Without Branching

The energy loss of an energetic on-shell parton in a medium is an extensively studied problem [1–9] and offers a possibility to compare the elastic energy loss in Jewel to other calculations. For this purpose the splitting is switched off and an on-shell parton of a given starting energy is propagated through a homogeneous medium with temperature T over a distance L. The scattering probability is then determined by the temperature, the path length and the cross section. Figure 5.8 shows the mean energy loss over a distance L as a function of the temperature for the different regularisations of the elastic scattering cross section (equations (5.22)–(5.24)). In all three cases the energy loss increases with temperature and projectile energy. The magnitude differs by up to a factor of 2 between the different cross sections. As expected, case I leads to the smallest energy loss; case II has a minimum momentum transfer and in case III there is no suppression of large momentum transfers due

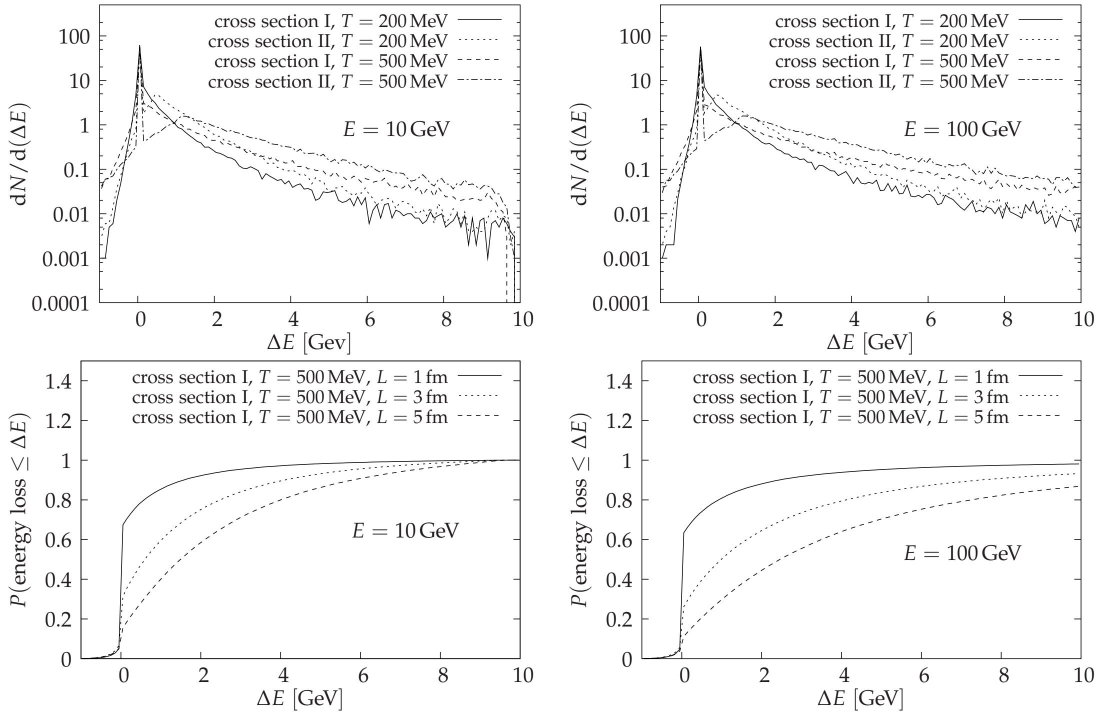

Figure 5.9.: Distribution of energy loss ΔE after a pathlength $L = 1\,\text{fm}$ in the medium for different parameter choices (top panels) and the probability for an energy loss smaller than ΔE after passage through a medium of length L (bottom panels).

to the running of the coupling. The energy loss of gluons is roughly twice that of quarks due to the larger colour factor. The temperature dependence is consistent with what was found in other calculations. On a quantitative level the three variants lie in the range of other results [1–9] (section 3.3.1), the factor 2 difference is of the same order as the differences between different computations.

For the suppression of steeply falling single-inclusive spectra the relevant quantity is not the mean but the most likely energy loss. Figure 5.9 shows the distribution of the energy loss ΔE for quarks, which is strongly peaked at 0. This is due to the relatively long mean free path, which is $\mathcal{O}(1\,\text{fm})$, and the fact that elastic scattering is dominated by small angle scattering, where the longitudinal momentum transfer vanishes in the high energy limit. ΔE can also be negative, because there is a small probability that a fast parton gains energy from the medium. The chances for losing or gaining a significant fraction of the projectile energy increase with temperature. There are marked differences between the regularisations I and II not only in the normalisation, but also in the shape of the distribution. Case II, where the integral is cut off at finite $|t|$, develops a characteristic double peak structure due to the minimal momentum transfer, which is also a regularisation of small angle scattering. The position of the secondary peak depends on temperature, because the Debye mass, which is used as infra-red regulator, does.

The scattering cross section (equation (5.21)) is at high energies only weakly s-dependent. This is also reflected in the ΔE distributions (figure 5.9 top), which are remarkably similar for 10 and 100 GeV quark energy. The mean energy loss can still be larger for higher energies, because the integral

$$\langle \Delta E \rangle = \frac{\int_0^E \mathrm{d}(\Delta E)\, \Delta E\, \frac{\mathrm{d}N}{\mathrm{d}\Delta E}}{\int_0^E \mathrm{d}(\Delta E)\, \frac{\mathrm{d}N}{\mathrm{d}\Delta E}} \tag{5.36}$$

extends to much higher energies. Contributions at large ΔE have a very small probability but a large weight. This illustrates again, that the mean energy loss is dominated by rare events with very large energy loss [26].

The probability for losing an amount of energy less than some ΔE can by computed from $\mathrm{d}N/\mathrm{d}(\Delta E')$ through integration up to ΔE and proper normalisation. As can be seen from the lower panels of figure 5.9 the probability for no energy loss at all after passage through 1 fm of a medium with a rather high temperature of 500 MeV is about 65 % for both projectile energies. After a path length of 3 fm still roughly 25 % of the quarks emerge without energy loss. It seems thus unlikely that collisional energy loss alone can account for a strong suppression of singe-inclusive hadron spectra.

5.2.3. Characterising the Recoiling Medium

The energy lost by a jet due to (elastic or inelastic) scattering from the medium is carried by the recoiling scattering centres. Characterising the recoil can help to disentangle elastic and inelastic energy loss and to understand the jet-induced modifications of the background. For the reconstruction of jets in nuclear collisions the background has to be carefully subtracted, therefore the modifications of the background may be important. Furthermore, scattering centres, that are scattered into the jet cone, will be identified as belonging to the jet.

In figure 5.10 the momentum distribution of recoiling scattering centres is compared to the undisturbed distribution. The upper panels show the results for an on-shell quark with 100 GeV energy that propagates through the medium without splitting, in the lower panels the splitting is included. The results are very similar indicating that the recoil is not very sensitive to the projectile energy. In the left panels $p_\perp$ is the transverse momentum relative to the beam axis, the jet is at midrapidity ($\eta = 0$). The undisturbed medium distribution shows the exponentially falling $p_\perp$-spectrum and isotropic momentum distribution expected for a thermal medium. The $p_\perp$-distribution of recoils, on the other hand, acquires a power-law tail at intermediate and large momenta due to the shape of the scattering cross section. The yield is, however, still mainly in the low $p_\perp$ region ($p_\perp \lesssim 2\,\mathrm{GeV}$). The recoiling scatterings centres move predominantly in the direction of the jet with a characteristic maximum at $\Delta\phi \simeq 0.8$ nearly independent of the temperature.

For the understanding of the recoil distributions it is instructive to study a simplified analytical model. It is assumed that an energetic projectile hits a parton with a thermal distribution. The elastic cross section is approximated by $\mathrm{d}\sigma/\mathrm{d}|t| \propto$

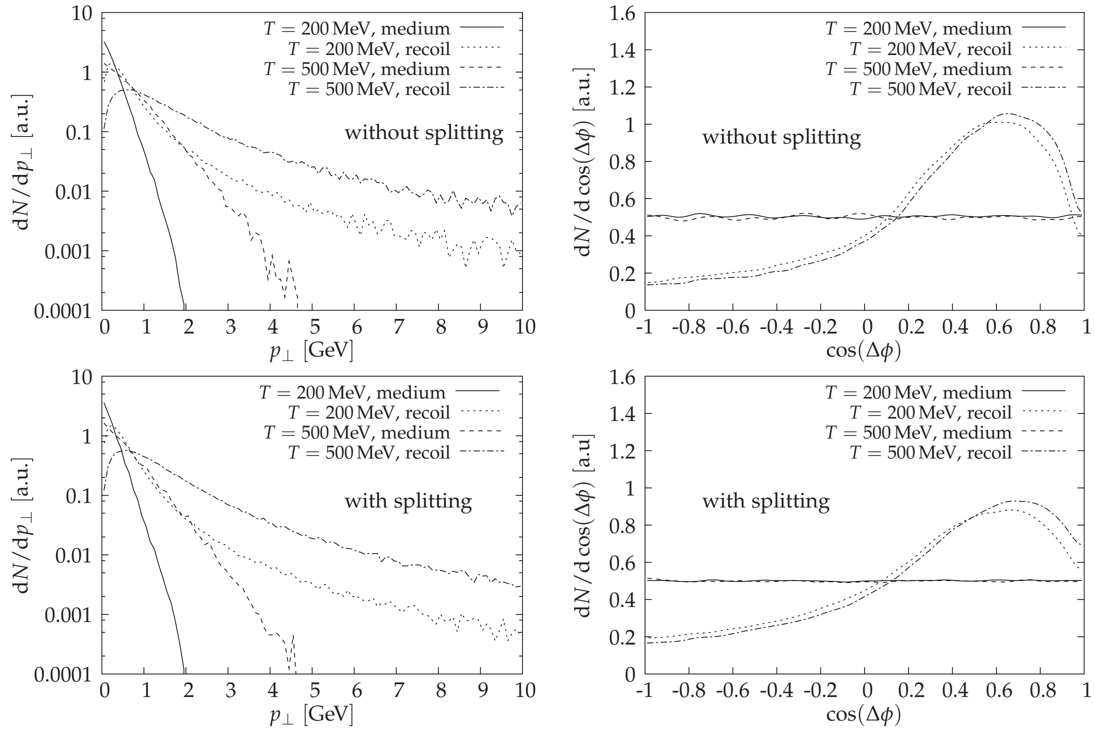

Figure 5.10.: Transverse momentum relative to beam axis and angle with respect to jet axis of recoiling scattering centres as compared to the undisturbed medium for different temperatures, with and without splitting of the projectile (cross section I, $E_{\text{jet}} = 100\,\text{GeV}$, $L = 1\,\text{fm}$). The jet is at mid-rapidity ($\eta = 0$). Hadronisation is not included but may affect these distributions significantly (see text for further discussion).

$(|t| + \mu_D^2)^{-2}$. In the rest frame of the medium the momentum transfer is related to the energy of the struck scattering centre via

$$t = 2(m_s^2 - E_{\text{in}} E_{\text{out}}) \tag{5.37}$$

where E_{in} and E_{out} are the energies of the incoming and outgoing scattering centre, respectively, and the average over the direction of the incoming scattering centre was taken. The energy distribution becomes

$$\frac{1}{\sigma}\frac{d\sigma}{dE_{\text{out}}} = \frac{1}{\sigma}\frac{2E_{\text{in}}}{(2(E_{\text{in}}E_{\text{out}} - m_s^2) + 2m_s^2)^2} = \frac{1}{\sigma}\frac{1}{2E_{\text{in}}E_{\text{out}}^2}\,, \tag{5.38}$$

where $\mu_D = \sqrt{2}m_s$ (as in the simulation) was used.

The energy and scattering angle of the recoiling scattering centres are strongly correlated. The most energetic recoils are closest to the jet axis. In the toymodel the scattering angle is – again after averaging over the incoming scattering centre's

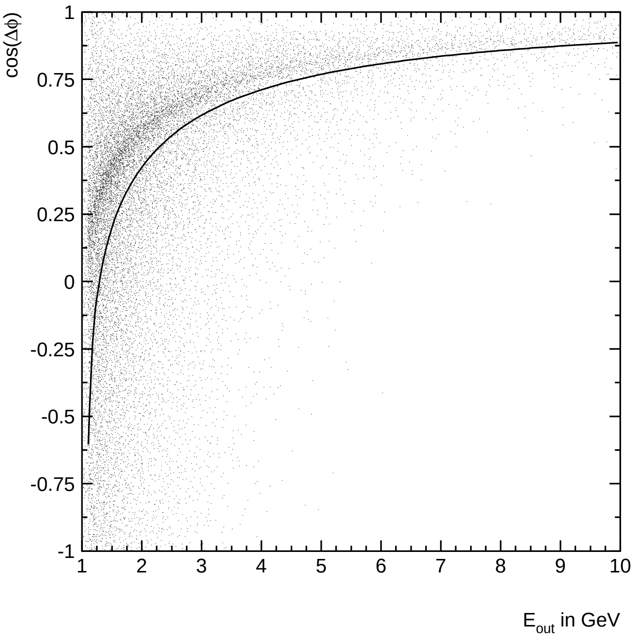

Figure 5.11.: Correlation of angle and momentum of recoiling scattering centres in the Monte Carlo simulation ($T = 500\,\mathrm{MeV}$, without splitting, $L = 1\,\mathrm{fm}$, $E = 100\,\mathrm{GeV}$) and analytical estimate (equation (5.39) for mean E_{in}).

direction – given by

$$\cos(\Delta\phi) = \frac{E_{\mathrm{out}}(E_{\mathrm{p}} + E_{\mathrm{in}}) - E_{\mathrm{p}}E_{\mathrm{in}} - E_{\mathrm{in}}^2}{p_{\mathrm{p}}\sqrt{E_{\mathrm{out}} - m_{\mathrm{s}}^2}}\,, \tag{5.39}$$

where the subscript p stands for the projectile. This result is compared to the simulation in figure 5.11, where for E_{in} the mean thermal energy was used. The model result gets the main features right, although there are deviations on a quantitative level. The spread of the Monte Carlo result is due to the energy and angular distribution of the scattering centres.

For the angular distribution the problem has to be further simplified, the scattering centre is now assumed to be at rest. This leads to

$$|t| = 2m_{\mathrm{s}}(E_{\mathrm{out}} - m_{\mathrm{s}}) \tag{5.40}$$

$$\cos(\Delta\phi) = \sqrt{\frac{E_{\mathrm{out}} - m_{\mathrm{s}}}{E_{\mathrm{out}} + m_{\mathrm{s}}}}\frac{E_{\mathrm{p}} + m_{\mathrm{s}}}{p_{\mathrm{p}}} = \sqrt{\frac{|t|}{|t| + 4m_{\mathrm{s}}}}\frac{E_{\mathrm{p}} + m_{\mathrm{s}}}{p_{\mathrm{p}}}\,. \tag{5.41}$$

When the scattering centre is at rest, $\cos(\Delta\phi)$ has to be positive. The scattering angle is shown in figure 5.12 as a function of the momentum transfer. The angular

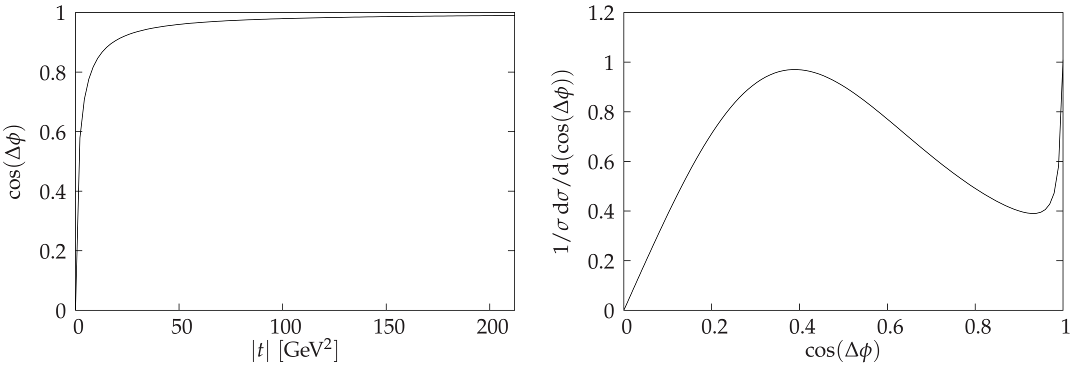

Figure 5.12.: **Left:** Scattering angle as function of the momentum transfer $|t|$ (equation (5.41)) for a 100 GeV projectile hitting a scattering centre with a mass corresponding to a temperature of 500 MeV, $\Delta\phi$ is the angle of the recoiling scattering centre relative to the incoming projectile. **Right:** Angular distribution (equation (5.42) for $\mu_\mathrm{D} = \sqrt{2}m_\mathrm{s}$) for the same parameters, the cross section is approximated as $\mathrm{d}\sigma/\mathrm{d}|t| \propto (|t| + \mu_\mathrm{D}^2)^{-2}$ with $\mu_\mathrm{D} = \sqrt{2}m_\mathrm{s}$.

distribution becomes

$$
\begin{aligned}
\frac{1}{\sigma}\frac{\mathrm{d}\sigma}{\mathrm{d}\cos(\Delta\phi)} =& \frac{1}{\sigma}\frac{\mathrm{d}|t|}{\mathrm{d}\cos(\Delta\phi)}\frac{\mathrm{d}\sigma}{\mathrm{d}|t|} \\
=& \frac{\mu_\mathrm{D}^2(2m_\mathrm{s}E_\mathrm{p} + \mu_\mathrm{D}^2)}{2m_\mathrm{s}E_\mathrm{p}} \frac{4m_\mathrm{s}^2 p_\mathrm{p}^2 2\cos(\Delta\phi)}{(E_\mathrm{p} + m_\mathrm{s})^2 - p_\mathrm{p}^2\cos^2(\Delta\phi)} \\
& \times \left(1 + \frac{p_\mathrm{p}^2\cos^2(\Delta\phi)}{(E_\mathrm{p} + m_\mathrm{s})^2 - p_\mathrm{p}^2\cos^2(\Delta\phi)}\right) \\
& \times \frac{(E_\mathrm{p} + m_\mathrm{s})^2 - p_\mathrm{p}^2\cos(\Delta\phi)}{(4m_\mathrm{s}^2 p_\mathrm{p}^2\cos^2(\Delta\phi) + \mu_\mathrm{D}^2((E_\mathrm{p} + m_\mathrm{s})^2 - p_\mathrm{p}^2\cos(\Delta\phi)))^2}
\end{aligned}
\tag{5.42}
$$

This distribution is qualitatively similar to the simulation result (figure 5.12 right), but the details are different. Equation (5.42) and the Monte Carlo result have, however, one important feature in common: Both are not very sensitive to the temperature. In order to specify this observation one has to find the position of the maximum of the angular distribution. Unfortunately, this leads only to implicit solutions. But – given the shape of the distribution – the position of the maximum can be approximated by the expectation value. This leads to

$$\begin{aligned}\langle\cos(\Delta\phi)\rangle =& \frac{1}{\sigma}\int_0^{2m_\mathrm{s}E_\mathrm{p}} \mathrm{d}|t|\,\cos(\Delta\phi)(|t|)\frac{\mathrm{d}\sigma}{\mathrm{d}|t|}\\ =&\frac{\mu_\mathrm{D}^2(2m_\mathrm{s}E_\mathrm{p}+\mu_\mathrm{D}^2)(E_\mathrm{p}+m_\mathrm{s})}{2m_\mathrm{s}p_\mathrm{p}E_\mathrm{p}}\\ &\times\left[\frac{4m_\mathrm{s}^2}{\mu_\mathrm{D}(4m_\mathrm{s}^2-\mu_\mathrm{D}^2)^{3/2}}\tan^{-1}\left(\frac{\sqrt{4m_\mathrm{s}^2-\mu_\mathrm{D}^2}\sqrt{2m_\mathrm{s}E_\mathrm{p}}}{\mu_\mathrm{D}\sqrt{4m_\mathrm{s}^2+2m_\mathrm{s}E_\mathrm{p}}}\right)\right.\\ &\left.-\frac{\sqrt{2m_\mathrm{s}E_\mathrm{p}}\sqrt{4m_\mathrm{s}^2+2m_\mathrm{s}E_\mathrm{p}}}{(4m_\mathrm{s}^2-\mu_\mathrm{D}^2)(2m_\mathrm{s}E_\mathrm{p}+\mu_\mathrm{D}^2)}\right]\end{aligned} \tag{5.43}$$

For $\mu_\mathrm{D}=\sqrt{2}m_\mathrm{s}$ and $p_\mathrm{p}=E_\mathrm{p}$ this simplifies to

$$\langle\cos(\Delta\phi)\rangle = \frac{E_\mathrm{p}+m_\mathrm{s}}{E_\mathrm{p}^2}\left[2(E_\mathrm{p}+m_\mathrm{s})\tan^{-1}\left(\sqrt{\frac{E_\mathrm{p}}{2m_\mathrm{s}+E_\mathrm{p}}}\right)-\sqrt{E_\mathrm{p}}\sqrt{2m_\mathrm{s}+E_\mathrm{p}}\right] \tag{5.44}$$

Typically, the temperature is small compared to the projectile energy so that one can expand equation (5.44) for small $m_\mathrm{s}=3T/\sqrt{2}$

$$\langle\cos(\Delta\phi)\rangle \simeq \left(\frac{\pi}{2}-1\right)+\frac{m_\mathrm{s}}{E_\mathrm{p}}(\pi-1)=\left(\frac{\pi}{2}-1\right)+\frac{3T}{\sqrt{2}E_\mathrm{p}}(\pi-1)\,, \tag{5.45}$$

which illustrates the weak temperature dependence. The peak position is, however, sensitive to the infra-red regulator. This can be seen by keeping μ_D and m_s as independent quantities and expanding equation (5.44) in μ_D around $\mu_\mathrm{D}=\sqrt{2}m_\mathrm{s}$. The shift of the maximum is then found to be

$$\begin{aligned}\Delta\langle\cos(\Delta\phi)\rangle =&\langle\cos(\Delta\phi)\rangle(\mu_\mathrm{D})-\langle\cos(\Delta\phi)\rangle(\sqrt{2}m_\mathrm{s})\\ \simeq&\frac{2\sqrt{2}}{m_\mathrm{s}}\frac{E_\mathrm{p}+m_\mathrm{s}}{p_\mathrm{p}E_\mathrm{p}}\left[\big(2(E_\mathrm{p}+m_\mathrm{s})+m_\mathrm{s}\big)\tan^{-1}\left(\sqrt{\frac{E_\mathrm{p}}{2m_\mathrm{s}+E_\mathrm{p}}}\right)\right.\\ &\left.-\frac{3}{2}\sqrt{E_\mathrm{p}}\sqrt{2m_\mathrm{s}+E_\mathrm{p}}\right](\mu_\mathrm{D}-\sqrt{2}m_\mathrm{s})\\ \simeq&2(\pi-3)\frac{\mu_\mathrm{D}-\sqrt{2}m_\mathrm{s}}{\sqrt{2}m_\mathrm{s}}\,,\end{aligned} \tag{5.46}$$

where m_s was again assumed to be small compared to the projectile energy.

At face value figures 5.10–5.11 indicate that an energetic jet is accompanied by additional particles with a characteristic angle. Recoils with high energy are close to the jet axis, but typical momentum transfers tend to scatter the recoil to a relatively large angle. The question, whether these structures are also visible on the hadron level, depends on the hadronisation model. Models that assume each parton to hadronise

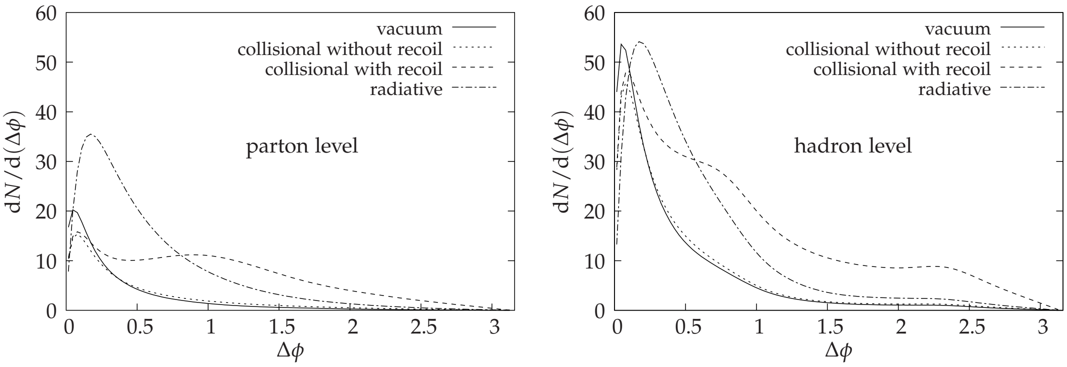

Figure 5.13.: Angle relative to the jet axis of particles in a 100 GeV quark jet (splitting is active) without hadronisation at $Q_0 = 1\,\mathrm{GeV}$ (left) and with hadronisation at $Q_0 = 1\,\mathrm{GeV}$ (right). The different energy loss models are collisional energy loss, where the recoils are either removed from the event or counted towards the jet, and the simplified version of radiative energy loss ($T = 500\,\mathrm{MeV}$, $L = 5\,\mathrm{fm}$, $f_{\mathrm{med}} = 3$).

independently are likely to preserve the angular structure seen in figure 5.10, while string fragmentation models smear the peak out if they connect the recoiling scattering centres to partons in the parton shower. This is seen in figure 5.13, which shows the angular distribution of particles in the jet before and after hadronisation. In the former case the recoiling scattering centres lead to a second maximum in the angular distribution. In the case of string fragmentation they are still visible as a shoulder at $\Delta\phi \simeq 0.8$ and an increase out to the largest $\Delta\phi$. This is partly due to string configurations where a recoil is connected to a 'remnant endpoint' at large rapidity. Details of this distribution should not be taken too seriously since they may be affected by the $|\eta| < 1$ requirement for hadrons. These two examples highlight conceptual difficulties of hadronisation in a nuclear environment. It is unclear what the colour topology is and if it is relevant, because it is uncertain whether the colour connections established in interactions with the medium survive or are destroyed or randomised due to multiple gluon exchanges. These questions are beyond the scope of this study.

5.2.4. Single-Inclusive Spectra

A different way of characterising the total energy loss is in terms of the nuclear modification factor, which describes the suppression of single-inclusive hadron spectra at high transverse momentum (section 3.2). It thus shows the effect of energy loss on the $p_\perp$-spectrum. Jewel does not simulate the hard matrix element, which produces the jets. But one can make use of the fact, that the $p_\perp$-spectrum has an approximate power-law behaviour

$$\frac{\mathrm{d}\sigma}{\mathrm{d}p_\perp} \propto p_\perp^{-n} \,. \tag{5.47}$$

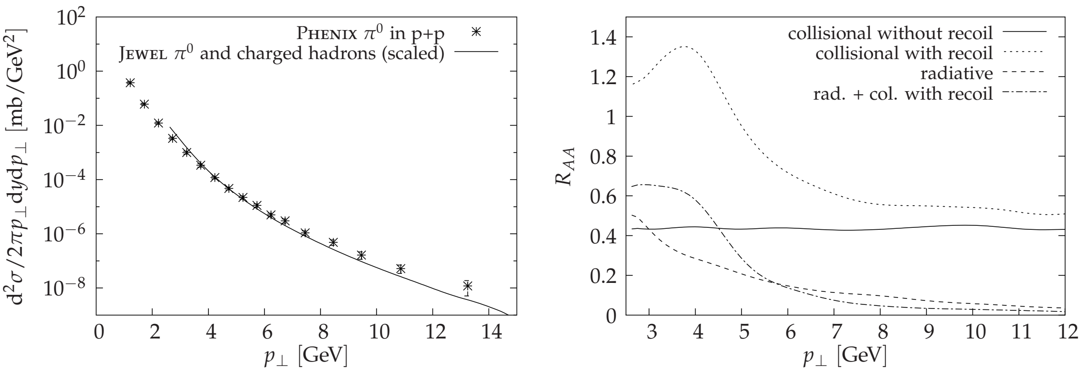

Figure 5.14.: **Left:** JEWEL $p_\perp$-spectrum of π^0 and charged hadrons in vacuum (jets at $\eta = 0$) compared to PHENIX p+p data at $\sqrt{s} = 200\,\text{GeV}$. The simulation result is scaled since JEWEL includes no hard scattering cross section and can thus not provide the normalisation of the spectrum. **Right:** Nuclear modification factor (hadron level) for different energy loss scenarios in JEWEL ($L = 5\,\text{fm}$, $T = 500\,\text{MeV}$, $f_\text{med} = 3$).

Strictly speaking, n is slightly $p_\perp$-dependent. In the simulation the parent partons are distributed according to equation (5.47). n is taken to be independent of $p_\perp$, the results shown here were obtained with $n = 7$. All jets are at midrapidity so that $p_\perp = E$ for the (massless) parent partons of the jets, the virtuality comes at the expense of the momentum. Figure 5.14 (left) shows the resulting $p_\perp$-spectrum of neutral pions and charged hadrons in vacuum. It is in reasonably good agreement with the π^0 spectrum measured by PHENIX in p+p collisions, although it it slightly steeper.

The right hand side of figure 5.14 shows the nuclear modification factor for different energy loss scenarios. The medium has a constant temperature of $T = 500\,\text{MeV}$ and the path length is $L = 5\,\text{fm}$, which possibly overestimates the collisional energy loss. Accordingly, the factor f_med, which controls the medium induced radiation, is chosen to be relatively large ($f_\text{med} = 3$). The medium effects may be somewhat unrealistic, but for the investigation of general features of partonic energy loss it is convenient to have sizeable effects. With the parameters chosen here the hadron suppression is of the same order as observed at RHIC.

Collisional energy loss alone leads to a significant suppression of about a factor 2 at high transverse momenta ($p_\perp \gtrsim 7\,\text{GeV}$), it is somewhat less if the recoiling scattering centres are hadronised together with the parton shower. The purely radiative scenario leads to a stronger suppression of roughly a factor 6 at high $p_\perp$, which is decreasing with $p_\perp$. In this case the suppression on the parton level is practically the same over the whole $p_\perp$ range shown here. Adding the collisional energy loss increases the nuclear modification factor at intermediate $p_\perp$ showing the same characteristic enhancement as the purely collisional model. At high $p_\perp$, on the other hand, the suppression is stronger than for radiative energy loss alone. Qualitatively, the result for collisional and radiative energy loss looks like the incoherent sum of

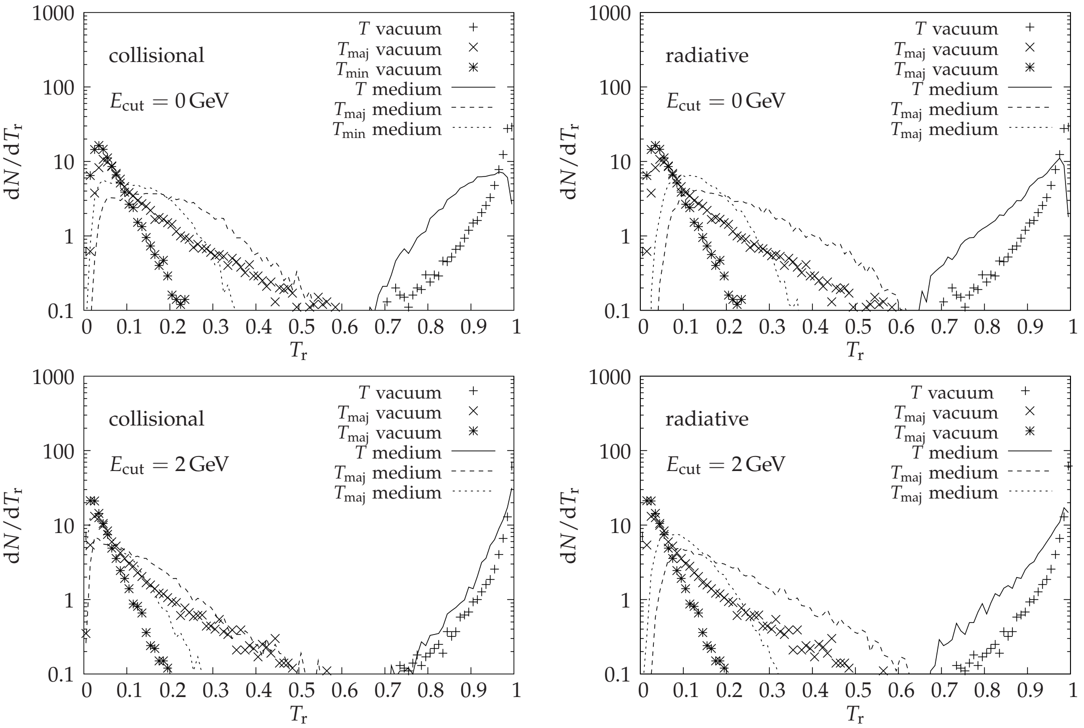

Figure 5.15.: Thrust, thrust major and thrust minor ($T_{\text{r}} = (T, T_{\text{maj}}, T_{\text{min}})$) for a single 100 GeV jet. The JEWEL parton shower in vacuum is compared to two scenarios including medium-induced parton energy loss. **Left:** Collisional energy loss for a medium of $T = 500\,\text{MeV}$ and in-medium path length $L = 5\,\text{fm}$ (the recoil is hadronised with the medium). **Right :** Radiative energy loss for $f_{\text{med}} = 3$ and $L = 5\,\text{fm}$. For the plots in the lower panel, only hadrons with energy above $E_{\text{cut}} = 2\,\text{GeV}$ are included.

both effects. With the simplified description of radiative energy loss one cannot make statements about the relative strength of the elastic and the inelastic contribution. For this one needs a microscopic description of the $2 \rightarrow 3$ process, which depends on the medium properties.

5.2.5. Medium Modifications of Jet Observables

In this section medium induced modifications of event shapes, jet rates and the ξ-distribution will be investigated. The medium parameters are the same as in the previous section, the jets are quark jets with 100 GeV energy. Unlike in the vacuum calculations of e^+e^- events there is now only one jet per event (also in the vacuum reference calculation). The jets have a significant soft component and also the recoiling scattering centres have relatively low energies, which cannot be identified in the large background of a nuclear collision. Studying modified jets in a background free environment is useful for the understanding of the mechanisms but is academic in the sense that the low energy part of the jets is experimentally not accessible. The event shapes and jet rates are thus calculated for the whole jet as well as for the energetic component only, where all hadrons with energy lower than a cut-off (here $E_{\mathrm{cut}} = 2\,\mathrm{GeV}$) are not included.

Thrust, thrust major and thrust minor can be calculated also for a single jet or only the hard component of a jet. They are then not infra-red safe any more, but they still characterise the momentum flow in the jet. A broadening of the jet, which is expected to arise from interactions with a medium, leads to wider distributions of T, T_{maj} and T_{min}. This effect is indeed observed in simulations with a medium (figure 5.15). In the case of collisional energy loss, however, this broadening is entirely due to recoils. The kinematics of elastic scattering is such that energetic particles have small scattering angles. When the recoiling scattering centres are removed from the event and the parton shower hadronises alone the thrust distributions are practically indistinguishable from the vacuum. The recoils have mostly relatively low momenta and those with high momenta have small angles relative to the jet, therefore the widening of the thrust distributions disappears when only hadrons with energies above $E_{\mathrm{cut}} = 2\,\mathrm{GeV}$ are considered. In the case of induced radiation, on the other hand, the probability for large transverse momenta of the radiated partons is much larger. Consequently, the broadening is also visible in the hard component.

The effect of elastic scattering on the jet rates is similar to the modification of the thrust distributions. First, there is a broadening of the parton shower, which is small due to the dominance of small momentum transfers and the kinematics of elastic scattering which forces energetic particles to small scattering angles. This effect is found to be negligible (figure 5.16). Second, the recoiling scattering centres can have a large transverse momentum relative to the jet. This translates into a larger distance y_{ij} between the recoil and jet partons so that the recoil will be counted as separate structure at relatively coarse scales. However, due to the comparatively low energy of recoils and the correlation between the energy and the angle, this effect can be expected to be visible only at relatively small values of y_{cut}, which are sensitive to small energies. Furthermore, it dies out at larger hadron energies. This behaviour is in fact seen in the simulation (figure 5.16). The larger transverse momentum of radiated partons, on the other hand, leads to a shift of the jet fractions to larger values of y_{cut} in the case of radiative energy loss. This means that at a given resolution more substructure is found in medium modified jets as compared to the vacuum. Again, the effect survives also when a background cut is applied.

The jet rates are not very sensitive to the total jet energy, but an inaccurate determination of the jet energy is dangerous, because it also shifts the n-jet fractions. A deviation of the reconstructed jet energy from the true value by 30 %, for instance, leads to a shift of $\log_{10}(1.3^2) \simeq 0.23$. This is of the same magnitude as the shift due to the medium modifications. Thus, event shapes and jet rates may provide a tool for disentangling collisional and radiative energy loss, but a careful treatment of experimental uncertainties is still missing.

These results were obtained with the simplified model for medium induced radiation. Given the small effects due to elastic collisions, however, one would not expect a dramatically different behaviour of the full $2 \to 3$ process. The structure of the radiation is similar and the recoil is found to have a small impact when the

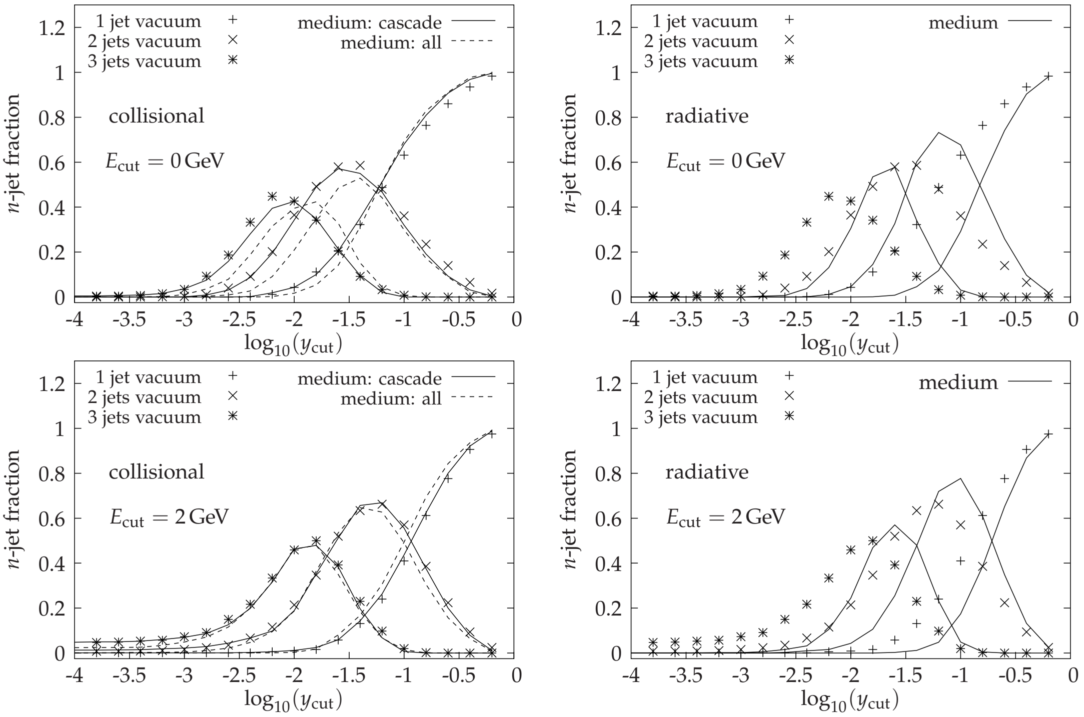

Figure 5.16.: Jet rates for a single 100 GeV quark jet after hadronisation in vacuum and with medium effects. **Left:** Collisional energy loss for $T = 500\,\mathrm{MeV}$ and $L = 5\,\mathrm{fm}$. Recoil partons are either hadronised together with the cascade ('all') or they are not included in the hadronisation ('cascade'). **Right:** Medium-induced radiation for $f_{\mathrm{med}} = 3$ and $L = 5\,\mathrm{fm}$. In the top row, all hadrons are included, while in the bottom row, only hadrons with energy above $E_{\mathrm{cut}} = 2\,\mathrm{GeV}$ are included.

background cut is applied.

Finally, figure 5.17 shows the modifications of the single-inclusive distribution $\mathrm{d}N/\mathrm{d}\xi$. The interactions with the medium lead to a softening of the distribution on the parton as well as on the hadron level. Elastic scattering can only increase the multiplicity if recoiling scattering centres are counted towards the jet. The increase in multiplicity due to recoils or enhanced radiation is more pronounced on the parton level due to the ability of the string fragmentation to recombine soft partons.

5.2.6. Transverse Momentum Broadening

Partonic energy loss is expected to lead to a characteristic broadening of the jet. Parametric estimates in the framework of radiative energy loss models suggest $\langle k_\perp^2 \rangle \simeq \hat{q}L/2$. In models of collisional energy loss one also expects $\langle k_\perp^2 \rangle \propto L$ due to transverse Brownian motion. In contrast to these parametric expectations, the strong suppression of leading hadrons observed experimentally is not accompanied by a visible broadening of jet-like two-particle correlations [16, 19].

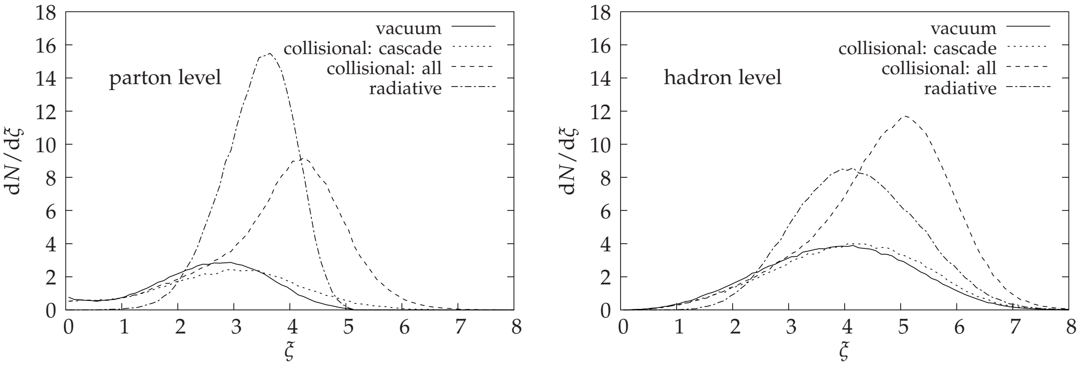

Figure 5.17.: The single inclusive distribution $\mathrm{d}N/\mathrm{d}\xi$ for a single medium-modified quark jet ($E_q = 100\,\mathrm{GeV}$) before and after hadronisation ($Q_0 = 1\,\mathrm{GeV}$). On the parton level (left), all partons are shown, but on the hadron level (right), only charged hadrons are included. Collisional energy loss is calculated for $T = 500\,\mathrm{MeV}$ and $L = 5\,\mathrm{fm}$, with recoil partons either hadronised together with the cascade ('all') or not included in the hadronisation ('cascade'). Medium induced radiation is calculated for $f_{\mathrm{med}} = 3$ and $L = 5\,\mathrm{fm}$.

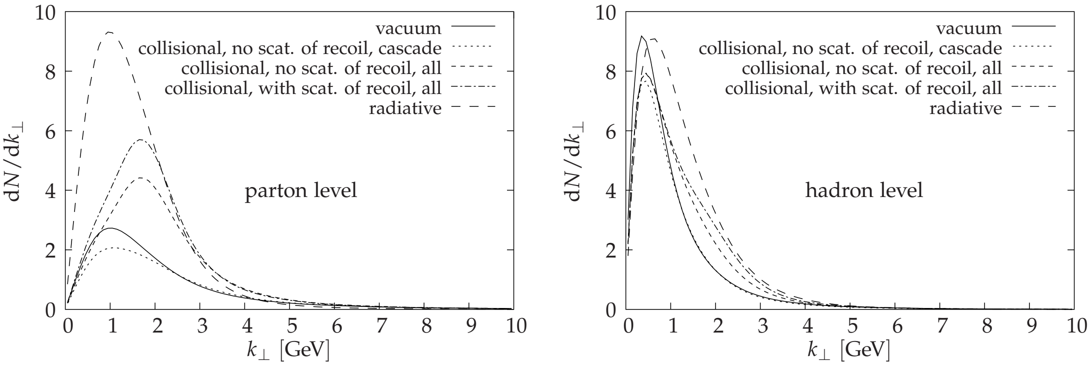

Figure 5.18.: Transverse momentum relative to the jet axis of particles with energy larger than $E_{\mathrm{cut}} = 2\,\mathrm{GeV}$ in a 100 GeV quark jet. In the collisional energy loss scenario the recoiling scattering centres can be ignored ('cascade') or counted towards the jet ('all') and they can themselves undergo multiple scattering ('with scattering of recoil') or propagate without interactions ('without scattering of recoil'). **Left:** Hadronisation with adapted string fragmentation after perturbative evolution down to $Q_0 = 1\,\mathrm{GeV}$. **Right:** parton shower evolution down to $Q_0 = 1\,\mathrm{GeV}$ without hadronisation ($T = 500\,\mathrm{MeV}$, $L = 5\,\mathrm{fm}$, $f_{\mathrm{med}} = 3$).

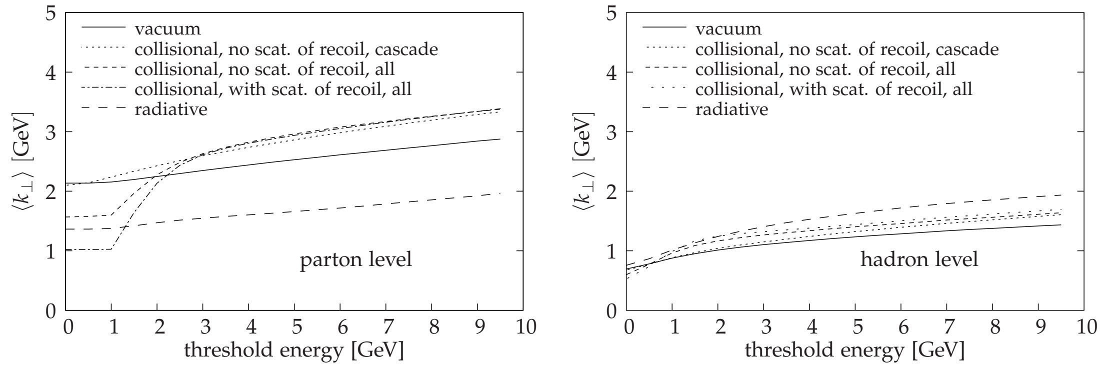

Figure 5.19.: Mean transverse momentum relative to the jet axis of particles with energy above the threshold energy, parameters and model variants as in figure 5.18.

Figure 5.18 shows the transverse momentum distribution of particles with energies larger than $E_{\text{cut}} = 2\,\text{GeV}$ in a 100 GeV jet for two different hadronisation models, string fragmentation and local parton hadron duality [87, 88] (section 2.2.5). When the recoiling scattering centres are not included elastic scattering reduces the multiplicity because less particles pass the energy threshold, but does not lead to a significant broadening. This is in line with the dominance of small angle scattering. On the parton level the recoiling scattering centres are visible as prominent peak at $k_\perp \simeq 1.75\,\text{GeV}$, which is the characteristic transverse momentum of scattering centres with 2 GeV energy recoiling from a 100 GeV projectile (section 5.2.3). When also the recoils experience multiple scattering the shape of the transverse momentum distribution remains unchanged. The (primary) recoiling scattering centres have already relatively low energy, so that a secondary recoil can only exceed the energy threshold if the momentum transfer was large and this means that the angle between the primary and the secondary recoil is small. With string fragmentation, on the other hand, including the recoils leads to a slight broadening of the distribution but there is no strong increase in multiplicity. The same observation applies to radiative energy loss in the string fragmentation scenario. Generally, string fragmentation softens the partonic distribution thus pushing particles below E_{cut} and washes out structures associated to relatively soft particles because it recombines soft partons and produces hadrons everywhere along the strings. This means for the induced radiation, which leads to a soft but wide shower at the parton level, that it does not lead to a strong increase of hadronic multiplicity as compared to vacuum jets, but the average transverse momentum increases slightly (figure 5.19). In the purely partonic scenario one observes a quite different effect: Here the mean $k_\perp$ decreases because of the strong increase in multiplicity. This suggests that energy-momentum conservation is an important constraint.

5.3. Further Improvements of the Model

In this section developments beyond Jewel 1.0, that are only partly implemented, are presented. Improving the description of the medium by including a realistic geometry and expansion is a straightforward generalisation. The most important improvement will be to include a microscopic model for radiative energy loss based on 2 → 3 matrix elements. Following the idea outlined in section 5.3.2 such a model can be obtained, which is by construction incoherent. Finally, in section 5.3.3 a procedure how the LPM suppression can be implemented in Monte Carlo models is presented.

5.3.1. Realistic Geometry and Expansion

The simulation can be equipped with a realistic geometry and a position and time dependent density. Geometrical aspects are obtained from a simple Glauber model [89] (section 3.1.1) with a Woods-Saxon potential, numerical values given in this section are calculated for Au+Au collisions at $\sigma_{\mathrm{NN}}^{\mathrm{inel}} = 42\,\mathrm{mb}$ corresponding roughly to $\sqrt{s_{\mathrm{NN}}} = 200\,\mathrm{GeV}$, but the results for Pb+Pb collisions at Lhc energies are very similar.

Since the experiments characterise nucleus-nucleus collisions by their centrality, i.e. the fraction of the total geometrical cross section covered, rather than the impact parameter, it is convenient to do the same in the simulation. The cross section and thus the centrality increase quadratically with impact parameter, for centralities up to 90 % the relation can be very well approximated by

$$b = \sqrt{2.25\,\mathrm{fm}^2 \cdot \text{centrality}\,[\%]}\,. \tag{5.48}$$

Only for very peripheral collisions the thinner edge of the nucleus becomes important. A given centrality class translates into an impact parameter range, from which the impact parameter for a specific event has to be chosen according to the cross section. For centralities up to 90 % one finds

$$\frac{\mathrm{d}\sigma}{\mathrm{d}b} = 6.28 \cdot b\,. \tag{5.49}$$

The coordinate system is chosen such that the impact parameter and thus the short axis of the overlap region is in x direction.

Jet production is a hard process that scales with the number of binary nucleon-nucleon collisions. Therefore, the transverse components of the production points for the hard parent partons are distributed in the resulting overlap region according to the number of binary collisions per transverse area

$$n_{\mathrm{bin}}(x,y) = T_A\left(\sqrt{(x-b/2)^2+y^2}\right) \cdot T_A\left(\sqrt{(x+b/2)^2+y^2}\right)\,. \tag{5.50}$$

The nuclei appear strongly Lorentz contracted in the longitudinal direction and therefore all parent partons are assumed to be produced at $z = 0$. The emission directions are uniformly distributed in azimuthal angle.

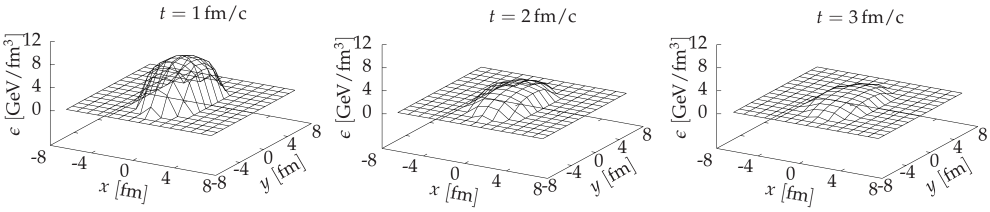

Figure 5.20.: Energy density profile at $z = 0$ for $b = 4\,\mathrm{fm}$ at different times.

The energy production in the fireball, which is a soft process, is expected to scale with the number of participating nucleons. The energy density in the medium is thus assumed to have a transverse profile that is given by the transverse density of participants. The model parameter ϵ_0 regulating the density is the equivalent initial density, which is the mean density at a proper time τ_0 in a central ($b = 0$) collision. For any centrality the density profile is then given by

$$\epsilon(x, y, b, \tau_0) = \epsilon_0 n_{\text{part}}(x, y, b) \frac{\pi R_A^2}{2A} \tag{5.51}$$

with

$$\begin{aligned} n_{\text{part}}(x, y, b) = {} & T_A\left(\sqrt{(x - b/2)^2 + y^2}\right)\left[1 - e^{-\sigma_{\text{NN}}^{\text{inel}} T_A\left(\sqrt{(x+b/2)^2+y^2}\right)}\right] \\ & + T_A\left(\sqrt{(x + b/2)^2 + y^2}\right)\left[1 - e^{-\sigma_{\text{NN}}^{\text{inel}} T_A\left(\sqrt{(x-b/2)^2+y^2}\right)}\right] . \end{aligned} \tag{5.52}$$

This means that the mean density increases with centrality.

Furthermore, the equation of state and the time evolution have to be specified. The ideal gas equation of state was already used in the static case to relate the particle density to the temperature. Here, it is supplemented with a Bjorken-like longitudinal expansion [91] (section 3.1.3) leading to

$$\epsilon(x, y, b, \tau) = \epsilon(x, y, b, \tau_0) \left(\frac{\tau_0}{\tau}\right)^{\frac{1}{3}} \tag{5.53}$$

for $\tau \geq \tau_0$. For $\tau < \tau_0$ the energy density is assumed to be the same as at τ_0. Interactions with the medium can only take place as long as the local temperature is higher than the critical temperature. The critical density and the formation time τ_0 as well as the equivalent initial temperature, which replaces the equivalent initial density, are the model parameters regulating the density. This simple model for the medium can easily be replaced by a more realistic calculation, a hydrodynamic evolution for instance. The temperature and density as a function of position and time could be tabulated and used in the simulation.

Not only the density, also the scattering cross section depends now on position and time through s, m_{s} and μ_{D}. The cross section decreases with temperature while the density increases, so that the resulting scattering probability depends only weakly on temperature. For the no-scattering probability the integral in equation (5.32) has to solved numerically.

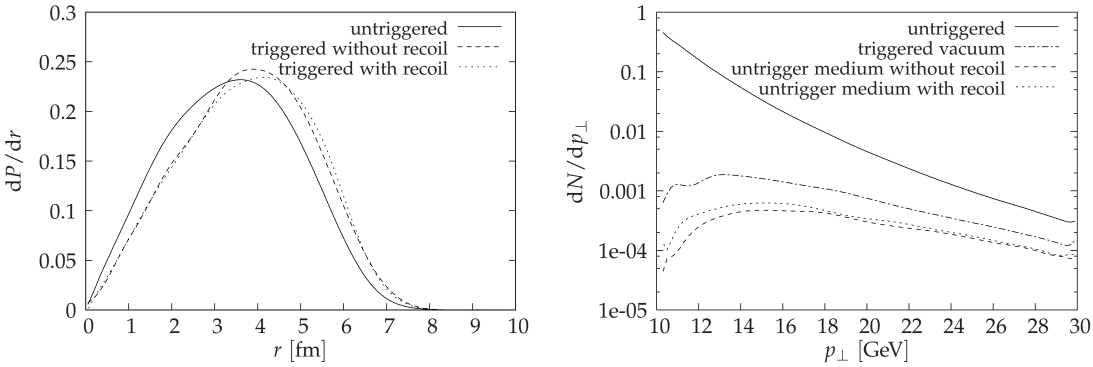

Figure 5.21.: Trigger bias in central ($b = 0$) nuclear collisions with only collisional energy loss. **Left:** Normalised distributions of the radial coordinate of the production points of jets that contain a trigger hadron compared to the untriggered distribution. The trigger condition is at least one hadron with energy larger than 10 GeV. **Right:** Transverse momentum spectrum of parent partons that produced a trigger hadron after jet evolution in the medium compared to the triggered distribution after vacuum evolution and the untriggered distribution. The parent $p_\perp$ can also be viewed as the total $p_\perp$ of the jet. The initial and critical temperature are $T_\mathrm{i} = 500\,\mathrm{MeV}$ and $T_\mathrm{c} = 170\,\mathrm{MeV}$, respectively, and $\tau_0 = 0.2\,\mathrm{fm}$.

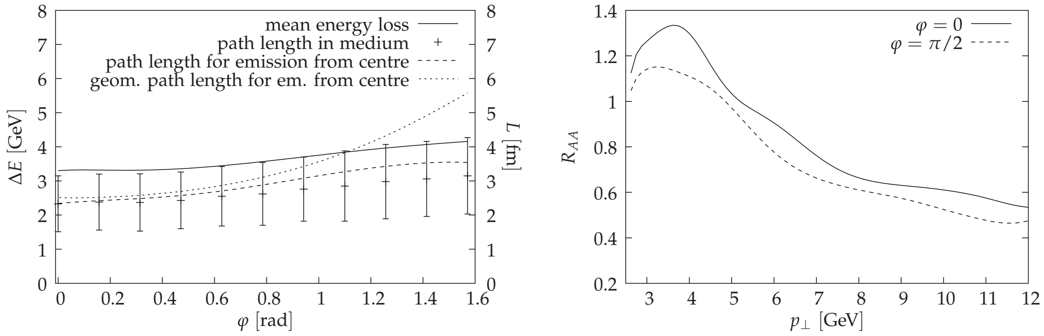

Figure 5.22.: **Left:** Mean collisional energy loss of an on-shell quark with $E = 100\,\mathrm{GeV}$ as a function of the emission angle for $40 - 50\,\%$ centrality. Also shown is the mean path length in the medium (the errorbars indicate the spread due to the distribution of production points in the overlap region), the path length of partons emitted from the centre of the overlap region and the geometrical path length (again for emission from the centre), which ignores the expansion and finite lifetime of the medium, for a nuclear radius $R_A = 7.5\,\mathrm{fm}$. **Right:** Nuclear modification factor for collisional energy loss including the recoiling scattering centres in the $40 - 50\,\%$ centrality class for jets emitted in the reaction plane ($\varphi = 0$) and out of plane ($\varphi = \pi/2$). The equivalent initial temperature is $T_\mathrm{i} = 500\,\mathrm{MeV}$, $T_\mathrm{c} = 170\,\mathrm{MeV}$, and $\tau_0 = 0.2\,\mathrm{fm}$.

The factor f_{med} in the simplified model for radiative energy loss does not contain any dependence on medium properties and does not allow for induced radiation off on-shell partons. Therefore, a study of effects of the geometry and expansion only makes sense for the collisional energy loss.

With a model for the geometry and expansion one can study trigger bias effects under realistic conditions. It is commonly believed that due to the energy loss in the medium triggering on energetic hadrons biases the sample towards jets that were emitted close to the surface and thus lost exceptionally little energy. But there is a competing effect and that is the chance to escape with little energy loss even after a considerable path length in the medium (cf. figure 5.9) and the vast majority of the jets is produced more than one mean free path away from the surface. In the simulation a significant but not very strong surface bias is observed for a set of parameters that leads to a suppression of high $p_\perp$ hadrons of about a factor 2 (figure 5.21 left).

A strong trigger bias would also imply that the triggered jets lost nearly no energy so that the shape of the triggered $p_\perp$ spectrum should be the same as in vacuum while the rate decreases. A significant energy loss, on the other hand, would shift the spectrum to higher momenta. In any case the effect is expected to die out at large transverse momenta when the production of a trigger particle has more support from the fragmentation function. Unfortunately, the result of the simulation for the triggered spectrum in medium is not conclusive (figure 5.21 right). There seems to be a shift of the maximum which could be interpreted as energy loss of the triggered jet.

A signature of non-central geometry that is also observed in data (section 3.2) is a dependence of the hadron suppression on the angle relative to the reaction plane. The left panel of figure 5.22 shows the variation of the energy loss and the path length with the emission angle for $40-50\,\%$ centrality. There is a clear increase of the path length with the angle, but the path length difference between in-plane and out-of-plane emission is seen to be much smaller than the spread due to the distribution of emission points in the overlap region. Also shown is the path length of partons emitted from the centre of the overlap region, which is very similar to the mean path length in the case of distributed emission points for small angles but is somewhat larger at large angles. At larger angles the finite lifetime limits the available path lengths. The geometrical path length, i.e. the path length in a static medium, is considerably longer at large emission angles than the path length in an expanding medium of the same size.

As expected, the collisional energy loss closely follows the path length, but here the variance is even larger. In addition to the variation of the path length the energy loss has a wide distribution already for a fixed path length and it is temperature dependent. The larger mean energy loss of partons emitted out-of-plane translates to a stronger suppression of hadrons in this direction (figure 5.22 right). However, the difference between in-plane and out-of-plane emission is smaller than observed in data.

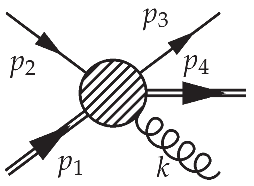

Figure 5.23.: Labelling of momenta in inelastic quark scattering, the double line represents the heavy quark.

5.3.2. First Steps Towards Inelastic Scattering

Implementing inelastic scattering on the same footing as the elastic process requires knowledge of the inelastic cross sections. Among the many different possible processes the inelastic scattering of a massless off a heavy quark has the advantages that it is relatively simple and the mass is a parameter that can be used to regulate the gluon radiation off the target. Furthermore, there exists a restframe of the medium.

The matrix element for this process,

$$q(p_2) + Q(p_1) \to q(p_3) + Q(p_4) + g(k)\,, \tag{5.54}$$

where q and g are massless and Q has mass m, is given by [182]

$$\begin{aligned}
&|\mathcal{M}^{\mathrm{qQ\to qQg}}|^2 = \\
&\frac{g^6}{4N^2}\left\{ \frac{(p_1p_3)^2 + (p_3p_4)^2 + (p_1p_2)^2 + (p_2p_4)^2 + m^2\left(-p_1p_4 - p_2p_3 + m^2\right)}{(p_2-p_3)^2\,(p_1-p_4)^2} \times \right.\\
&\qquad \times \left[\frac{4(N^2-1)^2}{N}\left(\frac{p_1p_3}{p_1k\;p_3k} + \frac{p_2p_4}{p_2k\;p_4k}\right)\right.\\
&\qquad + \frac{4(N^2-1)}{N}\left(\frac{2\,p_1p_2}{p_1k\;p_2k} + \frac{2\,p_3p_4}{p_3k\;p_4k} - \frac{p_2p_4}{p_2k\;p_4k}\right.\\
&\qquad\qquad \left.\left. - \frac{p_1p_3}{p_1k\;p_3k} - \frac{p_2p_3}{p_2k\;p_3k} - \frac{p_1p_4}{p_1k\;p_4k}\right)\right]\\
&- \frac{(N^2-1)(N^2-4)}{N}\frac{4m^2}{(p_2-p_3)^2\,(p_1-p_4)^2}\left(\frac{p_3p_4 + p_2p_4}{p_1k} - \frac{p_1p_3 + p_1p_2}{p_4k}\right)\\
&+ \frac{4(N^2-1)^2}{N}m^2\left[-\frac{(p_3k)^2 + (p_2k)^2}{(p_1-p_4)^4\;p_3k\;p_2k}\right.\\
&\qquad - \frac{1}{2\,(p_1-p_4)^2}\left(-\frac{1}{p_1k} - \frac{1}{p_2k} + \frac{1}{p_3k} + \frac{1}{p_4k}\right)\\
&\qquad - \frac{1}{2\,(p_2-p_3)^2}\left(-\frac{1}{p_1k} + \frac{1}{p_4k} + \frac{m^2}{(p_1k)^2} + \frac{m^2}{(p_4k)^2} + \frac{4}{(p_1-p_4)^2}\right)\\
&\qquad - \frac{1}{(p_2-p_3)^4}\left(\left(\frac{p_1p_3}{p_4k} + \frac{2\,p_3k}{(p_1-p_4)^2}\right)^2 + \left(\frac{p_1p_2}{p_4k} + \frac{2\,p_2k}{(p_1-p_4)^2}\right)^2\right.\\
&\qquad\qquad \left.\left. + \left(\frac{p_3p_4}{p_1k} + \frac{2\,p_3k}{(p_1-p_4)^2}\right)^2 + \left(\frac{p_2p_4}{p_1k} + \frac{2\,p_2k}{(p_1-p_4)^2}\right)^2\right)\right]
\end{aligned}$$

$$
\begin{aligned}
&-\frac{(N^2-1)}{N}\,\frac{4m^2}{(p_2-p_3)^2\,(p_1-p_4)^2}\times\\
&\qquad\times\Bigg[1-\frac{2\,p_2p_3}{(p_1-p_4)^2}-\frac{m^2}{p_1k}+\frac{m^2}{p_4k}-\frac{(p_3k)^2+(p_2k)^2}{p_1k\;p_4k}\\
&\qquad-\frac{2\,(p_1p_2-p_1p_3)}{(p_2-p_3)^2}\left(\frac{p_1p_3}{p_4k}+\frac{2\,p_3k}{(p_1-p_4)^2}+\frac{p_1p_2}{p_4k}+\frac{2\,p_2k}{(p_1-p_4)^2}\right)\\
&\qquad-\frac{2\,(p_3p_4+p_2p_4)}{(p_2-p_3)^2}\left(\frac{p_3p_4}{p_1k}+\frac{2\,p_3k}{(p_1-p_4)^2}+\frac{p_2p_4}{p_1k}+\frac{2\,p_2k}{(p_1-p_4)^2}\right)\Bigg]\Bigg\}
\end{aligned}
\tag{5.55}
$$

It has the usual singularities when one of the massless particles is soft, a pair of massless particles is collinear or the momentum transfer to the heavy quark vanishes. Formally, this amounts to 7 singularities. Apart from that the three-particle final state is described by 5 independent variables, which makes a direct Monte Carlo implementation of the process extremely difficult. Instead, one has to identify the important properties and features.

The singularities associated with the radiated gluon are of the form $1/(p_2k\;p_3k)$, so that the matrix element can be written as $1/(p_2k\;p_3k)$ times an expression that is finite for all $k=(\omega,\vec{k})$ [183].

$$
\begin{aligned}
&|\mathcal{M}^{\mathrm{qQ}\to\mathrm{qQg}}|^2=\frac{1}{p_2k\;p_3k}\,\frac{g^6}{4N^2}\times\\
&\times\Bigg\{\frac{(p_1p_3)^2+(p_3p_4)^2+(p_1p_2)^2+(p_2p_4)^2+m^2\left(-p_1p_4-p_2p_3+m^2\right)}{(p_2-p_3)^2\,(p_1-p_4)^2}\times\\
&\qquad\times\Bigg[\frac{4(N^2-1)^2}{N}\left(\frac{p_1p_3\;p_2k}{p_1k}+\frac{p_2p_4\;p_3k}{p_4k}\right)\\
&\qquad+\frac{4(N^2-1)}{N}\Bigg(\frac{2\,p_1p_2\;p_3k}{p_1k}+\frac{2\,p_3p_4\;p_2k}{p_3k}-\frac{p_2p_4\;p_3k}{p_4k}\\
&\qquad\qquad-\frac{p_1p_3\;p_2k}{p_1k}-p_2p_3-\frac{p_1p_4\;p_2k\;p_3k}{p_1k\;p_4k}\Bigg)\Bigg]\\
&-\frac{(N^2-1)(N^2-4)}{N}\,\frac{4m^2}{(p_2-p_3)^2\,(p_1-p_4)^2}\times\\
&\qquad\times\left(\frac{(p_3p_4+p_2p_4)\;p_2k\;p_3k}{p_1k}-\frac{(p_1p_3+p_1p_2)\;p_2kp_3k}{p_4k}\right)
\end{aligned}
$$

$$
\begin{aligned}
&+\frac{4(N^2-1)^2}{N}m^2\Bigg[-\frac{(p_3k)^2+(p_2k)^2}{(p_1-p_4)^4}-\frac{1}{2\,(p_1-p_4)^2}\left(-\frac{p_2k\;p_3k}{p_1k}-p_3k+p_2k+\frac{p_2k\;p_3k}{p_4k}\right)\\
&\quad-\frac{1}{2\,(p_2-p_3)^2}\left(-\frac{p_2k\;p_3k}{p_1k}+\frac{p_2k\;p_3k}{p_4k}+\frac{m^2\,p_2k\;p_3k}{(p_1k)^2}+\frac{m^2\,p_2k\;p_3k}{(p_4k)^2}+\frac{4\,p_2k\;p_3k}{(p_1-p_4)^2}\right)\\
&\qquad-\frac{1}{(p_2-p_3)^4}\Bigg(\frac{(p_1p_3)^2\,p_2k\;p_3k}{(p_4k)^2}+\frac{4\,p_1p_3\;p_2k\,(p_3k)^2}{p_4k\,(p_1-p_4)^2}+\frac{4\,p_2k\,(p_3k)^3}{(p_1-p_4)^4}\\
&\qquad\qquad+\frac{(p_1p_2)^2\,p_2k\;p_3k}{(p_4k)^2}+\frac{4\,p_1p_2\;(p_2k)^2\,p_3k}{p_4k\,(p_1-p_4)^2}+\frac{4\,(p_2k)^3\,p_3k}{(p_1-p_4)^4}\\
&\qquad\qquad+\frac{(p_3p_4)^2\,p_2k\;p_3k}{(p_1k)^2}+\frac{4\,p_3p_4\;p_2k\,(p_3k)^2}{p_1k\,(p_1-p_4)^2}+\frac{4\,p_2k\,(p_3k)^3}{(p_1-p_4)^4}\\
&\qquad\qquad\qquad+\frac{(p_2p_4)^2\,p_2k\;p_3k}{(p_1k)^2}+\frac{4\,p_2p_4\;(p_2k)^2\,p_3k}{p_1k\,(p_1-p_4)^2}+\frac{4\,(p_2k)^3\,p_3k}{(p_1-p_4)^4}\Bigg)\Bigg]\\
&-\frac{(N^2-1)}{N}\frac{4m^2}{(p_2-p_3)^2\,(p_1-p_4)^2}\times\\
&\times\Bigg[p_2k\;p_3k-\frac{2\,p_2p_3\;p_2k\;p_3k}{(p_1-p_4)^2}-\frac{m^2\,p_2k\;p_3k}{p_1k}+\frac{m^2\,p_2k\;p_3k}{p_4k}-\frac{\left((p_3k)^2+(p_2k)^2\right)\;p_2k\;p_3k}{p_1k\;p_4k}\\
&\quad-\frac{2\,(p_1p_2-p_1p_3)}{(p_2-p_3)^2}\left(\frac{p_1p_3\;p_2k\;p_3k}{p_4k}+\frac{2\,p_2k\,(p_2k)^2}{(p_1-p_4)^2}+\frac{p_1p_2\;p_2k\;p_3k}{p_4k}+\frac{2\,p_2k\;p_2k\;p_3k}{(p_1-p_4)^2}\right)\\
&\quad-\frac{2\,(p_3p_4+p_2p_4)}{(p_2-p_3)^2}\left(\frac{p_3p_4\;p_2k\;p_3k}{p_1k}+\frac{2\,p_3k\;p_2k\;p_3k}{(p_1-p_4)^2}+\frac{p_2p_4\;p_2k\;p_3k}{p_1k}+\frac{2\,(p_2k)^2\,p_3k}{(p_1-p_4)^2}\right)\Bigg]\Bigg\}
\end{aligned}
\qquad (5.56)
$$

In the soft gluon approximation, where all terms in the finite piece that grow with ω are neglected and the quark momenta are assumed to be given by $2 \to 2$ kinematics, the matrix element simplifies considerably to [182]

$$
\begin{aligned}
|\mathcal{M}^{\mathrm{qQ}\to\mathrm{qQg}}|^2=\frac{1}{p_2k\;p_3k}\frac{g^6}{4N^2}\Bigg\{&\frac{2\,(p_1p_3)^2+2\,(p_1p_2)^2-2\,m^2\,p_2p_3}{(p_2-p_3)^4}\times\\
&\times\Bigg[\frac{4(N^2-1)^2}{N}\left(\frac{p_1p_3\;p_2k}{p_1k}+\frac{p_2p_4\;p_3k}{p_4k}\right)\\
&\quad+\frac{4(N^2-1)}{N}\Bigg(\frac{2\,p_1p_2\;p_3k}{p_1k}+\frac{2\,p_3p_4\;p_2k}{p_3k}-\frac{p_2p_4\;p_3k}{p_4k}\\
&\qquad-\frac{p_1p_3\;p_2k}{p_1k}-p_2p_3-\frac{p_1p_4\;p_2k\;p_3k}{p_1k\;p_4k}\Bigg)\Bigg]\\
&+\frac{4(N^2-1)^2}{N}m^2\Bigg[-\frac{1}{2\,(p_2-p_3)^2}\left(\frac{m^2\,p_2k\;p_3k}{(p_1k)^2}+\frac{m^2\,p_2k\;p_3k}{(p_4k)^2}\right)\\
&\quad-\frac{1}{(p_2-p_3)^4}\Bigg(\frac{(p_1p_3)^2\,p_2k\;p_3k}{(p_4k)^2}+\frac{(p_1p_2)^2\,p_2k\;p_3k}{(p_4k)^2}\\
&\qquad+\frac{(p_3p_4)^2\,p_2k\;p_3k}{(p_1k)^2}+\frac{(p_2p_4)^2\,p_2k\;p_3k}{(p_1k)^2}\Bigg)\Bigg]\Bigg\}
\end{aligned}
$$

$$
\begin{aligned}
&= \frac{1}{p_2k\;p_3k}\,g^2\,\frac{g^4(N^2-1)}{2N^2}\left\{\frac{(p_1p_2)^2+(p_1p_3)^2-m^2p_2p_3}{(p_2p_3)^2}\times\right.\\
&\qquad\times\left[\frac{N^2-1}{N}\left(\frac{p_1p_3\;p_2k}{p_1k}+\frac{p_2p_4\;p_3k}{p_4k}\right)\right.\\
&\qquad+\frac{1}{N}\left(\frac{2\,p_1p_2\;p_3k}{p_1k}+\frac{2\,p_3p_4\;p_2k}{p_3k}-\frac{p_2p_4\;p_3k}{p_4k}\right.\\
&\qquad\left.\left.-\frac{p_1p_3\;p_2k}{p_1k}-p_2p_3-\frac{p_1p_4\;p_2k\;p_3k}{p_1k\;p_4k}\right)\right]\\
&\qquad-\frac{N^2-1}{2N}\frac{1}{(p_2p_3)^2}\left[\frac{m^2\,p_2k\;p_3k}{(p_1k)^2}\left((p_1p_2)^2+(p_1p_3)^2-m^2\,p_2p_3\right)\right)\\
&\qquad\left.\left.\frac{m^2\,p_2k\;p_3k}{(p_4k)^2}\left((p_1p_2)^2+(p_1p_3)^2-m^2\,p_2p_3\right)\right)\right]\right\}\\
&= \frac{1}{p_2k\;p_3k}\,g^2|\mathcal{M}^{\mathrm{qQ}\to\mathrm{qQ}}|^2\left[C_{\mathrm{F}}\left(2\frac{p_1p_3\;p_2k}{p_1k}+2\frac{p_2p_4\;p_3k}{p_4k}\right.\right.\\
&\qquad\left.-\frac{m^2\,p_2k\;p_3k}{(p_1k)^2}-\frac{m^2\,p_2k\;p_3k}{(p_4k)^2}\right)\\
&\qquad+\frac{1}{N}\left(2\frac{p_1p_2\;p_3k}{p_1k}+2\frac{p_3p_4\;p_2k}{p_4k}\right.\\
&\qquad\left.\left.-\frac{p_1p_3\;p_2k}{p_1k}-\frac{p_2p_4\;p_3k}{p_4k}-\frac{p_1p_4\;p_2k\;p_3k}{p_1k\;p_4k}-p_2p_3\right)\right]\,,
\end{aligned}
\tag{5.57}
$$

where the matrix element describing the 2 → 2 quark scattering is given by

$$
|\mathcal{M}^{\mathrm{qQ}\to\mathrm{qQ}}|^2=\frac{g^4(N^2-1)}{2N^2}\frac{(p_1p_2)^2+(p_1p_3)^2-m^2p_2p_3}{(p_2p_3)^2}\,. \tag{5.58}
$$

In the soft gluon limit there is no radiation from the virtual gluon line. The singular factor can be rewritten as

$$
\begin{aligned}
\frac{1}{p_2k\;p_3k}&=\frac{1}{\omega^2E_2E_3(1-\cos\vartheta_{2\mathrm{g}})(1-\cos\vartheta_{3\mathrm{g}})}\\
&=\frac{1}{\omega^2}\left(\frac{1}{1-\cos\vartheta_{2\mathrm{g}}}+\frac{1}{1-\cos\vartheta_{3\mathrm{g}}}\right)\frac{1}{(1-\cos\vartheta_{2\mathrm{g}})+(1-\cos\vartheta_{3\mathrm{g}})}\frac{1}{E_2E_3}\,.
\end{aligned}
\tag{5.59}
$$

In the target rest frame, where $p_1 = (m, 0, 0, 0)$, the matrix element takes the form

$$
\begin{aligned}
|\mathcal{M}^{\mathrm{qQ}\to\mathrm{qQg}}|^2 = \frac{1}{\omega^2}\left(\frac{1}{1-\cos\vartheta_{2\mathrm{g}}} + \frac{1}{1-\cos\vartheta_{3\mathrm{g}}}\right) g^2 |\mathcal{M}^{\mathrm{qQ}\to\mathrm{qQ}}|^2 C_\mathrm{F} \\
\times \frac{1}{(1-\cos\vartheta_{2\mathrm{g}}) + (1-\cos\vartheta_{3\mathrm{g}})} \\
\times \left(2\frac{(E_4 - \sqrt{E_4^2 - m^2}\cos\vartheta_{24})(1-\cos\vartheta_{3\mathrm{g}})}{E_4 - \sqrt{E_4^2 - m^2}\cos\vartheta_{4\mathrm{g}}} + 2(1-\cos\vartheta_{2\mathrm{g}}) \right. \\
\left. - \frac{m^2(1-\cos\vartheta_{2\mathrm{g}})(1-\cos\vartheta_{3\mathrm{g}})}{E_4 - \sqrt{(E_4^2 - m^2}\cos\vartheta_{4\mathrm{g}})^2} - (1-\cos\vartheta_{2\mathrm{g}})(1-\cos\vartheta_{3\mathrm{g}}) \right) . \qquad (5.60)
\end{aligned}
$$

This expression is not symmetric between $\vartheta_{2\mathrm{g}}$ and $\vartheta_{3\mathrm{g}}$ due to the induced radiation from the outgoing heavy quark. If the quark mass is large, this contribution becomes small. It can be neglected by setting $E_4 = m$ in the last factor, which describes the gluon radiation. Then the matrix element contains the contribution from the massless quark lines, which look the same, and a part from the heavy quark which has no collinear divergence.

$$
|\mathcal{M}^{\mathrm{qQ}\to\mathrm{qQg}}|^2 = \frac{1}{\omega^2}\left(\frac{1}{1-\cos\vartheta_{2\mathrm{g}}} + \frac{1}{1-\cos\vartheta_{3\mathrm{g}}} - 1\right) g^2 |\mathcal{M}^{\mathrm{qQ}\to\mathrm{qQ}}|^2 C_\mathrm{F} 2 \qquad (5.61)
$$

In this approximation the inelastic scattering cross section factorises into the elastic cross section times a part that describes the gluon radiation and which has the same structure as the perturbative 1 → 2 splitting.

$$
\begin{aligned}
\sigma^{\mathrm{qQ}\to\mathrm{qQg}} =& \frac{1}{2\sqrt{\lambda(s, m^2, 0)}(2\pi)^5} \\
&\times \int \frac{\mathrm{d}^3 p_3}{2E_3}\frac{\mathrm{d}^3 p_4}{2E_4}\frac{\mathrm{d}^3 k}{2\omega}\delta(p_1 + p_2 - p_3 - p_4 - k)|\mathcal{M}^{\mathrm{qQ}\to\mathrm{qQg}}|^2 & (5.62) \\
\simeq& \frac{\sigma^{\mathrm{qQ}\to\mathrm{qQ}}}{(2\pi)^3}\int \frac{\mathrm{d}^3 k}{2\omega}\frac{1}{\omega^2}\left(\frac{1}{1-\cos\vartheta_{2\mathrm{g}}} + \frac{1}{1-\cos\vartheta_{3\mathrm{g}}} - 1\right) g^2 C_\mathrm{F} 2 & (5.63) \\
=& \frac{\sigma^{\mathrm{qQ}\to\mathrm{qQ}}}{2\pi^2} C_\mathrm{F} \int \frac{\mathrm{d}\omega}{\omega} \sin\vartheta_\mathrm{g}\mathrm{d}\vartheta_\mathrm{g}\mathrm{d}\phi_\mathrm{g}\left(\frac{2}{1-\cos\vartheta_\mathrm{g}} - 1\right)\alpha_\mathrm{s} & (5.64)
\end{aligned}
$$

In the last step the symmetry of the integrand under exchange of $\vartheta_{2\mathrm{g}}$ and $\vartheta_{3\mathrm{g}}$ was exploited. Ignoring the ϑ_g dependence of the coupling and expanding the integrand one obtains

$$
\begin{aligned}
\sigma^{\mathrm{qQ}\to\mathrm{qQg}} \simeq& \frac{\sigma^{\mathrm{qQ}\to\mathrm{qQ}}}{\pi} C_\mathrm{F} \int \frac{\mathrm{d}\omega}{\omega}\frac{\mathrm{d}\vartheta_\mathrm{g}}{\vartheta_\mathrm{g}} 4\alpha_\mathrm{s} & (5.65) \\
\simeq& \frac{\sigma^{\mathrm{qQ}\to\mathrm{qQ}}}{\pi} C_\mathrm{F} 2 \int \frac{\mathrm{d}z}{1-z}\frac{\mathrm{d}Q^2}{Q^2}\alpha_\mathrm{s} \, , & (5.66)
\end{aligned}
$$

where z is the energy fraction, that the quark takes in the splitting process,

$$\omega = (1-z)E\,, \tag{5.67}$$

and the gluon angle is

$$\vartheta_{\mathrm{g}}^2 = \frac{zQ_a^2}{(1-z)E^2} \tag{5.68}$$

when the incoming projectile is off-shell and the daughters are produced on-shell and

$$\vartheta_{\mathrm{g}}^2 = -\frac{Q_b^2}{E^2} \tag{5.69}$$

when the incoming projectile is on-shell and the outgoing projectile goes off-shell. In this case Q_b^2 is negative. E is in both cases the incoming projectile's energy. In this approximation only radiation from the massless quark lines is left, because in expanding the integrand to leading order in ϑ_{g} the contribution from the heavy quark, which is not singular in ϑ_{g} is dropped. The integral in equation (5.66) can be interpreted as a splitting probability with a medium induced splitting function

$$\sigma^{\mathrm{qQ}\to\mathrm{qQg}} = \sigma^{\mathrm{qQ}\to\mathrm{qQ}} \int \mathrm{d}z \, \frac{\mathrm{d}Q^2}{Q^2} \, \frac{\alpha_{\mathrm{s}}}{2\pi} \hat{P}_{\mathrm{qq}}^{(\mathrm{med})}(z) \quad \text{with} \quad \hat{P}_{\mathrm{qq}}^{(\mathrm{med})}(z) = C_{\mathrm{F}} \frac{4}{1-z}\,. \tag{5.70}$$

The resemblance to the vacuum splitting process suggests to use $k_\perp^2$ as scale of α_{s} also in the case of medium induced radiation. Consequently, the minimum transverse momentum $k_\perp \geq f \cdot \Lambda_{\mathrm{QCD}}$ appears as a regulator. This means that the relative strength of the inelastic process compared to elastic scattering is already fixed. In this factorised form the cross section can be used in a Monte Carlo simulation.

The inelastic scattering process does not have to change the virtuality of the projectile. The internal quark line can be off-shell, which allows the radiated gluon to carry transverse momentum. Although one could imagine that a virtual parton in a medium reduces its virtuality not only through 1 → 2 but also through 2 → 3 processes, it is here assumed that inelastic scattering does not affect the fast parton's virtuality. This choice avoids extra modelling of the virtuality reducing scattering and ensures that the inelastic scattering process is the same for virtual and real partons. Furthermore, the elastic and the inelastic scattering then appear as two contributions to the scattering process in the model and are formally treated equally. The total scattering cross section is the sum of the elastic and the inelastic part

$$\sigma^{\mathrm{scat}} = \sigma^{\mathrm{qQ}\to\mathrm{qQ}} \left(1 + \int \mathrm{d}z \, \frac{\mathrm{d}Q^2}{Q^2} \, \frac{\alpha_{\mathrm{s}}}{2\pi} \hat{P}_{\mathrm{qq}}^{(\mathrm{med})}(z) \right)\,. \tag{5.71}$$

The t-channel contributions to the other inelastic processes with induced gluon radiation can as a first approximation be mimicked by replacing C_{F} by the appropriate Casimir factor in equation (5.70) and the elastic cross section. The other processes and medium induced splitting of gluons into quark pairs require a more careful treatment.

The no-scattering probability in a static and homogeneous medium becomes

$$P_{\text{no scatt}}(\tau) = e^{-(\sigma^{\mathrm{elas}}+\sigma^{\mathrm{inel}})n\tau\beta}\,. \tag{5.72}$$

Once it has been decided that the next process will be a scattering the elastic or inelastic process has to be chosen according to their contribution to the total cross section. If the inelastic process is selected six variables have to be chosen: z and Q^2 for the radiation from the medium splitting function, t for the elastic subprocess from the elastic scattering cross section, two azimuthal angles from flat distributions for the radiated gluon and the elastic part and it has to be decided whether the radiation happens before or after the elastic scattering. Radiation from the heavy quark line can also be reintroduced with a fraction of the inelastic cross section that has to be determined from the full expression in equation (5.64). Then, the kinematics in the elastic scattering and the radiation is constructed one after the other with the virtuality of the internal line given by Q^2. If the incoming projectile happens to be off-shell this virtuality can be treated like a rest mass during the simulation of the inelastic process. It will then emerge from the scattering with the same virtuality.

5.3.3. LPM-Suppression in a Probabilistic Monte Carlo Model

Analytic calculations of radiative energy loss indicate that the suppression of induced gluon radiation due to destructive interference (LPM effect) dominates the characteristics of radiative energy loss. These models work in the high energy limit and do not conserve energy and momentum exactly. It is thus not clear what the role of the LPM effect is at non-asymptotic energies with energy-momentum conservation. Monte Carlo models, on the other hand, can conserve energy and momentum exactly but including interference effects in probabilistic formulations is notoriously difficult. Existing Monte Carlo models circumvent the problem by generating incoherent emissions associated to single scattering centres from an effective radiation spectrum including the LPM suppression (section 3.3.3). However, the interpretation in terms of finite formation times sketched at the beginning of section 3.3.2 offers a possibility to include the LPM interference in a Monte Carlo model without modifying the single scattering radiation spectrum. This idea has been explored in a small test set-up.

The medium is characterised by the transport coefficient $\hat{q}$, the longitudinal density n_l along the projectile's trajectory and its length L. The projectile radiates gluons whose energy distribution is given by the spectrum associated to a single scattering

$$\frac{\mathrm{d}I^{(1)}}{\mathrm{d}\omega} \propto \frac{1}{\omega}\,. \tag{5.73}$$

The maximum energy that can be radiated is given by the characteristic gluon energy corresponding to the remaining path length l in the medium

$$\omega_\text{max} = \omega_\text{c}(l) = \frac{1}{2}\hat{q}l^2\,. \tag{5.74}$$

The spectrum is cut off at a low energy ω_min to regularise the divergence. The choice of ω_min does not influence the results but it is convenient to use a value that is smaller than the energy $\omega_\text{c}(\lambda)$ that can be radiated incoherently.

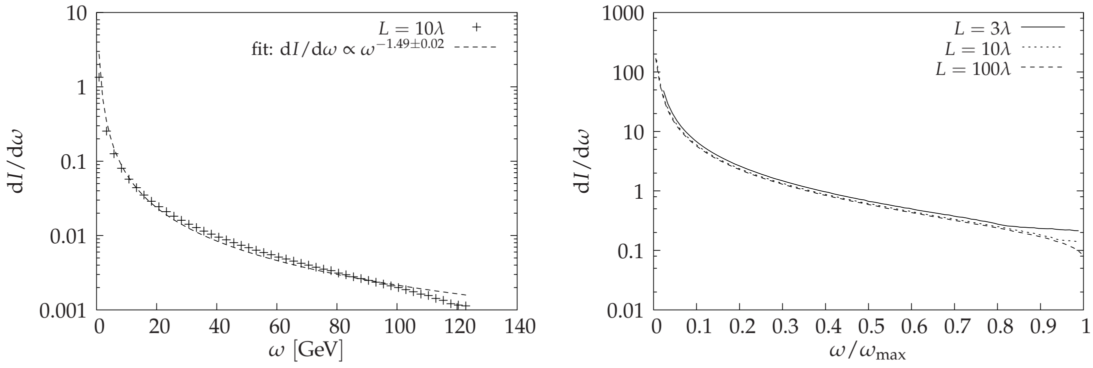

Figure 5.24.: Gluon spectra for different path lengths in a continuous medium ($\hat{q} = 0.5\,\mathrm{GeV}^2/\mathrm{fm}$, $\omega_{\mathrm{min}} = 100\,\mathrm{MeV}$, $n_{\mathrm{l}} = 1\,\mathrm{fm}^{-1}$); fit for $L = 10\lambda$: $\mathrm{d}I/\mathrm{d}\omega \propto \omega^{-1.49\pm0.02}$.

The radiated gluon has a formation time

$$t_{\mathrm{coh}} = \sqrt{\frac{2\omega}{\hat{q}}}\,. \tag{5.75}$$

The next gluon can be formed at $l - t_{\mathrm{coh}}$ and so the radiation of a single gluon is iterated until the projectile leaves the medium. The medium can either be thought of as consisting of single scattering centres, which implies that t_{coh} has to be a multiple of the mean free path λ. Alternatively, one can imagine that the medium continuously transfers transverse momentum to the projectile, in which case t_{coh} can take any value. At this stage there are no constraints due to a finite projectile energy, the incoming energy E_{i} is taken to be large compared to the total amount of energy that can be radiated during the passage through the medium. The resulting gluon spectrum is shown in figure 5.24 for the continuous medium. It shows the

$$\frac{\mathrm{d}I}{\mathrm{d}\omega} \propto \frac{1}{\omega^{3/2}} \tag{5.76}$$

shape characteristic for LPM suppression. The shape remains the same for all L (figure 5.24 right). The discrete medium (figure 5.25 left) leads to a stepwise suppression due to the requirement that always a multiple of the mean free path is needed to radiate the respective gluon. The shape of the spectrum is the same in both cases, but the number of radiated gluon is somewhat smaller in the discrete case.

The energy loss is proportional to L^2 in both cases (figure 5.25 right) as expected from the shape of the spectrum. The number of radiated gluons, on the other hand, grows only like $\sqrt{L}$.

With a finite initial projectile energy E_{i} the gluon energy cannot exceed this value, which means

$$\omega_{\mathrm{max}} = \min(\omega_{\mathrm{c}}, E_{\mathrm{i}})\,. \tag{5.77}$$

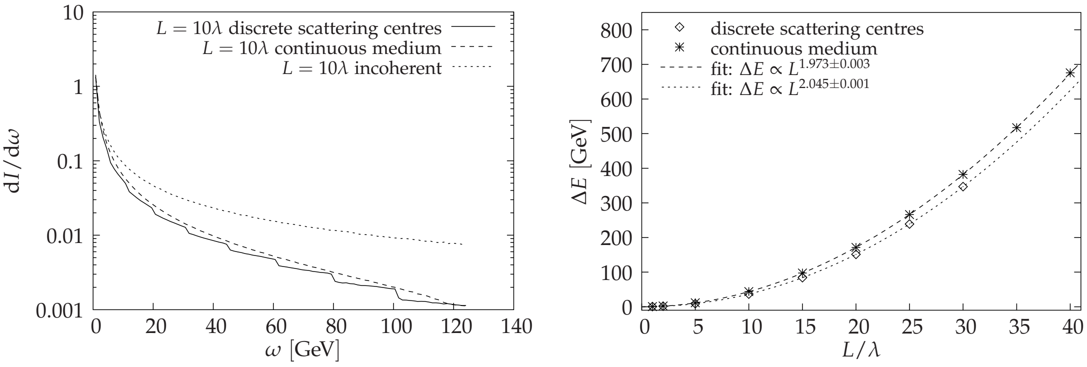

Figure 5.25.: **Left:** Gluon spectrum for $L = 10\lambda$ in a discrete and a continuous medium and the incoherent spectrum (with $\omega_{\max} = \omega_c(L)$). **Right:** Energy loss in a discrete ($\Delta E \propto L^{1.973\pm0.003}$) and a continuous medium ($\Delta E \propto L^{2.045\pm0.001}$); ($\hat{q} = 0.5\,\mathrm{GeV}^2/\mathrm{fm}$, $\omega_{\min} = 100\,\mathrm{MeV}$, $n_l = 1\,\mathrm{fm}^{-1}$).

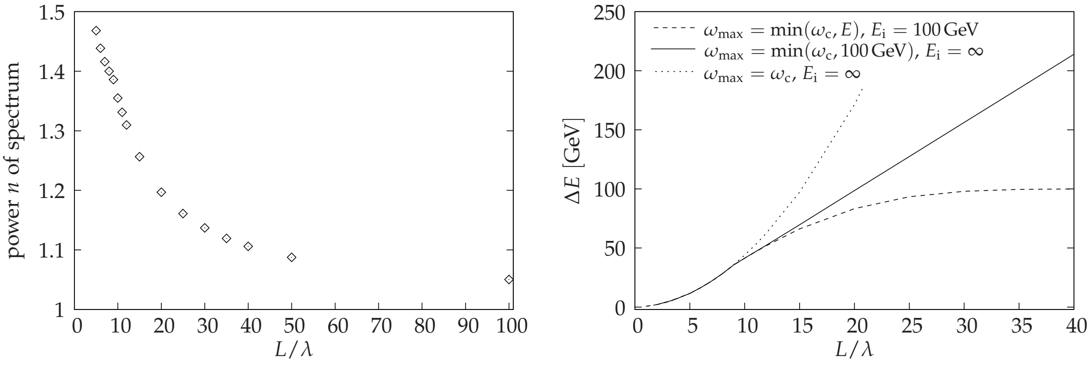

Figure 5.26.: **Left:** Power of the radiated gluon spectrum $dI/d\omega \propto \omega^{-n}$ with a cut-off of 100 GeV on the gluon spectrum induced by a single scattering but without constraint on the total radiated energy, $L_c = 9\lambda$. **Right:** Energy loss in the three cases explained in the caption of figure 5.27 ($\hat{q} = 0.5\,\mathrm{GeV}^2/\mathrm{fm}$, $\omega_{\min} = 100\,\mathrm{MeV}$, $n_l = 1\,\mathrm{fm}^{-1}$).

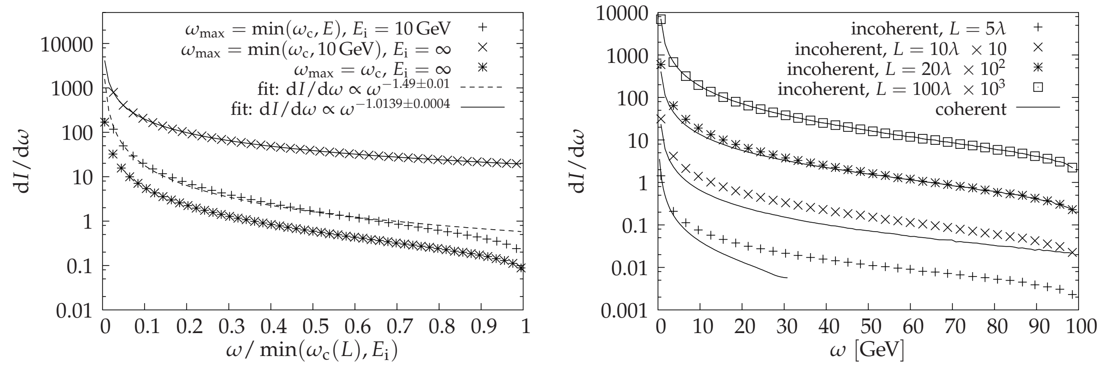

Figure 5.27.: **Left:** Gluon spectrum induced by a medium with length $L = 100\lambda$ with energy conservation ($E_i = 10\,\mathrm{GeV}$) ($dI/d\omega \propto \omega^{-1.49\pm0.01}$), with a cut-off on the gluon spectrum induced by a single scattering ($dI/d\omega \propto \omega^{-1.0139\pm0.0004}$) and without energy constraints ($dI/d\omega \propto \omega^{-1.49\pm0.02}$, figure 5.24 left). **Right:** Gluon spectra for different path lengths in a coherent and an incoherent calculation with energy conservation for $E_i = 100\,\mathrm{GeV}$ ($L_c = 9\,\mathrm{fm}$).

When the total radiated energy is left unconstrained (which is not realistic but instructive) a quasi-incoherent regime is reached for $L > L_c$ with

$$L_c = \sqrt{\frac{2E_i}{\hat{q}}}\,, \tag{5.78}$$

which is the path length needed to radiate the highest possible energy E_i. The power n of the gluon spectrum $dI/d\omega \propto \omega^{-n}$ decreases smoothly from $n = 3/2$ for $L \ll L_c$ to $n = 1$ as for the incoherent spectrum for $L \gg L_c$ (figure 5.26 left). Correspondingly, the energy loss increases quadratically with L below L_c and linearly above L_c (figure 5.26 right). Unlike the power of the spectrum, which varies smoothly over a large range in L, the energy loss shows a sharp transition from the coherent to the incoherent regime at $L = L_c$.

Finally, energy conservation can be implemented by requiring

$$\omega_{\max} = \min(\omega_c, E) \quad \text{with} \quad E = E_i - \sum_j \omega_j\,. \tag{5.79}$$

The sum runs over all gluons that have been radiated so far. This makes sure that the total radiated energy is not bigger than the incoming projectile energy. This has a similar effect as the finite path length in the scenario without energy constraints. In fact, the shape of the resulting spectrum is the same (figure 5.27 left). The normalisation, on the other hand, is different because the number of gluons is larger in the energy conserving scenario. The energy loss is proportional to L^2 for small L but then in levels off to reach $\Delta E = E_i$ at large L (figure 5.26 right).

For large path lengths ($L \gtrsim 2L_c$) the spectrum is dominated by the constraints due to energy conservation and the coherence plays only a minor role. This can be seen by comparing the coherent calculation with energy conservation to an incoherent calculation that also conserves energy (figure 5.27 right). In the incoherent case the spectrum looks for small path lengths very much like the incoherent sum of radiations induced by individual scatterings without further constraints. For $L \approx L_\mathrm{c}$ there is already a strong modification due to energy conservation and for larger L the spectrum approaches the coherent result.

One can thus conclude that the Monte Carlo implementation of the LPM effect based on the formation time of radiated gluons reproduces the characteristic features of LPM suppression. Furthermore, it can be supplemented with energy conservation, which is found to dominate the spectrum for large path lengths $L \gtrsim 2L_\mathrm{c}$ (or small projectile energies).

CHAPTER 6

Conclusions and Outlook

Monte Carlo models for hadronic and nuclear collisions are at the interface between the theory of QCD and experiment. Depending on the class of measurements and the status of the theory, they provide a bridge between QCD and data which involves a varying degree of model assumptions.

In this work the Monte Carlo model JEWEL for jet evolution in ultra-relativistic nuclear collisions is presented. It the absence of medium effects it passes into a standard parton shower evolution followed by a string fragmentation variant. It was shown to describe event shapes, jet rates and the intra-jet distribution $\mathrm{d}N/\mathrm{d}\xi$ measured in e^+e^- collisions sufficiently well. In the presence of a medium, which is in this study taken to be an ideal quark-gluon gas, the parton shower evolution is interleaved with scattering in the medium. It contains a microscopic description of elastic scattering, inelastic processes are at this stage included schematically using a phenomenological model. Ambiguities related to the treatment of recoiling scattering centres and hadronisation in a nuclear environment are outlined but are found to be of minor importance for event shapes and jet rates. Elastic scattering, although leading to a significant suppression of single-inclusive hadron spectra, does not affect these distributions when a soft background cut is applied. Medium induced splitting, on the other hand not only softens but also widens the jet significantly, which is reflected in the event shapes and jet rates. These quantities may thus be able to distinguish between elastic and inelastic energy loss. No strong broadening of the jet is observed, but the angular distributions are sensitive to hadronisation, in particular in connection with the recoiling medium. There are indications that they are largely constrained by energy-momentum conservation. Geometrical aspects and trigger bias effect can also be studied, as an example it was shown that there is no strong surface bias related to collisional energy loss.

Finally, a prescription how inelastic scattering can be included on the same footing as the elastic processes was outlined. There may even be a natural way to treat the LPM effect in the Monte Carlo model.

The microscopic mechanism(s) underlying jet quenching are not firmly established and their theoretical description is incomplete. In view of the complexity of this problem in heavy ion collisions, the Monte Carlo simulation method is particularly suitable for a detailed treatment. Amongst the many open problems in the theory and phenomenology of jet quenching, in particular the following points may be accessible by further developments of JEWEL:

Heavy flavour: The propagation of heavy quarks has recently attracted significant attention [4–7, 106]. The strong suppression of heavy flavours seems to contradict the conjectured dominance of radiative energy loss, which renewed the interest in elastic energy loss. The generalisation to massive quarks is a straightforward extension of JEWEL.

Multi-particle correlations are attractive due to their larger sensitivity to the underlying mechanisms. They are, however, also sensitive to hadronisation, as could be seen in the $k_\perp$ broadening. Therefore, although multi-particle correlations are easily accessible in Monte Carlo models, more careful investigations are needed.

Realistic description of the medium: In the extended version with geometry and expansion the simple model for the medium can easily be replaced by a more realistic scenario. This requires information about the position and time dependent density and temperature that can be obtained from hydrodynamic simulations [184–187].

Radiative energy loss: It is clearly desirable to have a microscopic description of inelastic scattering so that elastic and inelastic processes can be treated on equal footing. Future versions of JEWEL will be equipped with such a description of radiative energy loss in terms of $2 \to 3$ matrix elements, as outlined in section 5.3.2.

Interplay of strongly and weakly coupled regimes: While the splitting of highly virtual partons and their hard interactions are well described by perturbation theory this is not true for softer interactions and the propagation of soft particles through the medium. The uncertainties arising through the regularisation of the perturbative cross section are symptomatic for the appearance of non-perturbative physics. The same holds for the propagation and thermalisation of softer fragments which is not well described by $2 \to 2$ and $2 \to 3$ processes. This directly leads to the question how the parton cascade and the recoiling scattering centres accompanying it hadronise in a high multiplicity environment. These processes may become a test laboratory for understanding how a well-defined partonic projectile interacts and to what extent it thermalises within a finite size medium. From a pragmatic point of view, a parton shower may contribute to this issue by identifying the momentum scales at which a perturbative description breaks down.

There are many other open issues for improving our understanding of jet quenching in an interplay between theory and experiment. One of the most central ones may be how to best characterise a jet within a high multiplicity environment such that unambiguous information about its medium modifications can be obtained. Although it may not be able to resolve these issues, JEWEL can contribute by identifying classes of jet observables, which are sensitive to medium effects but remain sufficiently insensitive to operational uncertainties in the jet definition and theoretical uncertainties like hadronisation. By superimposing simulations of JEWEL on top of the simulated background of heavy ion collisions one can test the sensitivity of different jet observables. On the other hand, by simulating the redistribution of 'background' multiplicity due to the propagation of a jet, JEWEL provides a means to go beyond the simplifying assumption that the medium-modified jet is uncorrelated with the underlying background. These features of JEWEL may contribute to establish to what extent an operational procedure of characterising jet medium modifications is suited to draw model-independent conclusions.

Acknowledgements

First of all, I want to thank my supervisor Johanna Stachel, who always encouraged and supported me and taught me to be confident even in difficult times. She gave me a lot of freedom and was always patient (which was probably not always easy).

I am grateful to Urs Wiedemann for teaching so much about physics and life in physics and his dedication to this project. I also learned from him that working systematically is sometimes advantageous.

Many thanks also to Gunnar Ingelman and Johan Rathsman for many years of fruitful collaboration and for always being there and discussing things when I needed it. I also thank Hans-Jürgen Pirner for an interesting and instructive collaboration.

My thanks go to the students in Heidelberg, Uppsala and at CERN, especially my flat-mates Davide, Guillermo, Pantelis and Wolfgang, for many exciting, interesting and cheerful conversations and discussions and a great time.

Special thanks go to my husband Klaus for his support, his patience, the time we spent together in and around Heidelberg and a lot more things that I cannot list here because it would require a separate book. I want to thank my family, especially my parents and my sisters Anneke and Irene, who always stood by me and believed in me.

Without your support and your contributions I would never have been able to write this thesis.

Appendix

APPENDIX A

Monte Carlo Techniques

The Monte Carlo method[1] can be defined as representing the solution of a problem as a parameter of a hypothetical population, using a random sequence of numbers to construct a sample of the population, from which statistical estimates of the parameter can be obtained [190] . Monte Carlo methods are not only applicable to problems of probabilistic or statistical nature, although they typically amount to a straightforward simulation in these cases, but can also be used for perfectly deterministic or analytical problems. In Monte Carlo simulations of probabilistic or statistical problems the hypothetical population corresponds to the physical states of the system under consideration. Formally, all Monte Carlo calculations are equivalent to integrations. The Monte Carlo estimate $S(r_i, \ldots, r_n)$ of the solution to some problem is a function of the random numbers r_i used in the computation. Usually, these random numbers are distributed uniformly between 0 and 1. S is a Monte Carlo estimate of the integral

$$\int_0^1 \prod_{i=1}^{n} \mathrm{d}x_i S(x_1, \ldots, x_n)\,. \tag{A.1}$$

Important ingredients of Monte Carlo calculations are *random numbers*, that will be discussed later, and *random variables*. A random variable can take more than one discrete or continuous value, the value that will be taken is unpredictable. The probability, with which a particular value will be taken, is given by the *probability density function*. For a single continuous random variable x the probability density function $g(x)$ is defined via

$$g(x) = \frac{\mathrm{d}G(x)}{\mathrm{d}x} \qquad \text{with} \qquad G(x) = \int_{-\infty}^{x} \mathrm{d}x'\, g(x')\,. \tag{A.2}$$

---

[1] For a review of Monte Carlo techniques see also [23, 188, 189].

$G(x)$ is the probability to find a value smaller than x. Physicists often prefer to regard $g(x)\mathrm{d}x$ as the probability that a value between x and $x+\mathrm{d}x$ is taken. In physics probability densities need not be normalised to unity, in some cases the integral over a probability density function has itself a physical meaning. In scattering experiments, for instance, the scattering angle is a random variable and the probability density function is the differential cross section. The integral over the probability density is obviously the total cross section.

The expectation value of a function of a random variable is given by

$$\langle f \rangle = \int \mathrm{d}G(x)\, f(x) = \int \mathrm{d}x\, g(x) f(x) \tag{A.3}$$

and the variance is

$$\sigma^2(f) = \langle f - \langle f \rangle \rangle^2 = \int \mathrm{d}G(x)\, (f(x) - \langle f \rangle)^2 \,. \tag{A.4}$$

The integral of a function $f(x)$ in an interval $[a,b]$ can be estimated by choosing N values x_i distributed randomly in $[a,b]$, summing the function values $f(x_i)$ in these points and dividing by N. According to the law of large numbers the Monte Carlo estimate of an integral over a function f with finite variance converges (in the statistical sense) to its exact value as the number of points approaches infinity

$$\frac{1}{N} \sum_{i=1}^{N} f(x_i) \overset{N\to\infty}{\longrightarrow} \frac{1}{b-a} \int_a^b \mathrm{d}x\, f(x) \,. \tag{A.5}$$

Convergence in the statistical sense means that for every probability p and positive number ϵ there is a k such that for all $N > k$ the probability for the difference between the left- and the right-hand side of equation (A.5) to be smaller than ϵ is greater than p. The central limit theorem says that the Monte Carlo estimate is for large N normally distributed. It is unbiased for all N, i.e. its expectation value is given by the true value of the integral. The variance is for large N given by $\sigma^2(f)/N$.

The speed, with which the Monte Carlo estimate converges, does not depend explicitly on the number of dimensions (although other calculations in the algorithm might take more time in higher dimensions). This means that for small number of dimensions numerical quadrature will be much more efficient while the Monte Carlo integration clearly wins for higher number of dimensions. Since the variance also depends on the variance of the function f, the performance of the Monte Carlo calculation can also be improved by reducing $\sigma^2(f)$. A few of the most important variance reducing techniques are described below.

Integration by Monte Carlo methods is closely related to the problem of generating random numbers distributed according to some probability density $g(x)$. This is the central tool in Monte Carlo simulations but it is also essential for generating the measure $\mathrm{d}G(x) = g(x)\,\mathrm{d}x$ of an integral. Most random number generators provide (pseudo-) random numbers that are uniformly distributed between 0 and 1. The simplest way of generating from this distribution values that are distributed according to $g(x)$ defined on an interval $[a,b]$ is the *hit-or-miss Monte Carlo*. First an upper limit $g_{\max} \geq g(x) \forall x \in [a, b]$ of the function has to be found. Then a value x from a flat distribution on $[a, b]$ has to be generated, i.e. $x = a + R_1(b - a)$ when R_1 is a random number from a flat distribution on $]0, 1[$. The value is accepted with probability $g(x)/g_{\max}$, which means that a second random number R_2 is generated and the value is accepted if $R_2 < g(x)/g_{\max}$. Otherwise the x value is rejected and a new one has to be tried. The advantage of this mathod is that it works for practically all function $g(x)$ without singularities. The disadvantage is that the efficiency, which is given by

$$\frac{\int \mathrm{d}x \, g(x)}{(b - a) g_{\max}} , \tag{A.6}$$

can be vary small when the function strongly varies. In such cases it is advantageous to divide the interval $[a, b]$ into a number of subintervals with smaller variance. Then the sampling procedure has an additional step because before actually generating a value a subinterval has to be chosen. The probability of each subinterval is given by the fraction of the total integral over $g(x)$ it covers.

The best efficiency is reached by the *direct sampling* method, which is, however, only applicable to functions that have an invertible primitive function (which is a serious constraint). The direct sampling makes use of the relation

$$\int\limits_a^x \mathrm{d}x' \, g(x') = R \int\limits_a^b \mathrm{d}x' g(x') = R \left[G(b) - G(a) \right] , \tag{A.7}$$

from which one obtains

$$x = G^{-1} \left(G(a) + R \left[G(b) - G(a) \right] \right) . \tag{A.8}$$

The importance sampling obviously needs no rejection steps which makes it the most efficient method.

The efficiency can also be improved by generating more points in regions where the function values are large. This method in known as *importance sampling* and is also suited for functions that do not have an invertible primitive function. It is mathematically equivalent to a change of integration variable

$$g(x) \, \mathrm{d}x = \frac{g(x)}{h(x)} \, \mathrm{d}H(x) \qquad \text{where} \qquad \mathrm{d}H(x) = h(x) \, \mathrm{d}x . \tag{A.9}$$

In practice it works like this: First a suitable function $h(x)$ has to be chosen. It has to be as close to $g(x)$ as possible, it has to be larger than $g(x)$ on $[a, b]$ and it should be suited for importance sampling or a h-distributed random number generator should be available. Then an x value is generated from $h(x)$ and accepted with probability $g(x)/h(x)$. Importance sampling will improve the efficiency if $\sigma^2(g/h) < \sigma^2(g)$, but it suffers from the small number of available functions h.

For the simulations performed in Jewel a prescription that is a combination of these methods has proven very useful. The problem is how to handle probability densities that depend on many parameters and/or are calculated only during the

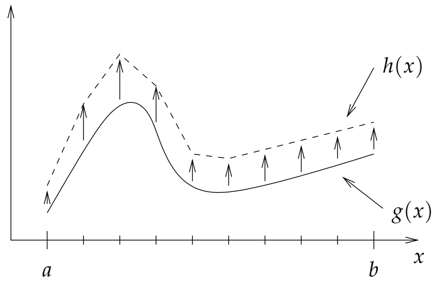

Figure A.1.: Example for a weight function $h(x)$ constructed from an a priori unknown probability density $g(x)$ in an adaptive sampling algorithm.

simulation so that there is no a priori knowledge about them. Often the evaluation of the probability density is costly in terms of run time because it involves numerical integrations. In these cases a weight function can be constructed by testing the function in a few points. For sufficiently smooth functions the prescription sketched in figure A.1 can be used: The probability density $g(x)$ is tested at a few points and the function values are multiplied with a number that is somewhat larger than unity. These points are connected by straight lines and this object is used as weight function $h(x)$ for importance sampling. Generating a value from $h(x)$ involves two steps, first the subinterval has to be chosen according to the integrals, then the value is generated from the straight line in that subinterval using direct sampling.

The advantages of this algorithm are the good efficiency and its flexibility, it is applicable to practically any reasonably smooth function including functions that have to be evaluated numerically or are tabulated. The danger is that the constructed weight function can become smaller than the probability density, especially when the latter varies quickly and/or has spikes that can be cut off. It is therefore advisable to monitor such problems and adjust the number of test points and the factor multiplying the function values at these points.

Other adaptive methods for function sampling and integration are available [188].

For a successful Monte Carlo calculation good random numbers are crucial. True random numbers are uncorrelated and unpredictable. They can only be obtained from physical processes like radioactive decay, noise in an electronic circuit or the time between the arrival of cosmic rays. Nowadays, true random numbers are rarely used in Monte Carlo computations because of the difficulties that come with the construction of devices that observe a suitable process being at the same accurate and very fast. In fact, extended simulations consume huge amounts of random numbers, so that great speed is required and reading in numbers that have been generated before the simulation and are stored on tape is no option. Instead of using true random numbers Monte Carlo codes generate pseudo-random numbers from a mathematical algorithm. Pseudo-random numbers are predictable because the algorithm is deterministic and will, when initialised with the same state, always produce the same sequence of numbers. This property is very useful in practice because it makes debugging of Monte Carlo code a lot easier. Ideally, pseudo-random numbers should be uncorrelated; a requirement that can never be met. Pseudo-random numbers always have some residual correlation, successive d-tuples of pseudo-random numbers generated by a multiplicative congruential generator [2], for instance, lie on a finite (and sometimes quite small) number of hyperplanes [191]. This means that pseudo-random number generators have to be tested and chosen with care and the results obtained from Monte Carlo calculations have to interpreted using common sense. Another important property of pseudo-random number generators is the period. Due to finite machine precision any algorithm will at some point generate a number that has occurred in the sequence before. Form this point on the sequence will repeat itself and therefore be useless.

JEWEL uses PYTHIA's generator, which is based on the algorithm proposed by Marsaglia, Zaman and Tsang [192] for a portable and machine independent generator. It has a period of over 10^{43} and almost 10^9 disjoint sequences that can be selected at initialisation. The state of the generator can be saved to a file at the end of the run and used to initialise the generator the next time so that a simulation can be continued by another run and simulations requiring a lot of statistics can be divided into different runs.

---

[2] Multiplicative congruential generators derive the pseudo-random numbers from the recursion relation $r_{i+1} = ar_i \bmod m$, where the 'mod' operation gives the remainder after dividing ar_i by m. The algorithm has to be initialised with a seed r_0. With suitable choice of the the modulus m and the multiplier a the generator will produce a sequence of pseudo-random numbers between 1 and $m - 1$.

APPENDIX B

Short Manual of JEWEL 1.0

In this section a technical summary of the Jewel 1.0 program will be given, the input parameters and the output format will be explained in somewhat more detail. Version 1.0 contains the full parton shower simulation, elastic scattering in an ideal quark-gluon gas and the effective model for induced radiation. The medium is homogeneous and isotropic and is entirely characterised by the temperature and the path length.

The simulation needs the following information for initialisation. The energy unit is GeV and times and lengths are measured in fm.

Filenames The simulation writes a log file with information about the status of the run and error messages in the directory `logs` and a file with the results in the directory `data`. Furthermore, the status of the pseudo-random number generator is written to a file in the `logs` directory every time one hundredth of the run is completed (including the end of the simulation). Every time a new status is written the old one is deleted so that the file only contains the latest status. These files have the same name but different extensions (`log`, `dat` and `ran`, respectively), the filename has to be specified by the user.

Number of events This is the number of events that will be simulated. Some of them may have to be rejected, the number of successfully simulated events is written to the data file at the end.

Initialisation of pseudo-random number generator It has to specified whether the generator is to be initialised with a status that is stored in a file in the `logs` directory. If this is the case the filename has to be given. Otherwise the default initialisation will be used.

Number of flavours The number of quark flavours is the same everywhere, i.e. the number of flavours in the medium and in the cascade is the same (it is also the number that enters α_s). Since all quarks are treated as massless n_f should not be larger than 3.

parameter	type	this study	sensible range
output filename	char. string		< 80 characters
number of events	integer	$\leq 10^4$	
read in random number gen. status	logical		`true/false`
random number gen. status file	char. string		< 80 characters
n_f	integer	3	$0-3$
Λ_QCD(splitting)	double	0.3 GeV	$0.1-0.5$ GeV
Λ_QCD(scattering)	double	0.25 GeV	$0.1-0.3$ GeV with scatt. of recoils $0.1-0.75$ GeV without scatt. of recoils
Q_0	double	1 GeV	$0.3\,\mathrm{GeV} - \min(E_\mathrm{jet})$
angular ordering	logical	`true`	`true/false`
parent parton	integer	1	$1,2,3,21$
power of energy spectrum	double	7.0	$1-20$
min. energy	double		> 2.5 GeV
max. energy	double		< 200 GeV with scatt. of recoils < 500 GeV without scatt. of recoils
temperature	double	0.5 GeV	$0.1-1$ GeV, $> \Lambda_\mathrm{QCD}(\mathrm{scattering})/3$
path length	double	0, 5 fm	$0-6$ fm with scatt. of recoils $0-10$ fm without scatt. of recoils
f_med	double	0, 3	$0-5$
scattering of recoils	logical		`true/false`
hadronisation	logical		`true/false`
hadronisation of recoils	logical		`true/false`
π^0 decay	logical	`false`	`true/false`

Table B.1.: JEWEL parameters, the values used in this study and sensible ranges for parameter values. These are more guidelines than strict limits.

Running coupling Two values of Λ_QCD have to be given, one for the splitting and one for the scattering processes. The value used for splittings also determines the minimum transverse momentum. Good agreement of the vacuum parton shower with LEP data was obtained with $\Lambda_\mathrm{QCD} = 0.3$ GeV for the branching processes. Results for jet evolution in the medium shown in this work were obtained with $\Lambda_\mathrm{QCD} = 0.25$ GeV for the scattering processes.

Infra-red cut-off Value of Q_0, down to which the perturbative parton shower evolution is simulated. Note that the effective cut-off is given by $\sqrt{Q_0^2 + 4(f \cdot \Lambda_\mathrm{QCD})^2}$ (equation (5.13)).

Angular ordering Angular ordering can be switched on or off. In the medium only subsequent branchings can be ordered, when a scattering occurred between two splittings the second emission will not be ordered even when angular ordering is active.

Parent parton The type of the parton initiating the shower has to be given. JEWEL uses the PYTHIA system for labelling the particles. The numbers corresponding to the quarks are 1 (down), 2 (up), 3 (strange), 4 (charm), 5 (beauty) and 6 (top), the gluon has 21. Since no mass effects are implemented only light quarks or gluons should be chosen.

Power of energy spectrum The energy of the parent parton is distributed according to E^{-n}, the power n has to be given by the user.

Energy range The minimum and maximum energy of the parent parton has to be given. The minimum should be at least 2.5 GeV but larger values are recommended because the use of perturbation theory is better justified for higher energies. Monoenergetic jets can be generated by setting the minimum and the maximum to the same value.

Temperature The temperature of the medium determines the density of scattering centres ($n \propto T^3$) and the Debye mass that is used the regularise the scattering cross section ($\mu_\mathrm{D} = 3T$ is used in the simulation). Therefore, $3T > \Lambda_\mathrm{QCD}(\mathrm{scattering})$ has to be satisfied in order to obtain a finite scattering cross section.

Path length This is the path length L in the medium. To be precise, it is the lifetime of the medium (which is better for practical reasons), which leads to a somewhat smaller path length for particles emitted at large angles relative to the jet axis than, for instance, a rectangular geometry with the same length.

Enhancement of splitting The user has to specify the value of f_med, that will enhance the splitting functions by a factor $(1 + f_\mathrm{med})$ inside the medium. Thus, $f_\mathrm{med} = 0$ reproduces the vacuum splitting.

Scattering of recoiling scattering centres Recoiling scattering centres can either scatter in the medium or propagate without scattering.

Hadronisation Hadronisation can be switched on and off. If it is switched on the user has to specify in addition whether recoiling scattering centres are to be hadronised or not.

π^0 **decay** The π^0 decay can be switched off to save memory in the event record since π^0 are usually quite numerous and produce many daughters.

The parameters are listed in table B.1 together with the values used in this study and the allowed ranges. Unfortunate choices of parameters can, however, upset the simulation even if each value is within the allowed range. The most frequently occurring problem is a lack of memory when the events contain too many particles.

All partons have vanishing rest mass. The shower is initiated by a parton with a certain energy, this information is provided by the user. The first step of the simulation is to assign this parton a virtuality, which is picked from the probability

status code	stage of simulation	meaning
1	parton shower	parton from the cascade that is allowed to split or scatter
2	parton shower	recoiling scattering centre that is allowed to scatter
3	parton shower	recoiling scattering centre that is not allowed to scatter
11	parton shower	parton that has branched
12	parton shower	parton from the shower that has been scattered
14	parton shower	recoiling scattering centre that has been scattered
16	preparation for hadronisation	final parton of the shower that was copied and arranged in strings (was 1 and 3 before)
17	preparation for hadronisation	intermediate partons of the shower (was 11, 12 and 14 before)
18	predation for hadronisation	gluon that was split into a quark-antiquark pair during string finding
22	preparation for hadronisation	recoiling scattering centres when they are not hadronised
23	hadron level	hadron that was removed because it has $\|\eta\| > 1$

Table B.2.: Status codes where they differ from the Pythia convention. In Jewel the meaning of status codes may be specific to a certain stage of the simulation.

distribution equation (5.14). For all practical matters the virtuality is treated as a virtual mass of the parton. The virtuality of the parent parton comes at the cost of the momentum, this is the only point in the simulation at which momentum is not conserved (the energy is conserved). The parton shower evolution is described in section 5. Jet evolution in vacuum is obtained by setting $T = 0$ and $L = 0$ ($T > 0$ and $L = 0$ will also do the job, but then the efficiency is worse). With $T > 0$, $L > 0$ and $f_{\text{med}} = 0$ only elastic scattering in the medium is active, $f_{\text{med}} > 0$ will produce induced splitting in addition. Only induced splitting without elastic scattering can be obtained by setting $T = 0$, $L > 0$ and $f_{\text{med}} > 0$. Partons that cannot split because their virtuality is smaller than Q_{min} are put on the mass-shell (i.e. $m = 0$) but can still scatter until they leave the medium (provided they were produced inside the medium). Hadronisation happens after all splitting and scattering processes, i.e. outside the medium.

The output is organised very much like the Pythia event record [23]. It can contain up to 5000 particles and gives the complete history of the parton shower evolution. The Jewel events can therefore be manipulated with Pythia routines. The first line in the event record is for temporary storage of particles and has no meaning. The second line contains the parent parton already with virtuality followed by all other intermediate and final partons in the parton shower. The event record only contains the scattering centres after the scattering. If hadronisation is switched on, the final partons of the shower are copied down in the record and rearranged into strings that are then hadronised by the Pythia hadronisation routine. All hadrons and their decay chains are listed in the event record. The lines of the event record contain the following information: The status code (`K(I,1)`) is mainly as in Pythia, the exceptions are listed in table B.2. The rest is exactly as in Pythia and will only be shortly summarised here. The particle flavour code (`K(I,2)`) identifies the particles, `K(I,3)` contains the line of the mother, `K(I,4)` the line of the first and `K(I,5)` the line of the last daughter. `P(I,1)` to `P(I,3)` is the three-momentum, `P(I,4)` the energy and `P(I,5)` the (virtual) mass of the particle. `V(I,4)` gives the production and `P(I,5)` the decay time. This is only used for the parton shower simulation. All information is given in the lab frame.

Bibliography

[1] J. D. Bjorken, FERMILAB-PUB-82-059-THY.

[2] M. H. Thoma and M. Gyulassy, Nucl. Phys. **B351** (1991) 491.

[3] E. Braaten and M. H. Thoma, Phys. Rev. **D44** (1991) 2625.

[4] M. Djordjevic, Phys. Rev. **C74** (2006) 064907, [arXiv:nucl-th/0603066].

[5] A. Adil, M. Gyulassy, W. A. Horowitz and S. Wicks, Phys. Rev. **C75** (2007) 044906, [arXiv:nucl-th/0606010].

[6] B. G. Zakharov, JETP Lett. **86** (2007) 444, [arXiv:0708.0816 [hep-ph]].

[7] S. Peigne and A. Peshier, Phys. Rev. **D77** (2008) 114017, [arXiv:0802.4364 [hep-ph]].

[8] K. Zapp, G. Ingelman, J. Rathsman and J. Stachel, Phys. Lett. **B637** (2006) 179, [arXiv:hep-ph/0512300].

[9] S. Domdey, G. Ingelman, J. Rathsman, J. Stachel and K. Zapp, Nucl. Phys. **A808** (2008) 178, [arXiv:0802.3282 [hep-ph]].

[10] M. Gyulassy and X.-n. Wang, Nucl. Phys. **B420** (1994) 583, [arXiv:nucl-th/9306003].

[11] R. Baier, Y. L. Dokshitzer, A. H. Mueller, S. Peigne and D. Schiff, Nucl. Phys. **B484** (1997) 265, [arXiv:hep-ph/9608322].

[12] B. G. Zakharov, JETP Lett. **65** (1997) 615, [arXiv:hep-ph/9704255].

[13] U. A. Wiedemann, Nucl. Phys. **B588** (2000) 303, [arXiv:hep-ph/0005129].

[14] M. Gyulassy, P. Levai and I. Vitev, Nucl. Phys. **B594** (2001) 371, [arXiv:nucl-th/0006010].

[15] X.-N. Wang and X.-f. Guo, Nucl. Phys. **A696** (2001) 788, [arXiv:hep-ph/0102230].

[16] PHENIX, K. Adcox *et al.*, Nucl. Phys. **A757** (2005) 184, [arXiv:nucl-ex/0410003].

[17] PHOBOS, B. B. Back *et al.*, Nucl. Phys. **A757** (2005) 28, [arXiv:nucl-ex/0410022].

[18] BRAHMS, I. Arsene *et al.*, Nucl. Phys. **A757** (2005) 1, [arXiv:nucl-ex/0410020].

[19] STAR, J. Adams *et al.*, Nucl. Phys. **A757** (2005) 102, [arXiv:nucl-ex/0501009].

[20] ALICE, F. Carminati *et al.*, J. Phys. **G30** (2004) 1517.

[21] ALICE, B. Alessandro *et al.*, J. Phys. **G32** (2006) 1295.

[22] CMS, D. G. d'Enterria *et al.*, J. Phys. **G34** (2007) 2307.

[23] T. Sjostrand, S. Mrenna and P. Skands, JHEP **05** (2006) 026, [arXiv:hep-ph/0603175].

[24] G. Marchesini *et al.*, Comput. Phys. Commun. **67** (1992) 465.

[25] T. Gleisberg *et al.*, JHEP **02** (2004) 056, [arXiv:hep-ph/0311263].

[26] R. Baier, Y. L. Dokshitzer, A. H. Mueller and D. Schiff, JHEP **09** (2001) 033, [arXiv:hep-ph/0106347].

[27] C. A. Salgado and U. A. Wiedemann, Phys. Rev. **D68** (2003) 014008, [arXiv:hep-ph/0302184].

[28] N. Armesto, L. Cunqueiro, C. A. Salgado and W.-C. Xiang, JHEP **02** (2008) 048, [arXiv:0710.3073 [hep-ph]].

[29] C. A. Salgado and U. A. Wiedemann, Phys. Rev. Lett. **93** (2004) 042301, [arXiv:hep-ph/0310079].

[30] A. D. Polosa and C. A. Salgado, Phys. Rev. **C75** (2007) 041901, [arXiv:hep-ph/0607295].

[31] A. Majumder and X.-N. Wang, Phys. Rev. **D72** (2005) 034007, [arXiv:hep-ph/0411174].

[32] N. Armesto, C. A. Salgado and U. A. Wiedemann, Phys. Rev. Lett. **93** (2004) 242301, [arXiv:hep-ph/0405301].

[33] N. Armesto, C. A. Salgado and U. A. Wiedemann, Phys. Rev. **C72** (2005) 064910, [arXiv:hep-ph/0411341].

[34] N. Borghini and U. A. Wiedemann, arXiv:hep-ph/0506218.

[35] S. Sapeta and U. A. Wiedemann, Eur. Phys. J. **C55** (2008) 293, [arXiv:0707.3494 [hep-ph]].

[36] R. K. Ellis, W. J. Stirling and B. R. Webber, *QCD and Collider Physics* (Cambridge University Press, Cambridge, United Kingdom, 1996).

[37] V. D. Barger and R. J. N. Phillips, *Collider Physics* (Perseus Publishing, Cambridge, Massachusetts, 1996).

[38] O. Nachtmann, *Elementary Particle Physics* (Springer Verlag, Berlin, 1990).

[39] J. D. Bjorken and S. D. Drell, *Relativistic Quantum Fields* (McGraw Hill, New York, 1964).

[40] C. Itzykson and J. Zuber, *Quantum Field Theory* (McGraw Hill, New York, 1980).

[41] M. E. Peskin and D. V. Schroeder, *An Introduction to Quantum Field Theory* (Addison-Wesley, Reading, Mass., 1995).

[42] G. 't Hooft, Nucl. Phys. **B33** (1971) 173.

[43] G. 't Hooft, Nucl. Phys. **B35** (1971) 167.

[44] G. 't Hooft and M. J. G. Veltman, Nucl. Phys. **B44** (1972) 189.

[45] G. 't Hooft and M. J. G. Veltman, Nucl. Phys. **B50** (1972) 318.

[46] E. C. G. Stueckelberg and A. Petermann, Helv. Phys. Acta **26** (1953) 499.

[47] H. D. Politzer, Phys. Rev. Lett. **30** (1973) 1346.

[48] D. J. Gross and F. Wilczek, Phys. Rev. Lett. **30** (1973) 1343.

[49] Particle Data Group, L. Montanet *et al.*, Phys. Rev. **D50** (1994) 1173.

[50] F. Bloch and A. Nordsieck, Phys. Rev. **52** (1937) 54.

[51] T. Kinoshita, J. Math. Phys. **3** (1962) 650.

[52] T. D. Lee and M. Nauenberg, Phys. Rev. **133** (1964) B1549.

[53] L. N. Lipatov, Sov. J. Nucl. Phys. **20** (1975) 94.

[54] V. N. Gribov and L. N. Lipatov, Sov. J. Nucl. Phys. **15** (1972) 438.

[55] G. Altarelli and G. Parisi, Nucl. Phys. **B126** (1977) 298.

[56] Y. L. Dokshitzer, Sov. Phys. JETP **46** (1977) 641.

[57] V. V. Sudakov, Sov. Phys. JETP **3** (1956) 65.

[58] A. E. Chudakov, Izv. Akad. Naut. SSSR, Ser. Fiz. **19** (1955) 650.

[59] A. H. Mueller, Phys. Lett. **B104** (1981) 161.

[60] B. I. Ermolaev and V. S. Fadin, JETP Lett. **33** (1981) 269.

[61] S. Brandt, C. Peyrou, R. Sosnowski and A. Wroblewski, Phys. Lett. **12** (1964) 57.

[62] E. Farhi, Phys. Rev. Lett. **39** (1977) 1587.

[63] H. Georgi and M. Machacek, Phys. Rev. Lett. **39** (1977) 1237.

[64] R. K. Ellis, D. A. Ross and A. E. Terrano, Nucl. Phys. **B178** (1981) 421.

[65] S. Catani, Y. L. Dokshitzer, M. Olsson, G. Turnock and B. R. Webber, Phys. Lett. **B269** (1991) 432.

[66] B. L. Combridge, J. Kripfganz and J. Ranft, Phys. Lett. **B70** (1977) 234.

[67] S. M. Berman, J. D. Bjorken and J. B. Kogut, Phys. Rev. **D4** (1971) 3388.

[68] R. Blankenbecler, S. J. Brodsky and J. F. Gunion, Phys. Lett. **B42** (1972) 461.

[69] J. F. Owens, E. Reya and M. Gluck, Phys. Rev. **D18** (1978) 1501.

[70] X. Artru and G. Mennessier, Nucl. Phys. **B70** (1974) 93.

[71] M. G. Bowler, Zeit. Phys. **C11** (1981) 169.

[72] B. Andersson, G. Gustafson and B. Soderberg, Z. Phys. **C20** (1983) 317.

[73] B. Andersson, G. Gustafson and B. Soderberg, Nucl. Phys. **B264** (1986) 29.

[74] B. Andersson, G. Gustafson, G. Ingelman and T. Sjostrand, Phys. Rept. **97** (1983) 31.

[75] R. D. Field and R. P. Feynman, Phys. Rev. **D15** (1977) 2590.

[76] R. D. Field and R. P. Feynman, Nucl. Phys. **B136** (1978) 1.

[77] J. Finkelstein and R. D. Peccei, Phys. Rev. **D6** (1972) 2606.

[78] A. Krzywicki and B. Petersson, Phys. Rev. **D6** (1973) 924.

[79] P. Hoyer, P. Osland, H. G. Sander, T. F. Walsh and P. M. Zerwas, Nucl. Phys. **B161** (1979) 349.

[80] A. Ali, E. Pietarinen, G. Kramer and J. Willrodt, Phys. Lett. **B93** (1980) 155.

[81] A. Ali, J. G. Korner, G. Kramer and J. Willrodt, Nucl. Phys. **B168** (1980) 409.

[82] R. D. Field and S. Wolfram, Nucl. Phys. **B213** (1983) 65.

[83] B. R. Webber, Nucl. Phys. **B238** (1984) 492.

[84] T. D. Gottschalk, Nucl. Phys. **B214** (1983) 201.

[85] D. Amati and G. Veneziano, Phys. Lett. **B83** (1979) 87.

[86] A. Bassetto, M. Ciafaloni and G. Marchesini, Phys. Lett. **B83** (1979) 207.

[87] Y. I. Azimov, Y. L. Dokshitzer, V. A. Khoze and S. I. Troian, Phys. Lett. **B165** (1985) 147.

[88] Y. I. Azimov, Y. L. Dokshitzer, V. A. Khoze and S. I. Troyan, Z. Phys. **C27** (1985) 65.

[89] K. J. Eskola, K. Kajantie and J. Lindfors, Nucl. Phys. **B323** (1989) 37, see also `http://www-aix.gsi.de/~misko/overlap`.

[90] L. D. Landau and E. M. Lifshitz, *Course of Theoretical Physics Vol. V: Statistical Physics* (Pergamon Press, Oxford, 2001).

[91] J. D. Bjorken, Phys. Rev. **D27** (1983) 140.

[92] for the STAR, S. Salur, arXiv:0809.1609 [nucl-ex].

[93] J. Putschke and f. t. S. Collaboration, arXiv:0809.1419 [nucl-ex].

[94] A. M. Hamed, arXiv:0809.1462 [nucl-ex].

[95] M. Cacciari and G. P. Salam, Phys. Lett. **B641** (2006) 57, [arXiv:hep-ph/0512210].

[96] M. Cacciari and G. P. Salam, Phys. Lett. **B659** (2008) 119, [arXiv:0707.1378 [hep-ph]].

[97] PHENIX, S. S. Adler *et al.*, Phys. Rev. **C76** (2007) 034904, [arXiv:nucl-ex/0611007].

[98] PHENIX, A. Adare *et al.*, arXiv:0801.4020 [nucl-ex].

[99] PHENIX, S. S. Adler *et al.*, Phys. Rev. **C69** (2004) 034910, [arXiv:nucl-ex/0308006].

[100] PHENIX, S. S. Adler *et al.*, Phys. Rev. Lett. **91** (2003) 072303, [arXiv:nucl-ex/0306021].

[101] PHENIX, S. S. Adler *et al.*, Phys. Rev. **C75** (2007) 024909, [arXiv:nucl-ex/0611006].

[102] STAR, J. Adams *et al.*, Phys. Rev. **C72** (2005) 014904, [arXiv:nucl-ex/0409033].

[103] STAR, B. I. Abelev *et al.*, Phys. Rev. Lett. **98** (2007) 192301, [arXiv:nucl-ex/0607012].

[104] STAR, A. Mischke, arXiv:0804.4601 [nucl-ex].

[105] PHENIX, Y. Morino, arXiv:0805.3871 [hep-ex].

[106] K. Zapp, G. Ingelman, J. Rathsman and J. Stachel, Int. J. Mod. Phys. **E16** (2007) 2072, [arXiv:hep-ph/0702201].

[107] N. Armesto, M. Cacciari, A. Dainese, C. A. Salgado and U. A. Wiedemann, Phys. Lett. **B637** (2006) 362, [arXiv:hep-ph/0511257].

[108] PHENIX, S. S. Adler *et al.*, Phys. Rev. **C74** (2006) 024904, [arXiv:nucl-ex/0603010].

[109] D. Molnar and S. A. Voloshin, Phys. Rev. Lett. **91** (2003) 092301, [arXiv:nucl-th/0302014].

[110] R. J. Fries, B. Mueller, C. Nonaka and S. A. Bass, Phys. Rev. Lett. **90** (2003) 202303, [arXiv:nucl-th/0301087].

[111] V. Greco, C. M. Ko and P. Levai, Phys. Rev. Lett. **90** (2003) 202302, [arXiv:nucl-th/0301093].

[112] R. C. Hwa and C. B. Yang, Phys. Rev. **C67** (2003) 034902, [arXiv:nucl-th/0211010].

[113] R. J. Fries, B. Mueller, C. Nonaka and S. A. Bass, Phys. Rev. **C68** (2003) 044902, [arXiv:nucl-th/0306027].

[114] STAR, J. Adams *et al.*, Phys. Rev. Lett. **91** (2003) 072304, [arXiv:nucl-ex/0306024].

[115] STAR, J. Adams *et al.*, Phys. Rev. Lett. **93** (2004) 252301, [arXiv:nucl-ex/0407007].

[116] STAR, J. Adams *et al.*, Phys. Rev. Lett. **95** (2005) 152301, [arXiv:nucl-ex/0501016].

[117] STAR, D. Magestro, Nucl. Phys. **A774** (2006) 573, [arXiv:nucl-ex/0510002].

[118] H. Stoecker, Nucl. Phys. **A750** (2005) 121, [arXiv:nucl-th/0406018].

[119] J. Casalderrey-Solana, E. V. Shuryak and D. Teaney, J. Phys. Conf. Ser. **27** (2005) 22, [arXiv:hep-ph/0411315].

[120] J. Ruppert and B. Mueller, Phys. Lett. **B618** (2005) 123, [arXiv:hep-ph/0503158].

[121] A. K. Chaudhuri and U. Heinz, Phys. Rev. Lett. **97** (2006) 062301, [arXiv:nucl-th/0503028].

[122] R. B. Neufeld, B. Mueller and J. Ruppert, arXiv:0802.2254 [hep-ph].

[123] B. Betz, M. Gyulassy, D. H. Rischke, H. Stocker and G. Torrieri, arXiv:0804.4408 [hep-ph].

[124] I. M. Dremin, M. R. Kirakosyan, A. V. Leonidov and A. V. Vinogradov, arXiv:0809.2472 [hep-ph].

[125] V. Koch, A. Majumder and X.-N. Wang, Phys. Rev. Lett. **96** (2006) 172302, [arXiv:nucl-th/0507063].

[126] I. M. Dremin, JETP Lett. **30** (1979) 140.

[127] A. V. Apanasenko, N. A. Dobrotin, I. M. Dremin and K. A. Kotelnikov, JETP Lett. **30** (1979) 145.

[128] I. Vitev, Phys. Lett. **B630** (2005) 78, [arXiv:hep-ph/0501255].

[129] C. B. Chiu and R. C. Hwa, Phys. Rev. **C74** (2006) 064909, [arXiv:nucl-th/0609038].

[130] STAR, B. I. Abelev *et al.*, arXiv:0805.0622 [nucl-ex].

[131] PHENIX, A. Adare *et al.*, Phys. Rev. **C77** (2008) 011901, [arXiv:0705.3238 [nucl-ex]].

[132] PHENIX, A. Adare *et al.*, Phys. Rev. **C78** (2008) 014901, [arXiv:0801.4545 [nucl-ex]].

[133] C. B. Chiu and R. C. Hwa, Phys. Rev. **C72** (2005) 034903, [arXiv:nucl-th/0505014].

[134] S. A. Voloshin, Phys. Lett. **B632** (2006) 490, [arXiv:nucl-th/0312065].

[135] G. L. Ma *et al.*, arXiv:0807.3987 [nucl-th].

[136] C.-Y. Wong, arXiv:0806.2154 [hep-ph].

[137] M. H. Thoma, Phys. Lett. **B273** (1991) 128.

[138] A. K. Dutt-Mazumder, J.-e. Alam, P. Roy and B. Sinha, Phys. Rev. **D71** (2005) 094016, [arXiv:hep-ph/0411015].

[139] M. H. Thoma, arXiv:hep-ph/9503400.

[140] E. Braaten and R. D. Pisarski, Nucl. Phys. **B337** (1990) 569.

[141] E. Braaten and T. C. Yuan, Phys. Rev. Lett. **66** (1991) 2183.

[142] H. A. Weldon, Phys. Rev. **D28** (1983) 2007.

[143] W. Keil, Phys. Rev. **D40** (1989) 1176.

[144] E. Braaten and M. H. Thoma, Phys. Rev. **D44** (1991) 1298.

[145] A. Accardi *et al.*, arXiv:hep-ph/0310274.

[146] R. Baier, D. Schiff and B. G. Zakharov, Ann. Rev. Nucl. Part. Sci. **50** (2000) 37, [arXiv:hep-ph/0002198].

[147] L. D. Landau and I. Pomeranchuk, Dokl. Akad. Nauk Ser. Fiz. **92** (1953) 735.

[148] A. B. Migdal, Phys. Rev. **103** (1956) 1811.

[149] R. Baier, Y. L. Dokshitzer, A. H. Mueller, S. Peigne and D. Schiff, Nucl. Phys. **B483** (1997) 291, [arXiv:hep-ph/9607355].

[150] M. Gyulassy, P. Levai and I. Vitev, Phys. Rev. Lett. **85** (2000) 5535, [arXiv:nucl-th/0005032].

[151] M. Gyulassy, I. Vitev, X.-N. Wang and B.-W. Zhang, arXiv:nucl-th/0302077.

[152] U. A. Wiedemann, Nucl. Phys. **A690** (2001) 731, [arXiv:hep-ph/0008241].

[153] A. Kovner and U. A. Wiedemann, arXiv:hep-ph/0304151.

[154] B. G. Zakharov, Phys. Atom. Nucl. **61** (1998) 838, [arXiv:hep-ph/9807540].

[155] B. G. Zakharov, JETP Lett. **63** (1996) 952, [arXiv:hep-ph/9607440].

[156] M. Gyulassy, P. Levai and I. Vitev, Phys. Lett. **B538** (2002) 282, [arXiv:nucl-th/0112071].

[157] X.-N. Wang, Z. Huang and I. Sarcevic, Phys. Rev. Lett. **77** (1996) 231, [arXiv:hep-ph/9605213].

[158] X.-f. Guo and X.-N. Wang, Phys. Rev. Lett. **85** (2000) 3591, [arXiv:hep-ph/0005044].

[159] B.-W. Zhang and X.-N. Wang, Nucl. Phys. **A720** (2003) 429, [arXiv:hep-ph/0301195].

[160] P. Arnold, G. D. Moore and L. G. Yaffe, JHEP **11** (2000) 001, [arXiv:hep-ph/0010177].

[161] P. Arnold, G. D. Moore and L. G. Yaffe, JHEP **11** (2001) 057, [arXiv:hep-ph/0109064].

[162] S. Jeon and G. D. Moore, Phys. Rev. **C71** (2005) 034901, [arXiv:hep-ph/0309332].

[163] S. Turbide, C. Gale, S. Jeon and G. D. Moore, Phys. Rev. **C72** (2005) 014906, [arXiv:hep-ph/0502248].

[164] S. A. Bass *et al.*, arXiv:0808.0908 [nucl-th].

[165] A. Majumder, J. Phys. **G34** (2007) S377, [arXiv:nucl-th/0702066].

[166] X.-N. Wang and M. Gyulassy, Phys. Rev. **D44** (1991) 3501.

[167] I. P. Lokhtin and A. M. Snigirev, Eur. Phys. J. **C45** (2006) 211, [arXiv:hep-ph/0506189].

[168] A. Dainese, C. Loizides and G. Paic, Eur. Phys. J. **C38** (2005) 461, [arXiv:hep-ph/0406201].

[169] T. Renk, arXiv:0806.0305 [hep-ph].

[170] N. Armesto, L. Cunqueiro and C. A. Salgado, arXiv:0809.4433 [hep-ph].

[171] K. J. Eskola, K. Kajantie, P. V. Ruuskanen and K. Tuominen, Nucl. Phys. **B570** (2000) 379, [arXiv:hep-ph/9909456].

[172] W. H. Press, B. P. Flannery, S. A. Teukolsky and W. T. Vetterling, *Numerical Recipes – The Art of Scientific Computing* (Cambridge University Press, Cambridge, 1989).

[173] B. A. Kniehl, G. Kramer and B. Potter, Nucl. Phys. **B582** (2000) 514, [arXiv:hep-ph/0010289].

[174] J. Braun and H.-J. Pirner, Phys. Rev. **D75** (2007) 054031, [arXiv:hep-ph/0610331].

[175] K. Zapp, G. Ingelman, J. Rathsman, J. Stachel and U. A. Wiedemann, arXiv:0804.3568 [hep-ph].

[176] K. Zapp, G. Ingelman, J. Rathsman, J. Stachel and U. A. Wiedemann, arXiv:0805.4759 [hep-ph].

[177] D. Amati, A. Bassetto, M. Ciafaloni, G. Marchesini and G. Veneziano, Nucl. Phys. **B173** (1980) 429.

[178] G. Curci, W. Furmanski and R. Petronzio, Nucl. Phys. **B175** (1980) 27.

[179] W. Liu and R. J. Fries, Phys. Rev. **C77** (2008) 054902, [arXiv:0801.0453 [nucl-th]].

[180] ALEPH, A. Heister *et al.*, Eur. Phys. J. **C35** (2004) 457.

[181] S. Zhang and J. M. Jin, *Computation of Special Functions* (John Wiley & Sons, New York, 1996), `FORTRAN` routines are provided by the authors (`http://jin.ece.uiuc.edu`).

[182] R. K. Ellis and J. C. Sexton, Nucl. Phys. **B282** (1987) 642.

[183] S. Frixione, P. Nason and B. R. Webber, JHEP **08** (2003) 007, [arXiv:hep-ph/0305252].

[184] P. F. Kolb, U. W. Heinz, P. Huovinen, K. J. Eskola and K. Tuominen, Nucl. Phys. **A696** (2001) 197, [arXiv:hep-ph/0103234].

[185] H. Song and U. W. Heinz, Phys. Rev. **C77** (2008) 064901, [arXiv:0712.3715 [nucl-th]].

[186] P. Romatschke and U. Romatschke, Phys. Rev. Lett. **99** (2007) 172301, [arXiv:0706.1522 [nucl-th]].

[187] T. Renk, J. Ruppert, C. Nonaka and S. A. Bass, Phys. Rev. **C75** (2007) 031902, [arXiv:nucl-th/0611027].

[188] F. James, Rept. Prog. Phys. **43** (1980) 1145.

[189] P. R. Bevington and D. K. Robinson, *Data reduction and error analysis for the physical sciences* (McGraw-Hill, Boston, Mass., 1969).

[190] J. H. Halton, SIAM Review **12** (1970) 1.

[191] G. Marsaglia, Proc. Nat. Acad. Sci. **61** (1968) 25.

[192] G. Marsaglia, A. Zaman and W.-W. Tsang, Stat. Prob. Lett. **9** (1990) 35.